# Applying Bayesian models to improve luminescence-based chronologies of Middle to Upper Palaeolithic sites in Iran

Maryam Heydari

Université Bordeaux Montaigne

École Doctorale Montaigne Humanités (ED 480)

THÈSE DE DOCTORAT EN PHYSIQUE DES ARCHÉOMATÉRIAUX

---

# Applying Bayesian models to improve luminescence-based chronologies of Middle to Upper Palaeolithic sites in Iran

*Application des modèles bayésiens pour améliorer la précision des chronologies par luminescence de sites du Paléolithique moyen et supérieur en Iran*

Présentée et soutenue publiquement le 27 août 2020 par

**Maryam HEYDARI**

Sous la direction de Chantal Tribolo
&
Pierre Guibert et Guillaume Guérin

Membres du jury

| | |
|---|---|
| Mme Sanda BALESCU, Maître de conférences, Université de Lille - France | Rapporteuse |
| M. Jean-Guillaume BORDES, Maître de conférences, Université de Bordeaux - France | Rapporteur |
| M. Gilles BERILLON, Directeur de Recherche, Musée de l'Homme - France | Examinateur |
| M. Nicolas CONARD, Professeur, Université de Tübingen - Allemagne | Examinateur |
| Mme Julie DURCAN, Chercheuse, Université de Oxford - Royaume-Uni | Examinatrice |
| M. Morteza FATTAHI, Professeur, Université de Téhéran - Iran | Examinateur |
| Mme Chantal TRIBOLO, Chargée de recherche, IRAMAT-CRP2A - France | Directrice |

This document was typeset with LaTeX.

[library version: February 1, 2021]

آفتابی در یکی ذره نهان
ناگهان آن ذره بگشاید دهان

مولوی

“A sun hidden in a grain: suddenly that grain
opens its mouth and reveals the sun.”

Rumi

# Abstract (FR)

L'analyse statistique des données est un aspect crucial de la datation par luminescence. Pendant des décennies, le traitement de données a principalement eu recours à l'école de pensée classique, dite fréquentiste. Ce n'est que récemment qu'une alternative a pu être fournie grâce au développement de la modélisation bayésienne appliquée à la datation par luminescence dans un environnement R. Cette thèse a pour objectif premièrement, d'étudier les avantages de l'utilisation de ces modèles bayésiens en comparaison avec l'approche fréquentiste et deuxièmement, d'apporter les premières chronologies par luminescence pour des sites majeurs du Paléolithique moyen et supérieur en Iran. De par sa localisation au carrefour de l'Afrique, l'Europe et l'Asie centrale, le plateau iranien est essentiel pour retracer dans le temps les dispersions humaines. Malgré tout, il n'existe à l'heure actuelle que très peu de chronologies couvrant la période du Paléolithique en Iran.

Cette thèse se concentre sur trois sites majeurs : Mirak, situé en marge du désert central iranien, le site de Ghār-e Boof dans la région sud des Montagnes du Zagros, et Bawa Yawan, dans la région centrale des Montagnes du Zagros. La modélisation bayésienne des données chronologiques produites pour le site de Mirak, a abouti pour les assemblages du Paléolithique supérieur, intermédiaire et moyen à des intervalles de, respectivement 21–28 ka, 26–33 ka et 43–55 ka (95 % CI). Pour le gisement de Ghār-e Boof, nous avons daté la culture du Paléolithique supérieure à 37–42 ka (95 % CI), et la culture du Paléolithique moyen à 44–84 ka (95 % CI). Pour le site de Bawa Yawan, des âges compris entre 56 et 90 ka (95 % CI) ont été obtenus pour des assemblages attribués au Paléolithique moyen. L'étude chronologique a également révélé un âge compris dans l'intervalle 12–16 ka pour une unité attribuée à la culture de l'Epipaléolithique.

Basée sur l'étude de ces gisements, cette thèse met en évidence l'intérêt de la mise en application des méthodes bayésiennes dans le cadre de la datation par luminescence. Nous avons notamment remarqué les avantages que présentent les modèles bayésiens testés pour tenir compte des erreurs systématiques partagées par les échantillons, ainsi pour que leur capacité à intégrer des informations chronologiques indépendantes, telles que les contraintes chrono-stratigraphiques ou les âges carbone 14. Ceci nous a ainsi permis d'améliorer la précision des chronologies paléolithiques pour l'Iran. De plus, cette thèse teste la capacité de ces modèles bayésiens à obtenir une dose centrale juste pour les échantillons bien blanchis, contrairement aux modèles fréquentistes, lorsque les signaux de quartz sont proches de la limite de saturation ou lorsque l'hétérogénéité du débit de dose bêta dans le sédiment environnant est élevée.

# Abstract (EN)

Statistical data analysis is a fundamental aspect of luminescence dating. For decades, data processing predominantly employed the frequentist (classic) school of thinking. Only recently, the development of Bayesian modelling specifically for luminescence dating in R environment, has provided an alternative. This thesis aims firstly to provide the first luminescence-based chronologies for Middle-Upper Palaeolithic key sites in Iran, and secondly to discuss the benefits of applying Bayesian models over the frequentist approach. Due to its location at the intersection between Africa, Europe and Central Asia, the Iranian plateau is vital in tracking human dispersal over time. Despite this, there are very few chronologies spanning the Palaeolithic period in Iran.

This thesis focuses on three key sites: Mirak, located at the margin of the central Iranian desert, the site of Ghār-e Boof in the southern Zagros Mountains, and Bawa Yawan in the central Zagros Mountains. Bayesian modelling of chronologies produced for the site of Mirak, date Upper, Intermediate and Middle Palaeolithic assemblages to 21–28 ka, 26–33 ka and 43–55 ka (95 % CI) respectively. For the site of Ghār-e Boof, I dated the Upper Palaeolithic culture to 37–42 ka (95 % CI) and the Middle Palaeolithic culture to 44–84 ka (95 % CI). For the site of Bawa Yawan, ages spanning 56–90 ka (95 % CI) were obtained for assemblages attributed to the Middle Palaeolithic. The chronological study also revealed an age range of 12–16 ka for a unit attributed to the Epipalaeolithic culture.

Based on the study of these sites, this thesis discusses the essential aspect of applying Bayesian methods in luminescence dating. I particularly note the benefits of Bayesian models to address systematic shared errors between samples and the ability to include independent chronological information, such as stratigraphic constraints or radiocarbon ages. This has helped to improve the precision of the Palaeolithic chronologies for Iran. Furthermore, this thesis tests Bayesian models' ability to obtain an accurate central dose for well-bleached samples compared to one frequentist model, when quartz signals are close to saturation or when beta-dose rate heterogeneity in the surrounding sediment is high.

# Résumé étendu

La modélisation bayésienne pour la datation au carbone 14 a été développée il y a plus de vingt ans. Elle est aujourd'hui devenue un outil habituel : ses propriétés permettent d'intégrer les contraintes chrono-stratigraphiques de façon à augmenter la précision des chronologies établies par le carbone 14.

Le développement de la modélisation bayésienne pour la datation par luminescence a été plus lente, et ce, en raison de problèmes additionnels, comme par exemple le nombre important de paramètres à prendre en considération dans l'équation d'âge, ou encore la difficulté à gérer certaines incertitudes de mesures telles que les erreurs systématiques partagées. Ce n'est que récemment qu'un ensemble d'outils adéquats a été développé dans un environnement R, pour d'une part, déterminer la dose équivalente pertinente à partir de la distribution des données de luminescence pour un échantillon donné, et d'autre part, calculer un ensemble d'âges en prenant en compte les contraintes chrono-stratigraphiques ou d'autres informations indépendantes tels des âges carbone 14. Cependant, les tests et la mise en pratique de ces nouveaux outils sont restés anecdotiques jusqu'à aujourd'hui.

Dans cette thèse, la modélisation bayésienne pour la chronologie par luminescence stimulée a été amplement testée et mise en œuvre, permettant ainsi de fournir des chronologies précises pour des gisements majeurs du Paléolithique moyen et du Paléolithique supérieur en Iran.

Les sites paléolithiques d'Iran sont d'une importance cruciale pour comprendre les anciennes dispersions humaines, de par leur localisation dans une région qui connecte l'Europe, l'Afrique et l'Asie. En effet, un nombre considérable de modèles de dispersion suggère que les routes de migration des hommes anatomiquement modernes (HAM) provenant d'Afrique traversaient l'Iran pour rejoindre l'Asie. De plus, une partie du pays est également étudiée dans le cadre des recherches sur l'occupation néandertalienne. Malheureusement, les données chronologiques attribuées aux occupations humaines pendant la période du Paléolithique moyen et supérieur sont très peu nombreuses, rendant difficile l'intégration des découvertes dans un cadre plus large. Dans cette thèse, les premières chronologies par luminescence ont été établies pour trois gisements majeurs du Paléolithique moyen et supérieur en Iran, en collaboration avec l'Université de Tarbiat Modares en Iran, Le Musée de l'Homme en France, l'Université de Tübingen et le Musée de l'Homme de Néandertal en Allemagne.

En complément aux deux chapitres fournissant des données détaillées respectivement sur le Paléolithique en Iran, et sur la méthode de datation par luminescence et les analyses bayési-

ennes, ce travail est structuré en quatre chapitres, parmi lesquels trois sont constitués d'articles publiés ou soumis. Ces chapitres correspondent à quatre études fondamentales s'articulant autour de deux objectifs principaux : 1) établir un cadre chronologique pour les gisements du Paléolithique moyen et supérieur en testant et en appliquant les modèles bayésiens de datation par luminescence ; 2) proposer une réflexion et alimenter le débat autour des potentiels avantages de l'application des modèles bayésiens dans la datation par luminescence, en comparaison avec les modèles classiques utilisés communément par l'école fréquentiste.

La première étude (Ch. 2) est axée sur la mise en application des modèles statistiques bayésiens dans le cadre de deux expériences réalisées en laboratoire, avec l'objectif de débattre du potentiel de la modélisation bayésienne pour estimer la dose équivalente centrale d'échantillons bien blanchis. La justesse de la mesure de la dose centrale a notamment était testée à l'aune de deux problématiques importantes : la saturation du signal, lorsque l'on travaille avec de fortes doses, et les fortes dispersions des doses équivalentes des grains (ou parties aliquotes de l'échantillon) dues, quant à elle, à l'hétérogénéité du débit de dose bêta. Différents modèles de distributions ont été testés afin de découvrir le meilleur paramétrage grâce auquel une dose centrale juste pourrait être obtenue.

Dans la seconde étude (Ch. 3), la modélisation bayésienne a été employée pour établir les premières données chronologiques sur le site du Paléolithique moyen et supérieur de Mirak. Ce gisement est situé à la limite nord du désert central iranien, Dasht-e Kavir, et délimité au sud par des cônes de déjection alluviale des Montagnes d'Alborz. Ce couloir entre les Montagnes d'Alborz, au nord, et le désert de Dasht-e Kavir, au sud, est considéré comme une route probable de dispersion pendant les Paléolithique moyen et supérieur. Les assemblages archéologiques in situ sur le gisement de Mirak ont été associés, soit au Paléolithique moyen, soit au Paléolithique supérieur. Une couche intermédiaire a également été observée ; elle comprenait des traces d'industries attribuables à la fois au Paléolithique moyen et au Paléolithique supérieur. Un large nombre d'échantillons provenant de ce gisement, vingt-deux en tout, ont été étudiés pour fournir une chronologie complète par datation par luminescence basée sur les analyses des quartz et des feldspaths. Le modèle bayésien ainsi que le modèle classique fréquentiste ont été mis en application pour comparer leur précision. L'analyse portait notamment sur la gestion des erreurs systématiques partagées par les échantillons, erreurs dues principalement aux instruments de mesure utilisés, ainsi que sur l'effet de l'intégration de l'ordre chrono-stratigraphique.

Dans la troisième étude (Ch. 4), un premier cadre chronologique basé sur la datation par luminescence a été établi pour le gisement du Paléolithique moyen et supérieur de Ghār-e Boof dans le sud du Zagros. De par sa situation géographique, à la fois proche du Levant et de la Péninsule arabique, le site pourrait avoir été un passage fréquenté par les HAM venant d'Afrique et se dirigeant vers l'Asie Centrale. Ghār-e Boof est bien connu pour ses riches assemblages, attribués à la période du Paléolithique supérieur nommée Rostamien, et déjà datés par carbone

14. Nous avons réussi, dans le cadre de cette thèse, à fournir une chronologie complète du gisement pour les périodes du Paléolithique moyen et du Paléolithique supérieur. Nous avons notamment analysé l'intégration de l'ordre chrono-stratigraphique, et des données de datation par carbone 14 disponibles, à la datation par luminescence dans le cadre de la modélisation bayésienne des âges.

Enfin, dans notre quatrième et dernière étude (Ch. 5), nos recherches se sont concentrées sur le site de Bawa Yawan, dans les Montagnes centrales du Zagros, dans la Province du Kermanshah. La plupart des restes humains (HAM et Néandertaliens) ont jusqu'à présent été découverts dans cette région, d'où son importance dans les recherches sur le Paléolithique. Le gisement comprend une large séquence allant du Paléolithique moyen au Paléolithique supérieur et à l'Epipaléolithique. Les assemblages sont actuellement en cours d'étude, et aucune attribution culturelle précise n'a encore été déterminée. La modélisation bayésienne a été utilisée pour palier le problème de la saturation du signal du quartz, observée dans la plupart des échantillons, prévenant ainsi une sous-estimation des doses équivalentes. Des estimations préliminaires de datations sont ici présentées. Il s'agit de la première chronologie par luminescence portant sur la région centrale du Zagros.

Cette thèse démontre que les modèles bayésiens semblent plus adéquats que les modèles classiques utilisés pour évaluer la dose équivalente centrale. Nous avons notamment prouvé, grâce à nos expériences réalisées en laboratoire, que le modèle classique et largement utilisé du Central Age (en réalité Dose) Model sous-estime la dose centrale vraie lorsque celle-ci est proche de la saturation du signal, tandis que l'approche bayésienne permet de fournir des résultats justes. La même observation a été réalisée pour des distributions de dose équivalente asymétriques, c'est-à-dire des distributions de dose équivalente sur-dispersées du fait de l'hétérogénéité du débit de dose bêta. Nous en avons conclu que les modélisations par des distributions gaussiennes et log-normales utilisant l'inférence bayésienne sont plus aptes à estimer de façon juste la dose centrale des échantillons blanchis. Par conséquent, en nous basant sur les résultats de cette étude, nous avons utilisé la distribution gaussienne du modèle bayésien pour établir une chronologie complète pour le reste de nos travaux.

Les données chronologiques obtenues dans cette thèse comprennent une séquence temporelle longue, allant du Paléolithique moyen au Paléolithique supérieur, ainsi qu'un âge supplémentaire associé à l'Epipaléolithique. La chronologie établie pour la culture du Paléolithique moyen est comprise entre 43 ka et 55 ka (95 % CI) pour le gisement de Mirak, en marge du désert de Dasht-e Kavir. Ainsi, l'occupation sur ce site, associée à la pratique de la méthode Levallois typique du Moustérien du Zagros est attribuable au Paléolithique moyen tardif. Bien que plusieurs gisements du Paléolithique moyen aient été découverts à proximité du désert central iranien, il s'agit de la première chronologie associée à cette culture pour cette région.

La chronologie du Paléolithique moyen établie pour le gisement de Ghār-e Boof est comprise

entre 44 ka et 84 ka (95 % CI) pour les couches IV, V et VI. En général, les assemblages sont de faible densité et indiquent des occupations temporaires. Là encore, il s'agit des premières données chronologiques obtenues pour la période du Paléolithique moyen dans la région sud du Zagros. En ce qui concerne la région centrale du Zagros, pour le gisement de Bawa Yawan, nos données chronologiques pour les assemblages du Paléolithique moyen donnent un intervalle compris entre 56 ka et 90 ka (95 % CI). Ce résultat pourrait concorder avec la datation de Ghār-e Boof, mais les recherches actuelles ne permettent pas encore de comparer les assemblages. De plus, cet intervalle chronologique s'avère être plus ancien que celui établi par le carbone 14 pour les mêmes niveaux dans ce site. Ainsi, il sera essentiel, dans les travaux à venir, de découvrir les raisons de cette divergence. Les résultats chronologiques des couches dites de transition, dans lesquelles ont été découverts des assemblages du Paléolithique moyen et du Paléolithique supérieur sur les sites de Mirak et de Ghār-e Boof (AH Ivd), s'étendent sur une période comprise entre 26 ka et 33 ka (95 % CI) pour le premier et entre 44 ka et 50 ka (95 % CI) pour le second site. À Ghār-e Boof, la chronologie que nous avons établie concorde avec la période transitionnelle que nous connaissons au Levant. Cependant, la période obtenue pour le gisement de Mirak est bien plus récente comparée à celles établies pour les niveaux intermédiaires à Zagros, et au Levant en général. Cela pourrait être dû à un éventuel remaniement post-dépositionnel dans le sédiment. En parallèle, une analyse typo-technologique révèle certaines similarités avec les industries trouvées dans les couches de transition du Zagros.

La contribution qu'apporte cette thèse aux chronologies des assemblages attribués au Paléolithique supérieur à la périphérie de Dasht-e Kavir, sur le gisement de Mirak, est comprise entre 21 ka et 28 ka (95 % CI). Les industries lithiques de ce gisement montrent des similarités avec les cultures du Paléolithique supérieur du Zagros (Baradostien ou Aurignacien du Zagros). Néanmoins, en raison de la faible densité des assemblages lithiques découverts et de l'éventuel remaniement post-dépositionnel mentionné plus haut, l'attribution chronologique devrait être utilisée avec précaution. La chronologie par luminescence établie pour la culture dite du Rostamien découverte sur le gisement de Ghār-e Boof (unités AHs IIIa, b, c et AHs IV) est comprise entre 37 ka et 42 ka (95 % CI). Ces dates concordent avec celles livrées par le carbone 14 pour cette culture (35–42 ka cal. BP, établi pour AHs III, IIIa, b, c et AHs IV). La chronologie du Paléolithique supérieur de Ghār-e Boof concorde avec quelques-unes des chronologies disponibles établies pour la région centrale du Zagros, bien que celles-ci fassent référence à deux cultures distinctes, le Rostamien d'un côté, et le Baradostien ou Aurignacien de l'autre.

L'âge attribué aux assemblages de l'Epipaléolithique sur le gisement de Bawa Yawan est compris entre 12 ka et 16 ka ($2\sigma$). Il n'existe pas d'autres âges obtenus par des méthodes physiques attribués à cette période en Iran. Néanmoins, cet âge s'intègre bien dans la période associée à cette culture au Levant.

En résumé, cette thèse fournit avec succès les premières datations par luminescence pour des

gisements du Paléolithique moyen et du Paléolithique supérieur – comprenant également un âge correspondant à l'Epipaléolithique – dans trois différentes zones géographiques en Iran. Les chronologies établies pour le Paléolithique supérieur à la limite nord du désert central iranien, à Mirak, sont plus récentes que celles obtenues pour la région sud et centrale des Montagnes du Zagros, respectivement à Ghār-e Boof et à Bawa-Yawan. La chronologie du Paléolithique supérieur pour le gisement de Ghār-e Boof est conforme aux chronologies établies pour les gisements de la région centrale du Zagros. L'âge obtenu pour l'Epipaléolithique à Bawa-Yawan s'inscrit dans la période établie pour les assemblages similaires au Levant.

Nous avons testé plusieurs aspects des modèles bayésiens, pour mettre en évidence tout son potentiel et ses avantages par rapport aux modèles classiques de référence, dans le contexte de la datation par luminescence appliquée à l'archéologie. Nous avons démontré que les résultats bayésiens sont plus justes dans deux cas spécifiques : lorsque les doses sont proches de la limite de saturation, et dans le cas de distributions de débits de dose bêta (et par conséquent, de doses équivalentes) fortement asymétriques. Ces deux cas spécifiques mis à part, nous avons aussi démontré que, dans la plupart des cas, l'apport de la modélisation bayésienne n'est pas significatif en l'absence d'informations chronologiques supplémentaires, telles que l'ordre chronostratigraphiques et les âges carbone 14. Par conséquent, la modélisation bayésienne pourrait s'avérer ne pas être le premier choix dans de nombreux contextes d'applications, notamment à cause de la dimension extrêmement chronophage du calcul des modèles. De plus, l'emploi de ces modèles exige une maîtrise et une compréhension de chaque étape de l'analyse qui, dans le cas contraire, peut conduire à des résultats erronés. Néanmoins, lorsque les contraintes stratigraphiques et les âges carbone 14 indépendants sont disponibles, les chronologies basées sur les modèles bayésiens sont préférables aux modèles classiques puisque l'amélioration de la précision des résultats finaux devient significative. Cependant, il serait avantageux, à l'avenir, de mesurer les performances des modèles bayésiens et fréquentistes, tels que mis en pratique dans cette thèse, dans le cadre d'expériences extrêmement contrôlées, en utilisant par exemple des ensembles de données crées artificiellement.

# Extended Summary

Over the last 20 years, Bayesian modelling has been developed for radiocarbon ($^{14}$C) dating and has become a common tool in data processing. It enables the inclusion of knowledge about stratigraphic order to increase the precision of the $^{14}$C chronologies. The development of Bayesian modelling for luminescence dating data, however, has been slower, as there are a number of additional issues to incorporate. These include the high number of parameters considered within the age equation, and the complexity in handling uncertainties, such as shared systematic errors. Only recently, a set of appropriate tools have been developed in the R environment. This has enabled both the determination of the equivalent dose from luminescence data distributions, and the calculation of a set of ages (with an ability to include stratigraphic constraints and independent age information, e.g., $^{14}$C ages). However, testing and application of these new tools has remained anecdotal to date.

In this thesis, Bayesian modelling has been extensively tested and employed in luminescence dating to provide precise chronologies for key Middle-Upper Palaeolithic sites in Iran. Due to its location connecting Europe, Africa, and Asia, Iran is of importance in understanding ancient human dispersal routes. A considerable number of dispersal models assume migration routes of Anatomically Modern Humans (AMH) from Africa, through Iran and into Asia. Part of Iran is also considered in studies focused on Neanderthal occupation. Unfortunately, chronological data attributed to human settlements in the Middle-Upper Palaeolithic period are very scarce. This makes it difficult to constrain the succession of past events in space and time. In this thesis, I established the first luminescence-based chronologies for three key Middle-Upper Palaeolithic sites in Iran. This work was in collaboration with the University of Tarbiat Modares (Iran), the Museum of Man (France), the University of Tübingen (Germany) and the Neanderthal Museum (Germany).

In addition to introductory chapters on the Palaeolithic in Iran, luminescence dating, and Bayesian analyses, this manuscript is structured into four chapters corresponding to four primary studies. Three of these studies have been published or submitted for publication. These studies pursue two main aims: (1) to establish chronological frameworks for Middle-Upper Palaeolithic sites while testing and applying Bayesian models to luminescence dating, and (2) to discuss potential advantages of applying Bayesian models to luminescence dating in comparison with commonly used classical models from the frequentist school. During this thesis, I developed four different studies to achieve primary aims summarised as follows.

The first study (Ch. 2), focuses on the application of statistical models for two laboratory-controlled experiments to discuss the potential of Bayesian modelling in estimating the central dose of well-bleached samples. In particular, the accuracy of central dose determination was tested in relation to two important issues: signal saturation (when dealing with high doses), and overdispersion due to beta-dose rate heterogeneity. Distributions were assessed to investigate the best parameterisation to accurately obtain a central dose.

This thesis shows that Bayesian models appear to be more suitable for estimation of a central dose compared to the classical models used. In particular, our laboratory-controlled experiments show that the classical and widely used Central Age (Dose) Model (CDM) underestimates the true central dose when a signal is close to saturation, whilst the Bayesian approach leads to a more accurate result. A similar finding was observed for skewed equivalent dose distributions, i.e. where distributions displaying high over-dispersion due to beta dose rates heterogeneity. Here, I concluded that Gaussian and lognormal distributions using Bayesian inference are most likely to accurately estimate the central dose of well-bleached samples. Based on the results of this study, the Gaussian distribution of the Bayesian model was used for establishing the full chronologies for the subsequent studies.

In the second study (Ch. 3), Bayesian modelling was employed to establish the first chronological data for the Middle-Upper Palaeolithic site of Mirak. The site is located at the northern fringe of the central Iranian desert (Dasht-e Kavir) and is bordered by alluvial fans from the Alborz Mountains to the south. This corridor between the Alborz Mountains and the Dasht-e Kavir is considered to have been a potential route for human dispersal during the Late Palaeolithic. In situ archaeological assemblages at Mirak are associated with the Middle or the Upper Palaeolithic. A more intermediate layer, with signs of both Middle and Upper Palaeolithic industries, was also observed. Based on both quartz and feldspar analysis, a complete luminescence dating chronology is presented for this site through 22 samples. A comparison was undertaken between Bayesian and classical frequentists models to discuss the precision of each model. In particular, I assessed the role of addressing systematic shared errors between samples and the influence of including stratigraphic constraints.

In the third study (Ch. 4), the first luminescence-based chronological framework for the Middle-Upper Palaeolithic site of Ghār-e Boof in the southern Zagros was established. Due to its relative proximity to the Levant and the Arabian Peninsula, this site has the potential to have rendered an essential passage for AMH from Africa towards central Asia. Ghār-e Boof is well-known for its rich Rostamian assemblages attributed to an Upper Palaeolithic period, which had been previously dated using $^{14}$C. Here, I aimed to provide a complete chronologies for the Middle to Upper Palaeolithic of the site. In particular, I tested the influence of including $^{14}$C with stratigraphic constraints within the luminescence data for Bayesian modelling of the ages.

The fourth study (Ch. 5) focused on the site of Bawa Yawan, located in the central Zagros

Mountains (Kermanshah province). This region is of significant importance to Palaeolithic studies due to the discovery of human remains (AMH and Neanderthals). The site contains an extended sequence from Middle to Upper and Epipalaeolithic periods. This site is currently under investigation, and so no precise cultural attribution has been undertaken yet. In this study, Bayesian modelling was used to address the prevalence of quartz signal saturation to prevent dose underestimation. Preliminary age estimate presented in this study provide the first luminescence chronology for central Zagros region.

The chronological data presented in this thesis details a long temporal sequence from the Middle to the Upper Palaeolithic period plus one age associated with the Epipalaeolithic. The established chronology for Middle Palaeolithic culture spans 43–55 ka (95 % CI) at Mirak. This period refers to the Late Middle Palaeolithic, encompassing Levallois technique attributed to Mousterian in the site. Although several Middle Palaeolithic sites have been discovered in the proximity of the central Iranian desert, this is the first chronology assigned for this culture in the area.

The Middle Palaeolithic chronology established for the site of Ghār-e Boof falls within 44–84 ka (95 % CI) for layers IV, V, and VI. These assemblages are generally based on flake production and indicate a temporary occupation. Here this study also presents the first chronological data associated to the Middle Palaeolithic period in southern Zagros.

In the central Zagros, at Bawa Yawan, our chronological data assigned to Middle Palaeolithic encompasses 56–90 ka. This is potentially consistent with the ages for Ghār-e Boof, but the study of this site is ongoing, and a comparison between the assemblages is required. In addition, the luminescence ages presented here are older than the corresponding chronologies determined using $^{14}$C for the site. Thus, to have more clarity here, it is essential to investigate the reason for this discrepancy.

The chronological results for Intermediate layers, in which both Middle and Upper Palaeolithic assemblages were discovered, at the site of Mirak and the site of Ghār-e Boof (AH IVd) range from 26—33 ka (95 % CI) and 44–50 ka (95 % CI) respectively. In Ghār-e Boof, our established chronology is consistent with the transitional period seen in the Levant. However, the range for the site of Mirak is much younger than other established periods referring to Intermediate levels in Zagros, and the Levant in general. This could be due to possible reworking of the sediment. Alongside this, techno-complex analysis has unravelled some similarities between industries found in the intermediate layers in Mirak and Zagros.

The contribution of this thesis to chronologies for the Upper Palaeolithic assemblages at the margin of Dasht-e Kavir (in the site of Mirak) resulted ages in the range 21–28 ka (95 % CI). The lithic artefacts from the site show similarities with Upper Palaeolithic cultures in Zagros (Baradostian or Zagros Aurignacian). Despite this, chronological attribution here should be employed with caution due to a sparse number of discovered lithic artefacts and the possibility of sediment

reworking at the site.

The luminescence chronology established for the Rostamian culture discovered in the site of Ghār-e Boof (units AHs IIIa, b, c and AHs IV) falls within the range of 37–42 ka (95 % CI). These ages are in agreement with the $^{14}$C ages (ca 35-42 ka cal. BP, established for AHs III, IIIa, b, c and AHs IV) determined for this culture. $^{14}$C ages are also available for an additional unit (III), attributed to the youngest Palaeolithic, but this unit was not sampled for luminescence dating. The Upper Palaeolithic chronology of Ghār-e Boof is consistent with available chronologies established for central Zagros, however these refer to two distinct cultures (Rostamian vs Baradostian or Zagros Aurignacian).

The age attribution to the Epipalaeolithic assemblages in the site of Bawa Yawan resulted in a range of 12–16 ka ($2\sigma$). There are no other reported ages attributed to this period in Iran, but the date does lie in the period associated with this culture in the Levant.

In summary, this thesis successfully provides the first luminescence ages for Middle and Upper Palaeolithic sites (with one age associated with the Epipalaeolithic period) in three different geographical locations in Iran. The established chronologies attributed to the north edge of central Iranian desert at Mirak are younger in comparison with ages associated with the southern (Ghār-e Boof) and central (Bawa Yawan) Zagros Mountains.

The Upper Palaeolithic chronology for the site of Ghār-e Boof is consistent with a few established chronologies available for the sites in central Zagros. The Epipalaeolithic age falls within the established period for Levantine assemblages.

I have tested various aspects of Bayesian models to unravel its potential and highlight its advantages over classical-based models in luminescence dating. I have shown that Bayesian outcomes are more accurate in cases where doses are close to the saturation limit, or where dose distributions are highly positively skewed. However, in the absence of additional independent chronological information (such as stratigraphic constraints and $^{14}$C ages) the advantage of Bayesian age models is not significant. Thus, as the computations of models is also very time-consuming, Bayesian modelling might not always be the first choice in many scenarios. In addition, employing these models requires a precise understanding of each step of analysis; or else it can be error-prone. Nevertheless, when well-established stratigraphic constraints, as well as independent $^{14}$C dates, are available, Bayesian-based chronologies models are preferred over classical models. Here, the improvement in precision of final ages can become significant. In future studies, it would be valuable to assess the performance of Bayesian and frequentist models, through highly controlled experimental settings, e.g., using artificially created datasets.

# Contents

# List of Tables

# List of Figures

# 1 Introduction

## 1.1 Preface

Once submitted, a PhD thesis becomes a condensed collection of new data and exciting new findings within a particular scientific discipline, presented with the hope of having added a tiny piece to a larger puzzle. Beyond this, every PhD thesis reflects a very personal recollection of experiences and events.

My journey in France started before my thesis even commenced. In January 2016, after finishing my master in geophysics, I arrived in Bordeaux as a self-financed guest researcher to work on a project entitled *"Luminescence chronology for the Lower, Middle and Upper Palaeolithic occupations of Kozarnika, Bulgaria"*. This project provided me with a unique opportunity to prepare 25 luminescence samples, apply various luminescence-dating techniques (OSL, IRSL and VSL) and produced a complete luminescence chronology for the site of Kozarnika (e.g., Guadelli et al., 2005; Sirakov et al., 2010; Tillier et al., 2017). During my first six months in Bordeaux, I applied for a LabEx PhD position at the IRAMAT-CRP2A to work on the project *"Origin, evolution and future of the Middle Palaeolithic in Iran: obtaining first chronological milestones by luminescence dating methods"*. In September 2016, I started work on this exciting project.

Unfortunately, accessing originally planned Middle Palaeolithic sites in Iran was harder than anticipated. The first fieldwork was delayed to my second year of the PhD, and had to focus on a different location to what was originally envisaged. Luckily, in my first year, I could continue analysing the samples from Kozarnika. Here, I tested the Violet Stimulated Luminescence (VSL, Jain 2009; Ankjærgaard et al. 2013, 2016) protocol and applied a new radiofluorescence (IR-RF, Trautmann et al. 1998, 1999) dating protocol on feldspar (developed in Bordeaux, Frouin et al. 2017) to the lower section of the sequence. In the meantime, I was introduced to exciting new research taking place at the IRAMAT-CRP2A: using Bayesian statistical modelling for data analysis in luminescence dating. Due to the delay of fieldwork to collect samples from Iran, I had the chance to learn more about Bayesian modelling. This situation created the foundation of my first paper. I applied Bayesian models to two laboratory-controlled experiments and discussed the potential advantages of such models.

Inspired by this new possibility, I was eager to continue investigating the application of Bayesian models in luminescence chronology and finally test and use these models to establish the first chronological milestones on Palaeolithic sites in Iran. With access gained to additional fieldwork sites in addition to those originally planned, the focus of my thesis shifted from the *"origin of the Middle Palaeolithic"* to *"the Middle-Upper Palaeolithic"*. As a result, a new thesis title was generated in my third year: *"Applying Bayesian models to improve luminescence-based chronologies of Middle to Upper Palaeolithic sites in Iran"*.

## 1.2 Background and objectives

Luminescence dating is a chronological method that has been developed and advanced in the last few decades. It has commonly been used in archaeological studies to track ancient human settlements over time and space. Luminescence dating estimates the time elapsed since last exposure of minerals to sunlight and heat, e.g., optically stimulated and thermo – luminescence dating. An age is calculated by the simple division of two parameters: the equivalent dose (an approximation of the total dose received by the minerals) by the dose rate (the rate at which this dose, predominantly emanating from the radioactive content of the sediments, was administered).

In reality, determination of these two parameters incorporates an estimation of many more factors. The fully developed equation to calculate a luminescence age comprises around 30 constants and variables, some of which result from numerous, complex, measurements. Thus, the data processing of these measurements and calculations is an important aspect of luminescence dating.

The foundation of data processing in luminescence-based chronology lies within the frequentist school of statistics. This school of thinking targets events that can repeatedly occur under identical conditions. However, where our knowledge is formed based on only a few events, the validity of such an inference might seem questionable. In such situations, Bayesian inference is preferred due to its ability to incorporate knowledge developed gradually at each stage of measurement (Buck and Meson, 2015). This approach can be used in the estimation of a single age or a full set of ages. When a set of ages is considered, Bayesian analysis enables an assessment of systematic shared errors between samples, which have the potential to arise through the use of a number of instruments to produce measurements, and so cannot be ignored. Bayesian analysis also enables the inclusion of additional independent chronological data, such as well-established stratigraphic constraints. This helps to improve the precision of the chronology. The Bayesian approach has now become routine for improving chronologies based on radiocarbon ($^{14}$C) (Ramsey, 1995), yet has been slower to be developed within the field of luminescence dating. Only recently, a new sets of statistical Bayesian models and code specifically developed in the R environment has become available (Mercier et al., 2016; Philippe et al., 2019).

One purpose of this thesis was to extensively test different features of Bayesian models designed for luminescence dating, with an aim to discuss whether these models result in a more precise or even accurate outcome compared to frequentist-based models.

In this thesis, Bayesian chronologies have been established for key Middle-Upper Palaeolithic sites in Iran. The Iranian plateau is of importance for human dispersal during the Palaeolithic period due to its key location, linking Europe and Africa to central Asia. Most of the proposed models that describe migration routes of Anatomically Modern Human (AMH) from Africa towards Asia cross through Iran. Besides, the range of Neanderthal's occupation also encompasses some parts of the Iran. Smith (1986) highlighted that a lack of chronologies from this region posed

a significant obstacle to Palaeolithic studies in Iran. Decades later, our chronological knowledge related to Middle Palaeolithic culture is still mainly limited to one age (Jaubert et al., 2009), and only a handful of reliable chronologies that have been reported relating to the Upper Palaeolithic culture (see Sec. 1.3.2.4).

As a result, this thesis was guided by two main aims: (1) to provide luminescence-based chronological frameworks for Middle-Upper Palaeolithic sites using Bayesian models designed specifically for luminescence-data analysis, and (2) to discuss potential advantages of applying Bayesian models to luminescence chronologies over the commonly used frequentist models. To achieve these aims, I split the work into four different studies. The first study focuses on applying Bayesian modelling to overcome two common luminescence dating issues (signal saturation and beta-dose rate heterogeneity), leading to more reliable results. The other studies were driven by the demand for new chronological data for the Middle-Upper Palaeolithic sites in Iran. These studies were combined with tests on various aspects of Bayesian modelling to probe their effect on the final ages' precision.

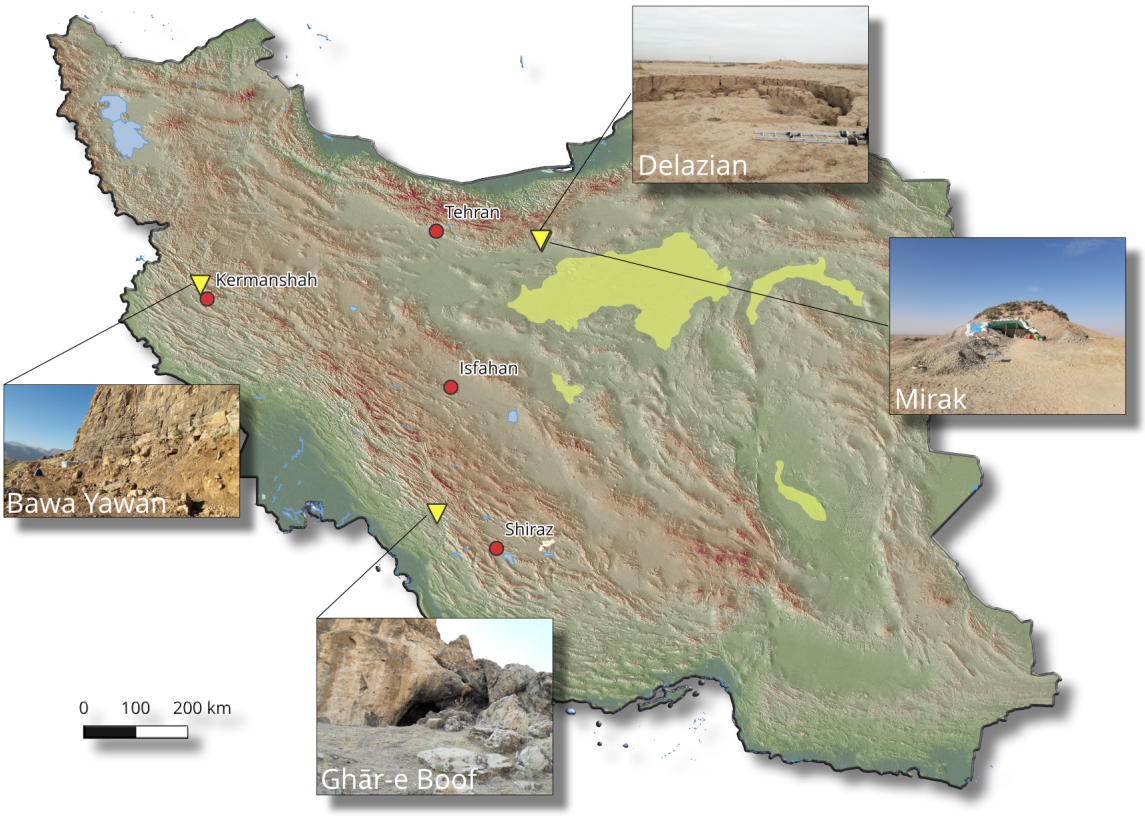


Figure 1.1: Map of Iran alongside the geographical locations with photos of the Palaeolithic sites dated for this thesis. Data sources: hillshade derived from ASTER GDEM 2. ASTER GDEM is a product of METI and NASA. Cities and desert margins: Natural Earth @ naturalearthdata.com and http://www.wikipedia.org. Photos: M. Heydari.

This thesis establishes new chronologies for three Palaeolithic sites (plus a preliminary contribution to a fourth site) spanning different geographical locations across Iran. The first set of sites (Mirak and Delazian) are located on the northern edge of the Central Iranian Desert (Dasht-e Kavir), south of the Alborz Mountains (e.g., Nasab et al., 2013; Vahdati Nasab and Clark, 2014; Nasab et al., 2019; Berillon et al., 2017). The passage between these two natural barriers established a potential route for human dispersal into central Asia during the Late Palaeolithic (Fig. 1.4). The second site, Ghār-e Boof (e.g., Conard and Ghasidian, 2011; Conard et al., 2013; Ghasidian et al., 2017), is located in the south of Iran in the southern Zagros foothills, above the Persian Gulf (Fig. 1.1). Close to a potential human dispersal route, this site is well-known for its rich Upper Palaeolithic assemblages. The third site, Bawa Yawan (Heydari-Guran and Ghasidian, 2017) , is situated close to the Bisotun Massif, central Zagros, where several Middle and Upper Palaeolithic sites have been reported. Of particular interest here are the Hunter (Shekarchian) and Wezmeh caves, in which Neanderthal remains have been found, and the Warwasi rock shelter and Wezmeh cave, where AMH remains have been discovered (see Sec. 1.3.2).

This thesis is a cumulative dissertation based on a collection of published and submitted articles, and one article under preparation. Each of these 'studies' forms a chapter of the thesis. The studies are preceded by an overview of the Palaeolithic in Iran (Sec. 1.3) and of luminescence dating (Sec. 1.4). The first study (Ch. 2, published) compares statistical models using frequentist and Bayesian approaches on two artificial laboratory experiments, to show the advantages of applying Bayesian models. The second study (Ch. 3, published) presents a complete chronological investigation of the site Mirak, alongside a consideration of whether Bayesian modelling leads to more precise chronologies compared to frequentist models. In the third study (Ch. 4), under review), a full chronological analysis is presented for the site of Ghār-e Boof, and I address the outcome of incorporating $^{14}$C dates with luminescence ages in the framework of the Bayesian approach. The last study (Ch. 5, in preparation) presents a luminescence chronology for the site Bawa Yawan. The thesis closes with a discussion, conclusion and outlook on potential future work.

## 1.3 Palaeolithic

In archaeology, the phase between ca 2.5 Ma to ca 10 ka is referred to as the Palaeolithic (Stone Age) (Klein, 2018). Within this period, hominins and humans employed stones to produce tools. This was a critical technology of their time. The period is divided into several eras, each attributed to various species and their characteristic technologies. During these 2.5 million years, vast numbers of hominins evolved and became extinct. The focus here will be on the Middle and Upper Palaeolithic of Iran, a period that encompasses the presence of Homo Neanderthals and Anatomically Modern Humans (AMH).

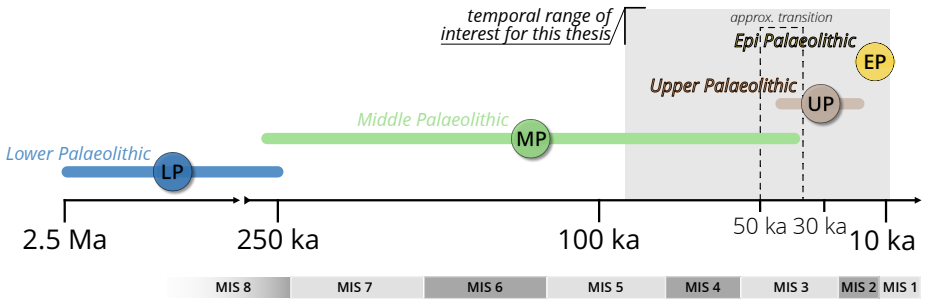


Figure 1.2: Approximated temporal boundaries for the Palaeolithic after Scarre (2018). The grey area highlights the temporal target range of this thesis. MIS boundaries according to Lisiecki and Raymo (2005).

The *Middle Palaeolithic* (MP) period started around 250 ka (Klein, 2018) and lasted ca 40 ka (Fig. 1.2). This period is contemporary with the presence of Homo Neanderthals in western Europe (Condemi, 1998; Hublin, 2009). The Homo Neanderthals travelled eastward to occupy Eurasia and onto central Asia (Shea, 2003; Krause et al., 2007a; Boivin et al., 2013; Groucutt et al., 2015). The lithic artefact industry within this period, the Mousterian, is after the site of 'le Moustier' in France (Bordes, 1961). This industry covers a broad range of various assemblages developed alongside with the evolution of Neanderthals (Turq et al., 2013).

In contrast, the period associated with the Middle Stone Age in Africa aligns with the emerging modern human traits of around 300 ka (MIS8/MIS9, Marine Isotope Stage (MIS): age boundaries used throughout, after Lisiecki and Raymo 2005) seen at the site of Jebel Irhoud (Marrocco, Hublin et al. 2017; Richter et al. 2017). Following this, the period 200–150 ka is known for the presence of Anatomically Modern Human (AMH) in the east of Africa in Ethiopia (Relethford, 2001; Trinkaus, 2005). The MP period terminated by the emerging *Upper Palaeolithic* period (UP, ca 40–10 ka). Although this period often coincides with the appearance and dominance of so-called modernity behaviours, cultural modernity is thought to be attributed to both the AMH and the Neanderthal (Zilhão, 2018). The start of Upper Palaeolithic is contemporaneous with the extinction of Neanderthal and dominance of early modern human in Africa, Europe and Asia (Bar-Yosef, 2002a).

During the Middle Palaeolithic, Neanderthals from Europe and AMH from Africa dispersed towards central Asia. One of the vital regions, which witnessed the first arrival of AHM from Africa, is the Levant. As the Levant is also considered as Neanderthal territory, it experienced both Neanderthal and AMH during the Middle Palaeolithic. For this reason, it is one of the most attractive regions for Palaeolithic studies. The importance of this region is reflected in the substantial number of excavations and prehistoric studies during Middle and Upper Palaeolithic periods. From a geographical position perspective, the Levant is located close to Iran, and Palaeolithic assemblages in Iran are often compared to Levantine Palaeolithic industries. I will therefore provide a

brief review of the important sites in the Levant during Middle to Upper Palaeolithic and consider the stages of human evolution within this region.

### 1.3.1 The Levant during the Middle-Upper Palaeolithic period

The Levant and the Arabian Peninsula are crucial regions for the understanding of human dispersal during the Late Pleistocene. They saw the early emergence of the AMH from Africa (Turner, 1999; Mellars, 2006a; Petraglia et al., 2010; Groucutt et al., 2015) along with simultaneous Neanderthals occupation of the region during Late Palaeolithic (Shea, 2003; Krause et al., 2007a; Boivin et al., 2013; Groucutt et al., 2015).

The initial dispersion of AMH out of Africa towards the north and the north-east was hampered due to the harsh and arid environment of North Africa during MIS 7 and MIS 6 until MIS 5; as indicated by the lack of records of human remains during these periods (Boivin et al., 2013). With improving climate conditions during MIS 5, the AMH dispersed towards the Levant and the Arabian Peninsula (Shea, 2008; Breeze et al., 2016). The Bab-el-Mandeb strait and the Sinai Peninsula are gates discussed for migrations out of Africa (Petraglia and Alsharekh, 2003; Timmermann and Friedrich, 2016).

Palaeohydrological investigation in the north of Arabian Peninsula revealed that the Tabuk corridor had an attractive climate (e.g., accessibility to water on land), and so was a potential passage for human dispersal during MIS 6/MIS 5e and MIS 5e (Breeze et al., 2016). Other studies, however, speculated that the dispersal of AMH during MIS 5 reflects an unsuccessful migration (Mellars, 2006a; Shea, 2008; Boivin et al., 2013). Contrary to this, Petraglia et al. (2007, 2010); Groucutt et al. (2015) postulated that this wave of migration successfully surged against India and South Asia earlier than MIS 4.

At the beginning of the MIS 5 when the first wave of AMH reached the Levant, the region was already inhabited by Neanderthals (Shea, 2003; Krause et al., 2007a; Boivin et al., 2013; Groucutt et al., 2015; Hershkovitz et al., 2018). Established chronological data, e.g., for the site of Tabun (encompassing a Neanderthal fossil), dated to $122 \pm 16$ ka (MIS 5e) (ESR dating; Grün and Stringer 2000, original data from Bar-Yosef and Callander 1999), which lies within the age range for the presence of AMH in Skhul (TL dating: $119 \pm 18$ ka, Mercier et al. (1993) and Qafzeh TL, 90–100 ka Valladas et al. (1988); $115 \pm 15$ ka, ESR on teeth Schwarcz et al. (1988)). The chronological results of these three sites revealed that both species inhabited the Levant around 100–130 ka (Grün et al., 2005). After these dates, the lack of Neanderthal fossils in the Late MIS 5 suggests that Neanderthals abandoned the Levant and moved back to western Eurasia (Shea, 2010) to move away from the warm condition that they were not well adapted for. This period was followed by a complete lack of AMH fossils in records spanning ca 45–75 ka. This might be explained by their extinction or their departure due to the harsh and cold environmental-climate condition during MIS 4 (Shea, 2010). A sudden shift in climate conditions towards a cold and dry

environment, however, does not seem to have had the same impact on Neanderthal populations, as they were more resistant against the cold environment (Shea, 2010). Fossil records dated in the sites of Kebara, Ksar Akil could indicate that another wave of AMH reached the Levant in MIS 3 when humid climate conditions prevailed (Bar-Yosef and Meignen, 2001).

This generation of dispersal is believed to constitute a successful diffusion from Africa into central and south Asia, with AMH finally reaching as far as Australia (Boivin et al., 2013; Timmermann and Friedrich, 2016).

The latest Neanderthal fossils found in the Levant featured the sites of Tabun, Kebara and Amud, which were dated to around 75–50 ka (outgoing MIS 5, early MIS 3) (Bar-Yosef and Meignen, 2001; Valladas et al., 1999; Bar-Yosef, 2002b). Afterwards, in the period of ca 47–42 ka there is no evidence of Neanderthal fossils, and it seems that they were extinct and superseded by AMH, e.g., in the sites of sr Akil and Qafzeh 1-2 (Mellars, 1996; Shea, 2008, 2010).

The period of ca 50–40 ka (Shea, 2003; Bar-Yosef and Belfer-Cohen, 2010) is known as a time of transition, in which the Mousterian industry, corresponding the Middle Palaeolithic period, was replaced with the innovative industry of Ahmarian, attributed to the Upper Palaeolithic period (Shea, 2003). This period in the Levant is also known by the term Initial Upper Palaeolithic or Emirian (Bar-Yosef, 2002b; Kuhn et al., 2009). The Initial Upper Palaeolithic refers to assemblages derived from a layer underlying the Mousterian industry, comprising tools that display not only the Upper Palaeolithic typology but also contain some of the Middle Palaeolithic technology features (Bar-Yosef and Belfer-Cohen, 2010). The transition period is followed by the Early Upper Palaeolithic Ahmaria culture (ca 45–30 ka Bar-Yosef and Belfer-Cohen 2010).

The Upper Palaeolithic period is a fascinating period for Palaeolithic studies due to the transition from many different species throughout hundreds of thousands of years in human evolution, to only one kind: our species (Bar-Yosef, 2002a). This period is famous for flourishing modernity behaviours expressed through an emergence of abstract thinking, advancements in ritual ceremonies, improved figurative ability followed by painting, making personal ornaments using bones, wood or shells, the development of the language, a standing social network, and a widened inhabited territory (Mcbrearty and Brooks, 2000; Henshilwood and Marean, 2003; d'Errico and Stringer, 2011). Innovative industry, such as blade and bladelet production, distinguishes the Upper Palaeolithic period from Mousterian tradition, and is one of the critical aspects of the cultural shift during this era in human evolution.

Scholars have diverse views on the emergence of these cultures. Some stress that the Upper Palaeolithic cultures gradually evolved due to improving human capability over time, and the idea of a radical shift or revolution from the Middle Palaeolithic period towards the Upper Palaeolithic does not seems applicable (e.g., Mcbrearty and Brooks, 2000). Other researchers believe that this evolution was not limited to a specific area, but instead ignited over the entirety of Europe and Asia simultaneously. Some argue that the first appearance of Upper Palaeolithic

evolution was restricted to Africa and that human dispersal spread this culture across the world. Others emphasise the fundamental role of climate change on human behaviour leading to cultural evolution. For instance, an increasing population during MIS 3, with warmer and humid environmental conditions compared to the cold and harsh conditions of MIS 4 (Shea, 2003; Bar-Yosef, 2002b), resulted in enhanced interactions between different groups of humans or potentially even competition over food for survival (Bar-Yosef, 2002b; Shea, 2003). These interactions led to an improvement in subsistence strategies and the creation of appropriate new tools. These tools became more delicate, e.g., blade and bladelet production (Mcbrearty and Brooks, 2000; Bar-Yosef, 2002a). The Upper Palaeolithic industry in the Levant terminated with the Epipaleolithic period in which a "microlithic-dominated" industry emerged (Bar-Yosef, 2002a). The variety of tools used in this period substantially increased, and their form became more complex, reaching a cultural climax of its own (Olszewski, 2008).

### 1.3.2 The Middle-Upper Palaeolithic in Iran

Further to the east, the situation contrasts starkly to the well-established and detailed archaeological studies in the Levant. Where the Iranian plateau surfaces, the number of systematic Palaeolithic investigations is very low compared to the extent of the country. Regardless of this, Iran's unique location at the intersection between Africa, Europe and Central Asia, gives it a significance in terms of tracking human dispersal during the Late Pleistocene. Most of the maps designed to chart the migration of AMH from Africa, or Neanderthals from Europe towards Asia, cross through Iran (Mellars, 2006b; Petraglia et al., 2010; Rosenberg et al., 2011; Bar-Yosef and Belfer-Cohen, 2013; Boivin et al., 2013; Nasab et al., 2013; López et al., 2016). Traces of Neanderthal occupation during Late Palaeolithic span a considerable part of Iran (see Fig. 1.3).

The north and the southern edges of the Alborz Mountains in the north of Iran are considered as two distinct corridors (see Fig. 1.4). The first is bordered by the Caspian Sea from the north (see Berillon et al., 2007; Berillon and Asgari Khaneghah, 2016), and the second restricted by the Central Iranian Desert (Dasht-e Kavir) in the south (Nasab et al., 2013). These corridors likely provided a feasible way for humans to disperse towards Central Asia during the Late Pleistocene. Several Palaeolithic sites, mainly in open-air sites, have recently been discovered in the northern and western edges of the Iranian Central Plateau and south of the central Alborz (e.g., see Conard et al., 2009; Nasab et al., 2013; Heydari-Guran et al., 2014; Vahdati Nasab and Clark, 2014; Vahdati Nasab and Hashemi, 2016; Nasab et al., 2019).

Furthermore, the Zagros Mountains in the western part of the Iranian plateau constituted the centre of prehistorical studies in Iran over time. These mountain chains formed from the collision of the Arabian plate with the Eurasian plates, and extend around 2,000 km from south-eastern Turkey, north of Iraq, spanning across north-west and west Iran, and disappear close to the Persian Gulf (Alavi, 1994; Agard et al., 2005). Palaeolithic investigations in the foothills

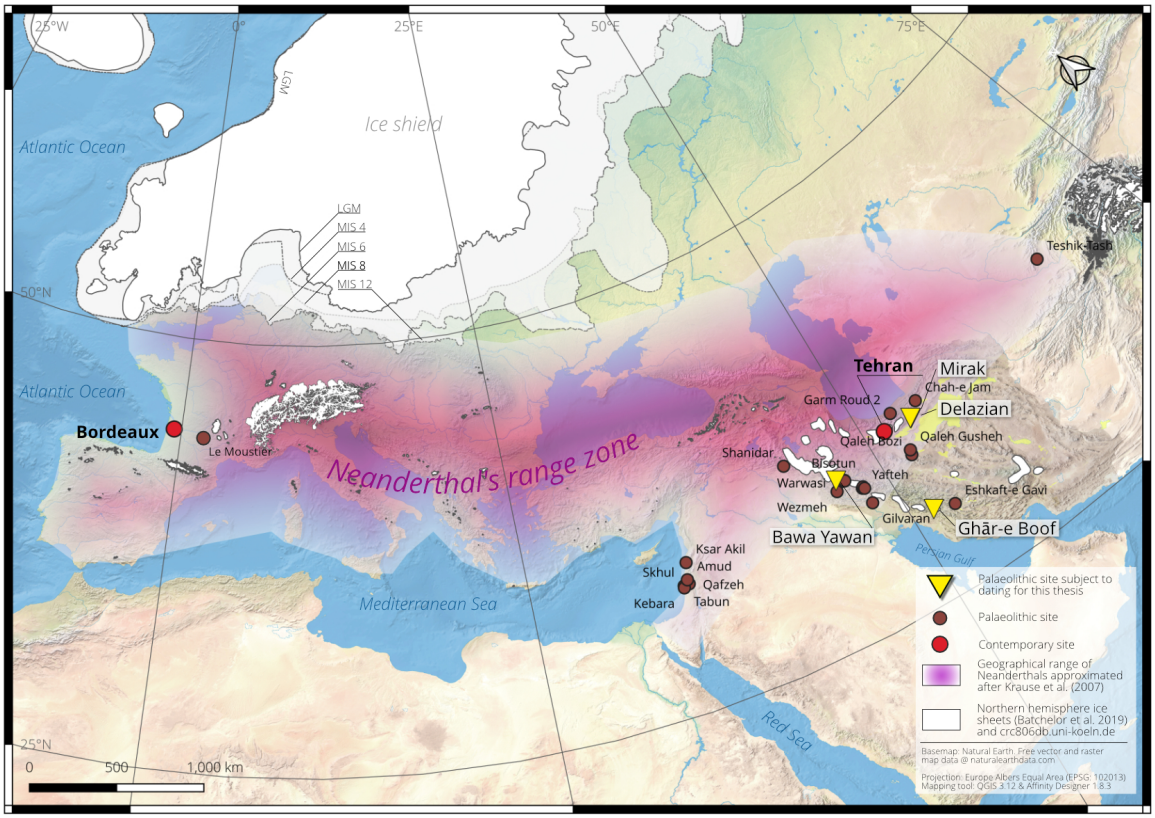


Figure 1.3: Approximated Neanderthal diffusion map in where Iran witnessed Neanderthal's presence. Important Middle-Upper Palaeolithic sites in Iran and the Levant as mentioned in the text are shown. Data sources: Coordinates palaeolithic sites according to cited articles and http://www.wikipedia.org. Basemap and populated places based on Natural Earth @ naturalearthdata.com. The ice margins base on Batchelor et al. (2019) and Becker et al. (2015). Geographical dispersal of the Neanderthals approximated after Krause et al. (2007b).

of the Zagros mountains have been carried out not only to unravel the Middle and the Upper Palaeolithic cultures of this region but also to decipher the possibility of in situ developments of Upper Palaeolithic culture out of the underlying Middle Palaeolithic culture (e.g., Garrod, 1953; Solecki, 1955; Hole and Flannery, 1968; Olszewski and Dibble, 1994; Biglari, 2001; Jaubert et al., 2009; Conard and Ghasidian, 2011; Shidrang et al., 2016; Heydari-Guran and Ghasidian, 2017; Bazgir et al., 2017).

Although this long mountain chain could be seen as a natural barrier to human dispersal during the Pleistocene (Heydari-Guran, 2014; Ghasidian et al., 2019), for instance, note the presence of valleys and plains within the elevated Zagros Mountains, which provide important routes for traversing and fostering cultural settlements. In general, the topographic features along the Zagros belt are not homogeneous. Despite the harsh environment in the snow-covered towering

mountain range in the central Zagros, the southern Zagros landscape is smoother and contains vast plains and shallow valleys. Therefore, even if the north and the centre of the Zagros belt hampered human migrations from west Eurasia into central Asia, the gentle topographic features of southern Zagros may have supported human migration from the south-west of Iran towards the east.

Human fossil remains provide a record of the presence of both Neanderthal and AMH in Zagros' sites. The set of skeletons from Shanidar (Solecki, 1955; Trinkaus, 1983; Pomeroy et al., 2017), as well as fragmented bones and premolar from the site of Shekarchian (Hunter'cave) in Bisotun Massif (Trinkaus and Biglari, 2006) and Wezmeh (Zanolli et al., 2019) in the Middle Palaeolithic assemblages, are associated with Neanderthals. The scarce discovery of AMH fossil remains in the site of Wezmeh (Trinkaus et al., 2008), Warwasi (Tsanova, 2013) and Eshkaft-e Gavi (Scott and Marean, 2009) were attributed to the Upper Palaeolithic. However, due to poor preservation on the premolar, there is doubt about whether the finding in Wezmeh is related to AMH or a different species (Trinkaus et al., 2008). Due to sparse human remains in Palaeolithic sites in Iran, particularly in the Zagros Mountains, most of the investigations to date have focussed on lithic artefacts. While the Upper Palaeolithic industry is restricted to AMH in all locations, the Middle Palaeolithic industry can likely be attributed to both Neanderthals and AMH, similar to the situation found in the Levant (e.g., Bar-Yosef, 2002b; Shea, 2010). In Europe, only Neanderthals are associated with the Middle Palaeolithic culture. Contrary, in Iran, because of the sparse amount of available data concerning human fossils, the Palaeolithic history remains vague, and an ongoing debate exists on whether AMH were also responsible for creating Middle Palaeolithic period industry (Ghasidian et al., 2019).

#### 1.3.2.1 The Middle Palaeolithic

In the following, I reference some important sites encompassing Mousterian assemblages in the Zagros Mountains and close the Central Iranian Desert. These sites are relevant in the broader context of this thesis.

**1.3.2.1.1 Central Zagros Mountains** One of the first investigations on Middle Palaeolithic sites in Iran was carried out in the cave of Shekarchian by Coon in 1948, in the Bisotun Massif in the Kermanshah province, central Zagros (Coon, 1951; Biglari, 2001). This investigation resulted in the discovery of the Mousterian industry of Zagros. Another famous cave in the Bisotun Massif is Ghār-e Khar (Khar cave). The cave was first discovered by Smith in 1965 (Smith, 1986) and contained a complete sequence from the Middle Palaeolithic to the Upper Palaeolithic and the Epipalaeolithic (Shidrang et al., 2016). Other Palaeolithic caves discovered in the Bisotun Massif are Mar-Tarik and Mar-Aftab, both linked to the Mousterian culture (Biglari, 2001; Jaubert et al., 2006). However, Mar Dodar cave, like the site of Shekarchian, encompasses

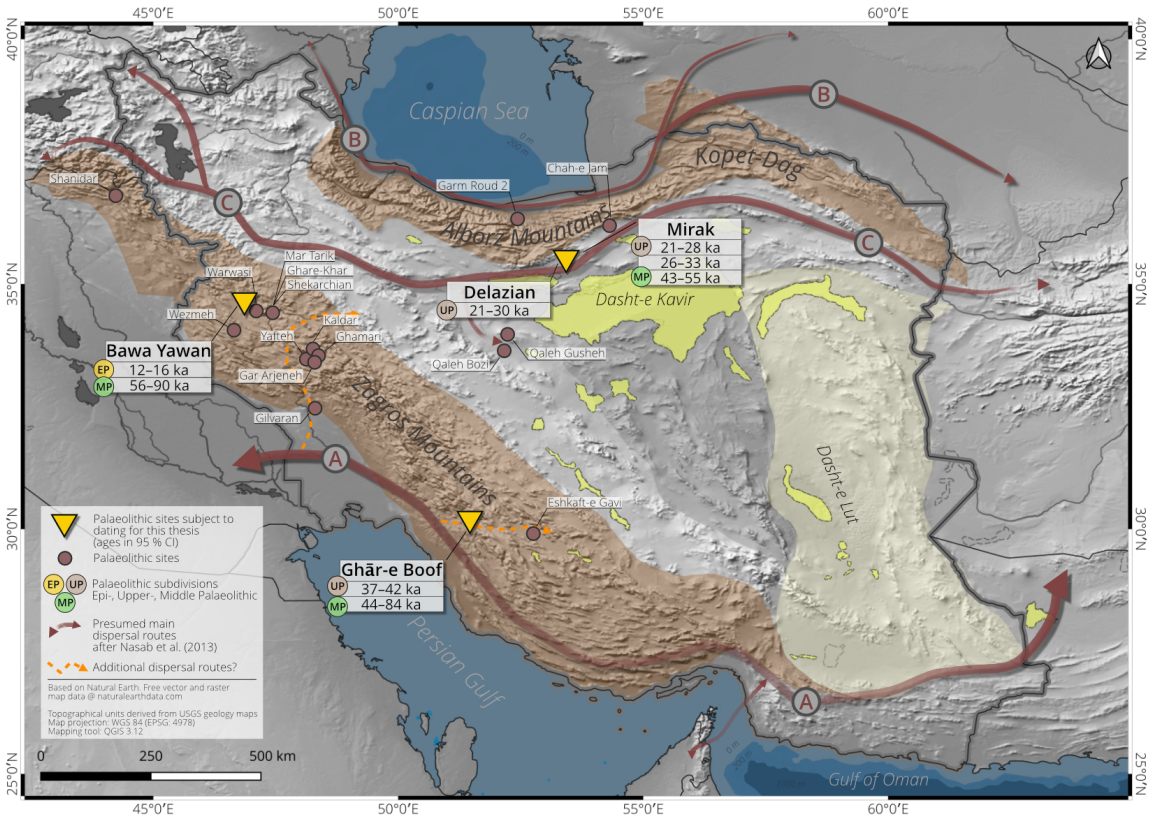


Figure 1.4: Map of Iran alongside three presumed dispersal routes according to Nasab et al. (2013) (their Fig. 10). Sites dated for this thesis are displayed with their age ranges. More Palaeolithic sites are know in Iran, however, they are not are shown for illustrative reasons. Data sources: Coordinates palaeolithic sites according to cited articles and http://www.wikipedia.org. Basemap and populated places based on Natural Earth @ naturalearthdata.com. Geological mountain ranges slightly modified after Pollastro et al. (1997).

Upper and Epipalaeolithic assemblages on the top of the Mousterian culture (Biglari, 2001). The abundance of the Mousterian industry in the various caves in the Bisotun Massif underlies the importance of this region, making it a preferred target for further Palaeolithic investigations. Biglari (2001) concluded that Pleistocene humans had widely exploited this area as a seasonal settlement. He emphasised the unique environmental setting of an extensive area for forage between the Zagros foothills and the plains in Kermanshah, which provided enough food supply to support subsistence (Biglari, 2001). Access to sufficient water supply in the vicinity of the Bisotun area, such as the Gamasiab and Dinevar rivers, created an attractive environment for human settlement during the Late Pleistocene (Biglari, 2001).

Another essential site located in the central Zagros region (Kermanshah Province) is the Warwasi rock shelter. This was first excavated by Braidwood and Howe in 1961 (Braidwood et al.,

1961). The investigation unravelled the presence of Mousterian, Upper Palaeolithic and on the top, the Epipalaeolithic culture. Heydari-Guran and Ghasidian (2020) divided Kermanshah province (a key region encompassing Middle-Upper Palaeolithic sites), into four major zones based on geological and topographical information. A preliminary survey charted 260 new sites and discovered the presence of Mousterian as well as Upper Palaeolithic industries. The authors emphasised the importance of rock shelters for Palaeolithic studies, as in situ sediments in slopes of mountains or river terraces were likely to have been washed away by erosional processes (Heydari-Guran and Ghasidian, 2020).

**1.3.2.1.2 Dasht-e Kavir** At the northern edge of Dasht-e Kavir, the sites of Mirak and Chah-e jam contain evidence of Middle Palaeolithic, with the use of the Levallois technique being attributed to the Mousterian culture (e.g., Nasab et al., 2013; Vahdati Nasab and Hashemi, 2016). In the Isfahan province, the west part of the border to the Central Iranian Desert, two rock-shelters and one cave in Qaleh Bozi Mountain contain evidence of the Mousterian industry (Biglari et al., 2009). Additionally, in the Isfahan province, several open-air sites on the dune system of Galeh Gusheh have been discovered (Conard et al., 2009). The Galeh Gusheh forms part of the giant mobile dune system of Rig Boland, and the sites here have been attributed to the Middle Palaeolithic. However, due to agricultural irrigation in this region, most of the sites have been destroyed, hampering further investigation (Conard et al., 2009; Heydari-Guran et al., 2014). The assemblages discovered in the open-air site of Bardia in Galeh Gusheh have been attributed to both the Upper and the Epipalaeolithic period, but in general have been described more broadly as coming from the Late Palaeolithic (Conard et al., 2009). It is interesting to compare the Mousterian industry, close to the central Iranian plateau, with corresponding assemblages in the Zagros Mountains. Whilst additional detailed studies are required in order to address similarities and differences between two regions, a key aspect to note is that a higher concentration of Levallios techniques have been found in the assemblages of central Iranian plateau as compared to Zagros sites (Nasab et al., 2013).

### 1.3.2.2 The transition from the Middle to the Upper Palaeolithic period

The period spanning 50–40 ka, is a point of significant importance in Late Pleistocene studies, but has also raised much controversy within discussions. This period refers to a time when the Neanderthal population disappeared, and modern humans dominated the entirety of Eurasia. Numerous absolute chronologies have been established to more precisely frame this period of transition in Europe and Levant. However, in Iran, a lack of reliable absolute chronologies in sites potentially containing evidence of this transition has hampered efforts to reach a complete understanding of the shift from the Middle to the Upper Palaeolithic period. Several sites in Iran contain archaeological assemblages spanning both the Middle and Upper Palaeolithic, and

occasionally Epipalaeolithic period. Among them is the Warwasi rock shelter in the central Zagros region, in the Kermanshah Province. Olszewski and Dibble (2006) proposed the possibility of a local evolution of Zagros Aurignacian (Late Upper Palaeolithic period) out of Zagros Mousterian, based on evidence of continuity between assemblages from the Middle Palaeolithic period to the Upper Palaeolithic period, and also the resemblance between Baradostian (Upper Palaeolithic tradition in north Zagros) and the Aurignacian culture in Europe and the Levant. Olszewski (1993) also suggested the possibility of a transition from Baradostian to Zarzian (Epipalaeolithic tradition in the north of Zagros) in an extended sequence of the Upper Palaeolithic period in Warwasi. Although Middle Palaeolithic assemblages in the initial Upper Palaeolithic layer at Warwasi could be used as evidence for in situ development of the Upper Palaeolithic out of Middle Palaeolithic industry (as was the case in early Ahmarian assemblages, Levant), sparse availability of data from Zagros' sites means that there is insufficient evidence to support a local transition theory (Tsanova, 2013). Tsanova (2013) stressed the need for more precise chronologies for the assemblages at Warwasi, in order to better understand the transition between the Middle and Upper Palaeolithic. Ghasidian et al. (2019) suggested that if an *in situ* transition at the site is disregarded, the presence of both Middle and Upper Palaeolithic features in the early Upper Palaeolithic assemblages could imply a temporary exploitation of the site by industry makers of both periods.

Khar cave, situated in Bisotun Massif, Kermanshah Province, encompasses assemblages from the Middle, Upper and Epipalaeolithic. Investigations here, however, do not provide strong indications for a transition or continuity from the Mousterian industry towards the Baradostian culture (Shidrang et al., 2016), despite there being an intermediate layer between the Middle and Upper Palaeolithic which contained assemblages relating to both periods. Gar Arjeneh rock shelter, located in central Zagros, Khoramababd Province, also covered both Mousterian and Baradostian assemblages. However, investigations noted reworking within the layer between the distinct periods, and were unable to show any substantial evidence of continuity between the periods (Hole and Flannery, 1968; Shidrang, 2018). In southern Zagros, in the Marvdasht plain, Rosenberg excavated a cave named Eshkaft-e Gavi, which contained both assemblages from the Middle Palaeolithic (Mousterian) and the Upper Palaeolithic (Baradostian) (Rosenberg 1985 complied in Ghasidian et al. 2017; Shidrang 2018). He noted a resemblance between the Upper Palaeolithic in this cave with assemblages found in the Lurestan and Kermanshah Provinces. He therefore categorised the Upper Palaeolithic industry at Eshkaft-e Gavi as Baradostian culture (Ghasidian et al., 2017; Shidrang, 2018). The Middle Palaeolithic features were not observed in the Early Upper Palaeolithic assemblages, in contrast to the Central Zagros sites, and therefore these assemblages could not be used to imply continuity at Eshkaft-e Gavi (Shidrang, 2018). Chronological data from this site highlights a possibility of stratigraphic disturbance, which rendered further conclusions difficult (Shidrang, 2018) (see Sec. 1.3.2.4). Assemblages

at Gilvaran cave, in Khoramabad Province, comprise of both Middle and Upper Palaeolithic period. Although a stratum has been observed between the Middle and Upper Palaeolithic period that contains tools corresponding to both periods, the techno-typological investigation did not document the transition (Bazgir et al., 2014). In the Kaldar cave, Upper Palaeolithic assemblages have been found on top of the underlying Middle Palaeolithic period. This site has confirmed the possibility of a transition and evolution of Zagros Aurignacian out of the Zagros Mousterian. Whilst the chronological data available partly supports this assumption, high dispersion within the data means that further investigation is required improve it's precision (Bazgir et al., 2017) (Sec. 1.3.2.4).

#### 1.3.2.3 The Upper Palaeolithic

In the Zagros region, the first investigation used to decipher the Upper Palaeolithic culture and its origin occurred in the Zarzi rock shelter in Iraqi Kurdistan, close to the border of Iran. This excavation aimed to test the possibility that the Upper Palaeolithic culture in Europe (Aurignacian) originated from a location outside of Europe (Garrod 1953; compiled in Shidrang 2018). These studies unravelled the Epipalaeolithic, Zarzian tradition (named after the cave Zarzi, Garrod 1953). This tradition was identified by the emergence of a microlithic industry, with assemblages often containing scrapers and bladelets (Olszewski, 2012; Ghasidian et al., 2017). Following this, Solecki (1958) excavated the site of Shanidar, located in the northern Zagros, in Iraqi Kurdistan, to understand the Upper Palaeolithic culture in the area. The blade industry, despite the similarities with the Aurignacian culture in Europe, displayed distinct features. This exhibited the local characteristic of the industry, which was consequently was classified as 'Baradostian' culture (blade industry) after the Baradost Mountain (Solecki, 1958). Olszewski and Dibble (1994) then focussed on the strong resemblance between Baradostian and the Aurignacian tradition in Europe and Levant. They proposed replacing the term of Baradostian with Zagros Aurignacian to emphasis the similarity of the two cultures, whilst still stressing regional differences. Inside the border of Iran, one of the first excavations to produce rich Upper Palaeolithic to Early Epipalaeolithic assemblages took place in the previously mentioned rock shelter of Warwasi (Kermanshah Province) and the site of Pasangar (Lurestan Province) located in central Zagros (Hole and Flannery, 1968).

First discovered by Hole in 1965 (Hole and Flannery, 1968), the Yafteh cave is another essential site with Upper Palaeolithic assemblages located in central Zagros (Lurestan Province). The rich Upper Palaeolithic Period assemblages have been grouped into three phases: the Upper, Middle and Lower Baradostian tradition (Hole and Flannery, 1968). Typo-technological analyses disclosed similarities between the lower parts of the sequence in Yafteh Cave with Early Ahmarian in the Levant. The middle and the upper part of the sequence were attributed to Ahmarian and Levantine Aurignacian, respectively (Otte et al., 2011). Based on the strong simi-

larity between the Upper Palaeolithic industry at Warwasi, Pasangar and Yafteh in central Zagros, Ghasidian et al. (2019) suggested that this resemblance might arise due to the developed social network in their foraging range. Compared to the north and centre of the Zagros region, the Palaeolithic sites in the south have been studied in less detail. Excavation the Eshkaft-e Gavi cave in the Marvdasht plain, northern Fars province, by Rosenberg Rosenberg (1985) unravelled Upper Palaeolithic assemblages that have been attributed to the Baradostian industry. These findings show a resemblance to similar assemblages in the Lurestan and Kermanshah provinces, located in central Zagros (Rosenberg 1985 compiled in Ghasidian et al. 2017; Shidrang 2018). Another attractive area for excavation was the Dasht-e Rostam region, north-west Fars Province. Field studies at Dasht-e Rostam plains discovered several Palaeolithic sites within open-air sites, rock shelters, and caves. A surface investigation by Heydari-Guran (2014) discovered abundant lithic artefacts predominately associated with the Upper Palaeolithic industry. The study area was divided into smaller zones (microhabitats) according to the density distribution of the lithic artefacts (Heydari-Guran, 2014), e.g., the Yagheh Sangar passage, the microhabitat with the highest concentration of lithic artefacts. This corridor is located in the middle of the Dasht-e Rostam plains, where it contains around 33 % of all the Palaeolithic sites in the area (Heydari-Guran, 2014). Located in the centre of the Yagheh Sangar corridor, the Ghār-e Boof is a site with the most abundant Upper Palaeolithic assemblages, containing blade and bladelet (Conard and Ghasidian, 2011) (see also Ch. 4). The Upper Palaeolithic culture in Ghār-e Boof is named the Rostamian tradition after Dasht-e Rostam. This emphasises the regional and distinctive characteristic of the assemblages (e.g., Conard and Ghasidian, 2011; Ghasidian, 2014).

Beyond the Zagros foothills, the northern fringe of the Alborz Mountains has been the focus of Palaeolithic investigations. As an example, bladelet production from the Late Baradostion culture has been found at the open-air site of Garm Roud 2 in Mazandaran Province. The open-air site of Delazian, located in the Semnan Province, south of the Alborz Mountains at the north edge of Central Iranian Desert, has been categorised as Upper Palaeolithic and likely Epipalaeolithic (Nasab et al., 2013; Vahdati Nasab and Clark, 2014; Nasab et al., 2019). The Middle-Upper Palaeolithic site of Chah-e Jam, located in the same province, contains assemblages from the Upper and Epipalaeolithic period (Vahdati Nasab and Hashemi, 2016).

#### 1.3.2.4 Known Palaeolithic chronologies in Iran

In contrast to Palaeolithic investigations in the Levant, chronological data is available for only for a handful of sites in Iran. Since $^{14}$C dating has been the most commonly used method in this field, chronological studies have been limited to only the Upper Palaeolithic period (or the Initial Upper Palaeolithic/transition period). For example, in central Zagros, despite the large number of the excavated sites mentioned earlier, chronological data is only for Yafteh cave (ca 35–42 ka cal. BP, Otte et al. 2011) and Kaldar cave (ca 37–54 ka cal. BP, relating to the probable transition period

in the site, Bazgir et al. 2017). In southern Zagros, chronological information is available for of the Upper Palaeolithic sequence Ghār-e Boof (ca 35–42 ka cal. BP; Conard and Ghasidian 2011; Baines et al. 2014; Becerra-Valdivia et al. 2017) and the assemblages at Eshkaft-e Gavi (ca 18–28 ka uncal. BP, Rosenberg 1985; compiled in Ghasidian et al. 2017; Shidrang 2018; Heydari-Guran and Ghasidian 2020). Here, I have refrained from calibrating these ages as detail relating to uncertainties is either not available, or uncertainties are large. Chronological data from the north of Iran, in particular for the north of the Alborz Mountains chain and south of the Caspian Sea, is restricted to the range of ca 28–35 ka cal. BP from the open-air site of Garm roud (Berillon et al., 2007; Antoine et al., 2016). Although the availability chronological data for the Upper Palaeolithic period in Iran is limited, knowledge of the Middle Palaeolithic period is even weaker, and our knowledge is mainly limited to one age $124 \pm 3$ ka (Mar-Tarik, Jaubert et al. 2009). It therefore emerges that determining reliable chronologies at Iranian sites for both periods, is of crucial importance. This thesis aims to establish a set of precise luminescence-based chronologies to fill some of the gaps in chronological data for the Middle-Upper Palaeolithic period in Iran. For this study, three sites were selected: (1) The open-air site of Mirak, in the north of Central Iranian Desert Semnan province, (2) the cave Ghār-e Boof, in southern Zagros Fars province, and (3) the rock shelter Bawa Yawan, in central Zagros Kermanshah province. The results aim to improve our understanding of human dispersal over time, in three crucial locations in the Iranian plateau.

## 1.4 Luminescence dating: a brief introduction

Luminescence dating is a chronological method used to determine the time elapsed since exposure of minerals to sunlight or heating. It has been applied extensively in the fields of environmental and archaeological science (e.g., Liritzis et al., 2013; Roberts et al., 2015). Luminescence dating is advantageous over $^{14}C$ in circumstances where organic material is absent or the presumed age of the target exceeds the age limit of $^{14}C$.

Luminescence dating relies on the emission of $\alpha$-and $\beta$-particles, and $\gamma$-photons, from natural concentrations of radionuclides within sediment. This energy is absorbed by minerals (dosimeters) such as quartz or feldspar, minerals that are abundant in most environmental settings. The amount of energy trapped within minerals can be determined in the laboratory by measuring the amount of light emitted (luminescence). Luminescence measurements estimate an equivalent of the absorbed dose (equivalent dose ($D_e$)) since the mineral was buried. An age is then calculated using the ratio of absorbed dose over the dose rate. The dose rate is the sum of $\alpha$, $\beta$-and $\gamma$-dose rate in the sedimentary environment ($\dot{D}_\alpha$, $\dot{D}_\beta$ and $\dot{D}_\gamma$) and the cosmic-dose rate ($\dot{D}_{cosm.}$: corresponds to the influx of high energy cosmic particles varying geographic position (Prescott and Hutton, 1994).

$$Age\,(ka) = \frac{D_e\,(\mathrm{Gy})}{\dot{D}\,(\mathrm{Gy\,ka^{-1}})} \tag{1.1}$$

while

$$\dot{D} = \dot{D}_\alpha + \dot{D}_\beta + \dot{D}_\gamma + \dot{D}_{cosm.} \tag{1.2}$$

Luminescence dating is most commonly employed through two methodological approaches: Optically Stimulated Luminescence (OSL, Huntley et al. 1985) on quartz grains or Infrared Stimulated Luminescence (IRSL, Hütt et al. 1988) on feldspar grains. These two methods cover a wide age range from around 25 a to 300 ka (Mahan and DeWitt, 2019). Based on typical $\dot{D}$ values of ca 1–3 $\mathrm{Gy\,ka^{-1}}$. Quantification of the upper dose limit (saturation dose) is crucial for assessing the characteristics of each dosimeter. Feldspar's saturation limit is 4–5 times larger than that of quartz, making it favourable for dating older samples. Feldspar, however, has limitations in the way it suffers from athermal fading (Wintle, 1973), unwanted signal loss over time, and that it is known to bleach less effectively than quartz (Godfrey-Smith et al., 1988).

Luminescence dating is an interdisciplinary method, built from knowledge developed from various fields. Whilst most commonly applied to archaeological and environmental sciences, luminescence theory itself is based on knowledge gained from solid-state physics. Energy transitions explain luminescence phenomena in the crystal lattice of the semiconductors or isolators, and assessment of dose rates require consideration of natural radioactivity by particles physics.

Instruments used to detect luminescence demand an understanding of electronic and signal detection, and the data produced can be processed through a number of statistical methods. In the following section, I outline the theoretical background of luminescence dating along with selected aspects that are of interest for this thesis: measurement of luminescence signals in quartz and feldspar, determination of dose rates, and statistical concepts such as the Bayesian approach to estimate the true equivalent dose.

### 1.4.1 The Luminescence phenomenon

Luminescence is a phenomenon in which minerals (e.g., quartz or feldspar) release previously-stored energy in the form of light. A number luminescence phenomena have been studied within the literature (e.g., phosphorescence, fluorescence, photoluminescence, thermoluminescence, etc.) with the earliest observation dating back to the reporting of light emission from a stone in Italy in the 17$^{th}$ century (Mahesh et al., 1989). In this thesis, our focus is on luminescence, which requires prior absorption of energy "from an external ionising source": the photophosphorescence (Yukihara and McKeever, 2011, p.2).

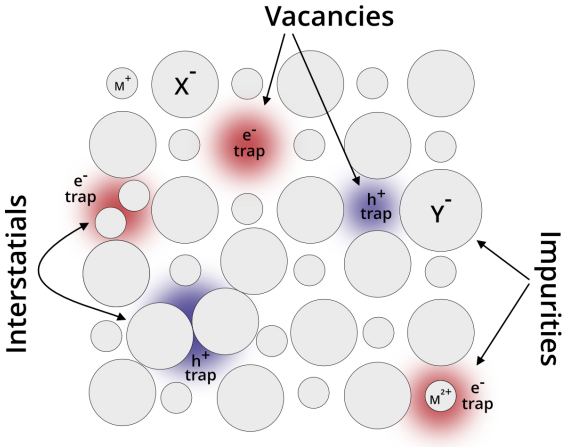


Figure 1.5: Common types of intrinsic defects in a crystal lattice. Figure redrawn and simplified after (King et al., 2016, their Fig. 1).

Luminescence phenomena rely on the presence of defects within the crystal lattice of minerals (Fig. 1.5). In a perfect crystal lattice, electron 'trapping' is not possible, yet where defects exist, electrons remain in metastable energy states. The average duration of an electron in a state depends on the characteristic of the defect, and the environmental conditions (Aitken, 1985). Defects in a crystal lattice can be described as either intrinsic or extrinsic (Preusser et al., 2009). Intrinsic (point) defects occur due to a number of reasons, such as a vacancy caused by missing atoms inside the crystal lattice (Schottky defects), by displacement of atoms (interstitial Frenkel

defect), or by atomic disorder (Mahesh et al., 1989). For example, in quartz, the most common intrinsic defect is an oxygen vacancy (Preusser et al., 2009). Extrinsic defects occur due to impurities in the crystal lattice, e.g. by substituting in trace elements. In quartz, Al, Ge, and Fe commonly replace Si (Preusser et al., 2009).

Energy-band models are commonly employed to explain luminescence processes. Valence bands represent an energy level fully occupied with electrons while conduction bands are usually assumed to be empty. In this theory possible metastable energy states for charges (electrons and holes) are located in the bandgap between the valance and conduction bands, often referred to as the 'forbidden zone'.

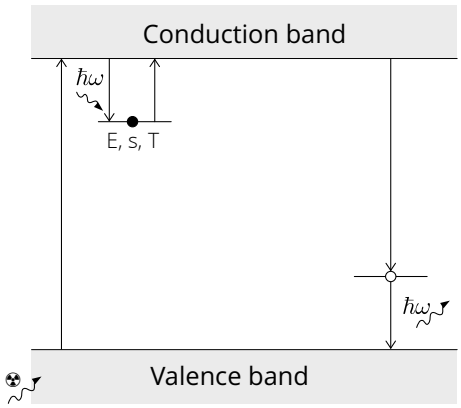


Figure 1.6: A simple energy-band model used to explain luminescence production. $E$ (eV) and $s$ ($s^{-1}$) are the depth trap and frequency factor. $T$ (K) is the temperature.

Figure 1.6 illustrates a simple energy band model with only one electron trap and one recombination centre (e.g., McKeever, 1988; Chen and Pagonis, 2011). When the system receives adequate energy (e.g., exposure to the ionisation radiation), it creates an electron-hole pair (in $cm^{-3}\,Gy^{-1}$). The electron from the valence band can jump up (excitation) to the conduction band and leaves behind a 'hole' in the valence band, which has a positive charge. Once the electron is in the conduction band, it can move 'freely' but constantly tries to reach the lower energy state eventually, the electron becomes captured in an electron trap depending on the capture rate ($\sigma = \pi r^2$, where $r$ is the radius of the trap, here usually in cm) and remains there for a certain amount of time. The duration an electron spends in a trap depends on the characteristics of the trap, defined by $E$ (eV) the trap depth, and $s$ ($s^{-1}$) the frequency factor. The thermal lifetime $\tau$ (in s) of a captured electron in one particular trap configuration is described by the Arrhenius equation (McKeever, 1988):

$$\tau = s^{-1} exp(\frac{E}{k_b T}) \tag{1.3}$$

where $k_b$ ($\mathrm{eV\,K^{-1}}$) is the Boltzmann constant and $T$ is the temperature in Kelvin. According to this equation, a trap with $E = 1.7\,\mathrm{eV}$ and $s = 5 \times 10^{13}$ ($\mathrm{s^{-1}}$) (the trap parameters for the fast OSL component according to Bailey 2001, see below) results in a lifetime of ca 500 Ma at 20 °C. This (thermal) stability is one of the fundamental assumptions in luminescence dating.

If the system receives sufficient energy in the form of heat (phonons) or light (photons), the electron can be freed from the trap. In the simplest case, if the electron reaches the conduction band, then the electron has two options: it either falls back to the valence band (non-radiative transitions), or the electron recombines with a hole (luminescence production). The recombination of the electron with the hole produces light, which can be detected. This describes the basic principle, but the processes actually occurring are much more complex. The light emitted by the recombination process, is not necessarily equal to the energy difference of the luminescence centre to the conduction band. General kinetic models on luminescence production, such as proposed by Bailey (2001) to explain OSL and TL of quartz, address this complexity by involving many different charge transitions.

Typical stimulation energies in OSL and IRSL dating range from 3.1 eV to 1.4 eV (ca 405–885 nm), and typical detection energies range from 3.8 eV to 2.6 eV (ca 330–470 nm). Luminescence dating relies on photophosphorescence in which stimulation is carried out with a larger wavelength and the detection performed in a shorter wavelength (anti-Stokes emission) (Aitken, 1998; Yukihara and McKeever, 2011; Mahan and DeWitt, 2019). A new approach, infrared photoluminescence (IR-PL, Prasad et al. 2017) is being developed which makes use of the Stokes emission.

While this simple model provides a basic understanding of luminescence production in minerals, more complex models involving multiple energy states and transitions have been proposed in the literature (e.g., for quartz and feldspar: Bailey, 2001; Jain and Ankjærgaard, 2011, respectively). A more detailed consideration of these factors is beyond the scope of this thesis, however.

### 1.4.2 The OSL signal

Figure 1.7 (left) shows a typical quartz signal derived by continuous-wave (CW-) OSL (in which a stimulation power is kept constant over the stimulation time): stimulated with blue light (ca 470 nm) and detected in the ultraviolet (UV) wavelength range (ca 340 nm).

The rate of the released electrons from the corresponding trap during CW-OSL can be explained using a first-order kinetic assumption:

$$\frac{dn(t)}{dt} = -Pn(t) \tag{1.4}$$

in which $n(t)$ is the number of the electrons in the trap at time $t$ (s), and $P$ ($\mathrm{s^{-1}}$) is the

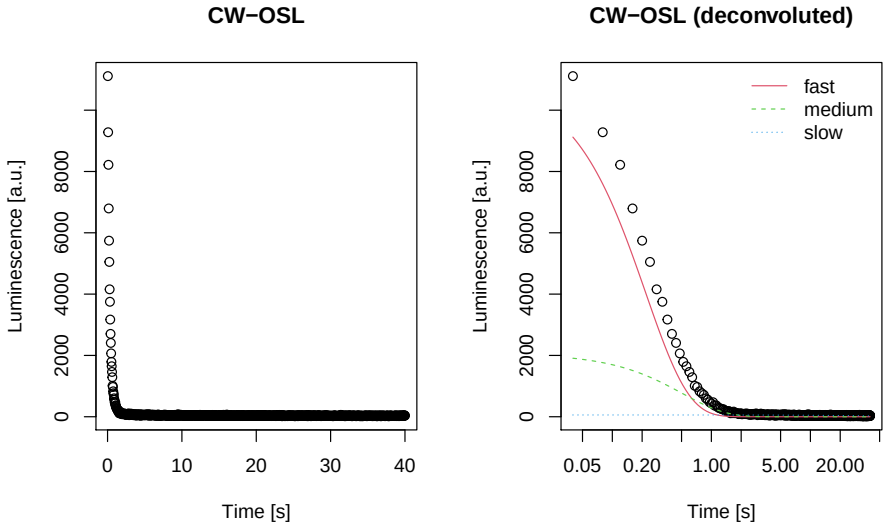


Figure 1.7: A typical quartz signal stimulated with continuous-wave (CW-) OSL (left). The same OSL signal deconvolved and the components detailed (right). These plots use example data from the R package 'Luminescence' (Kreutzer et al., 2019).

probability of releasing electrons per time interval. Equation 1.5 implies a single exponential decay for the related luminescence intensity, which can be described as:

$$I(t) = I_0 exp(-Pt) \text{ and } P = \sigma I_0 \tag{1.5}$$

in which $I_0$ ($s^{-1}\,cm^{-2}$) is the initial intensity (at $t = 0$), and $\sigma$ ($cm^2$) is photoionisation cross-section. The photoionisation cross-section is the efficiency of a photon to release an electron from the trap. It depends on the optical stimulation energy and the temperature (e.g., Chruścińska and Kijek, 2016). Therefore, the function $P$ (detrapping probability) is related to the stimulation mode.

Smith and Rhodes (1994) recognised that a quartz OSL signal consists of several components with different signal characteristics, described by different cross-sections (Fig. 1.7 right), so:

$$I(t) = \sum_{i=1}^{n} N_i exp(-P_i t) \tag{1.6}$$

Bailey et al. (1997) attributed particular bleaching characteristics to these components and categorised them into fast, medium and slow components ordered by their bleachability. A rapid and efficient resetting of the luminescence signal by sunlight exposure is one of the underlying fundamental assumptions in luminescence dating (Godfrey-Smith et al., 1988). As Bailey et al. (1997) have shown, the fast component is of most interest, as it can be bleached within a few

seconds compared to other components. If components with slower bleachability contribute significantly to the sum OSL signal, the visual perception is that the sum curve flattens.

### 1.4.3 Linearly modulated stimulation

Bulur (1996) suggested a method in which the stimulation power ramps linearly (linear modulation OSL, LM-OSL), instead of being constant (CW-OSL), to release electrons gradually from the traps. As discussed above, the efficiency of electrons evicted from traps is defined by the photoionisation cross-section. Applying LM-OSL technique results in TL like curve shape (Fig. 1.8), which is believed to be of advantage to separate signal components, which is mathematically difficult for a sum of exponential components (cf. Istratov and Vyvenko, 1999), since it provides a better visualisation of the components.

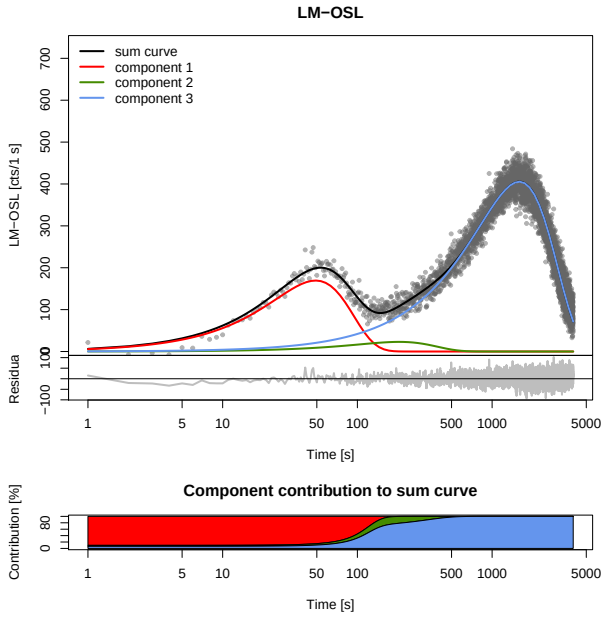


Figure 1.8: A quartz signal stimulated with linear modulation (LM-) OSL and its components. Example data from the R package 'Luminescence' (Kreutzer et al., 2019).

After Bulur (1996) Eq. 1.5 can be transformed to:

$$I(t) = N_0 \frac{\sigma I_0 t}{T} \; exp(\frac{\sigma I_0 t^2}{2T}) \tag{1.7}$$

Where $N_0$ is proportional to the number of captured electrons within the trap before stimulation, $I_0$ ($s^{-1}\,cm^{-2}$) is the maximum stimulation power intensity, and $T$ (s) refers to the total duration of measurement. In conjunction with mathematical curve fitting, LM-OSL has been extensively employed to characterise quartz luminescence signals (Singarayer and Bailey, 2003;

Jain et al., 2003; Singarayer and Bailey, 2004). These studies identified up to seven signal components: ultra-fast, fast, medium and four slow components (S1, S2, S3 and S4) with photoionisation cross-section values ranging from $10^{-16}$ ($cm^{-2}$) to $10^{-21}$ ($cm^{-2}$) (Jain et al., 2003). In addition to different bleaching characteristics, it was also found that the components have different thermal stabilities ($\tau$, Eq. 1.3) and saturation levels.

According to Choi et al. (2006), LM-OSL discrimination of the quartz OSL components to be more “effective and accurate" (Choi et al., 2006, p. 6) compared to CW-OSL. Unfortunately, the stimulation method is time-consuming (ca $10^2$ s, for CW-OSL compared to ca $10^4$ s, for LM-OSL for single curve) and for both, CW-OSL and LM-OSL, the fitting procedure is error-prone (Durcan and Duller, 2011). For these reasons, LM-OSL is not widely applied in luminescence dating. Nevertheless, it can provide valuable insights into the signal components within a quartz sample, and is of interest to this thesis.

### 1.4.4 Extracting the fast-decaying signal component

As mentioned above, the fastest bleachable component in quartz OSL is the most attractive component for conventional dating, as it has the highest likelihood that the signal was sufficiently reset before burial (within a few seconds). It has also been reported that the fast component is more thermally stable compared to some of the slow components (Wintle and Murray, 2006). The fast component detected in the UV wavelength range becomes saturated at relatively low doses (e.g., $D_0$ values between 78–129 Gy Singarayer 2002), yet is still sufficient for many dating studies where the equivalent doses are low enough (e.g., for most upper Palaeolithic dating studies). In contrast, the medium component is thought to lead to inaccurate equivalent dose estimations and often underestimations (Bailey, 2010). Alongside LM-OSL, other techniques have been proposed to separate the fast component from the bulk signal. For instance, Ballarini et al. (2007) and Cunningham and Wallinga (2010) proposed an early background subtraction (instead of the commonly applied late background subtraction), to reduce the contribution of unwanted components (medium and slow) to the bulk signal. However, if the contribution of the medium component is dominant in the first few seconds, this approach may fail (Wintle and Murray, 2006).

Bailey et al. (2011) suggested a more promising approach, employing the use of green OSL rather than blue OSL. This technique developed from Singarayer and Bailey (2004) who monitored the relationship between the photoionisation cross-sections of the fast and the medium component using different stimulation wavelengths. Their investigation showed that by increasing the stimulation wavelength, the ratio $\sigma_{fast}/\sigma_{medium}$ increased substantially. Precisely, by increasing the stimulation wavelength from 375 nm to 590 nm, the ratio increased from 1.4 to 30.6. This showed that photoionisation cross sections depend on the stimulation wavelength

($\lambda$), following the empirical relationship after Bailey et al. (2011):

$$log_{10}(\sigma_{fast}) = -71.4 + (0.307\lambda) + (-5.46 \times 10^{-4}\lambda^2) + (2.97 \times 10^{-7}\lambda^3) \quad (1.8)$$

$$log_{10}(\sigma_{medium}) = -57.5 + (0.225\lambda) + (-3.83 \times 10^{-4}\lambda^2) + (1.83 \times 10^{-7}\lambda^3) \quad (1.9)$$

Graphical representations of these formulas are displayed in Fig. 1.9. If a sample has a strong medium component contribution, this equation argues that it is favourable to stimulate with green light instead of blue light, as this reduces the probability that electrons within the medium component will be stimulated. Consequently, in this thesis, green light stimulation (rather than blue) was used for samples that exhibited a steady medium component (see Sec. 3.3.5.2).

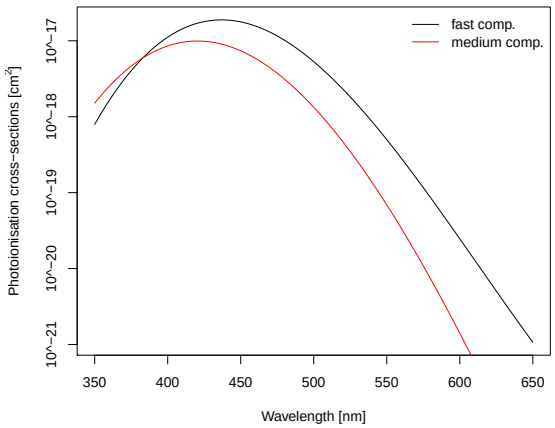


Figure 1.9: Relationship between photoionisation cross-section and the stimulation for the fast and medium components using the fitted data from Bailey et al. (2011).

### 1.4.5 Estimating of the $D_e$ of quartz using the SAR protocol

The Single Aliquot Regenerative (SAR) dose protocol (Murray and Wintle, 2000; Wintle and Murray, 2006) is the most widely used measurement sequence to estimate the equivalent dose ($D_e$) of quartz (see Table 1.1). This protocol consists of several steps of heating, irradiation and optical stimulation to build-up a dose-response curve (a curve representing the relationship between energy doses and luminescence signals) from which a $D_e$ can be determined.

The SAR protocol consists of several cycles, each attributed to one regenerative dose, except for the first cycle where the natural signal is measured (the corresponding regenerative dose is 0). Prior to optical stimulations, the protocol involves a thermal treatment to remove the contribution of unstable traps to the luminescence signal. To select an appropriate temperature

Table 1.1: SAR protocol after Wintle and Murray (2006).

| # | Step | Observation |
|---|---|---|
| 1 | Irradiation (regenerative dose) | |
| 2 | Thermal treatment (preheat 200–300 °C) | |
| 3 | Optical stimulation (e.g., for 40 s at 125 °C) | $L_n, L_x$ |
| 4 | Irradiation (test-dose) | |
| 5 | Thermal treatment (cut heat 200-300 °C) | |
| 6 | Optical stimulation (e.g., for 40 s at 125 °C) | $T_n, T_x$ |
| 7 | (Hotbleach, e.g., stimulation for 40 s at 280 °C) | |

for each sample, a preheat test is commonly carried out spanning from 200 °C to 300 °C. This temperature range is sufficient to remove thermal transfer caused luminescence signals from the shallow traps into the fast component in quartz. The selected preheat temperature must not affect the true $D_e$. An inappropriate preheat temperature will either result in an underestimation of the $D_e$ by thermally depleting the fast component signal, or lead to an overestimation of the $D_e$ by not sufficiently removing unstable signals from shallow traps. A test is performed in which the $D_e$ is determined for a range of temperatures, and the temperatures for which $D_e$ lies in a plateau can be selected as an appropriate temperature for measurement. After a preheat, the natural signal is measured using blue or green optical stimulation. To build up a dose-response curve, the sample receives a different dose (regenerative points) for each SAR cycle, and the corresponding OSL signals are measured accordingly. Thermal treatment and irradiation, can both affect the density of radiative and non-radiative recombination centres, which may lead to a change in luminescence efficiency (Wintle and Murray, 2000). To monitor this sensitivity change of quartz grains during irradiation and preheat, the sample is irradiated with a low 'test' dose (typically between ca 10 % to 20 % of the natural dose; Murray and Wintle 2000), after measuring each regenerative dose signal. The OSL signal of regenerative dose at each step is normalised to this constant test dose. The test dose is followed by a cut-heat to remove the contribution of a thermally unstable component to the luminescence signal as a result of measurement of the test dose signal.

After the highest regenerative dose has been reached, the sample receives a zero dose, the 'recuperation test'. A ratio is calculated comparing the normalised signal for this zero dose to the normalised natural signal to test whether thermal transfer has occurred as a result of preheating within the SAR cycle. A rejection criteria of $< 5$ % is normally set (Murray and Wintle, 2000). In cases where recuperation values are high, Murray and Wintle (2003) suggest to add an additional 'hot bleach' to each SAR cycle (e.g., 280 °C) to minimise thermal transfer from non-radiative traps to the fast component.

The efficiency of the monitoring of sensitivity change is checked systematically: the first regenerative dose of the SAR protocol is repeated in the last cycle after the regenerative cycles. The normalised luminescence signal in this step should be comparable with the normalised lumines-

cence signal of the first regenerative point (a rejection criteria of within 10 % of unity is normally accepted). However, this rejection criterion is not always appropriate for assessing the validity of the $D_e$. In this thesis, I have found a number of examples where the recycling ratio failed, yet the estimated $D_e$ s were consistent with what we believed is the true $D_e$ (see Sec. 2.4.2.2).

Finally, to check for feldspar contamination within quartz samples, an infrared light stimulation (IRSL, Hütt et al. 1988) test can be performed. At the end of the SAR protocol, the sample is irradiated with the first regenerative dose for a third time, followed by stimulation with IRSL at 50 °C, and then by blue stimulation. Feldspar is highly sensitive to IRSL, yet quartz grains are not. In the absence of feldspar grains, this normalised OSL signal should be indistinguishable (within 10 % of unity) from the signal of the first regenerative dose (Duller, 2003).

To test the efficiency of the SAR protocol, a dose-recovery test is often performed. This test includes bleaching of the samples using blue LEDs or solar simulation, followed by a pause to allow the unstable shallow traps to empty and for charge to transfer back to the stable (fast component) OSL traps. Optical stimulation is then performed to empty the stable trap. Finally, the sample receives a dose approximate to the $D_e$ of the sample, and the SAR protocol is applied. The protocol is assumed to be valid if the ratio of the obtained dose to the given dose lies within 10 % of unity. However, the dose-recovery test does not always seem to be the best indication of the validity of the SAR protocol (see Sec. 4.2.4.1).

For each sample measured, it is important to note the parameters used within the SAR protocol, as the requirements for specific measurements are sample dependent.

### 1.4.6 The $D_e$ estimation using (K-) feldspar

In addition to quartz, feldspar (particularly K-feldspar) has been used extensively for luminescence dating as a natural dosimeter (e.g., Wallinga et al., 2000). K-feldspar has several advantages over quartz, and is often required for analysis in some geological settings where quartz abundance is low. Crucially, feldspar has higher dose saturation range than quartz (4–5 times, Buylaert et al. 2012), making it possible to date samples older than ca 100-150 ka. The IRSL signal from feldspar also usually shows higher signal intensities, allowing for the precision of the signal measurements to be higher (e.g., Li and Li, 2011). However, feldspar suffers from athermal fading (Wintle, 1973; Aitken, 1985), which makes accurate estimation of palaeodoses challenging. Fading is thought to be caused by a quantum mechanics phenomenon 'tunnelling', in which a captured electron passes a wall of the trap without the need for input of energy, e.g., optical stimulation (Spooner, 1992).

One of the most widely used procedures to measure luminescence signals from K-feldspar is to stimulate with an infrared wavelength, at ca 50 °C, and conduct measurements in the blue-violet wavelength range. This is called the IRSL. The IRSL stimulation provides enough energy to transfer an electron from the ground state to the excited state (ca 1.4 eV). In the exited sate,

the electron can either travel to nearby recombination centres (via excited state tunnelling), or it can move towards the band tails below the conduction band to access recombination centres further away from the electron trap (Thomsen et al., 2008). This results in the production of a luminescence signal (Poolton et al., 2002a,b).

Huntley and Lamothe (2001), amongst others (see King et al., 2018, for review), proposed a method for fading correction which has been applied widely on IRSL signal on K-feldspar. Attempts have been made to decipher the tunnelling mechanism in K-feldspar traps in an aim to minimise its effect and discover a signal with the lowest possible fading (e.g., Thomsen et al., 2008; Jain and Ankjærgaard, 2011; Li and Li, 2011).

Several investigations have been carried out to decipher the relationship between stimulation energy and fading rate (e.g., Thomsen et al., 2008; Li and Li, 2011). They reported that by increasing stimulation energy, fading rate decreases. This could be because, if the stimulation energy is higher than IRSL at 50 °C (ca 1.4 eV), it provides enough energy for captured electrons to not only pass into the excited state of the trap but also to reach the conduction band in which distant recombination centres can be reached. The probability of tunnelling from the excited state to close recombination centres therefore decreases. Although (ground state) tunnelling is not a thermally assisted phenomenon, temperature can play a fundamental role in transferring an electron from the excited state to the higher energy of the bandtail and reaching more distant recombination centres (Thomsen et al., 2008). Tunnelling from the lower state energy of the band tail is also possible based through the model proposed by (Jain and Ankjærgaard, 2011, band-tail tunnelling, their Fig. 3). As a result, attempts towards to measurement of a non-fading signal should not only avoid tunnelling from the excited state (laboratory fading) but also from the lower part of the band tail during stimulation (Thomsen et al., 2008). The corresponding experiments by Thomsen et al. (2008) resulted in a SAR-like protocol that is believed to not suffer from athermal fading: post-IR-IRSL at elevated temperature (e.g., 290 °C; Thiel et al. 2011; Buylaert et al. 2012). The first step of the protocol, an IRSL stimulation at 50 °C, results in the removal of the part of the signal related to electrons that have tunnelled to recombination centres in close proximity. The second IR stimulation at higher temperatures (e.g., 225 °C or 290 °C) transfers electrons to the excited energy state, from which charges can be thermally transferred to the higher energy state in the band-tail, where the possibility of tunnelling is reduced. Through the bandtail states, an electron can migrate to distant recombination centres, and a 'non-fading' signal can be measured.

In this thesis, the post-IR IRSL protocol at 290 °C (see Table 1.2 after Buylaert et al. 2012) was therefore employed for dating some of the samples composed of K-feldspar grains and for the polymineral fraction (see Secs. 3.3.5.3, 4.3.3, 5.2.5).

Table 1.2: The post-IR IRSL protocol at 290 °C after Buylaert et al. (2012).

| # | Step | Observation |
|---|---|---|
| 1 | Irradiation (regenerative dose) | |
| 2 | Thermal treatment (preheat 320 °C) | |
| 3 | IRSL stimulation (for 200 s at 50 °C) | |
| 4 | IRSL stimulation (for 200 s at 290 °C) | $L_n, L_x$ |
| 5 | Irradiation (test-dose) | |
| 6 | Thermal treatment (preheat 320 °C) | |
| 7 | IRSL stimulation (for 200 s at 50 °C) | |
| 8 | IRSL stimulation (for 200 s at 290 °C) | $T_n, T_x$ |
| 9 | IRSL stimulation (for 200 s at 325 °C) | |

### 1.4.7 Statistical models to estimate the Palaeodose

Estimation of the palaeodose (the true burial dose, the equivalent dose is the best estimation of it) for each sample can be undertaken through two conventional approaches: multi-grain and single-grain techniques. In the multi-grain approach, up to ca $10^6$ grains are mounted on a sample carrier (depending on the grain size, Duller 2008). The resulting luminescence signal is the sum of the signals from all of these grains. In the single-grain technique, however, the $D_e$ is determined for each individual grain located in a hole within a special single grain disc. In environments where all grains within a sample belong to a particular unit that has been sufficiently bleached and has no signs of post-depositional sediment mixing, the outcome from multi-grain and single grain analysis would be expected to be similar, so either approach could be used. However, in environments where the possibility of insufficient bleaching or mixing between layers cannot be ruled out, the single grain approach has significant advantages. Here, signals from individual grains can be assessed to identify the bleached grains.

In this thesis, I have monitored the bleachability of quartz grains by measuring post-IR $IRSL_{290}$ signals on K-feldspars and the polymineral fraction and compared them to signals derived from OSL on quartz. Since the bleaching rate of the blue OSL signal is much faster than post-IR $IRSL_{290}$ (Murray et al., 2012), consistency between ages shows evidence of sufficient bleaching. A general agreement is seen between OSL ages and post-IR $IRSL_{290}$ for the samples of Ghār-e Boof and Bawa Yawan, indicating that the quartz grains were sufficiently bleached. For this reason, the multi-grain approach was deemed acceptable, and measurements were continued in this manner. For samples from the site Mirak (Ch. 3), a discrepancy was seen between the ages produced by both protocols. Here, older ages obtained from the post-IR $IRSL_{290}$ analysis on K-feldspars represent insufficient beaching, and an age overestimation. This is thought to be the result of the alluvial nature of the sediment transport, as well as the occurrence of a reparative flood. Whilst it would be advantageous to perform single-grain measurements for a few samples to monitor the dispersion between grains signals, availability of measurement time was limited during this thesis. Here, I hypothesised that insufficient bleaching of the K-feldspar grains does

not have the same weighting on quartz grains, due to their distinctly different bleaching rates. These was also supported by the inherent consistency between the quartz OSL ages.

In both cases (multi and single grain measurements), a dose-response curve can be produced using the results from the normalised regenerative dose points (after applying SAR protocol) using fitting functions available in the *Analyst* (Duller, 2015) or in the R (R Core Team, 2019) package 'Luminescence' (Kreutzer et al., 2012). In this thesis, *Analyst* was used for single grain measurements, and both *Analyst* and 'Luminescence' were used for multi-grain measurements.

A single saturating exponential function ($\frac{L}{T} = A(1 - exp(\frac{-x}{D_0}))$ is often used for fitting as it addresses luminescence signals dominated by a single component. However, due to signal averaging effects, this function can lead to poor fitting, particularly for the multi-grain approach. Instead, an exponential plus linear function ($\frac{L}{T} = A(1 - exp(\frac{-x}{D_0})) + Cx)$) with a higher number of degrees of freedom can be employed.

I determined $D_e$s using different fitting functions to generate dose-response curves for four randomly selected samples from the site of Mirak. These functions included: single saturating exponential plus linear, single saturating exponential, and sum of two single saturating exponentials (data not shown). The obtained $D_e$ s from all three functions were in a good agreement (albeit one sample in which the single saturating exponential led to 10 % lower $D_e$ compared to the other methods), justifying the use a single saturating exponential plus linear function for fitting a dose-response curve.

Uncertainty on $D_e$s can be caused by errors in photon counting statistics (Galbraith, 2002), curve fitting uncertainties (Duller, 2007), and uncertainties related to the reproducibility of the measurement conditions (e.g., dispersion in stimulation intensity or temperature) (Thomsen et al., 2005). A Monto Carlo method and error propagation, both, are available in *Analyst* to estimate the uncertainty on $D_e$. The final $D_e$ and its corresponding error are estimated using Gaussian probability density parameterisation.

Once equivalent doses and corresponding uncertainties have been determined, an appropriate statistical model is then required to obtain a representative $D_e$ and assess its uncertainty for the distribution. In an ideal case, where all grains had been sufficiently bleached before deposition, and the possibility of grains mixing between layers can be ruled out, a common statistical model that can be used to determine the central dose (the relevant equivalent dose), is the Central Dose Model (CDM) also well known as CAM (Central Age Model, Galbraith et al. 1999).

Equation 1.10 shows how the CDM estimator leads to the central dose (in the logarithm scale). $d_j$ is the log of the equivalent dose of aliquot $j$ ($D_j$), and $\sigma_j$ is the corresponding relative uncertainty (Galbraith and Roberts, 2012). $\sigma$ refers to overdispersion within the sample ("relative standard deviation", Galbraith et al. 1999, p. 359), to describe any additional dispersion in the distribution of individual equivalent doses beyond what would be expected from analytical

uncertainty alone

$$d_{CDM} = \frac{\sum_j^n \frac{d_j}{\sigma_j^2+\sigma^2}}{\sum_j^n \frac{1}{\sigma_j^2+\sigma^2}}. \tag{1.10}$$

The formula shows that the CDM estimator is the weighted mean of $d_j$ in which the value of $\sigma$ and the relative analytical uncertainty ($\sigma_j$) play roles in the final dose estimation. In cases where $\sigma \gg \sigma_j$, the formula can be written as:

$$d = \frac{\sum_j^n \frac{d_j}{\sigma^2}}{\sum_j^n \frac{1}{\sigma^2}} = \sum_j^n \frac{d_j}{n} \tag{1.11}$$

Therefore

$$log(D_{CDM}) = \frac{\sum_j log(D_j)}{n} \tag{1.12}$$

and

$$D_{CDM} = (\prod_j^n D_j)^{1/n}. \tag{1.13}$$

As a result, when the overdispersion is large, the CDM calculates the geometric mean rather than the arithmetic mean and the CDM estimator leads to the median of the lognormal distribution (Guérin et al., 2015b). This becomes an issue when calculating an age, as the age equation divides the equivalent dose (here a geometric mean) by the dose rate (arithmetic mean, not a geometric mean, Guérin et al. 2017). Consequently, these authors found the CDM to underestimate the true equivalent dose, as the geometric mean is less or equal to the arithmetic mean.

To overcome this dose-underestimation in cases of large overdispersion, the Average Dose Model (ADM) was proposed by Guérin et al. (2017).

$$d_{ADM} = \frac{\sum_j^n \frac{d_j+\frac{\sigma_d^2}{2}}{\sigma_j^2+\sigma_m^2+\sigma_d^2}}{\sum_j^n \frac{1}{\sigma_j^2+\sigma_m^2+\sigma_d^2}} \tag{1.14}$$

In general, substituting $d_j$ by $d_j+\frac{\sigma_d^2}{2}$ in Eq. 1.10 always leads to the arithmetic mean in the ADM even for a large overdispersion. In Eq. 1.14 (the ADM), a distinction is made between intrinsic overdispersion ($\sigma_m$) (Thomsen et al., 2005) and extrinsic overdispersion ($\sigma_d$) for modelling. Intrinsic overdispersion is the variability we observe in the $D_e$ distribution when all grains receive an identical dose. Scatter in the measured $D_e$ is thought to come from differences between quartz grain characteristics. This value can be calculated from dose-recovery experiments. Extrinsic

overdispersion $\sigma_d$, in contrast refers to the dispersion in the dose distribution, which commonly occurs due to $\beta$-(or $\alpha$-) dose-rate heterogeneity in well-bleached samples. The central dose of ADM and $\sigma_d$ is determined using bootstrapping.

ADM is advantageous over CDM for the estimation of a central dose of a $D_e$ distribution in cases where external overdispersion $\sigma_d$ is high, e.g., due to $\beta$-dose rate heterogeneities (K-rich hotspot). In cases where external overdispersion is low, both models would produce comparable estimated doses.

In this thesis, I designed a laboratory-controlled experiment to simulate a lognormal positively skewed dose distribution consistent with what is observed in nature due to the presence of a hotspot (K-rich feldspar) in the sediment. I compared the estimated $D_e$ from the artificially created lognormal distributions with the various dispersions using CDM and ADM to monitor the extent to which the estimated central doses differ (see Ch. 2).

Besides, these two models, $D_e$ distributions can be defined by Gaussian parameterisation, then the arithmetic mean of the $D_e$ distribution can be presented as a true equivalent dose of the sample, and the standard deviation of the mean represents the uncertainty on the palaeodose. This approach was followed to determine the palaeodose for the samples of the sites Mirak, Ghār-e Boof and Bawa Yawan.

### 1.4.8 Dose rate determination

To estimate the burial time of the minerals (e.g., quartz and feldspar), the equivalent dose ($D_e$), is divided by the dose rate (Eq. 1.1). The equivalent dose represents the amount of energy stored in the dosimeter and the dose rate represents the energy emitted by radionuclides per mass (dose) and per time (dose rate).

Natural radioactivity of radio-elements such as $^{238}$U, $^{232}$Th and $^{40}$K in the sediment surrounding natural dosimeters such as quartz and feldspar, form the external primary source of energy in this system. Cosmic rays are also important as an external source of energy. The cosmic dose rate depends predominantly on the geographical location of the sample collection (primarily elevation above sea level, but also latitude and longitude) and the thickness and density of the overlying material (Prescott and Hutton, 1994). Radioactive nuclides within the quartz and feldspar dosimeters also contribute an internal source of energy. To determine the external dose rate, the equivalent mass concentration of radionuclides (primarily $^{238}$U, $^{232}$Th and $^{40}$K) in the sediment sample needs to be determined. This can be undertaken using high-resolution, low-level background $\gamma$-ray spectrometry (Guibert and Schvoerer, 1991) to obtain a $\gamma$-emission spectrum of the radionuclides. The spectrum obtained is calibrated using spectrum from samples of known nuclide mass concentrations, to obtain an estimation of the radionuclides equivalent mass concentrations in the sample studied. These equivalent concentrations can be converted to a dose-rate using the “infinite matrix assumption". This assumption states that “the rate of

energy absorption is equal to the rate of energy emission" (Aitken, 1985, p.66). Conversion factors need to be applied (e.g., Adamiec and Aitken, 1998; Guérin et al., 2011) to convert nuclide concentrations into dose rates.

Due to radionuclides emitting $\alpha$-and $\beta$-particles, and $\gamma$-photons, the effective external dose rate can be subdivided into $\alpha$, $\beta$-and $\gamma$-dose rates. As the stopping power range of $\gamma$-ray is much larger than the grain-size analysed in luminescence, particle attenuation needs to be applied to only the $\alpha$-and $\beta$-particles (e.g., Aitken, 1985; Guérin et al., 2012).

The efficiency of induced luminescence by $\alpha$-particles is significantly lower than that of $\beta$-particles and $\gamma$-photons (per $\mathrm{J\,kg^{-1}}$). During penetration of an $\alpha$-particle into a grain, the heavy $\alpha$-particles deposit energy along only a localised path (Mauz et al., 2006). To estimate the $\alpha$-efficiency, a comparison can be made between the luminescence signal obtained after $\beta$-or $\gamma$-irradiation, with that obtained after only $\alpha$-radiation. This relationship between the $\beta/\gamma$-and $\alpha$-induced luminescence signal can be expressed as a dimensionless $a$-value (e.g., Mauz et al., 2006), and is an important value to take into account when calculating the $\alpha$-dose rate contribution (for an overview see Kreutzer et al. 2018a.

The internal dose rate from within a grain can be determined by estimation of the $\alpha$-dose rate derived of the concentrations of $^{238}$U and $^{232}$Th within a quartz grain. Internal dose rates from quartz often have only a minor contribution to the overall dose, so are often not considered. However, the value of $0.06 \pm 0.03\,\mathrm{Gy\,ka^{-1}}$ has been used as a representative internal dose rate (for sand size quartz grains) (approximated after Mejdahl, 1987). In contrast, the internal dose rate of K-feldspar is dominated by its significant potassium concentration. This concentration is often assumed to be $12.5 \pm 0.5$ % if K-feldspar grains are extracted from other minerals (Huntley and Baril, 1997).

The $\alpha$-particles only interact with the outer 20–25 $\mu$m of a grain. When focusing on sand-sized quartz, conventional sample preparation techniques treat grains with hydrofluoric acid (40 %) to remove the outer layer of the grains (for an overview of etching procedures, see Porat et al. 2015), enabling the $\alpha$-dose rate to be considered zero.

In this thesis, this etching method was performed for preparation of samples from the site of Mirak (Ch. 3) and Delazian (Appendix C.2) (grain size: 80–140 $\mu$m) and so the $\alpha$-dose rate contribution did not need to be calculated. For two other sites, Ghār- e Boof (Ch. 4) and Bawa Yawan (Ch. 5) (grain sizes: 41–60 $\mu$m and 20–41 $\mu$m), the contribution of $\alpha$-dose rate for quartz and feldspar grains were calculated by applying an $a$-value obtained from the literature (e.g., Mauz et al., 2006; Schmidt et al., 2018).

#### 1.4.8.1 Water content

The presence of water in sediment leads to difficulties in estimating dose rates. The absorption coefficients for $\alpha$- and $\beta$-particles and $\gamma$-photons in water differ in comparison to a dry sediment

matrix (*"[...] water absorbs more than its fair share of energy from nuclear radiations [...]"*; Aitken 1985, p. 69). Thus, the dose rate needs to be corrected for the effect of water in the sediment. The relationship between dry and moist sediment is described in the following (e.g., Zimmerman, 1971; Aitken, 1985):

$$\dot{D}_{moist} = \frac{\dot{D}_{dry}}{1 + kWF} \tag{1.15}$$

where $k$ is a dimensionless correction factor defined separately for $\alpha$-, $\beta$-particles and $\gamma$-photons (Aitken, 1985; Guérin and Mercier, 2012).

$W$ is the water saturation level estimated as the maximum weight of water in the sediment over the weight of dry sediment, and $F$ is a fraction of $W$, describing the amount of water content (as found) in the sediment.

One common methods used to estimate the water content ($WF$) is to dry the sediment after sampling to determine the amount of evaporated water. However, this 'as found' water content does not always truly reflect the water content at burial. Additional granulometric analysis can help to estimate the fraction of the saturated water content of a sediment type (e.g., Nelson and Rittenour, 2015). This value can be used to correct for the effect of water in dose rate determination.

In this thesis, the water content was determined after sampling for three sites, but was not possible for the site of Ghār-e Boof (Ch. 4) as the samples arrived months after sampling, and had dried out entirely. Grain-size analysis estimates a value of $15 \pm 6$ % should be used as a probable water content during burial, but I have increased this value to $20 \pm 8$ % for the last layer in the site, due to observed moisture at the time of sampling. Here, I attributed 40 % of the water content as uncertainty, allowing a broader range to be covered.

#### 1.4.8.2 Disequilibria in the uranium decay chain

An underlying assumption of the luminescence dating age equation is that the dose rate remained stable over time. However, in some environmental settings, disequilibria in the uranium decay chain is inevitable, and can lead to variation of the radioisotope content throughout a burial history, and hence a variation in dose rate over time. Radioactive disequilibria can occur due to: (1) increasing chemical mobility of $^{234}$U due to its solubility in oxidation form (Krbetschek et al., 1994) which could lead to leaching from one sedimentary boundary to another, (2) leaching of $^{226}$Ra due to its high chemical mobility (Guibert et al., 2009), (3) an influx of $^{210}$Pb through the soil water, and (4) loss of $^{222}$Rn due to diffusion through pores in the sediment. An assessment of the exact source of disequilibrium is not straightforward, and requires further chemical analysis. A feasible method to check for evidence of disequilibria in the $^{238}$U decay chain is to obtain the equivalent mass concentration of U at the top and bottom of the decay chain using high-resolution

$\gamma$-ray spectrometry. The emissions from $^{234}$Th, $^{234m}$Pa and $^{234}$U correspond to the top (pre-Ra), and emission from $^{214}$Pb and $^{214}$Bi correspond to the bottom of the chain (post-Ra). Disequilibria can be inferred if the equivalent concentration from the top and bottom of the decay chain are not consistent. This can be taken into account by either assuming that disequilibrium happened recently (so we only consider the equivalent concentration from either the top or the bottom), or that disequilibrium has taken place gradually over time (we could calculate the average of the equivalent mass concentrations delivered from the top and the bottom of the chain (Guibert et al., 2009)). In this thesis, disequilibria has been observed in the $^{238}$U decay chain for some samples. The average uptake scenario was applied to 5 out of 22 samples from the site Mirak to minimise the effect of the disequilibrium. This averaging method resulted in older ages (compared with the non-average uptake scenario) by around 3–4 % for most samples, but was as high as 7 % to 16 % in extreme samples. For the site Ghār-e Boof (Ch. 4), the average uptake scenario was applied to 6 out of 14 samples, which resulted in an age decrease of around 1–3 % compared to not applying this scenario. For all samples from Bawa Yawan (Ch. 5), the $^{238}$U concentration from the top for the decay chain was used for calculation of the dose rate.

#### 1.4.8.3 In situ $\gamma$-dose rate estimation

The $\gamma$-dose rate can be calculated using a high-resolution $\gamma$-ray spectrometry in the laboratory if grain sizes and composition of the sediment are homogeneous, yet this is not always the case. The radiation range of $\gamma$-rays spans 30 cm, so it is often more appropriate to measure the $\gamma$-dose rate in situ. An in situ $\gamma$-dose rate estimation can be obtained using aluminium oxide ($\alpha$-$Al_2O_3$:C) chips (Akselrod et al., 1993) as they are highly sensitive artificial dosimeters (Whitley and McKeever, 2000; Akselrod et al., 1998; Erfurt et al., 2000). In this procedure, the chips are first bleached at 910 °C for 10 min to remove any residual dose (Kreutzer et al., 2018b), and then bleached by blue stimulation in a bleaching box. Three chips are stored in a 30 cm aluminium tube of which is then inserted into the stratigraphic section. After several months within the sediment, the tubes can be retrieved, and the dose measured in the laboratory.

### 1.4.9 Luminescence data analysis using the Bayesian approach

Statistical data processing is a vital step for any field using measured data, such as luminescence dating. Statistical analysis is commonly follows either a frequentist (classic) approach, or a Bayesian approach.

The frequentist approach can only be applied to the events that arose from repetitive experiments. Hence, the frequentist interpretation of the probability of occurrence of one event is described after a large set of repeated experiments, all under similar conditions (Carlin and Louis, 2000; Gelman et al., 2013). As examples, the statistical models of CDM and ADM apply this approach.

In contrast, the Bayesian approach estimates a probability of occurrence of an event under a conditional situation. The probability of an event happening is dependent on another phenomenon. This approach often begins with a prior belief about the current state of knowledge before any data is observed or measurements are run. The distribution of results can be explained as a weighted average of the initial knowledge (prior distribution) and the probabilistic model containing the observed data (likelihood function, cf. Gelman et al. 2013). The Bayes formula (or Bayes' rule), after Thomas Bayes (1701–1761, Bayes 1763) arises from the conditional probability as follows:

$$P(H|D) = \frac{P(D|H)P(H)}{P(D)} \tag{1.16}$$

If $H$ is our hypothesis about the probability of observing an event, and $D$ is our observation (real data), then the Bayes formula exhibits the (conditional) probability of certainty of the hypothesis $H$ given that the observation $D$. This is written as $P(H|D)$. Bayes formula renders that the probability of occurring $(H|D)$ is related to the probability of occurring $(H)$ and a chosen likelihood function, which contains the observation data $(D|H)$. Since no relationship exists between $P(D)$ and $H$, $P(D)$ can be considered as a constant (Gelman et al., 2013). Equation 1.16 therefore yields Eq. 1.17:

$$P(H|D) \propto P(D|H)P(H) \tag{1.17}$$

Equation 1.17 can also be described by the following:

$$Posterioir\ distribution \propto Likelihood\ function \times Prior\ distribution \tag{1.18}$$

The prior distribution (a key aspect of the Bayesian inference) represents the knowledge or belief one has about parameters of interest before considering the observations. When there is sufficient information available, it can have a significant influence on the final estimation. However, when prior knowledge is limited, or the information is vague, this prior distribution is not informative. Due to the importance of the prior distribution, it should be defined cautiously. The corresponding likelihood function can be constructed based on observed data. The likelihood function describes the probability of observing real data in the descriptive model previously designed. Finally, the posterior distribution renders the probability of the parameters, which describes the resulting distribution after observing the data.

Due to its complexity, the parameters of the posterior distribution cannot be determined analytically. A numerical simulation method, the Monto Carlo Markov Chain (MCMC) sampling, is therefore commonly used (Buck and Millard, 2004). This sampling algorithm plays a fundamental role in estimating complex probability distributions within an appropriate time (Andrieu et al., 2003). This sampler approximates posterior distributions by taking a large number of

samples to fully characterise a distribution (Gelman et al., 2013). Three chains of MCMC start from different initial points to monitor convergence in iterations. When the chains converge, the distribution is constructed by Markov-chain. Finally, the parameters are represented by the highest posterior density region (HPD) in 95 % or 68 % credible interval, a region in which most of the estimated distribution in each run lies.

#### 1.4.9.1 The Bayesian approach in luminescence-based chronologies

The Bayesian paradigm is used in numerical dating methods rather than the classical frequentist approach. In particular, the Bayesian paradigm is favourable when a study focuses on non-repeatable events or when access to observations is limited (Buck and Meson, 2015). Applying Bayesian inference allows other available chronological information to be combined before running measurements (prior belief). For example, the stratigraphic order of samples from a site can be incorporated into chronological modelling using a Bayesian approach. As this prior knowledge can have a significant effect on the final chronology, it is critical that the stratigraphic order is well-established to avoid under or overestimates in age.

Whilst the frequentist approach formed a fundamental core of luminescence data analysis for decades, the Bayesian approach has only recently risen in prominence in this field (e.g. Rhodes et al., 2003; Huntriss, 2008; Zink, 2013, 2015; Combès et al., 2015; Combès and Philippe, 2017; Mercier et al., 2016; Philippe et al., 2019). The R (R Core Team, 2019) package 'BayLum' (Christophe et al., 2020) designed after Combès et al. (2015); Combès and Philippe (2017), and implemented by Philippe et al. (2019), is the latest attempt to enrol Bayesian data analysis in luminescence dating.

'BayLum' is based on a hierarchical model. It runs all stages of estimations simultaneously, thus preventing individual analysis steps, and producing a result that aligns strongly with the raw data (Combès et al., 2015). In particular, for data analysis in luminescence dating that deals with a considerable amount of measurement data, obtaining several parameters with corresponding uncertainties is important for addressing systematic errors. It is this ability of Bayesian inference to model systematic shared error, that is crucial in luminescence data analysis. When combined with other independent ages such as $^{14}$C dates for the same event, the effect of systematic shared error can be minimised.

Programs such as *OxCal* (Ramsey, 1995) and *Chronomodel* (Lanos and Dufresne, 2019), which were, amongst others, designed for Bayesian data analysis of $^{14}$C ages, also allow for inputs of other chronological information such as luminescence ages or the stratigraphic order for the final age calculation. Here, the luminescence ages inserted need to have previously been determined. The chronologies derived by *OxCal* or *Chronomodel* therefore differ from those obtained through 'BayLum', in which **all** data is analysed under the Bayesian School to estimate the $D_e$. Additionally, 'BayLum' allows including dose rates and addressing shared systematic errors to estimate

luminescence chronologies, thus 'BayLum' was selected rather than *OxCal* and *Chronomodel* in this instance.

**1.4.9.1.1 Running 'BayLum'** To process data in 'BayLum', luminescence signal measurements are imported from binary files (BIN or BINX-files created by the luminescence readers). The number of grains or aliquots measured, the laboratory dose rate, and its uncertainty, must first be defined. With this information, a dose-response curve can be built using fitting functions available in 'BayLum' (by default 'BayLum' is designed to employ single exponential function for fitting, but can be altered to exponential plus linear function). Next, the palaeodose or central dose of $D_e$ distribution and uncertainty can be estimated according to Gaussian, lognormal or Cauchy parametrisation designed in 'BayLum'. In this thesis, I first estimated a central dose of two laboratory-controlled experiments using 'BayLum' (see Ch. 2). I found that the average in Gaussian and lognormal distribution are the best representative parameters to exhibit the accurate central dose.

'BayLum' also provides an option for incorporating data on the environmental dose rate, and so has the ability to calculate ages. By defining the stratigraphic relationship between samples before running the model, we were also able to include the stratigraphic order to affect the final chronologies. The systematic shared error between samples was modelled using the age covariance matrix. An appropriate number of iterations to reach convergence was defined according to the amount of data incorporated in the calculations (Fig. 1.10). A exemplary workflow chart for running 'BayLum' is displayed in Fig. B.5.

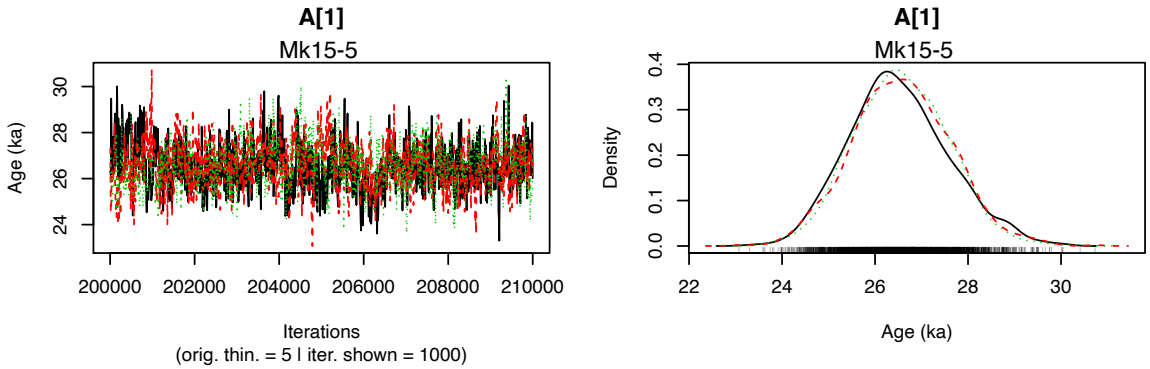


Figure 1.10: Illustration of three independent MCMC chains convergence. The convergence indicates that all chains, give statistically indistinguishable results. The right plot shows the resulting posterior distribution.

**1.4.9.1.2 Addressing systematic errors** Due to the involvement of various instruments in luminescence dating studies, it is important to assess systematic errors. Additionally, systematic

uncertainty can arise when a specific assumption is used to determine the ages of a profile (Buck and Juarez, 2017), and all ages are affected in one direction (e.g., estimation of internal dose rate). 'BayLum' has a capacity to model the systematic shared errors.

The systematic uncertainty in this study is mainly derived from the use of the high-resolution $\gamma$-ray spectrometer and OSL readers, which are modelled in 'BayLum' using a covariance matrix (Combès and Philippe, 2017).

The covariance matrix illustrates whether any two pairs of variables are dependent or not. This probable dependency between the two variables (e.g., ages) shows whether both are affected in the same direction by the same systematic errors. The Theta matrix, in which all individual and in particular systematic errors of the dose rate are incorporated after Gaussian parameterisation, can be modelled in 'BayLum'. The systematic error of the palaeodose can also be included. Details of creating the Theta matrix can be found in Sec. 3.7.5.

**1.4.9.1.3 Visual perception** Here, I study three samples from a profile to consider the effect of applying stratigraphic ordering and the impact of systematic shared error. The Bayesian age estimated for these samples is shown in Fig. 1.11. To highlight the relationship between each pair of ages, 'BayLum' can create scatter plot matrices showing the correlation between two parameters (here we are interested in correlation between ages). Each plot within Fig. 1.12 8 details the age distribution of two samples (MK15-5 vs Mk15-6, MK15-6 vs Mk15-7 and MK15-5 vs Mk15-7).

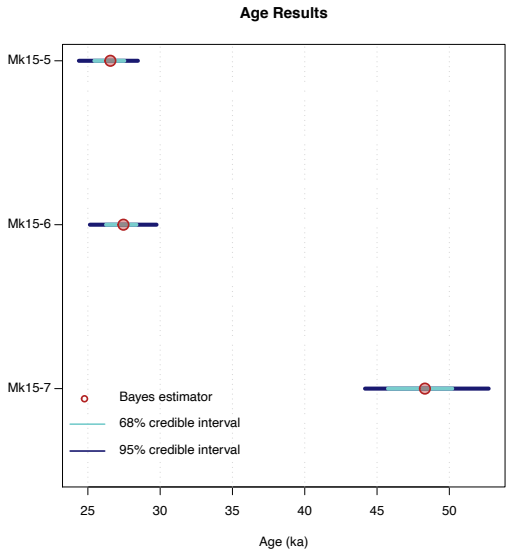


Figure 1.11: Bayesian chronology results for three samples mentioned in the text. Error bands show the 68 % and 95 % credible interval respectively. These three samples are from the site Mirak.

Based on stratigraphic order, I know that the ages follow MK15-5<Mk15-6<Mk15-7. Since the age distribution of sample MK15-5 and Mk15-6 overlap, this distribution is truncated, illustrating the effect of the stratigraphic ordering between these two samples. This truncation is not observed for the age distribution of samples Mk15-6 and Mk15-7, because their age intervals (including uncertainty) do not overlap. In such a case, the stratigraphic order does not have a major impact on the obtained ages of samples. A positive correlation between ages can be seen in the age distribution between MK15-5 and Mk15-7. This represents the systematic shared error between the two samples. Figure 1.12B details the same data with the addition of kernel density estimates. The contour lines represent similar densities to show whether two ages are dependent on each other not.

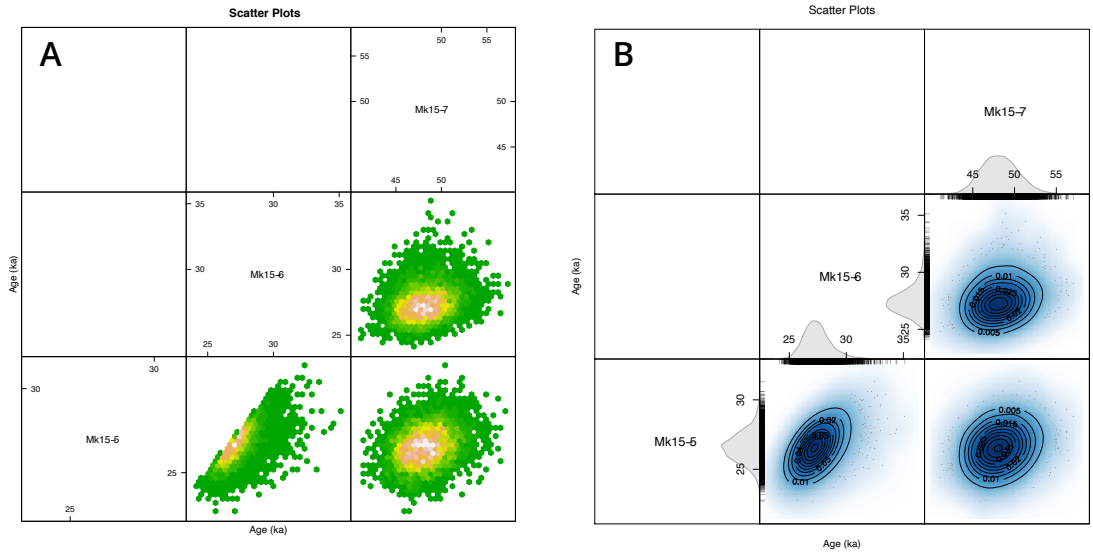


Figure 1.12: Scatter plots for the three samples in Fig. 1.11. Each point shows the probability density age estimations of two samples (hexagon plots) (a) Smooth scatter plot with contour lines showing systematic shared error between ages. The margins show kernel density estimates of age distributions (b).

## 1.5 The structure of this thesis

### 1.5.1 Comparing statistical models

#### 1.5.1.1 Towards accurate dose estimation in quartz signal saturation using Bayesian dose models

Quartz luminescence signals stimulated with blue light and detected in the UV wavelength range, saturates at relatively low doses (ca 100–200 Gy, e.g., Singarayer 2002). This dose range often

lies in the non-linear part of the dose-response curve, where asymmetric dose distribution means that Gaussian parametrisation often does not apply (see Fig. 1.13B, 1.13C, 1.13D). Consequently, the accuracy of the estimated error in the equivalent dose is low (Duller, 2007).

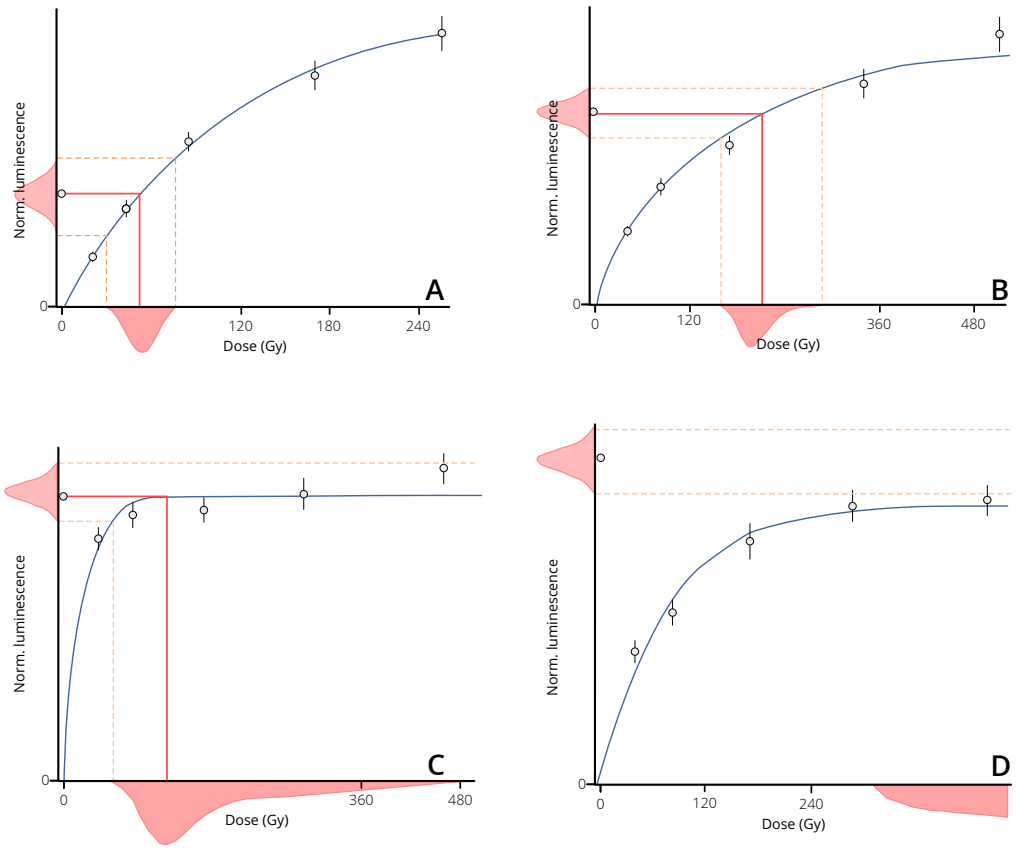


Figure 1.13: Dose-response curves redrawn and modified after being created in *Analyst* (Duller, 2015) for single grain data. This figure details four scenarios: (A) where the sensitivity corrected natural quartz signal ($L_n/T_n$) intersects with the linear part of the dose-response curve, the dose distribution follows Gaussian parametrisation, (B) where a quartz signal intersects the non-linear part of the dose-response curve the dose distribution appears asymmetric, (C) where a quartz signal is at the edge of saturation, the upper part of the dose distribution cannot be defined, and (D) where a quartz signal is completely saturated, and no dose can be attributed to the signal.

As shown in Fig. 1.13, Gaussian parametrisation is used to describe the sensitivity corrected quartz signals ($L_n/T_n$) and their corresponding errors. Projection of this distribution onto the linear part of the dose-response curve (Fig. 1.13A) results in a Gaussian distribution for the equivalent dose in which the error can easily be determined. However, when focusing on the non-linear part of the dose-response curve, Gaussian parametrisation is not applicable. For cases of asymmetric dose distribution, an error can still be calculated in *Analyst* (Duller, 2007), but the

dose might be underestimated. In Fig. 1.13C an underestimation of the $D_e$ is compounded by an inability to define the error. In Fig. 1.13D, the quartz signal is saturated. Here, a dose cannot be calculated, and this grain should be rejected for data analysis.

Underestimation of doses and calculation of an asymmetric errors lead to underestimating the central dose distribution. This is particularly seen when the statistical model designed for well-bleached samples, the CDM (also known as CAM, Galbraith et al. 1999) is applied to estimate the true equivalent dose of the dose distribution. This is because the model is designed for errors estimated from a Gaussian distribution. As such, when signals lie in the non-linear part of a dose-response curve, CDM is not appropriate for estimating a central dose. Thomsen et al. (2016) suggested discarding grains with low $D_0$ (the curvature measure of the dose-response curve ($\frac{L}{T} = A(1-exp(-D/D_0))$). $D_0$ filtering can be used as a criteria for grain selection, where it requires the curvature measure of its dose-response curve ($D_0$) to be larger than its corresponding dose. Although this approach is successful in principle, in practice, it could lead to rejection of a large number of grains, and the lower confidence of results.

In contrast, Bayesian models (for luminescence-dating applications) are designed differently. Rather than requiring Gaussian parametrisation for equivalent dose estimation from the dose-response curve (Combès et al., 2015; Guérin et al., 2015a), Bayesian models instead, use Markov Chain Monte Carlo (MCMC) simulations to generate dose-response curves. Followed by an estimation of the equivalent dose distribution, a $D_e$ and its associated error can be calculated. This error can be calculated in *Analyst* using Monto Carlo stimulations (Duller, 2007) but its approach differs from Bayesian modelling (Combès et al., 2015). The posterior distribution of $D_e$ obtained using Bayesian modelling is determined based on defined prior distributions on the parameters of the dose-response curve. Samples are taken from these prior distributions to generate dose-response curves (see Combès et al. 2015 their section 4 in particular 4.2.1). Since truncated Gaussian distributions are modelled for parameters of the dose-response curve (except for $D_0$ value) (see Combès et al. 2015 section 4 in particular 4.2.1), the distribution of dose-response curves always contains curves, even above the saturation level. As such, even for Fig. 1.13D, Bayesian models can estimate a $D_e$ and corresponding error.

To test the outcome of Bayesian models in such a case, I ran a dose recovery experiment at high doses (ca 150–255 Gy), and compared the results obtained using Bayesian models and the CDM. I found that regardless of the distribution in Bayesian modelling selected for estimation of the dose recovery ratio (Cauchy, Gaussian or lognormal parametrisation), the ratio was always within 10 % of unity. In contrast, the CDM led to significant dose underestimation (see Sec. 2.3.2). In cases of signal saturation, I therefore concluded that the Bayesian models in 'BayLum' are more accurate than the CDM. Moreover, Bayesian models appear to be not sensitive to low $D_0$ values. This means that $D_0$ filtering is not required, and the obtained results are more precise and in line with the raw data.

#### 1.5.1.2 $\beta$-dose rate variability and underestimated $D_e$

In Sec. 1.4.7 I have discussed that applying the CDM leads to underestimated $D_e$s in cases where $\beta$-dose rate heterogeneity in well-bleached samples has caused significant external overdispersion. The presence of hot spots within surrounding sediment (e.g., from K-rich feldspar grains) results in asymmetric $\beta$-emission towards quartz grains and can lead to a positively skewed lognormal dose distribution (Mayya et al., 2006; Cunningham et al., 2012; Guérin et al., 2015b).

In a laboratory-controlled experiment, I created various lognormal distributions with dispersions varying from 10 % to 90 % (see Fig. B1), using quartz grains that had received a $\beta$-dose inside the OSL reader. The maximum given dose was 35 Gy, a relatively low value to ensure signal saturation was not reached. The probability density function for a lognormal distribution was used to define a number of grains with specific doses, to create each distribution according to the average and standard deviation of the logged dose distribution (for details see Sec. 2.2.3.2). The central dose $D_e$ for each artificially created distribution was determined using two different frequentist models (CDM and Average Dose Model; Guérin et al. 2017), and a Bayesian central dose modelled using a Gaussian, a lognormal-average, and a lognormal-median parametrisation. A comparison of the central dose derived from lognormal-average and lognormal-median showed that while the dispersion in $D_e$ increases, the difference between average and median in lognormal distribution increases. The CDM, which is designed to approach the median of the lognormal distribution, leads to an underestimation of the true central $D_e$. Therefore, when external overdispersion is greater than 40 %, application of the CDM results in a dose underestimation of at least 10 %. This study concluded that employing a Gaussian or lognormal distribution (which converge to the average) in the Bayesian approach or ADM in the frequentist approach leads to an accurate dose estimation for well-bleached samples.

These Bayesian models have been further tested and applied to establish the chronology of Middle-Upper Palaeolithic sites in Iran. This is detailed in the next section.

### 1.5.2 Bayesian chronologies for Middle-Upper Palaeolithic sites in Iran

This section presents the chronological findings from Palaeolithic sites. The first site of Mirak and Delazian (two luminescence ages) was studied in collaboration with Dr Hamed Vahdati Nasab (Tarbiat Modares University, Tehran, Iran) and Dr Gilles Berillon (Musée de l'Homme, Paris, France). Investigation of the second site, Ghār-e Boof, was undertaken in collaboration with Prof Nicholas Conard and Dr Mohsen Zeidi (University of Tübingen, Germany). The third site, Bawa Yawn, was studied in collaboration with Dr Saman Heydari-Guran (Neanderthal Museum, Germany).

#### 1.5.2.1 Mirak

The Palaeolithic site of Mirak is located in a dry floodplain close to the margin of Dasht-e Kavir. This flood plain extends towards the fluvial fans of the Alborz Mountains from the north (e.g., Nasab et al., 2013, 2019, see Fig. 1.1). Several shadow dunes located in the alluvial fan systems were formed by aeolian activity (Berillon et al., 2017; Kharazian Akhavan et al., 2018). A considerable number of lithic artefacts have been found on the surface of this region, with particular concentration seen on one mound (n.8) at an altitude of 1,035 m (a.s.l.). This mound was therefore selected for the excavation. In addition, the presence of a pit nearby (S2) provided a unique possibility for primary investigations on the presence of in situ archaeological material (for details see Sec. 3.2.1). Three main sections have been excavated in the northern, eastern and southern slope of the mound. These unravelled three main in situ archaeological assemblages, particularly in the north and east sections (Berillon et al., 2017; Nasab et al., 2019). At the top of the sequence, a sparse assemblage is associated with the Upper Palaeolithic period. Below, two assemblages were observed containing both Middle and Upper Palaeolithic industries (intermediate level). Rich Middle Palaeolithic assemblages were discovered at the bottom of the sequence. Twenty-two sediment samples were taken from various spots in the north and especially in the east trenches to provide a precise chronology covering all geological units and archaeological assemblages. The dating results of these 20 samples are included in Ch. 3. Additional ages from pit S2 are detailed in Sec. C.1, as the Palaeolithic investigation and ESR dating are currently in progress. This study had two aims: first, to provide a solid chronology, and secondly to apply Bayesian models implemented in 'BayLum' to improve the precision outcome by incorporating well-establish stratigraphic order. I also modelled systematic shared errors between samples by creating a Theta matrix after Combès and Philippe (2017) (see Sec. 3.3.6.1 and Sec. 3.7.5). I defined distinct scenarios including stratigraphic order and Theta matrix to discuss how their contributions affected the final ages. In particular, I aimed to address the question of whether applying Bayesian models in 'BayLum' result in chronologies that are more precise compared to commonly used frequentist models. The comparison between frequentist and Bayesian chronologies showed that by including stratigraphic order, in particular where age intervals overlap one another, plays an essential role in reducing uncertainties.

The Bayesian chronology for sediment containing Upper Palaeolithic assemblages produced ages in the range 21–28 ka (95% CI). The intermediate sequence encompassed two separate assemblages, sub-layer 1 and sub-layer 2, dated respectively to 26–29 ka (95% CI) and 26–33 ka (95% CI). Due to the overlap in age range, and consistency in the nature of archaeological assemblages, these sublayers were considered together as one intermediate layer with the age of 26–33 ka (95% CI). The sediment containing the Middle Palaeolithic assemblages was dated to 43–55 ka (95% CI).

#### 1.5.2.2 Delazian

The open-air site of Delazian is located close to the site of Mirak, and it is well known for encompassing the Upper and Epipalaeolithic period (Vahdati Nasab and Clark, 2014). In a preliminary dating study, two blocks of samples were dated from this site. These dated to 21–25 ka (within $2\sigma$) and 25–30 ka (within $2\sigma$) (see Sec. C.2 for more details). Although our chronological contribution is limited to only two ages, which are not formally published yet, given the sparse amount of chronological data available for the north edge of the central desert, and the importance of this region as a route for human dispersal, these ages provide a starting point towards a better understanding of Palaeolithic history of the region.

#### 1.5.2.3 Ghār-e Boof

The second site is located at the foothills of the southern Zagros Mountains, in the Dasht-e Rostam plains. Surface surveys of these plains discovered a significant number of Palaeolithic sites. According to the affinities of lithic artefacts on the surface, they are often attributed to Upper Palaeolithic industries. The Yagheh sangar corridor, located in the middle of Dasht-e Rostam, encompasses around 33 % of the plains' Palaeolithic sites (Heydari-Guran, 2014). Ghār-e Boof is one of these sites.

Ghār-e Boof is well-known for its rich Upper Palaeolithic assemblages. Called the Rostamian tradition after Dasht-e Rostam, this tradition is distinguished from the Baradostian or general Zagros Aurignacian industry (e.g., Conard and Ghasidian, 2011; Conard et al., 2013; Ghasidian, 2014; Ghasidian et al., 2017) (see also Sec. 4.1.2.2).

The Upper Palaeolithic sequence of the cave was dated by $^{14}$C to 35–42 ka cal. BP (Conard and Ghasidian, 2011; Baines et al., 2014; Becerra-Valdivia et al., 2017). Later excavation unravelled Middle Palaeolithic assemblages in the cave (Bretzke and Conard, 2017; Conard and Zeidi, 2019; Zeidi and Conard, 2019). The aim of the study at this site was to establish a full chronological sequence from the Middle to the Upper Palaeolithic and to compare new luminescence ages from Upper Palaeolithic sequence with the existing $^{14}$C dates.

Preliminary results showed good agreement between the luminescence ages and the $^{14}$C dates for the Upper Palaeolithic sequence. The OSL ages and post-IR $IRSL_{290}$ were in good agreement for both the Middle and Upper Palaeolithic sequence. The availability of $^{14}$C dates for the Upper Palaeolithic part of the site provided a unique opportunity to incorporate $^{14}$C data with luminescence ages in 'BayLum'. Here, I tested whether including independent chronological events lead to more precise ages in comparison to the standard approach of not including such information. The systematic shared error between samples was modelled by creating a Theta matrix, as discussed in Sec. 3.7.5. The results showed that by including stratigraphic ordering and $^{14}$C dates, uncertainties in age intervals were reduced. The Bayesian OSL ages for the Upper Palaeolithic part of the sequence, attributed to AHs III (a-b-c) and AHs IV, dated to 37–42 ka (95% CI). The

ages from AH IVd and AH VI attributed to the Middle Palaeolithic assemblages resulted in 44–84 ka (95% CI). Middle Palaeolithic studies for this site are ongoing (Bretzke and Conard, 2017; Conard and Zeidi, 2019; Zeidi and Conard, 2019).

#### 1.5.2.4 Bawa Yawan

The third site investigated in this thesis was the Bawa Yawan rock shelter located in the west-central Zagros Mountains, Kermanshah province (Heydari-Guran and Ghasidian, 2017). This region is famous within Palaeolithic studies in Iran as it encompasses several important Middle-Upper Palaeolithic sites (see Sec. 1.3.2.1). Work on these samples began in my second year of the thesis after their arrival in the laboratory. After several months of work, from sample preparation to signal measurement (quartz and feldspar, multi-grains and single grain), I obtained ambiguous results that showed unexpected stratigraphic inversions. I suspect that is the result of technical problems during the sampling. Due to the importance of this site, a new set of six samples were collected during the last field trip in November 2018 (in the third year of my thesis). Single grain and multi-grain measurements were carried out. Multi-grain results presented in Ch. 5, and the single grain results are as yet unpublished.

While investigation on the site is still ongoing, six geological units have identified so far. Unit 2 to unit 6 encompass Epipalaeolithic, Upper, and Middle Palaeolithic assemblages. On the top of the lithic artefact assemblage, the most important discovery was a Neanderthal tooth in the upper part of geological unit 5 (Heydari-Guran and Ghasidian, 2019).

OSL quartz ages for geological unit 2, which contains an Epipalaeolithic assemblage, dated to 12–16 ka (within $2\sigma$). This is the first OSL age attributed to an Epipalaeolithic industry in Iran, in the literature so far no chronology is established for this period. The OSL ages for geological units 3, 4 and 5 resulted respectively in 56–69 ka, 64–82 ka and 61–78 ka (within $2\sigma$). These units contain Middle Palaeolithic assemblages attributed to the Neanderthal. In particular, unit 5 is very rich in Middle Palaeolithic assemblages. Unit 6, the lowest unit investigated so far, exhibited an age of 64–83 ka from an OSL sample taken in the profile, and an age of 69–90 ka (within $2\sigma$) for a sample that was vertically taken from the surface (with plans excavated further in next field season). Unfortunately, these obtained ages, except the youngest age (12–16 ka, which showed good agreement with corresponding $^{14}$C dating results) were not consistent with other $^{14}$C ages (personal communication with Saman Heydari-Guran). As these ages show an overestimation, this work was not incorporated into the submitted article before the end of this thesis. However, based on our results, the unit containing the Neanderthal teeth is dated to 61–78 ka. Further studies are needed in order to decipher discrepancies between the $^{14}$C ages and OSL ages. Nevertheless, the good agreement between OSL ages and post-IR $IRSL_{290}$ ages indicate that method inherent problems, such as insufficient bleaching, are unlikely. The gamma dose rate has not yet been measured in situ, and therefore, the final dose rate (and ages) could

differ slightly from these preliminary estimates. However, given the limestone rich nature of the sediment, I expect that the *in situ* $\gamma$-dose rate will be lower than the "laboratory-deduced" $\gamma$-dose rate, and so it is suspected that the ages will be even older.

## References

Adamiec, G. and Aitken, M. J.: Dose-rate conversion factors: update, Ancient TL, 16, 37–50, 1998.

Agard, P., Omrani, J., Jolivet, L., and Mouthereau, F.: Convergence history across Zagros (Iran): constraints from collisional and earlier deformation, International Journal of Earth Sciences, 94, 401–419, 2005.

Aitken, M. J.: Thermoluminescence dating, Studies in archaeological science, Academic Press, 1985.

Aitken, M. J.: An Introduction to Optical Dating, Oxford University Press, 1998.

Akselrod, M. S., Kortov, V., and Gorelova, E.: Preparation and Properties of $\alpha - Al_2O_3 : C$, Radiation Protection Dosimetry, 47, 159–164, 1993.

Akselrod, M. S., Lucas, A. C., Polf, J. C., and McKeever, S. W. S.: Optically stimulated luminescence of $Al_2O_3$, Radiation Measurements, 29, 391–399, 1998.

Alavi, M.: Tectonics of the zagros orogenic belt of iran: new data and interpretations, Tectonophysics, 229, 211–238, 1994.

Andrieu, C., de Freitas, N., Doucet, A., and Jordan, M. I.: An Introduction to MCMC for Machine Learning, Machine Learning, 50, 5–43, 2003.

Ankjærgaard, C., Jain, M., and Wallinga, J.: Towards dating Quaternary sediments using the quartz Violet Stimulated Luminescence (VSL) signal, Quaternary Geochronology, 18, 99–109, 2013.

Ankjærgaard, C., Guralnik, B., Buylaert, J. P., Reimann, T., Yi, S. W., and Wallinga, J.: Violet stimulated luminescence dating of quartz from Luochuan (Chinese loess plateau): Agreement with independent chronology up to ∼600 ka, Quaternary Geochronology, 34, 33–46, 2016.

Antoine, P., Bahain, J. J., Ghaleb, B., and Mercier, N.: The chronostratigraphic framework at Garm roud, in: Garm Roud. A Hunting Place in Iran, Upper Palaeolithic, edited by Berillon, G. and Asgari Khanegah, A., pp. 49–55, Editions IFRI & @rchéo-éditions (French- English-Persian), 2016.

Bailey, R. M.: Towards a general kinetic model for optically and thermally stimulated luminescence of quartz, Radiation Measurements, 33, 17–45, 2001.

Bailey, R. M.: Direct measurement of the fast component of quartz optically stimulated luminescence and implications for the accuracy of optical dating, Quaternary Geochronology, 5, 559–568, 2010.

Bailey, R. M., Smith, B. W., and Rhodes, E. J.: Partial Bleaching and the decay from characteristics of quartz OSL, Radiation Measurements, 27, 123–136, 1997.

Bailey, R. M., Yukihara, E. G., and McKeever, S. W. S.: Separation of quartz optically stimulated luminescence components using green (525 nm) stimulation, Radiation Measurements, 46, 643–648, 2011.

Baines, J. A., Riehl, S., Conard, N., and Zeidi-Kulehparcheh, M.: Upper Palaeolithic archaeobotany of Ghar-e Boof cave, Iran: a case study in site disturbance and methodology, Archaeological and Anthropological Sciences, 7, 245–256, 2014.

Ballarini, M., Wallinga, J., Wintle, A. G., and Bos, A. J. J.: A modified SAR protocol for optical dating of individual grains from young quartz samples, Radiation Measurements, 42, 360–369, 2007.

Bar-Yosef, O.: The Upper Paleolithic Revolution, Annual Review of Anthropology, 31, 363–393, 2002a.

Bar-Yosef, O.: The Chronology of the Middle Paleolithic of the Levant, in: Neandertals and Modern Humans in Western Asia, pp. 39–56, Kluwer Academic Publishers, Boston, 2002b.

Bar-Yosef, O. and Belfer-Cohen, A.: The Levantine Upper Palaeolithic and Epipalaeolithic, in: South-Eastern Mediterranean Peoples Between 130,000 and 10,000 Years Ago, edited by Garcea, E. A. A., pp. 144–167, Oxbow Books, 2010.

Bar-Yosef, O. and Belfer-Cohen, A.: Following Pleistocene road signs of human dispersals across Eurasia, Quaternary International, 285, 30–43, 2013.

Bar-Yosef, O. and Callander, J.: The woman from Tabun: Garrod's doubts in historical perspective, Journal of Human Evolution, 37, 879–885, 1999.

Bar-Yosef, O. and Meignen, L.: The Chronology of the Levantine Middle Palaeolithic Period in Retrospect, Bulletins et mémoires de la Société d'CAnthropologie de Paris, 13, 269–289, 2001.

Batchelor, C. L., Margold, M., Krapp, M., Murton, D. K., Dalton, A. S., Gibbard, P. L., Stokes, C. R., Murton, J. B., and Manica, A.: The configuration of Northern Hemisphere ice sheets through the Quaternary, Nature Communications, 10, PA1003–10, 2019.

Bayes, T.: LII. An essay towards solving a problem in the doctrine of chances. By the late Rev. Mr. Bayes, F. R. S. communicated by Mr. Price, in a letter to John Canton, A. M. F. R. S, Philosophical Transactions of the Royal Society of London, 53, 370–418, 1763.

Bazgir, B., Otte, M., Tumung, L., Ollé, A., Deo, S. G., Joglekar, P., López-García, J. M., Picin, A., Davoudi, D., and van der Made, J.: Test excavations and initial results at the Middle and Upper Paleolithic sites of Gilvaran, Kaldar, Ghamari caves and Gar Arjene Rockshelter, Khorramabad Valley, western Iran, Comptes Rendus Palevol, 13, 511–525, 2014.

Bazgir, B., Ollé, A., Tumung, L., Becerra-Valdivia, L., Douka, K., Higham, T., van der Made, J., Picin, A., Saladié, P., López-García, J. M., Blain, H.-A., Allue, E., Fernández-García, M., Rey-Rodríguez, I., Arceredillo, D., Bahrololoumi, F., Azimi, M., Otte, M., and Carbonell, E.: Understanding the emergence of modern humans and the disappearance of Neanderthals: Insights from Kaldar Cave (Khorramabad Valley, Western Iran), Scientific Reports, 7, 525–16, 2017.

Becerra-Valdivia, L., Douka, K., Comeskey, D., Bazgir, B., Conard, N. J., Marean, C. W., Ollé, A., Otte, M., Tumung, L., Zeidi, M., and Higham, T. F. G.: Chronometric investigations of the Middle to Upper Paleolithic transition in the Zagros Mountains using AMS radiocarbon dating and Bayesian age modelling, Journal of Human Evolution, 109, 57–69, 2017.

Becker, D., Verheul, J., Zickel, M., and Willmes, C.: LGM paleoenvironment of Europe - Map, CRC806-Database, https://doi.org/10.5880/SFB806.15, 2015.

Berillon, G. and Asgari Khaneghah, A., eds.: Garm Roud. A Hunting Place in Iran, Upper Palaeolithic, Editions IFRI & @rchéo-éditions (French- English-Persian), 2016.

Berillon, G., Asgari Khaneghah, A., Antoine, P., Bahain, J.-J., Chevrier, B., Zeitoun, V., Aminzadeh, N., Beheshti, M., Chanzanagh, H. E., and Nochadi, S.: Discovery of new open-air Paleolithic localities in Central Alborz, Northern Iran, Journal of Human Evolution, 52, 380–387, 2007.

Berillon, G., Nasab, H. V., Asgari Khaneghah, A., Jamet, G., Akhavan, M., Guérin, G., Heydari, M., Anvari, Z., Auguste, P., Bonilauri, S., Chevrier, B., Zeitoun, V., Mohammadkhani, K., Hashemi, M., Jayez, M., and Darvishi, J.: *Fouille du site Mirak 8:* Rapport Annuel. Programme Paléoanthropologique Franco-Iranien (FIPP), Tech. rep., 2017.

Biglari, F.: Recent Finds of Paleolithic Period from Bisitun, Central Western Zagros Mountains, Iranian Journal of Archaeology and History, 28, 50–60, 2001.

Biglari, F., Javeri, M., Mashkour, M., Yazdi, M., Shidrang, S., Tengberg, M., Taheri, K., and Darvish, J.: Test Excavations at the Middle Paleolithic Sites of Qaleh Bozi, Southwest of Central Iran, a Preliminary Report, in: Iran Paleolithic, Le Paléolithique d'Iran, edited by Otte, M., Biglari, F., and Jaubert, J., pp. 29–38, Bar International Series, 2009.

Boivin, N., Fuller, D. Q., Dennell, R., Allaby, R., and Petraglia, M. D.: Human dispersal across diverse environments of Asia during the Upper Pleistocene, Quaternary International, 300, 32–47, 2013.

Bordes, F.: Mousterian Cultures in France: Artifacts from recent excavation dispel some popular misconceptions about Neanderthal man, Science, 134, 803–810, 1961.

Braidwood, R. J., Howe, B., and Reed, C. A.: The Iranian Prehistoric Project: New problems arise as more is learned of the first attempts at food production and settled village life, Science, 133, 2008–2010, 1961.

Breeze, P. S., Groucutt, H. S., Drake, N. A., White, T. S., Jennings, R. P., and Petraglia, M. D.: Palaeohydrological corridors for hominin dispersals in the Middle East ∼250–70,000 years ago, Quaternary Science Reviews, 144, 155–185, 2016.

Bretzke, K. and Conard, N. J.: Not Just a Crossroad: Population Dynamics and Changing Material Culture in Southwestern Asia during the Late Pleistocene, Current Anthropology, 58, S449–S462, 2017.

Buck, C. E. and Juarez, M.: Bayesian radiocarbon modelling for beginners, arXiv.org, 2017.

Buck, C. E. and Meson, B.: On being a good Bayesian, World Archaeology, 47, 567–584, 2015.

Buck, C. E. and Millard, A. R.: Tools for Constructing Chronologies - Crossing Disciplinary Boundaries, vol. 177 of *Lecture Notes in Statistics*, Springer, 2004.

Bulur, E.: An Alternative Technique For Optically Stimulated Luminescence (OSL) Experiment, Radiation Measurements, 26, 701–709, 1996.

Buylaert, J. P., Jain, M., Murray, A. S., Thomsen, K. J., Thiel, C., and Sohbati, R.: A robust feldspar luminescence dating method for Middle and Late Pleistocene sediments, Boreas, 41, 435–451, 2012.

Carlin, B. P. and Louis, T. A.: Bayes and Empirical Bayes Methods for Data Analysis , Chapman & Hall/CRC, 2nd edn., 2000.

Chen, R. and Pagonis, V.: Thermally and Optically Stimulated Luminescence - A Simulation Approach, Thermally and Optically Stimulated Luminescence A Simulation Approach, John Wiley & Sons, Ltd, 2011.

Choi, J. H., Duller, G. A. T., and Wintle, A. G.: Analysis of quartz LM-OSL curves, Ancient TL, 24, 9–20, 2006.

Christophe, C., Philippe, A., Kreutzer, S., and Guerin, G.: BayLum: Chronological Bayesian Models Integrating Optically Stimulated Luminescence and Radiocarbon Age Dating, URL `https://CRAN.r-project.org/package=BayLum`, r package version 0.1.4.9000-40, 2020.

Chruścińska, A. and Kijek, N.: Thermally modulated optically stimulated luminescence (TM–OSL) as a tool of trap parameter analysis, Journal of Luminescence, 174, 42–48, 2016.

Combès, B. and Philippe, A.: Bayesian analysis of individual and systematic multiplicative errors for estimating ages with stratigraphic constraints in optically stimulated luminescence dating, Quaternary Geochronology, 39, 24–34, 2017.

Combès, B., Philippe, A., Lanos, P., Mercier, N., Tribolo, C., Guérin, G., Guibert, P., and Lahaye, C.: A Bayesian central equivalent dose model for optically stimulated luminescence dating, Quaternary Geochronology, 28, 62–70, 2015.

Conard, N. J. and Ghasidian, E.: The Rostamian cultural group and thetaxonomy of the Iranian Upper Paleolithic, in: Between Sand and Sea. The Archaeology and Human Ecology of Southwestern Asia, edited by Conard, N. J., Drechsler, P., and Morales, A., pp. 33–52, Kerns Verlag, Tübingen,Germany, 2011.

Conard, N. J. and Zeidi, M.: New research on the Paleolithic occupation of Ghar-e Boof, Fars Province, Archaeology, Journal of the Iranian Center for Archaeological Research, 2, 7–16, 2019.

Conard, N. J., Ghasidian, E., and Heydari-Guran, S.: The open-air Late Paleolithic site of Bardia and the Paleolithic occupation of the Galeh Gusheh sand dunes, Esfahan province, Iran, in: Iran Paleolithic, Le Paléolithique d'Iran, edited by Otte, M., Biglari, F., and Jaubert, J., pp. 141–154, Kerns Verlag, 2009.

Conard, N. J., Ghasidian, E., and Heydari-Guran, S.: The Paleolithic of Iran, in: The Oxford Handbook of Ancient Iran, edited by Potts, D. T., pp. 29–48, Oxford University Press, 2013.

Condemi, S.: The Neanderthals: a Cold-Adapted European Middle Pleistocene Population?, Anthropologie, 36, 35–42, 1998.

Coon, C. S.: Cave explorations in Iran, 1949., University Museum, University of Pennsylvania, Philadelphia, 1951.

Cunningham, A. C. and Wallinga, J.: Selection of integration time intervals for quartz OSL decay curves, Quaternary Geochronology, 5, 657–656, 2010.

Cunningham, A. C., DeVries, D. J., and Schaart, D. R.: Experimental and computational simulation of beta-dose heterogeneity in sediment, Radiation Measurements, 47, 1060–1067, 2012.

d'Errico, F. and Stringer, C. B.: Evolution, revolution or saltation scenario for the emergence of modern cultures?, Philosophical Transactions of the Royal Society B: Biological Sciences, 366, 1060–1069, 2011.

Duller, G. A. T.: Distinguishing quartz and feldspar in single grain luminescence measurements, Radiation Measurements, 37, 161–165, 2003.

Duller, G. A. T.: Assessing the error on equivalent dose estimates derived from single aliquot regenerative dose measurements, Ancient TL, 25, 15–24, 2007.

Duller, G. A. T.: Single-grain optical dating of Quaternary sediments: why aliquot size matters in luminescence dating, Boreas, 37, 589–612, 2008.

Duller, G. A. T.: The Analyst software package for luminescence data: overview and recent improvements , Ancient TL, 33, 35–42, 2015.

Durcan, J. A. and Duller, G. A. T.: The fast ratio: A rapid measure for testing the dominance of the fast component in the initial OSL signal from quartz, Radiation Measurements, 46, 1065–1072, 2011.

Erfurt, G., Krbetschek, M. R., Trautmann, T., and Stolz, W.: Radioluminescence (RL) behaviour of Al2O3:C-potential for dosimetric applications, Radiation Measurements, 32, 735–739, 2000.

Frouin, M., Huot, S., Kreutzer, S., Lahaye, C., Lamothe, M., Philippe, A., and Mercier, N.: An improved radiofluorescence single-aliquot regenerative dose protocol for K-feldspars, Quaternary Geochronology, 38, 13–24, 2017.

Galbraith, R. F.: A note on the variance of a background-corrected OSL count, Ancient TL, 20, 49–51, 2002.

Galbraith, R. F. and Roberts, R. G.: Statistical aspects of equivalent dose and error calculation and display in OSL dating: An overview and some recommendations, Quaternary Geochronology, 11, 1–27, 2012.

Galbraith, R. F., Roberts, R. G., Laslett, G. M., Yoshida, H., and Olley, J. M.: Optical dating of single and multiple grains of Quartz from Jinmium Rock Shelter, Northern Australia: Part I, Experimental design and statistical models, Archaeometry, 41, 339–364, 1999.

Garrod, D. A. E.: The relations between South West Asia and Europe in the later Palaeolithic Age, Journal of World Prehistory, 1, 13–18, 1953.

Gelman, A., Carlin, J. B., Stern, H. S., Dunson, D. B., Vehtari, A., and Rubin, D. B.: Bayesian Data Analysis, Third Edition, CRC Press, 2013.

Ghasidian, E.: The Early Upper Paleolithic Occupation at Ghār-e Boof Cave: A Reconstruction of Cultural Tradition in the Southern Zagros Mountains of Iran, Kerns Verlag, Tübingen, 2014.

Ghasidian, E., Bretzke, K., and Conard, N. J.: Excavations at Ghār-e Boof in the Fars Province of Iran and its bearing on models for the evolution of the Upper Palaeolithic in the Zagros Mountains, Journal of Anthropological Archaeology, 47, 33–49, 2017.

Ghasidian, E., Heydari-Guran, S., and Mirazón Lahr, M.: Upper Paleolithic cultural diversity in the Iranian Zagros Mountains and the expansion of modern humans into Eurasia, Journal of Human Evolution, 132, 101–118, 2019.

Godfrey-Smith, D. I., Huntley, D. J., and Chen, W. H.: Optical dating studies of quartz and feldspar sediment extracts, Quaternary Science Reviews, 7, 373–380, 1988.

Groucutt, H. S., Petraglia, M. D., Bailey, G., Scerri, E. M. L., Parton, A., Clark-Balzan, L., Jennings, R. P., Lewis, L., Blinkhorn, J., Drake, N. A., Breeze, P. S., Inglis, R. H., Devès, M. H., Meredith-Williams, M., Boivin, N., Thomas, M. G., and Scally, A.: Rethinking the dispersal of Homo sapiensout of Africa, Evolutionary Anthropology: Issues, News, and Reviews, 24, 149–164, 2015.

Grün, R. and Stringer, C.: Tabun revisited: revised ESR chronology and new ESR and U-series analyses of dental material from Tabun C1, Journal of Human Evolution, 39, 601–612, 2000.

Grün, R., Stringer, C., McDermott, F., Nathan, R., Porat, N., Robertson, S., Taylor, L., Mortimer, G., Eggins, S., and McCulloch, M.: U-series and ESR analyses of bones and teeth relating to the human burials from Skhul, Journal of Human Evolution, 49, 316–334, 2005.

Guadelli, J. L., Sirakov, N., Ivanova, S., Sirakova, S., Anastassova, E., Courtaud, P., Dimitrova, I., Djabarska, N., Fernandez, P., Ferrier, C., Fontugne, M., Gambier, D., Guadelli, A., Iordanova, D., Iordanova, N., Kovatcheva, M., Krumov, I., Leblanc, J. C., Mallye, J. B., Marinska, M., Miteva, V., Popov, V., Spasov, R., Taneva, S., Tisterat-Laborde, N., and Tsanova, T.: Une séquence du Paléolithique inférieur au Paléolithique récent dans les Balkans : La grotte Kozarnika à Oreshets (Nord-Ouest de la Bulgarie), in: Les premiers peuplements en Europe - Actes du colloque international «Données récentes sur les modalités de peuplement et sur le cadre chronostratigraphique, géologique et paléogéographique des industries du Paléolithique inférieur et moyen en Europe» Rennes, 22–25 septembre 2003, edited by Molines, N., Moncel, M. H., and Monnier, J. L., pp. 87–103, BAR, Oxford, 2005.

Guérin, G. and Mercier, N.: Preliminary insight into dose deposition processes in sedimentary media on a scale of single grains: Monte Carlo modelling of the effect of water on the gamma dose rate, Radiation Measurements, 47, 541–547, 2012.

Guérin, G., Mercier, N., and Adamiec, G.: Dose-rate conversion factors: update, Ancient TL, 29, 5–9, 2011.

Guérin, G., Mercier, N., Nathan, R., Adamiec, G., and Lefrais, Y.: On the use of the infinite matrix assumption and associated concepts: A critical review, Radiation Measurements, 47, 778–785, 2012.

Guérin, G., Combès, B., Lahaye, C., Thomsen, K. J., Tribolo, C., Urbanova, P., Guibert, P., Mercier, N., and Valladas, H.: Testing the accuracy of a Bayesian central-dose model for single-grain OSL, using known-age samples, Radiation Measurements, 81, 62–70, 2015a.

Guérin, G., Jain, M., Thomsen, K. J., Murray, A. S., and Mercier, N.: Modelling dose rate to single grains of quartz in well-sorted sand samples: The dispersion arising from the presence of potassium feldspars and implications for single grain OSL dating, Quaternary Geochronology, 27, 52–65, 2015b.

Guérin, G., Christophe, C., Philippe, A., Murray, A. S., Thomsen, K. J., Tribolo, C., Urbanova, P., Jain, M., Guibert, P., Mercier, N., Kreutzer, S., and Lahaye, C.: Absorbed dose, equivalent dose, measured dose rates, and implications for OSL age estimates: Introducing the Average Dose Model, Quaternary Geochronology, 41, 1–32, 2017.

Guibert, P. and Schvoerer, M.: TL dating: Low background gamma spectrometry as a tool for the determination of the annual dose, International Journal of Radiation Applications and Instrumentation. Part D. Nuclear Tracks and Radiation Measurements, 18, 231–238, 1991.

Guibert, P., Lahaye, C., and Bechtel, F.: The importance of U-series disequilibrium of sediments in luminescence dating: A case study at the Roc de Marsal Cave (Dordogne, France), Radiation Measurements, 44, 223–231, 2009.

Henshilwood, C. S. and Marean, C. W.: The Origin of Modern Human Behavior, Current Anthropology, 44, 627–651, 2003.

Hershkovitz, I., Weber, G. W., Quam, R., Duval, M., Grün, R., Kinsley, L., Ayalon, A., Bar-Matthews, M., Valladas, H., Mercier, N., Arsuaga, J. L., Martinón-Torres, M., Bermúdez de Castro, J. M., Fornai, C., Martín-Francés, L., Sarig, R., May, H., Krenn, V. A., Slon, V., Rodríguez, L., García, R., Lorenzo, C., Carretero, J. M., Frumkin, A., Shahack-Gross, R., Bar-Yosef Mayer, D. E., Cui, Y., Wu, X., Peled, N., Groman-Yaroslavski, I., Weissbrod, L., Yeshurun, R., Tsatskin, A., Zaidner, Y., and Weinstein-Evron, M.: The earliest modern humans outside Africa, Science, 359, 456–459, 2018.

Heydari-Guran, S.: Paleolithic Landscapes of Iran, Archaeopress, Oxford, 2014.

Heydari-Guran, S. and Ghasidian, E.: The MUP Zagros Project: tracking the Middle–Upper Palaeolithic transition in the Kermanshah region, west-central Zagros, Iran, Antiquity Project Gallery, 91, 40–7, 2017.

Heydari-Guran, S. and Ghasidian, E.: A report on the second season excavation in Bawa Yawan rocksheleter, 16th Annual Symposium of the Iranian Archaeology (a collection of short articles-2016-2017), in Farsi, 124–127, 2019.

Heydari-Guran, S. and Ghasidian, E.: Late Pleistocene hominin settlement patterns and population dynamics in the Zagros Mountains: Kermanshah region, Archaeological Research in Asia, 21, 100 161–28, 2020.

Heydari-Guran, S., Ghasidian, E., and Conard, N.: Middle Paleolithic settlements on the Iranian Central plateau, in: Settlement Dynamics of the Middle Paleolithic and Middle Stone Age, edited by Conard, N. and Delagnes, A., pp. 171–203, Tübingen Publication in Prehistory, 2014.

Hole, F. and Flannery, K. V.: The Prehistory of Southwestern Iran: A Preliminary Report, Proceedings of the Prehistoric Society, 33, 147–206, 1968.

Hublin, J. J.: The origin of Neandertals, Proceedings of the National Academy of Sciences, 106, 16 022–16 027, 2009.

Hublin, J.-J., Ben-Ncer, A., Bailey, S. E., Freidline, S. E., Neubauer, S., Skinner, M. M., Bergmann, I., Le Cabec, A., Benazzi, S., Harvati, K., and Gunz, P.: New fossils from Jebel Irhoud, Morocco and the pan-African origin of Homo sapiens, Nature Publishing Group, 546, 289–292, 2017.

Huntley, D. J. and Baril, M. R.: The K content of the K-feldspars being measured in optical dating or in the thermoluminescence dating, Ancient TL, 15, 11–13, 1997.

Huntley, D. J. and Lamothe, M.: Ubiquity of anomalous fading in K-feldspars and the measurement and correction for it in optical dating, Canadian Journal of Earth Sciences, 38, 1093–1106, 2001.

Huntley, D. J., Godfrey-Smith, D. I., and Thewalt, M. L. W.: Optical dating of sediments, Nature, 313, 105–107, 1985.

Huntriss, A.: A Bayesian analysis of luminescence dating , Ph.D. thesis, University of Durham, 2008.

Hütt, G., Jaek, I., and Tchonka, J.: Optical dating: K-Feldspars optical response stimulation spectra, Quaternary Science Reviews, 7, 381–385, 1988.

Istratov, A. A. and Vyvenko, O. F.: Exponential analysis in physical phenomena, Review of Scientific Instruments, 70, 1233–1257, 1999.

Jain, M.: Extending the dose range: Probing deep traps in quartz with 3.06 eV photons, Radiation Measurements, 44, 445–452, 2009.

Jain, M. and Ankjærgaard, C.: Towards a non-fading signal in feldspar: Insight into charge transport and tunnelling from time-resolved optically stimulated luminescence, Radiation Measurements, 46, 292–309, 2011.

Jain, M., Murray, A. S., and Bøtter-Jensen, L.: Characterisation of blue-light stimulated luminescence components in different quartz samples: implications for dose measurement, Radiation Measurements, 37, 441–449, 2003.

Jaubert, J., Biglari, F., Bordes, J. G., Bruxelles, L., Mourre, V., Shidrang, S., Naderi, R., and Alipour, S.: New Research on Paleolithic of Iran: Preliminary report of 2004 Iranian-French Joint Mission, Iranian Center for Archaeological Research, Tehran, Iran, Archaeological Reports, pp. 17–26, 2006.

Jaubert, J., Biglari, F., Mourre, V., Bruxelles, L., Bordes, J. G., Shidrang, S., Naderi, R., Mashkour, M., Maureille, B., Mallye, J. B., Quinif, Y., Rendu, W., and Laroulandie, V.: The Middle Paleolithic occupation of Mar-Tarik, a new Zagros Mousterian site in Bisotun massif (Kerman-shah, Iran), in: Iran Paleolithic, Le Paléolithique d'Iran, edited by Otte, M., Biglari, F., and Jaubert, J., pp. 7–27, Bar International Series, 2009.

Kharazian Akhavan, M., Jamet, G., Puaud, S., Heydari, M., Guérin, G., Hashemi, M., Vahdati Nasab, H., and Berillon, G.: The geoarchaeological study of Paleolithic open-air site of Mirak (Semnan, Iran) using sedimentological and physical-chemical analysis, Quater. J. Iran, 4, 273–290, 2018.

King, G. E., Guralnik, B., Valla, P. G., and Herman, F.: Trapped-charge thermochronometry and thermometry: A status review, Chemical Geology, pp. 1–15, 2016.

King, G. E., Burow, C., Roberts, H. M., and Pearce, N. J. G.: Age determination using feldspar: Evaluating fading-correction model performance, Radiation Measurements, 119, 58–73, 2018.

Klein, R. G.: Hominins dispersals in the old world, in: The Human Past, edited by Scarre, C., pp. 71–107, Thames & Hudson, 2018.

Krause, J., Orlando, L., Serre, D., Viola, B., Prüfer, K., Richards, M. P., Hublin, J.-J., Hänni, C., Derevianko, A. P., and Pääbo, S.: Neanderthals in central Asia and Siberia, Nature, 449, 902–904, 2007a.

Krause, J., Orlando, L., Serre, D., Viola, B., Prüfer, K., Richards, M. P., Hublin, J.-J., Hänni, C., Derevianko, A. P., and Pääbo, S.: Neanderthals in central Asia and Siberia, Nature, 449, 902–904, 2007b.

Krbetschek, M. R., Rieser, U., Zöller, L., and Heinicke, J.: Radioactive disequilibria in palaeodosimetric dating of sediments, Radiation Measurements, 23, 485–489, 1994.

Kreutzer, S., Schmidt, C., Fuchs, M. C., Dietze, M., Fischer, M., and Fuchs, M.: Introducing an R package for luminescence dating analysis, Ancient TL, 30, 1–8, 2012.

Kreutzer, S., Martin, L., Dubernet, S., and Mercier, N.: The IR-RF alpha-Efficiency of K-feldspar, Radiation Measurements, 120, 148–156, 2018a.

Kreutzer, S., Martin, L., Guérin, G., Tribolo, C., Selva, P., and Mercier, N.: Environmental Dose Rate Determination Using a Passive Dosimeter: Techniques and Workflow for alpha-$Al_2O_3$:C Chips, Geochronometria, 45, 56–67, 2018b.

Kreutzer, S., Burow, C., Dietze, M., Fuchs, M. C., Schmidt, C., Fischer, M., and Friedrich, J.: Luminescence: Comprehensive Luminescence Dating Data Analysis, URL `https://CRAN.R-project.org/package=Luminescence`, r package version 0.8.5, 2019.

Kuhn, S. L., Stiner, M. C., Güleç, E., Özer, I., Yılmaz, H., Baykara, I., Açıkkol, A., Goldberg, P., Molina, K. M., Ünay, E., and Suata-Alpaslan, F.: The early Upper Paleolithic occupations at Üçağızlı Cave (Hatay, Turkey), Journal of Human Evolution, 56, 87–113, 2009.

Lanos, P. and Dufresne, P.: Chronomodel version 2.0: Software for Chronological Modelling of Archaeological Data using Bayesian Statistics., 2019.

Li, B. and Li, S.-H.: Luminescence dating of K-feldspar from sediments: A protocol without anomalous fading correction, Quaternary Geochronology, 6, 468–479, 2011.

Liritzis, I., Singhvi, A. K., Feathers, J. K., Wagner, G. A., Kadereit, A., Zacharias, N., and Li, S.-H.: Luminescence Dating in Archaeology, Anthropology, and Geoarchaeology, SpringerBriefs in Earth System Sciences, Springer International Publishing, Heidelberg, 2013.

Lisiecki, L. E. and Raymo, M. E.: A Pliocene-Pleistocene stack of 57 globally distributed benthic $\delta\ ^{18}$O records, Paleoceanography, 20, 1–17, 2005.

López, S., Van Dorp, L., and Hellenthal, G.: Human Dispersal Out of Africa: A Lasting Debate, Evolutionary Bioinformatics, 11s2, EBO.S33 489–12, 2016.

Mahan, S. A. and DeWitt, R.: Principles and history of luminescence dating, in: Handbook of Luminescence Dating, edited by Bateman, M., pp. 1–39, Whittles Publishing, 2019.

Mahesh, K., Weng, P. S., and Furetta, C.: Thermoluminescence in solids and its application, Thermoluminescence in solids and its application, Nuclear Technology Publishing, England, 1989.

Mauz, B., Packman, S. C., and Lang, A.: The alpha effectiveness in silt-sized quartz: New data obtained by single and multiple aliquot protocols, Ancient TL, 24, 47–52, 2006.

Mayya, Y. S., Morthekai, P., Murari, M. K., and Singhvi, A. K.: Towards quantifying beta microdosimetric effects in single-grain quartz dose distribution, Radiation Measurements, 41, 1032–1039, 2006.

Mcbrearty, S. and Brooks, A. S.: The revolution that wasn't: a new interpretation of the origin of modern human behavior, Journal of Human Evolution, 39, 453–563, 2000.

McKeever, S. W. S.: Thermoluminescence of solids, Thermoluminescence of solids, Cambrigde University Press, 1988.

Mejdahl, V.: Internal radioactivity in quartz and feldspar grains, Ancient TL, 5, 10–17, 1987.

Mellars, P.: The Neanderthal Legacy, Princeton University Press, 1996.

Mellars, P.: Why did modern human populations disperse from Africa ca. 60,000 years ago? A new model, Proceedings of the National Academy of Sciences, 103, 9381–9386, 2006a.

Mellars, P.: Going East: New Genetic and Archaeological Perspectives on the Modern Human Colonization of Eurasia, Science, 313, 796–800, 2006b.

Mercier, N., Valladas, H., Bar-Yosef, O., Vandermeersch, B., Stringer, C., and Joron, J. L.: Thermoluminescence Date for the Mousterian Burial Site of Es-Skhul, Mt. Carmel, Journal of Archaeological Science, 20, 169–174, 1993.

Mercier, N., Kreutzer, S., Christophe, C., Guérin, G., Guibert, P., Lahaye, C., Lanos, P., Philippe, A., and Tribolo, C.: Bayesian statistics in luminescence dating: The 'baSAR'-model and its implementation in the R package 'Luminescence', Ancient TL, 34, 14–21, 2016.

Murray, A. S. and Wintle, A. G.: Luminescence dating of quartz using an improved single-aliquot regenerative-dose protocol, Radiation Measurements, 32, 57–73, 2000.

Murray, A. S. and Wintle, A. G.: The single aliquot regenerative dose protocol: potential for improvements in reliability, Radiation Measurements, 37, 377–381, 2003.

Murray, A. S., Thomsen, K. J., Masuda, N., Buylaert, J. P., and Jain, M.: Identifying well-bleached quartz using the different bleaching rates of quartz and feldspar luminescence signals, Radiation Measurements, 47, 688–695, 2012.

Nasab, H. V., Clark, G. A., and Torkamandi, S.: Late Pleistocene dispersal corridors across the Iranian Plateau: A case study from Mirak, a Middle Paleolithic site on the northern edge of the Iranian Central desert (Dasht-e Kavir), Quaternary International, 300, 267–281, 2013.

Nasab, H. V., Berillon, G., Jamet, G., Hashemi, M., Jayez, M., Khaksar, S., Anvari, Z., Guérin, G., Heydari, M., Kharazian, M. A., Puaud, S., Bonilauri, S., Zeitoun, V., Sévêque, N., Khatooni, J. D., and Asgari Khaneghah, A.: The open-air Paleolithic site of Mirak, northern edge of the Iranian Central Desert (Semnan, Iran): Evidence of repeated human occupations during the late Pleistocene, Comptes Rendus Palevol, 18, 465–478, 2019.

Nelson, M. S. and Rittenour, T. M.: Using grain-size characteristics to model soil water content: Application to dose-rate calculation for luminescence dating, Radiation Measurements, 81, 142–149, 2015.

Olszewski, D.: The Zarzian in the Context of the Epipaleolithic Middle East, International Journal of the Humanities, 19, 1–21, 2012.

Olszewski, D. I.: The Late Baradostian occupation at Warwasi rockshelter, Iran, in: The Paleolithic Prehistory of the Zagros-Taurus, edited by Olszewski, D. I. and Dibble, H., pp. 186–206, The University Museum of Archaeology and Anthropology. University of Pennsylvania, Philadelphia, 1993.

Olszewski, D. I.: The Palaeolithic Period, including the Epipalaeolithic, in: Jordan: an Archaeological Reader, edited by Adams, R. B., pp. 34–69, Equinox Pub., London, 2008.

Olszewski, D. I. and Dibble, H. L.: The Zagros Aurignacian, Current Anthropology, 35, 68–75, 1994.

Olszewski, D. I. and Dibble, H. L.: To be or not to be Aurignacian: The Zagros Upper Paleolithic, in: Towards a Definition of the Aurignacian, Proceedings of the Sympoisum held in Lisbon, Portugal, June 25-30, 2002, edited by Bar-Yosef, O. and Zilhão, J., pp. 355–373, Instituto Português de Arqueologia, 2006.

Otte, M., Shidrang, S., Zwyns, N., and Flas, D.: New radiocarbon dates for the Zagros Aurignacian from Yafteh cave, Iran, Journal of Human Evolution, 61, 340–346, 2011.

Petraglia, M., Korisettar, R., Boivin, N., Clarkson, C., Ditchfield, P., Jones, S., Koshy, J., Lahr, M. M., Oppenheimer, C., Pyle, D., Roberts, R., Schwenninger, J. L., Arnold, L., and White, K.: Middle Paleolithic Assemblages from the Indian Subcontinent Before and After the Toba Super-Eruption, Science, 317, 114–116, 2007.

Petraglia, M. D. and Alsharekh, A.: The Middle Palaeolithic of Arabia: Implications for modern human origins, behaviour and dispersals, Antiquity Project Gallery, 77, 671–684, 2003.

Petraglia, M. D., Haslam, M., Fuller, D. Q., Boivin, N., and Clarkson, C.: Out of Africa: new hypotheses and evidence for the dispersal of Homo sapiensalong the Indian Ocean rim, Annals of Human Biology, 37, 288–311, 2010.

Philippe, A., Guérin, G., and Kreutzer, S.: BayLum - An R package for Bayesian analysis of OSL ages: An introduction, Quaternary Geochronology, 49, 16–24, 2019.

Pollastro, R. M., Persits, F. M., and Steinshouer, D. W.: Maps showing geology, oil and gas fields, and geologic provinces of Iran, U.S. Geological Survey Open-File Report 97-470-G, https://doi.org/10.3133/ofr97470G, 1997.

Pomeroy, E., Mirazón Lahr, M., Crivellaro, F., Farr, L., Reynolds, T., Hunt, C. O., and Barker, G.: Newly discovered Neanderthal remains from Shanidar Cave, Iraqi Kurdistan, and their attribution to Shanidar 5, Journal of Human Evolution, 111, 102–118, 2017.

Poolton, N. R. J., Ozanyan, K. B., Wallinga, J., Murray, A. S., and Bøtter-Jensen, L.: Electrons in feldspar II: a consideration of the influence of conduction band-tail states on luminescence processes, Physics and Chemistry of Minerals, 29, 217–225, 2002a.

Poolton, N. R. J., Wallinga, J., Murray, A. S., Bulur, E., and Bøtter-Jensen, L.: Electrons in feldspar I: on the wavefunction of electrons trapped at simple lattice defects, Physics and Chemistry of Minerals, 29, 210–216, 2002b.

Porat, N., Faerstein, G., Medialdea, A., and Murray, A. S.: Re-examination of common extraction and purification methods of quartz and feldspar for luminescence dating, Ancient TL, 33, 22–30, 2015.

Prasad, A. K., Poolton, N. R. J., Kook, M., and Jain, M.: Optical dating in a new light: A direct, non-destructive probe of trapped electrons, Scientific Reports, 7, 461, 2017.

Prescott, J. R. and Hutton, J. T.: Cosmic ray contributions to dose rates for luminescence and ESR dating: Large depths and long-term time variations, Radiation Measurements, 23, 497–500, 1994.

Preusser, F., Chithambo, M. L., Götte, T., Martini, M., Ramseyer, K., Sendezera, E. J., Susino, G. J., and Wintle, A. G.: Quartz as a natural luminescence dosimeter, Earth-Science Reviews, 97, 184–214, 2009.

R Core Team: R: A Language and Environment for Statistical Computing, Vienna, Austria, URL `https://r-project.org`, 2019.

Ramsey, C. B.: Radiocarbon Calibration and Analysis of Stratigraphy: The OxCal Program, Radiocarbon, 37, 425–430, 1995.

Relethford, J. H.: Genetics and the Search for Modern Human Origins, Wiley-Liss, 2001.

Rhodes, E. J., Bronk Ramsey, C., Outram, Z., Batt, C., Willis, L., Dockrill, S., and Bond, J.: Bayesian methods applied to the interpretation of multiple OSL dates: high precision sediment ages from Old Scatness Broch excavations, Shetland Isles, Quaternary Science Reviews, 22, 1231–1244, 2003.

Richter, D., Grün, R., Joannes-Boyau, R., Steele, T. E., Amani, F., Rué, M., Fernandes, P., Raynal, J.-P., Geraads, D., Ben-Ncer, A., Hublin, J.-J., and McPherron, S. P.: The age of the hominin fossils from Jebel Irhoud, Morocco, and the origins of the Middle Stone Age, Nature Publishing Group, 546, 293–296, 2017.

Roberts, R. G., Jacobs, Z., Li, B., Jankowski, N. R., Cunningham, A. C., and Rosenfeld, A. B.: Optical dating in archaeology: thirty years in retrospect and grand challenges for the future, Journal of Archaeological Science, 56, 41–60, 2015.

Rosenberg, M.: Report on the 1978 Sondage at Eshkaft-e Gavi, Iran, 23, 51–62, 1985.

Rosenberg, T. M., Preusser, F., Fleitmann, D., Schwalb, A., Penkman, K., Schmid, T. W., Al-Shanti, M. A., Kadi, K., and Matter, A.: Humid periods in southern Arabia: Windows of opportunity for modern human dispersal, Geology, 39, 1115–1118, 2011.

Scarre, C., ed.: The Human Past, World Prehistory & the Development of Human Societies, Thames & Hudson, 4th edn., 2018.

Schmidt, C., Bösken, J., and Kolb, T.: Is there a common alpha-efficiency in polymineral samples measured by various infrared stimulated luminescence protocols?, Geochronometria, 45, 160–172, 2018.

Schwarcz, H. P., Grün, R., Vandermeersch, B., Bar-Yosef, O., Valladas, H., and Tchernov, E.: ESR dates for the hominid burial site of Qafzeh in Israel, Journal of Human Evolution, 17, 733–737, 1988.

Scott, J. E. and Marean, C. W.: Paleolithic hominin remains from Eshkaft-e Gavi (southern Zagros Mountains, Iran): description, affinities, and evidence for butchery, Journal of Human Evolution, 57, 248–259, 2009.

Shea, J.: Transitions or turnovers? Climatically-forced extinctions of Homo sapiens and Neanderthals in the east Mediterranean Levant, Quaternary Science Reviews, 27, 2253–2270, 2008.

Shea, J. J.: The Middle Paleolithic of the East Mediterranean Levant, Journal of World Prehistory, 17, 313–394, 2003.

Shea, J. J.: Neanderthals and Homo sapiens in the Levant, in: South-Eastern Mediterranean Peoples Between 130,000 and 10,000 Years Ago, edited by Garcea, E. A. A., pp. 126–143, Oxbow Books, 2010.

Shidrang, S.: The Middle to Upper Paleolithic Transition in the Zagros: The Appearance and Evolution of the Baradostian, in: The Middle and Upper Paleolithic Archeology of the Levant and Beyond, pp. 133–156, Springer Singapore, Singapore, 2018.

Shidrang, S., Biglari, F., Bordes, J. G., and Jaubert, J.: Continuity and Change in the Late Pleistocene Lithic Industries of the Central Zagros: A Typo-Technological Analysis of Lithic Assemblages from Ghar-E Khar Cave, Bisotun, Iran, Archaeology, Ethnology & Anthropology of Eurasia, 44, 27–38, 2016.

Singarayer, J. and Bailey, R. M.: Component-resolved bleaching spectra of quartz optically stimulated luminescence: preliminary results and implications for dating, Radiation Measurements, 38, 111–118, 2004.

Singarayer, J. S.: Linearly modulated optically stimulated luminescence of sedimentary quartz: physical mechanisms and implications for dating, Ph.D. thesis, University of Oxford, 2002.

Singarayer, J. S. and Bailey, R. M.: Further investigations of the quartz optically stimulated luminescence components using linear modulation, Radiation Measurements, 37, 451–458, 2003.

Sirakov, N., Guadelli, J. L., Ivanova, S., Sirakova, S., Boudadi-Maligne, M., Dimitrova, I., Ph, F., Ferrier, C., Guadelli, A., Iordanova, D., Iordanova, N., Kovatcheva, M., Krumov, I., Leblanc, J. C., Miteva, V., Popov, V., Spassov, R., Taneva, S., and Tsanova, T.: An ancient continuous human presence in the Balkans and the beginnings of human settlement in western Eurasia: A Lower Pleistocene example of the Lower Palaeolithic levels in Kozarnika cave (North-western Bulgaria), Quaternary International, 223-224, 94–106, 2010.

Smith, B. W. and Rhodes, E. J.: Charge movements in quartz and their relevance to optical dating, Radiation Measurements, 23, 239–333, 1994.

Smith, P. E. L.: Paleolithic archaeology in Iran, The American Institute of Iranian Studies Monograph 1, Philadelphia (PA): The University Museum, 1986.

Solecki, R. S.: Shanidar Cave, A Palaeolithic Site in Northern Iraq, Smithsonian Institution Annual Report for 1954, pp. 389–425, 1955.

Solecki, R. S.: The Baradostian Industry and the Upper Palaeolithic in the Near East, Ph.D. thesis, Columbia University, 1958.

Spooner, N. A.: Optical dating: Preliminary results on the anomalous fading of luminescence from feldspars, Quaternary Science Reviews, 11, 139–145, 1992.

Thiel, C., Buylaert, J. P., Murray, A., Terhorst, B., Hofer, I., Tsukamoto, S., and Frechen, M.: Luminescence dating of the Stratzing loess profile (Austria) - Testing the potential of an elevated temperature post-IR IRSL protocol, Quaternary International, 234, 23–31, 2011.

Thomsen, K. J., Murray, A. S., and Bøtter-Jensen, L.: Sources of variability in OSL dose measurements using single grains of quartz, Radiation Measurements, 39, 47–61, 2005.

Thomsen, K. J., Murray, A. S., Jain, M., and Bøtter-Jensen, L.: Laboratory fading rates of various luminescence signals from feldspar-rich sediment extracts, Radiation Measurements, 43, 1474–1486, 2008.

Thomsen, K. J., Murray, A. S., Buylaert, J. P., Jain, M., Hansen, J. H., and Aubry, T.: Testing single-grain quartz OSL methods using sediment samples with independent age control from the Bordes-Fitte rockshelter (Roches d'Abilly site, Central France), Quaternary Geochronology, 31, 77–96, 2016.

Tillier, A.-m., Sirakov, N., Guadelli, A., Fernandez, P., Sirakova, S., Dimitrova, I., Ferrier, C., Guérin, G., Heidari, M., Krumov, I., Leblanc, J.-C., Miteva, V., Popov, V., Taneva, S., and Guadelli, J.-L.: Evidence of Neanderthals in the Balkans: The infant radius from Kozarnika Cave (Bulgaria), Journal of Human Evolution, 111, 54–62, 2017.

Timmermann, A. and Friedrich, T.: Late Pleistocene climate drivers of early human migration, Nature, 538, 92–95, 2016.

Trautmann, T., Krbetschek, M. R., Dietrich, A., and Stolz, W.: Investigations of feldspar radioluminescence: potential for a new dating technique, Radiation Measurements, 29, 421–425, 1998.

Trautmann, T., Dietrich, A., Stolz, W., and Krbetschek, M. R.: Radioluminescence Dating: A New Tool for Quaternary Geology and Archaeology, Naturwissenschaften, 86, 441–444, 1999.

Trinkaus, E.: The Shanidar Neandertals, Academic press, 1983.

Trinkaus, E.: Early Modern Humans, Annual Review of Anthropology, 34, 207–230, 2005.

Trinkaus, E. and Biglari, F.: Middle Paleolithic Human Remains from Bisitun Cave, Iran, Paléorient, 32, 105–111, 2006.

Trinkaus, E., Biglari, F., Mashkour, M., Monchot, H., Reyss, J.-L., Rougier, H., Heydari, S., and Abdi, K.: Late Pleistocene human remains from Wezmeh Cave, western Iran, American Journal of Physical Anthropology, 135, 371–378, 2008.

Tsanova, T.: The beginning of the Upper Paleolithic in the Iranian Zagros. A taphonomic approach and techno-economic comparison of Early Baradostian assemblages from Warwasi and Yafteh (Iran), Journal of Human Evolution, 65, 39–64, 2013.

Turner, A.: Assessing earliest human settlement of Eurasia: Late Pliocene dispersions from Africa, Antiquity Project Gallery, 73, 563–570, 1999.

Turq, A., Roebroeks, W., Bourguignon, L., and Faivre, J.-P.: The fragmented character of Middle Palaeolithic stone tool technology, Journal of Human Evolution, 65, 641–655, 2013.

Vahdati Nasab, H. and Clark, G. A.: The upper paleolithic of the Iranian central desert: The Delazian sites, Semnan Province - A case study, Archäologische Mitteilungen aus Iran und Turan AMIT, 46, 1–21, 2014.

Vahdati Nasab, H. and Hashemi, M.: Playas and Middle Paleolithic settlement of the Iranian Central Desert: The discovery of the Chah-e Jam Middle Paleolithic site, Quaternary International, 408, 140–152, 2016.

Valladas, H., Reyss, J. L., Joron, J. L., Valladas, G., Bar-Yosef, O., and Vandermeersch, B.: Thermoluminescence dating of Mousterian Troto-Cro-Magnon' remains from Israel and the origin of modern man, Nature, 331, 614–616, 1988.

Valladas, H., Mercier, N., Froget, L., Hovers, E., Joron, J. L., Kimbel, W. H., and Rak, Y.: TL Dates for the Neanderthal Site of the Amud Cave, Israel, Journal of Archaeological Science, 26, 259–268, 1999.

Wallinga, J., Murray, A., and Wintle, A.: The single-aliquot regenerative-dose (SAR) protocol applied to coarse-grain feldspar, Radiation Measurements, 32, 529–533, 2000.

Whitley, V. H. and McKeever, S. W. S.: Photoionization of deep centers in Al2O3, Journal of Applied Physics, 87, 249–256, 2000.

Wintle, A. G.: Anomalous Fading of Thermoluminescence in Mineral Samples, Nature, 245, 143–144, 1973.

Wintle, A. G. and Murray, A. S.: Quartz OSL: Effects of thermal treatment and their relevance to laboratory dating procedures, Radiation Measurements, 32, 387–400, 2000.

Wintle, A. G. and Murray, A. S.: A review of quartz optically stimulated luminescence characteristics and their relevance in single-aliquot regeneration dating protocols, Radiation Measurements, 41, 369–391, 2006.

Yukihara, E. G. and McKeever, S. W. S.: Optically Stimulated Luminescence, Optically Stimulated Luminescence, Wiley, 2011.

Zanolli, C., Biglari, F., Mashkour, M., Abdi, K., Monchot, H., Debue, K., Mazurier, A., Bayle, P., Le Luyer, M., Rougier, H., Trinkaus, E., and Macchiarelli, R.: A Neanderthal from the Central Western Zagros, Iran. Structural reassessment of the Wezmeh 1 maxillary premolar, Journal of Human Evolution, 135, 102 643–12, 2019.

Zeidi, M. and Conard, N. J.: The forth season report of survey at Ghār-e Boof in city of Rostam at Fars Province, th Annual Symposium of the Iranian Archaeology, in Persian, 234–238, 2019.

Zilhão, J.: Modernity, Behavioral, in: The International Encyclopedia of Anthropology, edited by Callan, H., pp. 1–9, American Cancer Society, 2018.

Zimmerman, D. W.: Thermoluminescent dating using fine grains from pottery., Archaeometry, 13, 29–52, 1971.

Zink, A.: A coarse Bayesian approach to evaluate luminescence ages, Geochronometria, 40, 90–100, 2013.

Zink, A. J. C.: Bayesian analysis of luminescence measurements, Radiation Measurements, 81, 71–77, 2015.

# 2 Study I

Radiation Measurements 120 (2018) 96–103

Contents lists available at ScienceDirect

Radiation Measurements

journal homepage: www.elsevier.com/locate/radmeas

# OSL signal saturation and dose rate variability: Investigating the behaviour of different statistical models

Maryam Heydari*, Guillaume Guérin

*Institut de Recherche sur les Archéomatériaux, UMR 5060 CNRS - Université Bordeaux Montaigne, Centre de Recherche en Physique Appliquée à l'Archéologie (CRP2A), Maison de l'archéologie, 33607, Pessac cedex, France*

*corresponding author: maryam.heydari@u-bordeaux-montaigne.fr

**Radiation Measurements**

Year: 2018, Volume: 120, Pages: 96–103

- published -

https://doi.org/10.1016/j.radmeas.2018.05.005

## Abstract

Statistical models derived from two inferences, frequentist and Bayesian, are compared for OSL data analysis. Controlled laboratory experiments were designed to investigate: (1) dose-recovery behaviour and (2) dose variability. (1) Dose recovery tests were performed on single grains of quartz close to saturation. We test whether the Central Dose Model (CDM, Galbraith et al. 1999), which is the most commonly used model, is capable of converging towards the given dose. Furthermore, a set of new Bayesian age models developed by Combès and Philippe (2017) is applied to determine the dose recovery ratio. The results suggest that the CDM underestimates the given dose if no $D_0$ criterion is applied. (2) Bayesian models and frequentist models (CDM and Average Dose Model: ADM, Guérin et al. 2017a) are used in dose variability experiments to compare the estimated average dose. To mimic natural $\beta$-dose heterogeneity to single grains of quartz, log-normal dose distributions with different dispersions were created artificially. The results indicate an underestimation of the average dose by at least 10 % for CDM, lognormal-median and Cauchy for dispersion values greater than 40 %. Conversely, we show that the ADM, the Bayesian lognormal-average and Gaussian models converge towards the average of the distribution and display almost no underestimation, for a significant gain in accuracy.

## 2.1 Introduction

Optically Simulated Luminescence (OSL) dating requires a series of measurements and data processing steps to determine the palaeodose. Data processing methods are based on two different statistical inferences, the frequentist and the Bayesian approaches (Buck and Millard, 2004). Frequentist statistics can assign probabilities only to events or observations from repeatable experiments. The frequentist interpretation of probability explains outcomes for a large number of repeated experiments under similar conditions. In this approach, after repeated sampling from an unknown distribution, the probability distribution of the observed data is determined (Carlin and Louis, 2000).

Bayesian inference is based on conditional probability. This means that the probability of an event occurring is related to another phenomenon. This inference generally starts with an initial knowledge about an event, which reflects the current state of knowledge about the parameters of the distribution of interest before observing the data. Then a particular model is applied to show the probability of the parameters of the distribution which best represent the data. Finally, the resulting distribution can be explained as a weighted average between initial knowledge about the parameters before data is observed (prior distribution) and the information about the parameters contained in the observed data (likelihood function, cf. Gelman et al. 2013).

Since Bayesian inference proved to be a powerful tool to evaluate uncertainty (Gelman et al., 2013), it was implemented to express the source of uncertainty for luminescence data analysis (e.g., Rhodes et al., 2003; Huntriss, 2008; Zink, 2015; Combès et al., 2015; Combès and Philippe, 2017). However, the most common way of data processing in OSL dating has been by frequentist inference. For instance, to determine the palaedose using the Single Aliquot Regenerative (SAR) dose protocol (Murray and Wintle, 2000) usually the software *Analyst* (Duller, 2015) or the R (R Core Team, 2017) package 'Luminescence' (Kreutzer et al., 2012, 2017) can be used. In the SAR protocol, individual aliquots (e.g., quartz grains) repeatedly receive different regeneration doses, and the signals are monitored by a constant test dose for sensitivity changes. Such sets of signals with associated doses are used to construct a dose response curve. Following that, individual equivalent dose ($D_e$) values, which are parameterised by Gaussian probability densities, are obtained by the projection of the natural luminescence signal onto the dose response curve. The standard error for each equivalent dose is derived from counting statistics and curve fitting uncertainties (Galbraith, 2002; Duller, 2007) as well as measurement reproducibility (Thomsen et al., 2005). Frequentist models like the Central Age Model (Galbraith et al., 1999), henceforth termed CDM for Central Dose Model following Galbraith and Roberts (2012); Bailiff et al. (2013) and the Average Dose Model (ADM, Guérin et al. 2017a) are applied to the set of individual $D_e$ values and associated uncertainties to determine the palaeodose of the sample of interest. According to the depositional environment, different frequentist models may be used (Galbraith and Roberts, 2012). If no problem such as post-depositional mixing

and/or poor bleaching is suspected, generally the CDM is applied to determine the palaeodose. This model, which calculates a weighted average of individual equivalent doses, is robust to be applied to data with symmetric error (Duller, 2007). However, due to early saturation of the blue stimulated luminescence signal of quartz measured in the UV wavelength range, the natural signal of a significant number of grains is often not in the linear part of the dose response curve, where error asymmetry becomes essential. In such a situation, the accuracy of the SAR protocol must be considered as doubtful (Duller, 2007). To minimise the issue raised by this kind of grains, for which the natural signal lies close to, or above the laboratory saturation level, Thomsen et al. (2016) proposed a rejection criterion based on the curvature parameter of the dose response curves ($D_0$) when dose response curves are fitted with a single saturating exponential curve ($L/T = A(1 - exp(-D/D_0))$. By using this criterion, grains are accepted only if the curvature parameter ($D_0$) is larger than the natural dose. While satisfactory in principle, this approach leads to a (sometimes considerable) reduction of the number of accepted grains and finally leads to decreasing precision of the results (Thomsen et al., 2016). Furthermore, the CDM estimator calculates the weighted geometric mean of a $D_e$ distribution, which does not converge to the arithmetic average of the distribution. Using the latter quantity leads to dose underestimation, especially in situations with explicit $\beta$-dose heterogeneity (Guérin et al. 2017b; see also Guérin et al. 2015c). Beta-dose rate heterogeneity is one of the most critical sources of dispersion for single grains that are believed to be well bleached and that do not suffer from mixing problems (e.g., Mayya et al., 2006). The range of $\beta$-particles is small in comparison to that of $\gamma$-rays, thus local hotspots, such as potassium feldspar grains, the main $\beta$-dose emitter, can lead to a heterogeneous irradiation field. As a result, $\beta$-doses absorbed by quartz form a positively skewed distribution, which can be described by a lognormal distribution (Mayya et al., 2006; Cunningham et al., 2012; Guérin et al., 2015a). The CDM estimator converges to the median of such lognormal distributions. However, every statistical model should aim at estimating the average dose absorbed by the grains, since measurements of dose rates all provide an estimate of the average dose rate. This reason led Guérin et al. (2017a) to present a new model called the Average Dose Model (ADM), in which the central dose estimate converges to the arithmetic average of individual absorbed dose values.

Another way of data processing is via Bayesian inference; Combès et al. (2015) proposed a Bayesian central dose model. In this model, single grain $D_e$ probability density distributions are not parameterised, and a Monte Carlo approach allows taking into account grains commonly considered as in or near saturation. Since the model is a single hierarchical inference, the palaeodose estimate is obtained simultaneously with individual $D_e$ estimates. Subsequently, no high $D_e$ value is rejected. Combès et al. (2015) proposed a Cauchy distribution to describe the distribution of equivalent doses around the central dose. A Cauchy distribution is similar to a Gaussian distribution (it is symmetric and bell-shaped), but with heavy tails (undefined variance) which

make it more robust against outliers.

Following new models developed by Combès and Philippe (2017), an R package called 'BayLum' dedicated to Bayesian statistics was developed (Christophe et al. 2017; see also Philippe et al. 2019. With the implemented models, the central dose can be calculated using a Cauchy, a Gaussian, or a lognormal distribution. In the case of lognormal distribution models, there are two possibilities: the central dose can be estimated as the median or the average of the distribution. These models are available in the 'BayLum' package but so far have not been tested.

This study aims to apply frequentist and Bayesian models to analyse OSL data and compare the obtained results. We test whether both approaches can recover a known, target dose to a similar extent. Two laboratory experiments were designed. First, we apply all models to datasets obtained from high-dose, dose recovery experiments on single grains of quartz to investigate saturation issues. The term 'high-dose' refers to ca. 150–255 Gy, the dose for which most samples are in, or close to signal saturation. The purpose of the second experiment is to determine the central dose for a set of grains, which absorbed different $\beta$-doses to see which model can better converge to the average of doses. Various amounts of $\beta$-doses are given to single grains of quartz to create artificial lognormal distributions to mimic heterogeneous $\beta$-dose rate distributions encountered in nature. Then, frequentist (CDM, ADM) and Bayesian models are applied and their results compared to the average of absorbed doses; the ratio of estimated to average dose then becomes an indicator of the performance of the models.

## 2.2 Material and methods

### 2.2.1 Sample preparation

Risø calibration quartz batch 71 (100–150 $\mu$m) was used for both experiments. For comparison purposes, natural quartz grains in the size range 200–250 $\mu$m from the archaeological site of Covalejos (Sanguino and Montes, 2005) in northern Spain were additionally used in the saturation experiments. Before mineral separation, the sample was wet sieved to isolate the 200–250 $\mu$m fine sand fraction. These grains were then treated with HCl (10 %) to remove carbonates, and with hydrogen peroxide ($H_2O_2$) to remove organic contaminants. Both treatments were continued until no reaction was observed. The mineral quartz was extracted from the polymineral sample through density separation using a heavy liquid solution (density 2.62 g cm$^{-3}$). The fraction with a density $>$ 2.62 g cm$^{-3}$ was etched with HF (40 %) for 40 min to remove the alpha-irradiated outer layer ($\sim$20 $\mu$m) of the grains. The etched quartz grains were then treated with 10 % HCl for 60 min to remove any fluorides that could have been produced during HF etching, and then further rinsed in purified water. This fraction was then re-sieved to $>$ 200 $\mu$m to remove grains resulting from the dissolution of residual feldspar in the quartz-rich fraction, or of small quartz grains.

### 2.2.2 Instrumentation

All measurements were carried out on single grains of quartz extracts using three automated Risø TL/OSL readers (two DA-20, one DA20 DASH) at the IRAMAT-CRP2A laboratory. Each reader was fitted with a single grain attachment (Bøtter-Jensen et al., 2003). A green laser (532 nm) was used to stimulate each grain individually. For light detection in the UV wavelength range, a 7.5 mm Hoya U-340 glass filter (2.5 mm ± 5 mm for the DASH) was used in front of an EMI 9235QB photomultiplier tube (Electron tube PDM 9107Q-AP-TTL-03 for the DASH).

### 2.2.3 Dose variability experiment

To mimic heterogeneous $\beta$-dose rate distributions, lognormal distributions were created artificially using grains of calibration quartz, which received various $\beta$-doses in the laboratory. 34 single grain discs containing 100 holes with 150 $\mu$m in diameter and 150 $\mu$m in depth, on a 10×10 rectangular grid with 600 $\mu$m spacing between centres were prepared. Visual inspection under red light confirmed that only one grain was loaded into each hole. First, the 'natural' signal (4.81 Gy) was removed using the blue LEDs (470 Δ 20 nm; ca 70 mW cm$^{-2}$) for 100 s in the reader. The second blue-LED stimulation was performed after a pause of 10,000 s to allow full emptying of the electron trap associated with the 110 °C UV-TL peak (Murray and Wintle, 2003). Then each of the 34 discs received $\beta$-doses ($^{90}$Sr/$^{90}$Y $\beta$-source) from 1 Gy to 34 Gy (i.e. disc 1: 1 Gy, disc 2: 2 Gy, etc. until 34 Gy). This range was chosen to be far from signal saturation, but also to work with doses large enough to be rather easy to measure. The SAR protocol (Murray and Wintle, 2000) was used for $D_e$ determination. For single-grain measurements, the green laser stimulation was carried out at 125 °C for 1 s. A preheat temperature of 260 °C for 10 s and a cutheat temperature of 220 °C was used. A high-temperature blue bleach at 280 °C for 40 s was used to avoid recuperation effects (Murray and Wintle, 2003). The late light background subtraction approach was applied, since the luminescence signal of calibration quartz is dominated by the fast component (Hansen et al., 2015). The only rejection criteria applied to individual grains was the relative uncertainty on the first (natural) test dose signal, which was required to be less than 20 % (following e.g., Thomsen et al., 2016; Guérin et al., 2015b). Recycling and IR depletion ratios, and the intensity of the recuperation signal were not taken into account as selection criteria, since it was shown recently that selection based on these criteria often leads to a mere loss of grains without improvements in determining any statistical parameters or reduction in dispersion of the data Thomsen et al. (2016); Guérin et al. (2017b). A single saturating exponential function passing through the origin was used for fitting all dose response curves ($\frac{L}{T} = A(1 - exp(\frac{-D}{D_0}))$ to describe a single trap dominated luminescence signal. Although applying other options for fitting dose response curves, such as exponential plus linear functions, may lead to better curve fitting (due to an increased number of fitting parameters), it does not

describe signal saturation. Yet, saturation of single-grain OSL has been empirically observed (see for example Fig. 10 in Duller et al. 2015). Thus, single saturated exponential fitting were applied to all of the grains, even if the fitting was not perfect.

#### 2.2.3.1 Tests of the protocol

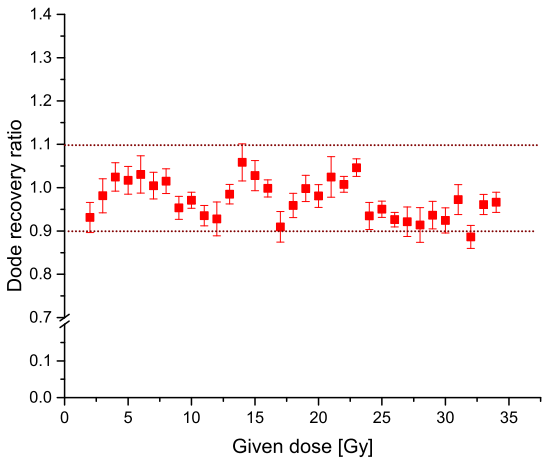


Figure 2.1: Dose recovery ratio for each disc; all ratios are within 10 % of unity, and the average is $0.98 \pm 0.01$, and the standard deviation is 0.06. Each point represents the measured to given dose ratio for a disc, estimated with the CDM.

Figure 2.1 displays the dose recovery ratios for each disc, based on the grains which passed the selection criterion. For each disc, we obtained between nine and forty-one accepted grains; the dose recovery ratio was estimated using the CDM. Figure 2.1 show all dose recovery ratios, which all are within 10 % of unity. The average dose recovery ratio is $0.98 \pm 0.01$, and the standard deviation is 0.06, which we deemed satisfying for further data analysis – in our view our SAR protocol was well-suited to the studied grains. As a result, we could sample this population of accepted grains to construct artificial distributions of absorbed doses.

#### 2.2.3.2 Constructing lognormal distributions

To define a lognormal distribution of a variable denoted $x$, two parameters are needed: $\mu$ (which is the average of the logged values; $exp(\mu)$ is the median of the $x$ values) and $\sigma$ (the standard deviation of the logged distribution). The probability for a given dose $x$ is then given by

$$\frac{1}{x\sigma\sqrt{2\pi}} e \frac{(ln(x)-\mu)^2}{2\sigma^2} \tag{2.1}$$

varied, while the average of given doses is then given by $e^{\mu+\frac{\sigma^2}{2}}$. To avoid saturation issues, we chose $ln(10)$ for $\mu$, and the relative standard deviation $\sigma$ was varied from 0.1 to 0.9.

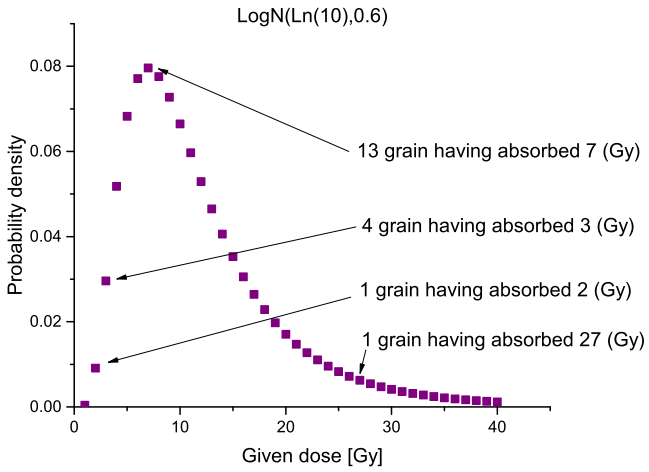


Figure 2.2: Exemplary created lognormal distribution with parameters ($\mu = ln(10)$, $\sigma = 0.6$). This figure shows the probability density function of lognormal distribution with 60 % dispersion for various given doses in Gy. The arrows exemplify for four cases the number of grains included in each point for a particular dose.

Figure 2.2 illustrates our procedure for creating a lognormal distribution with $\sigma = 0.6$. We first identified the dose value for which the probability was the greatest, here 7 Gy; we randomly picked 13 grains (among those for which the uncertainty on the test dose signal was smaller than 20 %, Sec. 2.2.3) from the disc having received a 7 Gy dose (note that 13 is arbitrary, we chose this number so that we could pick for each disc the required number of grains). Then, for all other discs (each with its own given dose value), the number of grains selected was determined by the ratio of the probabilities: thus, we picked 1 grain from the disc that was given a 2 Gy dose, 4 grains from the disc that was given a 3 Gy dose, etc. (see Table 2.1 for the number of grains selected from each disc).

The total number of grains selected for each value of $\sigma$ is given in Table 2.2 (the minimum and maximum total numbers are 48 and 163 grains, respectively). Finally, since we work with discrete dose values and discrete numbers of selected grains for each dose (in particular we cannot select less than 1 grain), the actual value of $\mu$ was not exactly constant (it slightly decreased with increasing dispersion, as the cut-off affected higher dose values more than lower dose values due to the positive skewness of lognormal distributions). As a result, in the following we used the actual values of the geometric and arithmetic means of the real distributions of selected grains.

### 2.2.4 Signal saturation experiment

Six single-grain discs of calibration quartz were given a dose of 150 Gy and twenty-four discs a dose of 200 Gy. Since calibration quartz grains generally displays a higher OSL sensitivity in comparison with usual 'natural' quartz, more discs were prepared for the archaeological quartz: for the sample from the archaeological site Covalejos (González and Barquín, 2005) forty-eight and thirty-six single grain discs absorbed doses of 164 Gy and 254 Gy, respectively. To characterise the dose response curve and calculate the $D_0$ values, a wide range of regeneration doses were used. The largest regeneration doses for given doses of 150 Gy, 164 Gy, 200 Gy and 254 Gy were 450 Gy, 419 Gy, 562 Gy and 477 Gy, respectively. Instrumentation and OSL measurement conditions were the same as in the dose variability experiment (see Sec. 2.2.2 & Sec. 2.2.3). Typical dose response curves (with a range of $D_0$ values) for all dose recovery experiments are shown in Fig. 2.8.

### 2.2.5 Bayesian models

In the Bayesian single inference model designed by Combès et al. (2015), individual $D_e$ values and the palaeodose are estimated at the same time. Bayesian curve fitting is performed as follows: the model starts with sampling from normal distributions, which are defined as a prior, to generate the parameters of each dose response curve. For instance, if a single saturating exponential ($L/T = A(1-exp(-D/D_0))$ is chosen to fit a dose response curve, two different Gaussian distributions are assumed for $A$ and $D_0$ which define the priors (see Sec. 4.2.1 in Combès et al. 2015, for a definition of these priors). Monto Carlo runs sample these parameter distributions to generate dose response curves. The most likely values for the parameters of the dose-response curves are those for which the curve fitting is best. A so-called burn-in process ensures that the Markov Chain Monte Carlo (MCMC) process has enough time to reach an equilibrium distribution, i.e. to find the best fit to the regenerative points. The output of the model is a set of probability densities estimated for each individual $D_e$ and for the central dose (note: at present the probability densities for the parameters of the dose response curves are not provided as output of the 'BayLum' functions, but in principle they could be). The user can choose whether the distribution of all the estimated individual equivalent doses are distributed around the central dose following a Gaussian, Cauchy or log-normal distribution, and based on that selection the central dose is determined (see also Philippe et al., 2019).

### 2.2.6 Software

Data analysis for this study was carried out using the statistical programming framework R. For calculating the CDM and the ADM, the functions `calc_CentralDose()` (Burow, 2017) and `calc_AverageDose()` (Guérin et al., 2017a) from the R package 'Luminescence' (Kreutzer

et al., 2012, 2017) were used. For running the Bayesian models, the R package 'BayLum' (Christophe et al., 2017; Philippe et al., 2019) was used. To run the calculations, one folder should be prepared containing all BIN-files and associated information, such as the position of the selected grains and the laboratory dose rate (Philippe et al., 2019). Typical calculation times for Bayesian models for a single set of data (typically including from 200 to ~1,000 grains) ranged from days to weeks on the multicore *RStudio*® (`https://www.rstudio.com`) server environment hosted at the IRAMAT-CRP2A (note: the number of iterations needed to reach convergence strongly depends on the selected model; for example, in general Cauchy distributions require larger numbers of iterations).

## 2.3 Results

### 2.3.1 Dose variability

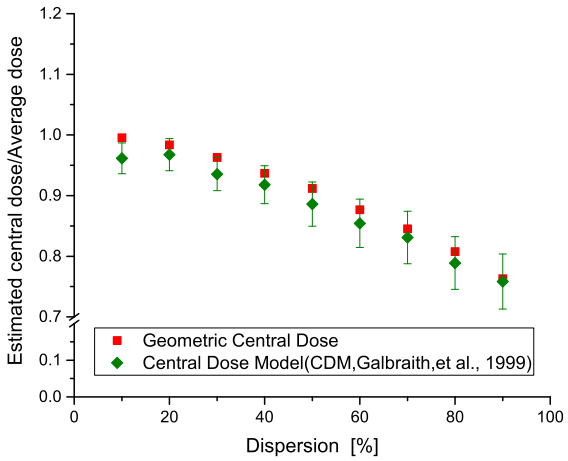


Figure 2.3: CDM (Galbraith et al., 1999) to average absorbed dose ratio, compared with the geometric to arithmetic mean ratio, as a function of the dispersion in absorbed doses. Both values are in good agreement with each other.

The CDM estimator calculates the geometric weighted mean, which converges towards the median of the assumed lognormal distribution. If the overdispersion dominates the weighting term of each $D_e$ estimate (i.e., if it is larger than the relative error of each individual $D_e$), then the central dose tends toward the unweighted geometric mean of observed $D_e$ values (Guérin et al., 2017a). For each of the created lognormal distributions (Sec. 2.2.3.2), both the arithmetic and geometric means were calculated. Figure 2.3 shows the geometric to arithmetic mean ratio and the CDM dose to average (arithmetic mean) dose ratio; both are in good agreement. This figure

illustrates that with increasing dispersion, the difference between geometric mean and arithmetic means is increased, as is the dose underestimation when using the CDM. This underestimation reaches ∼25 % of the average dose for $\sigma = 0.9$ (in this case, the actual standard deviation in the logarithm of given doses is $\sigma = 0.76$, due to the truncation of the lognormal distributions described in Sec. 2.2.3.2). For all the above presented artificial lognormal distributions, the central doses were determined with frequentist (CDM and ADM) and Bayesian models (Gaussian, lognormal-average, lognormal-median and Cauchy). The term central dose is used here to reflect the outcome of a model and does not always correspond to the same statistical parameter (e.g., it corresponds to the median of equivalent doses in the CDM but to the average in the ADM). The central dose obtained with each model was normalised to the average absorbed dose, illustrating the ability of each model to retrieve the average absorbed dose.

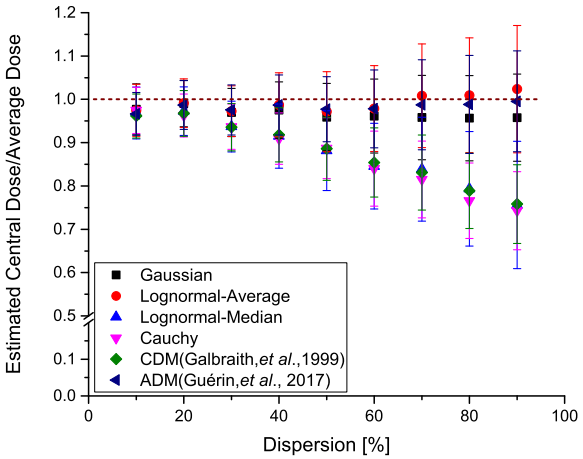


Figure 2.4: Comparison of the central dose estimated with frequentist models (CDM, Galbraith et al. 1999) and ADM, Guérin et al. 2017a) with that estimated with Bayesian models, as a function of the dispersion of the artificial lognormal distributions. The CDM, Cauchy and lognormal-median models show systematic dose underestimation with increasing dose dispersion. Conversely, the ADM, Gaussian and lognormal-average models converge to the average of the distribution. (Note: for the sake of comparison with the CDM and ADM, for the Bayesian models each point indicates the middle of the 95 % credibility interval; the associated error bar corresponds to the length of this interval divided by 4).

Figure 2.4 shows the determined ratios as a function of the dispersion of the artificial lognormal distributions. Results using the CDM, Cauchy and lognormalmedian models systematically underestimate the average absorbed dose, especially when the dispersion is increased. For these three models, when the dispersion was increased from 10 % to 90 % (note: Table 2.1 lists the corresponding 'true' dispersion values together with the CDM overdispersion values), the depar-

ture from unity increased from ∼5 % to ∼25 %. In general, we observe an underestimation of the average absorbed dose greater than 10 % for $\sigma$ values greater than 40 %. This observation argues against the application of the CDM, lognormal-median and Cauchy in such cases (high dose dispersion). By contrast, the Gaussian model underestimates the average absorbed dose by ca 5 %, which is indistinguishable from the expected underestimation of 2 % (cf. average dose recovery ratio on all discs, Fig. 2.1). Conversely, the ADM and lognormal-average model show almost no underestimation, even for high dispersion values (up to 90 %).

### 2.3.2 Signal saturation

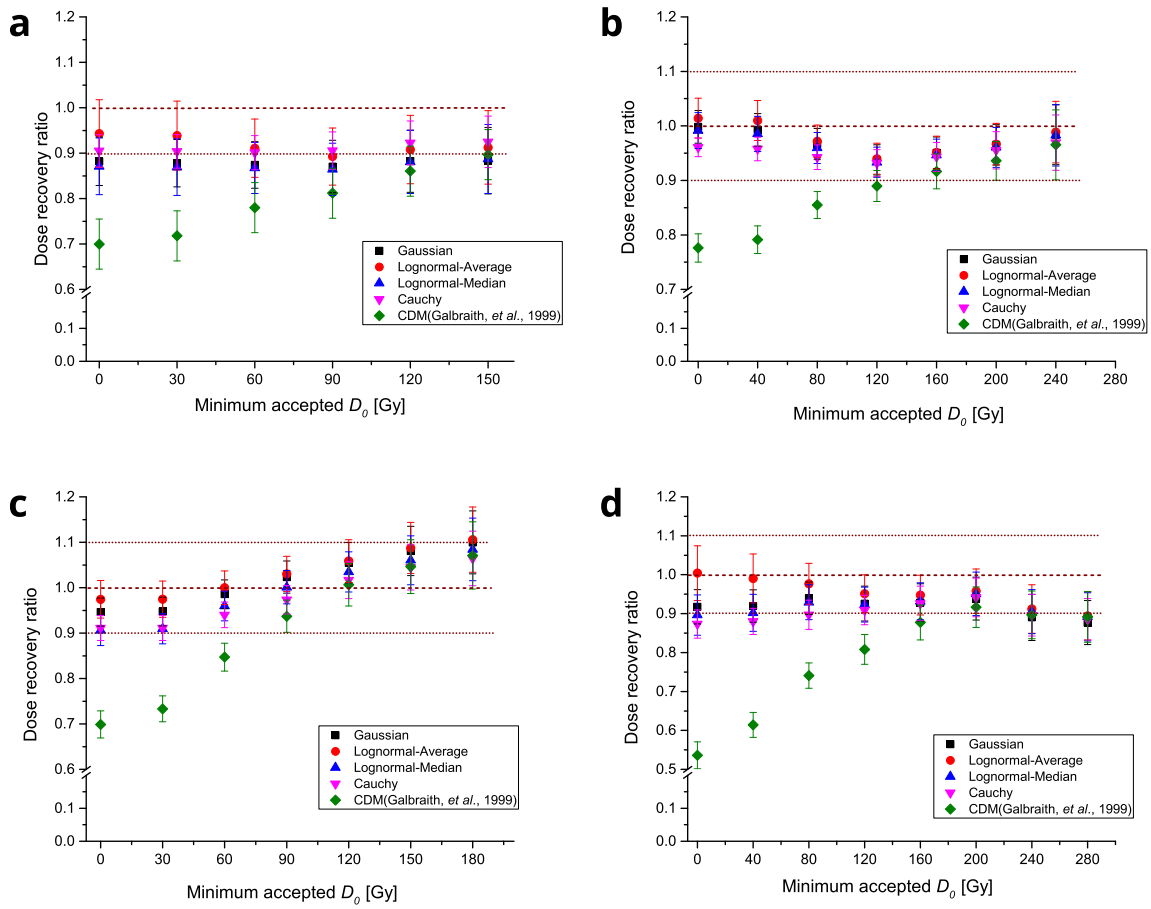


Figure 2.5: Comparison of dose recovery ratios obtained with all tested models as a function of minimum accepted $D_0$ value for calibration quartz (given doses: 150 Gy (a) and 200 Gy (b)) and the Covalejos quartz sample (given doses: 164 Gy (c) and 254 Gy (d)). (Note: for the sake of comparison with the CDM, for the Bayesian models each point indicates the middle of the 95 % credibility interval; the associated error bar corresponds to the length of this interval divided by 4)

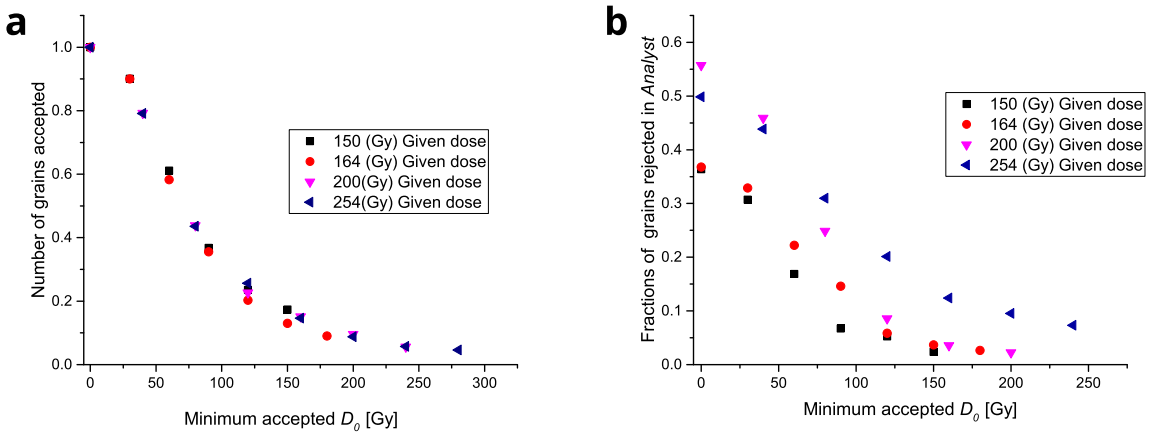


Figure 2.6: (a) Fraction of accepted grains based on the minimum accepted $D_0$ value for all dose recovery experiments, regardless of saturation issues. By increasing the $D_0$ value, a significant number of grains becomes rejected due to low $D_0$ values. (b) Fractions of grains rejected in *Analyst* due to saturation as a function of the minimum accepted $D_0$ (see Sec. 2.3.2 for details).

Figures 2.5a–d show the dose recovery ratios for each experiment based on the minimum accepted $D_0$ value. If the $D_0$ value of individual grains is not taken into consideration, for calibration quartz the dose recovery ratio obtained with the CDM is $0.70 \pm 0.06$ (150 Gy given dose) and $0.78 \pm 0.03$ (200 Gy), and for the Covalejos sample $0.70 \pm 0.03$ (164 Gy) and $0.54 \pm 0.03$ (254 Gy), respectively. In other words, this leads to 22–30 % underestimation of the given dose for the calibration quartz and to 30–45 % underestimation for grains from the Covalejos sample. By applying the $D_0$ criterion, the dose recovery ratios are steadily improving and getting closer to unity. However, for three out of four samples, even after applying the $D_0$ larger than given dose criterion, 10 % underestimation is observed. These improved ratios were obtained by rejecting a significant number of grains (83 %, 90 %, 91 % and 94 % of the total grain population, respectively for the 150 Gy, 164 Gy, 200 Gy and 254 Gy experiments; see Fig. 2.6a). On the other hand, almost all the ratios determined with the Bayesian models – no matter if the $D_0$ criterion was applied or not – are within 10 % of unity. Moreover, even by not taking into account the $D_0$ filter, the dose recovery ratios estimated by Bayesian models are indistinguishable from unity within errors (i.e. the 95 % credible intervals include 1). It should be noted here that the ADM does not apply to dose recovery experiments, since this model only applies to cases where the measured grains have absorbed different doses (if applied, it would give the same result as the CDM; provided the input OD value used to run the ADM is equal to the OD of the dose recovery distribution, i.e. the intrinsic OD).

## 2.4 Discussion

### 2.4.1 Dose variability

Dose distributions of single grains having been exposed to heterogeneous irradiation fields (e.g., K-feldspar $\beta$-dose hotspots) can be mimicked by artificial lognormal distributions. In such cases, the CDM (which has long been considered the model of choice for well-bleached samples unaffected by post-depositional mixing) converges towards the median of the distribution instead of the average, which in this experiment (and for dating purposes) is the value of interest. The discrepancy between median and average is becoming larger when the dispersion is increased. Thus, by increasing the dispersion the CDM and lognormal-median model show increasing dose underestimation. However, no matter which inference is used, the result of lognormal-median and CDM are in good agreement because both calculate the same quantity (here the median). At least 10 % of underestimation should be taken into consideration for a dispersion of 40 % (see Table 2.2 for the corresponding true dispersion and CDM overdispersion value) by applying these two models. Moreover, the Bayesian model using a Cauchy distribution follows the same trend as these two models, since it is attracted by the mode of the $D_e$ distribution, which is closer to the median than to the average. Although this Cauchy-based model is robust (as demonstrated by Combès et al. 2015), it is not accurate, which could explain the systematic age underestimation for the known-age samples reported by Guérin et al. (2015a). On the other hand, we showed that the ADM, as well as the lognormal-average and Gaussian Bayesian models converge towards the arithmetic average of the distribution, and thus provide accurate dose estimates.

### 2.4.2 OSL signal saturation

Dose-recovery tests on single grains of quartz were undertaken to check, which models best determine a high laboratory given dose. The results indicate that the CDM is not capable of estimating the true dose for grains close to saturation, unless early saturating grains are rejected using the $D_0$ filter suggested by Thomsen et al. (2016). Accepting only the grains with $D_0$ values larger than the given dose results in a dose recovery ratio close to one, but still ∼10 % below unity. One possible explanation for this small underestimation (assuming it is meaningful) even after $D_0$ filtering could be a bias in the $D_e$ estimates (as required for the application of the CDM) towards low doses. This underestimation is caused by the procedure to estimate individual $D_e$ values and associated uncertainties. In this procedure, described by Duller (2007), the natural luminescence signal ($\frac{L_n}{T_n}$) is projected onto the dose response curve to obtain the $D_e$ estimate. The uncertainty associated to this estimate is then derived from the length of the interval corresponding to the projection of ($\frac{L_n}{T_n} + \sigma_{L_n T_n}$) and ($\frac{L_n}{T_n} - \sigma_{L_n T_n}$), $\sigma_{L_n T_n}$ is the uncertainty on $\frac{L_n}{T_n}$, on the dose-response curve. When the dose-response curve is linear, this approach is not problematic; however, when it becomes non-linear the probability density of $D_e$ values becomes increasingly skewed – as can

be seen by using Monte Carlo simulations in *Analyst* (Duller et al., 2015) unfortunately, the CDM cannot accommodate such variable probability density functions). In addition, some grains are being rejected in the *Analyst* because $\frac{L_n}{T_n}$ or $(\frac{L_n}{T_n}+\sigma_{L_nT_n})$ does not intersect the dose-response curve (see Fig. S17 in Singh et al. 2017). For our dataset, the fractions of rejected grains in *Analyst* due to saturation as a function of the minimum accepted $D_0$ value are shown in Fig. 2.6b. About half of the grains are rejected if the $D_0$ criterion is not applied (especially for the two highest given dose experiments: 200 Gy and 254 Gy). By increasing the minimum accepted $D_0$ value, the fractions of rejected grains decrease dramatically. These fractions reach about zero when the minimum accepted $D_0$ value is set equal to the given dose.

Moreover, when applying the $D_0$ criterion, the dose recovery ratio is obtained by rejecting a significant number of grains, which implies a significant loss of information. In contrast, the Bayesian models implemented in 'BayLum' use Markov Chain Monte Carlo computations which do not require parameterisation of equivalent doses, and thus include all of the grains. As a result, the $D_0$ criterion appears to be no longer required and the central dose calculated with this approach is more coherent with the original dataset.

Although no significant difference is observed between the four Bayesian models, it seems that the lognormal-average model is better suited to determine the central dose compared to the other Bayesian models applied in our experiments (it seems to give the most accurate dose estimates). However, given the small number of experiments, it is difficult to be conclusive about the best Bayesian model to use when confronted with saturation issues. Moreover, the difference between the Bayesian models and the CDM for the dose recovery ratio with a given dose of 254 Gy is greater than for a given dose of 164 Gy. This observation is in agreement with the findings by Guérin et al. (2015a) (their Sec. 4.3 and their Fig. 6) on known-age samples. They mentioned that the higher the dose, the greater the difference becomes between the Bayesian model and CDM in terms of dose estimation. In particular, they showed that the accuracy of CDM-based OSL ages decreased with increasing age, whereas such a trend was not observed with their Cauchy-based Bayesian model. Thus, our observations could explain why OSL ages calculated with Bayesian models are closer to the reference ages than those obtained with frequentist models when working with increasing palaeodose values (Guérin et al., 2015a). In the next two sections, we tried to explain our observations by investigating two different routes: (i) how do the models respond to low $D_0$ grains and (ii) how does the recycling ratio influences $D_0$ and thus the $D_0$ filter?

#### 2.4.2.1 Saturation, low $D_0$ values and tests of robustness

To investigate further the behaviour of the here tested models when approaching saturation, we decided to select the earliest saturating grains – in an approach completely opposite to that advocated by Thomsen et al. (2016), who suggested to reject low $D_0$ grains in an attempt to

correct for a bias in $D_e$ distributions (for an illustration, see e.g. Fig. S17 in Singh et al. 2017). While we implemented the latter approach in our Figs. 2.4–2.6, where the grains were filtered based on minimum accepted $D_0$, in this section the grains were filtered by maximum accepted $D_0$ values; low maximum $D_0$ values indicate that we only selected early saturating grains.

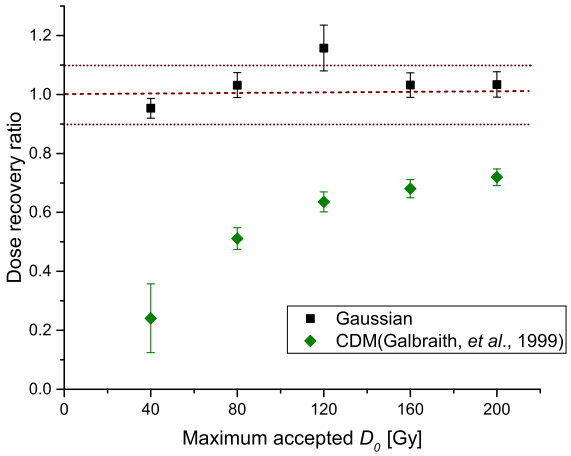


Figure 2.7: Dose recovery ratios obtained with the Bayesian Gaussian model and the CDM as a function of the maximum accepted $D_0$ value for the calibration quartz, 200 Gy dose-recovery experiment.

Figure 2.7 displays the dose recovery ratio values determined with the Gaussian Bayesian model and the CDM for the 200 Gy, calibration quartz, dose recovery experiment (corresponding to Fig. 2.5b discussed above) when selecting early saturating grains. Most of the grains are close or in saturation when the maximum accepted $D_0$ value is 40 Gy. In total, 192 grains have $D_0$ value smaller than 40 Gy; only for 13 of those does *Analyst* give finite estimates for the $D_e$ and associated uncertainty. Based on these 13 grains, the CDM-based dose-recovery ratio is $0.24 \pm 0.06$. Conversely, the 95 % credible interval obtained with the Bayesian Gaussian model is of [184; 197] Gy, which is very close to 200 Gy (and the Bayes estimate of the central dose gives a measured to given dose ratio equal to 0.95). This result obtained using the Bayesian model is rather counter-intuitive. It is in particular striking to see that even when selecting only grains whose $D_0$ value is at least five times lower than the given dose, the dose recovery ratio estimated using the Bayesian Gaussian model is within 5 % of unity. For higher maximum allowed $D_0$ values, the dose recovery ratios determined with the Bayesian model are almost constant and consistent with unity. On the contrary, with the CDM the dose recovery ratios are improving, but still lead to 28 % underestimation for a maximum $D_0$ of ca 200 Gy. One potential reason for the success of the Bayesian models in 'BayLum' to determine an accurate dose recovery ratio for early saturating grains may be due to the non-parameterised probability

density distribution for the parameters of the dose response curve for each grain: whereas Analyst characterises this curve by one unique $D_0$ value, the MCMC implemented in 'BayLum' allows a range of $D_0$ value depending on OSL measurement uncertainties. Figures S9 and S10 in Combès et al. (2015) illustrate the non-parameterised probability density distributions for two grains and the resulting non-parameterised $D_e$ distributions. Although the probability of $L_n/T_n$ intersecting the dose-response curve for 'saturated' grains (saturated in the sense of classical analysis with the *Analyst* software) is low, the Bayesian models take this kind of grains into account. We assume that it is the inclusion of such grains, even although not very informative, which contributes to the significant gain in accuracy for our dose recovery experiments.

#### 2.4.2.2 The relationship between recycling ratio and $D_0$ value

For our data analysis, the recycling ratio was not used as a rejection criterion. However, if sensitivity changes are not correctly monitored by the SAR protocol, one could imagine a progressive increase (resp. decrease) in normalised OSL signals from one regeneration dose to the other. This might affect the estimation of $D_0$ for such grains displaying poor recycling ratios, so we investigated the influence of the recycling ratio on the outcome of two experiments: the 200 Gy and 254 Gy does recovery experiments (performed on the calibration and Covalejos quartz, respectively). Since the recycling ratio comes with an uncertainty estimate, we first investigated the nature of these errors; Fig. 2.9, b shows the relationship between recycling ratio and its associated uncertainty. The positive correlation indicates multiplicative error properties, as could be expected from first principles (see Galbraith and Roberts, 2012). As a result, the logged recycling ratios are expected to follow a Gaussian distribution, centred on $ln(1) = 0$, where 1 is the expected value for the recycling ratio. Thus, for each grain we calculated the standardised residual of the logged recycling ratio, i.e. the logged recycling ratio divided by its uncertainty (which we assume to be equal to the relative uncertainty on the recycling ratio – see Galbraith and Roberts 2012 for the mathematical justification of our approach).

First, we plotted the standardised residual recycling ratio as a function of $D_0$ (Fig. 2.9c,d); the scatter plots are symmetric and indicate no relationship between these two parameters. Furthermore, on these graphs we could isolate the grains showing a recycling ratio consistent with 1 at 2 standard errors, from those inconsistent with 1 at two standard errors (in practice these are the points for which the standardised residual falls outside the [-2; 2] interval). We decided to calculate the dose recovery ratio for the grains inside and outside of the [-2; 2] interval after $D_0$ filtering larger than the given dose. The ratio was not determined for 254 Gy experiment because there were only 3 grains outsideof the [-2; 2] interval after $D_0$ filtering ($D_0$ greater than 254 Gy). The determined dose recovery ratio for the 200 Gy experiment is $0.93 \pm 0.02$ for 'good-recycling' grains, and $0.98 \pm 0.09$ for 'bad recycling grains'. The obtained results for the 200 Gy dataset are in agreement with each other and we conclude in our experiments that the recycling ratio is not

a valid selection criterion; furthermore, there is no essential relationship between recycling ratio and $D_0$ value.

## 2.5 Conclusion

We presented controlled laboratory experiments to compare frequentist models (CDM, ADM) with Bayesian models (Cauchy, Gaussian, Lognormal-Average and Lognormal-Median; for an application to the dating of an archaeological site, the reader is referred to the case study presented by Lahaye et al. 2019). Two experiments were designed: (1) dose recovery on quartz grains in or close to dose saturation and (2) determination of the central dose of quartz grains having absorbed different $\beta$-doses (dose variability experiment). For our measurements, two samples, namely a calibration quartz and a natural quartz sample, were used. We conclude the following:

1. The CDM is not well-suited to recover high given doses (here: 150–255 Gy) if no $D_0$ filter is used, it leads to systematic underestimation of the given dose. The dose recovery ratio is improved by applying $D_0$ filters at the cost of a decreased grain population.

2. By contrast, all Bayesian models show satisfying dose recovery ratios within 10 % of unity, even without applying a $D_0$ filter. In practice, it means that the dating range of single-grain OSL might be significantly expanded by the use of these models, since the need for a large number of great $D_0$ grains is much less pronounced when using the models implemented in the 'BayLum' package.

3. The CDM, as well as the Bayesian lognormal-median and Cauchy models, result in an underestimation of the average dose when grains have absorbed variable doses. The ADM, as well as the Bayesian lognormal-average and Gaussian models are able to satisfactorily estimate the average dose of a lognormal distribution.

As a result, our laboratory-controlled experiments indicate that the Gaussian and lognormal-average Bayesian models implemented in the R 'BayLum' package are the most accurate models for palaeodose estimation in cases of saturation and dose variability issues; in such conditions, if a $D_0$ filter is applied, the ADM also provides accurate estimates.

## Acknowledgements

We are thankful to one anonymous reviewer and Geoff Duller for constructive comments and suggestions. The authors are grateful for the financial supports of Région Aquitaine (in particular through the CHROQUI programme). MH is financed by a programme supported by the ANR

n° ANR-10-LABX-52. Sebastian Kreutzer helped with the data analysis in R and running the 'BayLum' models. Christoph Schmidt and Sebastian Kreutzer are thanked for their comments on an earlier version of this manuscript.

## 2.6 Supplement

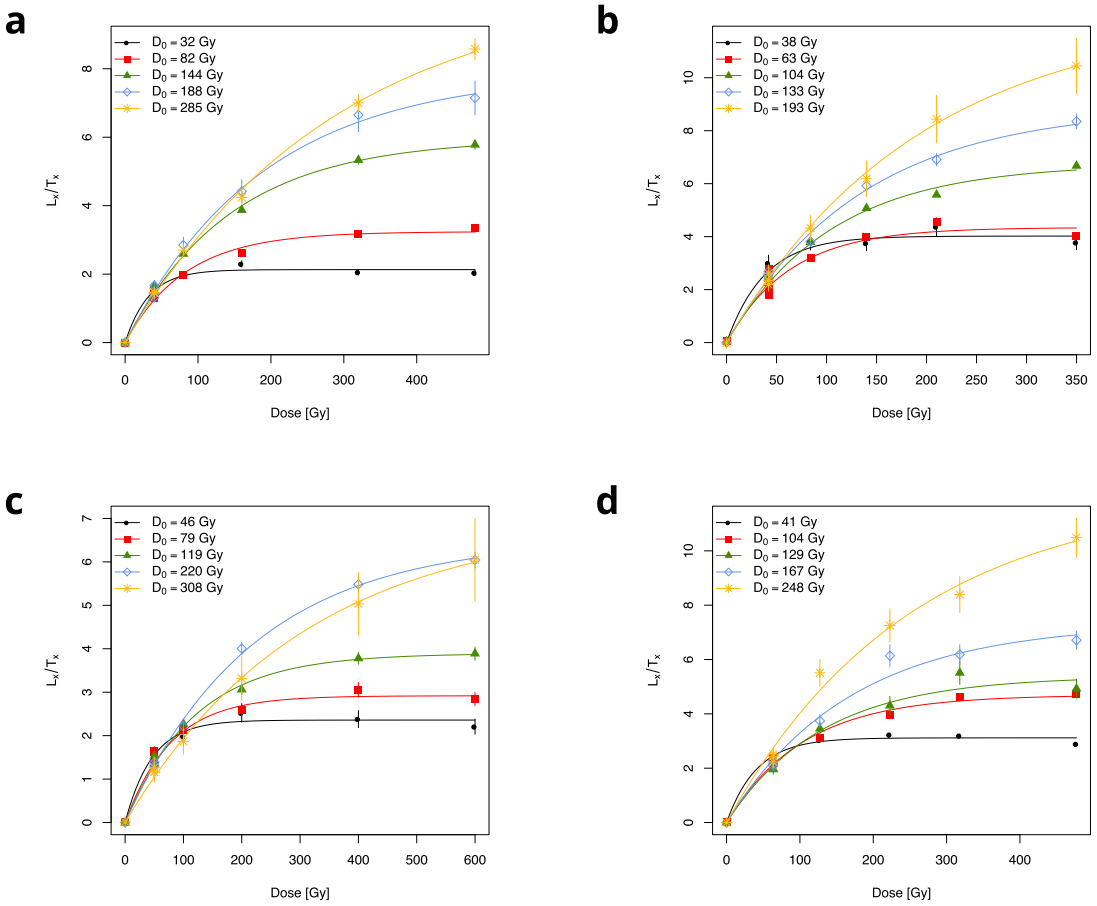


Figure 2.8: Typical dose response curves for dose recovery experiments (given dose (a) 150 Gy, (b) 164 Gy, (c) 200 Gy, (d) 254 Gy) with a range of $D_0$ values.

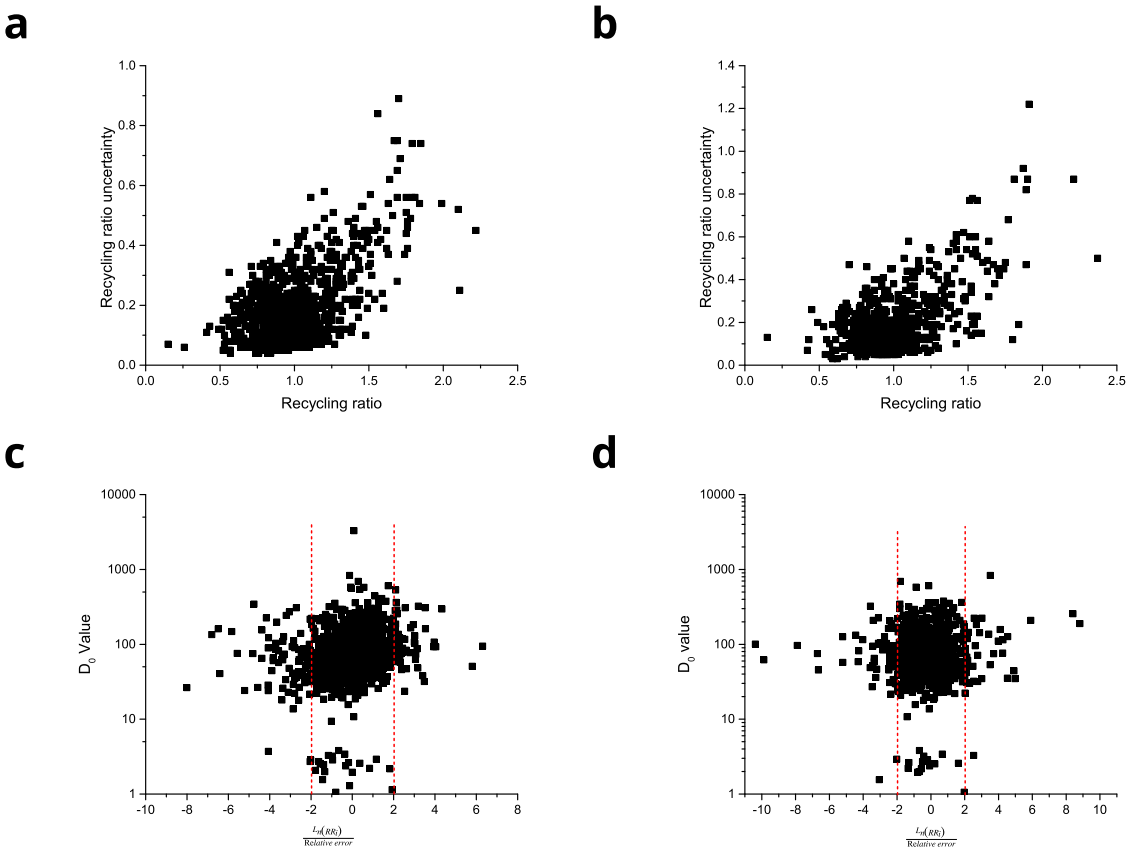


Figure 2.9: The relationship between recycling ratio and analytical uncertainty for (a) 200 Gy and (b) 254 Gy given dose. The trends indicate multiplicative errors. Subfigures (c) and (d) show the log-standardized recycling ratio against the individual $D_0$ values for a given dose of (c) 200 Gy and (D) 254 Gy. No relationship between recycling ratio and $D_0$ is observed. Red dashed vertical lines (c, d), indicate the 2-$\sigma$ range of the standardised recycling ratio. A number of points with very low $D_0$ values corresponds to grains for which the fitting was not satisfactory using the *Analyst* software

Table 2.1: Probability density function (PDF) calculated for each variable dose in the lognormal distribution using a dispersion of 60 %. The number of grains to be sampled based on the PDF are listed in the 3$^{rd}$ column.

| **Given dose** [Gy] | **Proba. LogN** | **Nb grains** |
|---|---|---|
| 1 | 0.000 | 0 |
| 2 | 0.009 | 1 |
| 3 | 0.030 | 4 |
| 4 | 0.052 | 8 |
| 5 | 0.068 | 11 |
| 6 | 0.077 | 12 |
| 7 | 0.080 | 13 |
| 8 | 0.078 | 12 |
| 9 | 0.073 | 11 |
| 10 | 0.066 | 10 |
| 11 | 0.060 | 9 |
| 12 | 0.053 | 8 |
| 13 | 0.046 | 7 |
| 14 | 0.041 | 6 |
| 15 | 0.035 | 5 |
| 16 | 0.031 | 4 |
| 17 | 0.026 | 4 |
| 18 | 0.023 | 3 |
| 19 | 0.020 | 3 |
| 20 | 0.017 | 2 |
| 21 | 0.015 | 2 |
| 22 | 0.013 | 2 |
| 23 | 0.011 | 1 |
| 24 | 0.010 | 1 |
| 25 | 0.008 | 1 |
| 26 | 0.007 | 1 |
| 27 | 0.006 | 1 |
| 28 | 0.005 | 0 |
| 29 | 0.005 | 0 |
| 30 | 0.004 | 0 |
| 31 | 0.004 | 0 |
| 32 | 0.003 | 0 |
| 33 | 0.003 | 0 |
| 34 | 0.002 | 0 |

Table 2.2: Characteristics of the lognormal distributions used in the dose variability experiments. 'Input $\sigma$ (%)' corresponds to the dispersion parameter that was used to generate the probability density functions for the lognormal distributions. 'Number of grains' is the total number of grains used for statistical analysis. 'True' $\sigma$ (%) corresponds to the actual dispersion in the lognormal distribution: because we work with integer numbers of grains, the probability density functions are truncated, and the true dispersion parameter is smaller than the input dispersion parameter. 'CDM OD' (%) is the overdispersion estimated with the CDM; and 'Extrinsic OD' (%) is the quadratic difference between the CDM overdispersion and the average intrinsic overdispersion.

| Input $\sigma$ (%) | Number of grains | 'True' $\sigma$ (%) | CDM OD (%) | Extrinsic OD (%) |
|---|---|---|---|---|
| 10 | 48 | 10 | 11 | 10 |
| 20 | 95 | 19 | 21 | 20 |
| 30 | 137 | 27 | 29 | 29 |
| 40 | 156 | 37 | 38 | 38 |
| 50 | 139 | 44 | 45 | 45 |
| 60 | 142 | 53 | 52 | 52 |
| 70 | 142 | 60 | 59 | 59 |
| 80 | 162 | 68 | 67 | 67 |
| 90 | 163 | 76 | 74 | 74 |

## Study I: References


Bailiff, I. K., Lewis, S. G., Drinkall, H. C., and White, M. J.: Luminescence dating of sediments from a Palaeolithic site associated with a solution feature on the North Downs of Kent, UK, Quaternary Geochronology, 18, 135–148, 2013.

Bøtter-Jensen, L., Andersen, C. E., Duller, G. A. T., and Murray, A. S.: Developments in radiation, stimulation and oberservation facilities in luminescence measurements, Radiation Measurements, 37, 535–541, 2003.

Buck, C. E. and Millard, A. R.: Tools for Constructing Chronologies - Crossing Disciplinary Boundaries, vol. 177 of *Lecture Notes in Statistics*, Springer, 2004.

Burow, C.: `calc_CentralDose()`: Apply the central age model (CAM) after Galbraith et al. (1999) to a given $D_e$ distribution, in: Kreutzer, S., Burow, C., Dietze, M., Fuchs, M.C., Schmidt, C., Fischer, M., Friedrich, J., 2017. Luminescence: Comprehensive Luminescence Dating Data Analysis. R package version 0.7.5., vol. version: 1.3.2, Luminescence, URL `https://CRAN.R-project.org/package=Luminescence`, 2017.

Carlin, B. P. and Louis, T. A.: Bayes and Empirical Bayes Methods for Data Analysis , Chapman & Hall/CRC, 2nd edn., 2000.

Christophe, C., Philippe, A., and Kreutzer, S., G.: BayLum: Chronological Bayesian Models Integrating Optically Stimulated Luminescence and Radiocarbon Age Dating, URL `https://CRAN.R-project.org/package=BayLum`, r package version 0.1.1, 2017.

Combès, B. and Philippe, A.: Bayesian analysis of individual and systematic multiplicative errors for estimating ages with stratigraphic constraints in optically stimulated luminescence dating, Quaternary Geochronology, 39, 24–34, 2017.

Combès, B., Philippe, A., Lanos, P., Mercier, N., Tribolo, C., Guérin, G., Guibert, P., and Lahaye, C.: A Bayesian central equivalent dose model for optically stimulated luminescence dating, Quaternary Geochronology, 28, 62–70, 2015.

Cunningham, A. C., DeVries, D. J., and Schaart, D. R.: Experimental and computational simulation of beta-dose heterogeneity in sediment, Radiation Measurements, 47, 1060–1067, 2012.

Duller, G. A. T.: Assessing the error on equivalent dose estimates derived from single aliquot regenerative dose measurements, Ancient TL, 25, 15–24, 2007.

Duller, G. A. T.: The Analyst software package for luminescence data: overview and recent improvements , Ancient TL, 33, 35–42, 2015.

Duller, G. A. T., Tooth, S., Barham, L., and Tsukamoto, S.: New investigations at Kalambo Falls, Zambia: Luminescence chronology, site formation, and archaeological significance, Journal of Human Evolution, 85, 111–125, 2015.

Galbraith, R. F.: A note on the variance of a background-corrected OSL count, Ancient TL, 20, 49–51, 2002.

Galbraith, R. F. and Roberts, R. G.: Statistical aspects of equivalent dose and error calculation and display in OSL dating: An overview and some recommendations, Quaternary Geochronology, 11, 1–27, 2012.

Galbraith, R. F., Roberts, R. G., Laslett, G. M., Yoshida, H., and Olley, J. M.: Optical dating of single and multiple grains of Quartz from Jinmium Rock Shelter, Northern Australia: Part I, Experimental design and statistical models, Archaeometry, 41, 339–364, 1999.

Gelman, A., Carlin, J. B., Stern, H. S., Dunson, D. B., Vehtari, A., and Rubin, D. B.: Bayesian Data Analysis, Third Edition, CRC Press, 2013.

González, J. S. and Barquín, R. M.: Nuevos datos para el conocimiento del Paleolítico Medio en el centro de la Regióon Cantábrica, in: Neandertales cantábricos, estado de la cuestión: actas de la reunión científica: celebrada en el Museo de Altamira los días 20-22 de octubre de 2004, edited by Corruchaga, J. A. L. and Barquín, R. M., pp. 489–504, Museo Nacional y Centro de Investigación de Altamira, 2005.

Guérin, G., Combès, B., Lahaye, C., Thomsen, K. J., Tribolo, C., Urbanova, P., Guibert, P., Mercier, N., and Valladas, H.: Testing the accuracy of a Bayesian central-dose model for single-grain OSL, using known-age samples, Radiation Measurements, 81, 62–70, 2015a.

Guérin, G., Frouin, M., Talamo, S., Aldeias, V., Bruxelles, L., Chiotti, L., Dibble, H. L., Goldberg, P., Hublin, J.-J., Jain, M., Lahaye, C., Madelaine, S., Maureille, B., McPherron, S. J. P., Mercier, N., Murray, A. S., Sandgathe, D., Steele, T. E., Thomsen, K. J., and Turq, A.: A multi-method luminescence dating of the Palaeolithic sequence of La Ferrassie based on new excavations adjacent to the La Ferrassie 1 and 2 skeletons, Journal of Archaeological Science, 58, 147–166, 2015b.

Guérin, G., Jain, M., Thomsen, K. J., Murray, A. S., and Mercier, N.: Modelling dose rate to single grains of quartz in well-sorted sand samples: The dispersion arising from the presence of potassium feldspars and implications for single grain OSL dating, Quaternary Geochronology, 27, 52–65, 2015c.

Guérin, G., Christophe, C., Philippe, A., Murray, A. S., Thomsen, K. J., Tribolo, C., Urbanova, P., Jain, M., Guibert, P., Mercier, N., Kreutzer, S., and Lahaye, C.: Absorbed dose, equivalent dose,

measured dose rates, and implications for OSL age estimates: Introducing the Average Dose Model, Quaternary Geochronology, 41, 1–32, 2017a.

Guérin, G., Frouin, M., Tuquoi, J., Thomsen, K. J., Goldberg, P., Aldeias, V., Lahaye, C., Mercier, N., Guibert, P., Jain, M., Sandgathe, D., McPherron, S. J. P., Turq, A., and Dibble, H. L.: The complementarity of luminescence dating methods illustrated on the Mousterian sequence of the Roc de Marsal: A series of reindeer-dominated, Quina Mousterian layers dated to MIS 3, Quaternary International, 433, 102–115, 2017b.

Hansen, V., Murray, A., Buylaert, J.-P., Yeo, E.-Y., and Thomsen, K.: A new irradiated quartz for beta source calibration, Radiation Measurements, 81, 123–127, 2015.

Huntriss, A.: A Bayesian analysis of luminescence dating , Ph.D. thesis, University of Durham, URL `http://etheses.dur.ac.uk/2928/1/2928_759.pdf?UkUDh:CyT`, 2008.

Kreutzer, S., Schmidt, C., Fuchs, M. C., Dietze, M., Fischer, M., and Fuchs, M.: Introducing an R package for luminescence dating analysis, Ancient TL, 30, 1–8, 2012.

Kreutzer, S., Burow, C., Dietze, M., Fuchs, M. C., Schmidt, C., Fischer, M., and Friedrich, J.: Luminescence: Comprehensive Luminescence Dating Data Analysis, URL `https://CRAN.R-project.org/package=Luminescence`, r package version 0.7.5, 2017.

Lahaye, C., Guérin, G., Gluchy, M., Hatté, C., Fontugne, M., Clemente-Conte, I., Santos, J. C., Villagran, X. S., Da Costa, A., Borges, C., Guidon, N., and Boëda, E.: Another site, same old song: The Pleistocene-Holocene archaeological sequence of Toca da Janela da Barra do Antonião-North, Piauí, Brazil, Quaternary Geochronology, 49, 223–229, 2019.

Mayya, Y. S., Morthekai, P., Murari, M. K., and Singhvi, A. K.: Towards quantifying beta microdosimetric effects in single-grain quartz dose distribution, Radiation Measurements, 41, 1032–1039, 2006.

Murray, A. S. and Wintle, A. G.: Luminescence dating of quartz using an improved single-aliquot regenerative-dose protocol, Radiation Measurements, 32, 57–73, 2000.

Murray, A. S. and Wintle, A. G.: The single aliquot regenerative dose protocol: potential for improvements in reliability, Radiation Measurements, 37, 377–381, 2003.

Philippe, A., Guérin, G., and Kreutzer, S.: BayLum - An R package for Bayesian analysis of OSL ages: An introduction, Quaternary Geochronology, 49, 16–24, 2019.

R Core Team: R: A Language and Environment for Statistical Computing, Vienna, Austria, URL `https://r-project.org`, 2017.

Rhodes, E. J., Bronk Ramsey, C., Outram, Z., Batt, C., Willis, L., Dockrill, S., and Bond, J.: Bayesian methods applied to the interpretation of multiple OSL dates: high precision sediment ages from Old Scatness Broch excavations, Shetland Isles, Quaternary Science Reviews, 22, 1231–1244, 2003.

Singh, A., Thomsen, K. J., Sinha, R., Buylaert, J.-P., Carter, A., Mark, D. F., Mason, P. J., Densmore, A. L., Murray, A. S., Jain, M., Paul, D., and Gupta, S.: Counter-intuitive influence of Himalayan river morphodynamics on Indus Civilisation urban settlements, Nature Communications, pp. 1–14, 2017.

Thomsen, K. J., Murray, A. S., and Bøtter-Jensen, L.: Sources of variability in OSL dose measurements using single grains of quartz, Radiation Measurements, 39, 47–61, 2005.

Thomsen, K. J., Murray, A. S., Buylaert, J. P., Jain, M., Hansen, J. H., and Aubry, T.: Testing single-grain quartz OSL methods using sediment samples with independent age control from the Bordes-Fitte rockshelter (Roches d'Abilly site, Central France), Quaternary Geochronology, 31, 77–96, 2016.

Zink, A. J. C.: Bayesian analysis of luminescence measurements, Radiation Measurements, 81, 71–77, 2015.

# 3 Study II

Quaternary Geochronology 59 (2020) 101082

Contents lists available at ScienceDirect

Quaternary Geochronology

journal homepage: http://www.elsevier.com/locate/quageo

# Do Bayesian methods lead to more precise chronologies? 'BayLum' and a first OSL-based chronology for the Palaeolithic open-air site of Mirak (Iran)

Maryam Heydari [a,*], Guillaume Guérin [a], Sebastian Kreutzer [a,b], Guillaume Jamet [c], Mohammad Akhavan Kharazian [d,e], Milad Hashemi [d], Hamed Vahdati Nasab [d], Gilles Berillon [e]

[a] IRAMAT-CRP2A, UMR 5060, CNRS-Université Bordeaux Montaigne, Maison de l'Archéologie, 33607, Pessac Cedex, France
[b] Geography & Earth Sciences, Aberystwyth University, Aberystwyth, United Kingdom
[c] GéoArchÉon/UMR CNRS 8591, Laboratoire de Géographie Physique, 75016, Meudon, France
[d] Department of Archaeology, Tarbiat Modares University, Tehran, Iran
[e] UMR7194 MNHN–CNRS–UPVD/Département Homme et Environnement, Musée de l'Homme, Palais de Chaillot, 75016, Paris, France

*corresponding author: mariheyd@gmail.com

**Quaternary Geochronology**

Year: 2020, Volume: 59, Pages: 101082

- published -

https://doi.org/10.1016/j.quageo.2020.101082

## Abstract

Bayesian inference has been applied extensively to chronologies in archaeological science since it provides several advantages over the (classic) frequentist approach. One of the most important aspects of applying Bayesian methods is their capacity to consider the stratigraphic relationship between ages. In luminescence dating, a crucial motivation for applying Bayesian modelling is the ability to address the systematic shared uncertainty. The recently deployed R package 'BayLum' was developed to ameliorate luminescence-based chronologies by employing Bayesian modelling. Our contribution aims at estimating the impact of stratigraphic order and systematic shared uncertainty on the age results. In this paper, for the first time, we present a comprehensive luminescence-based chronology for the Middle- Upper Palaeolithic site of Mirak. This open-air site is located in the northern fringes of the Iranian central desert, which is considered to be one of the dispersal corridors for hominins (Neanderthal and modern human) living across western and central Asia. We compare chronologies derived by frequentist and Bayesian methods to discuss the effect of stratigraphic ordering and the correlation between samples due to systematic shared uncertainty. Our investigations indicate that applying the stratigraphic order, when age uncertainty overlap one another, plays a fundamental role in reducing the uncertainty. At the site Mirak the obtained Bayesian chronology considering the stratigraphic order for the layer containing predominately Upper Palaeolithic techno- complex results in 21–28 ka. The age of the intermediate layer is in the range of 26–33 ka, and the lower- most layer containing Middle Palaeolithic assemblage gives the age-range of 43–55 ka. These results indicate that Late Pleistocene humans have exploited the site during MIS 3–2. Furthermore, the chronology gives further evidence to the hypothesis that the Iranian central plateau served as a frequently used habitat and dispersal corridor for human groups populating western and central Asia.

## 3.1 Introduction

A reliable chronology is an indispensable component for studying Palaeolithic sites. Optically Stimulated Luminescence (OSL, Huntley et al. 1985) on sediments is an important chronological method applied in archaeological science (e.g., Roberts et al., 2015; Liritzis et al., 2013). The luminescence age is the product of several separate stages of computation, fusing a considerable amount of measurements and variables (e.g., Aitken, 1985; Zink, 2013). Each stage estimates parameters with their uncertainties, hence, making the statistical data analysis an integral part of such chronological studies. Generally, two schools of statistics, frequentist (classic) and Bayesian can be applied (e.g., Buck and Millard, 2004). Classic statistical inference 'prefers' reproducible experiments, where the probability of observing an unknown variable is determined after repeated runs under similar conditions (Carlin and Louis, 2000; Gelman et al., 2013). However, such an approach may not be the proper paradigm where *one-off* (non-repeatable) events are the study subjects or where the number of observations is small (Buck and Meson, 2015). Geochronology and archaeological science are the fields in which the classic inference does not always seem to be the most judicious approach to data analysis (Buck and Meson, 2015; Orton et al., 1998). This circumstance may be seen as one of the reasons why Bayesian inference has become prevalent. However, to date, classic statistical inference dominates the data treatment in luminescence dating, but Bayesian statistics has gained some attention (e.g., Rhodes et al., 2003; Huntriss, 2008; Zink, 2013, 2015; Combès et al., 2015; Mercier et al., 2016; Philippe et al., 2019). Applying Bayesian modelling potentially prevents information loss between analysis steps by deploying a model that runs simultaneously over all parameters of the measurements, leading to more consistent results, which better reflect original data (Combès et al., 2015). For instance, in the case of OSL dating, a single instrument may have been used for all measurements; consequently, the source of systematic uncertainty (e.g., the calibration of the radioactive source) is identical to all samples. In such a situation Bayesian inference should be used due to its capacity to address different kinds of uncertainty (Huntriss, 2008; Zink, 2015). Moreover, Bayesian modelling provides an option to include independent ages with higher precision, such as available from $^{14}$C dating, to reduce uncertainties and thus results in an improved overall age precision (Rhodes et al., 2003; Philippe et al., 2019). However, the advantages of applying Bayesian inference in dating applications are not solely restricted to the improvement of the precision, but it also allows considering preliminary information of the dating. The stratigraphic order is such a kind of pre-knowledge ('prior belief') which results in chronologies consistent with the stratigraphy. This allows to include data that belong to different parts of the site, given that their stratigraphic sequence is well known and unbiased, to provide a synthetic chronology (Buck and Millard, 2004).

The R (R Core Team, 2019) package 'BayLum', based on Combès et al. (2015); Combès and Philippe (2017) and implemented by Philippe et al. (2019) claims to play out the power of

Bayesian methods by employing hierarchical Bayesian models to analyse OSL signals and estimate palaeodoses. Heydari and Guérin (2018) showed in two laboratory-controlled experiments that the Bayesian models result in most accurate estimations of the palaeodose compared to conventional methods. Lahaye et al. (2019) reported the first application of it in a dating study. Beyond, a full-scale application of 'BayLum' in a large dating study under 'non-perfect' conditions is still uncharted territory raising the question of whether "these new Bayesian methods do lead to more precise chronologies" and it leads to the here presented threefold contribution:

1. First, we present a large set of luminescence dates using frequentist statistics for the open-air site of Mirak, which has been excavated by the Joint French-Iranian Palaeoanthropological Project (FIPP) between 2015 and 2017. The site is located 12 km in the south of the city Semnan in a belt-like region bordered by two natural barriers, the Alborz Mountains to the north and the Iranian central desert to the south (Rezvani, 1990; Rezvani and Vahdati Nasab, 2010; Nasab et al., 2013; Vahdati Nasab et al., 2019) (Fig. 3.1). First results of the multidisciplinary investigations indicate that humans occupied the area several times during Late Pleistocene (Vahdati Nasab et al., 2019). Hence, we provide the first comprehensive chronological framework for the palaeoenvironmental studies of this area, which has been unknown so far. A few preliminary luminescence dating results were already published using the frequentist approach (Vahdati Nasab et al., 2019).

2. We apply, for the first time, Bayesian models as implemented in 'BayLum' on combined stratigraphic sequences from the Palaeolithic open-air site of Mirak. We test different scenarios on the data set and discuss the application of Bayesian modelling as implemented in 'BayLum'. In particular, we test whether stratigraphic ordering and addressing the correlation between samples caused by systematic shared uncertainty results in a chronology, statistically indistinguishable from the 'conventional' frequentist approach ($H_0$) or indeed yields to a more precise chronology ($H_A$).

3. The first investigation clarified three main in situ archaeological layers in the site (Vahdati Nasab et al., 2019) in which the uppermost and the lowermost layers indicate characteristics associated to Upper and Middle Palaeolithic affinities. In addition, the intermediate assemblage indicated a mixed nature comprising characteristics of both Upper and Middle Palaeolithic lithic affinities. Hints in the intermediate deposit imply the existence of two separated sub-layers. Thus, here, using the determined chronological framework, we discuss whether these two sub-layers may address two distinct Palaeolithic assemblages or whether they both can be considered as one archaeological layer.

In summary, by combining dating application with methodological research, our study responds to the high demand for reliable chronologies, and the question of whether Bayesian

methods may be of advantage to tackle this task. Finally, we contribute to the understanding of the local Palaeolithic cultures by deciphering the environmental and occupation history of the northern edge of the Iranian central plateau.

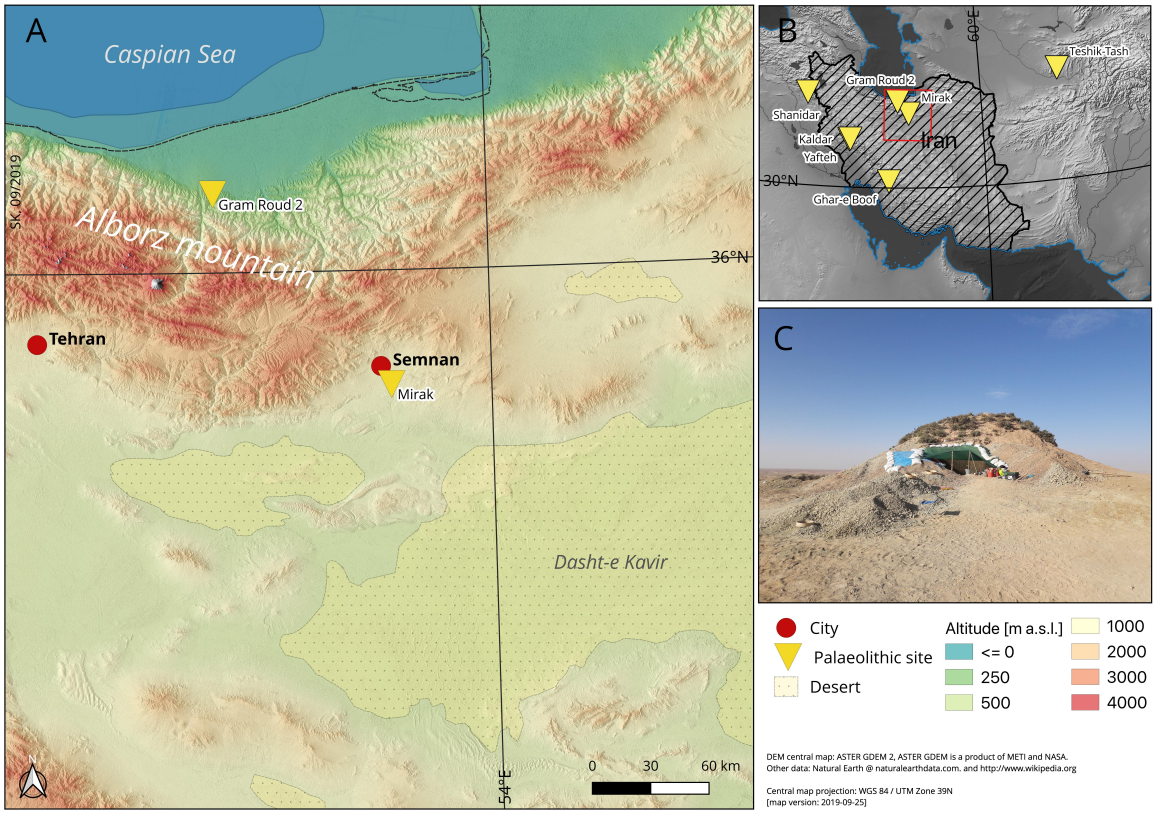


Figure 3.1: (A) Location of the open-air site Mirak between the Alborz Mountains to the north and the Iranian central desert to the south. (B) Location of the Palaeolithic sites mentioned in the text and the site of Mirak. (C) Mirak in the landscape. The red rectangle in (B) displays the enlarged area in (A).

## 3.2 Mirak open-air site in a prehistorical context

The Iranian plateau is essential for tracking the routes of human dispersal during the Late Pleistocene due to its particular location on a prehistoric intersection connecting Africa and Europe to central Asia. Discovered in the last century, human remains close to the borders of this plateau emphasize the notability of this region; for instance, the unique set of Neanderthal skeletons in Shanidar (Solecki, 1955; Trinkaus, 1983) in the Iraqi Kurdistan, as well as the skeleton of a Neanderthal child in Teshik Tash, south of Uzbekistan (Okladnikow, 1949). However, so far, Late Pleistocene human remains in Iran (Trinkaus and Biglari, 2006; Zanolli et al., 2019) are scarce.

On the contrary, considerable lithic assemblages associated to the Middle Palaeolithic (Zagros Mousterian; Dibble 1984) and Upper Palaeolithic (Zagros Aurignacian: Olszewski and Dibble 1994; Baradostian: Solecki 1958; Rostamian: Conard and Ghasidian 2011) are known to be concentrated in the Zagros foothills (mainly in caves and rock shelters) (e.g., Biglari, 2001; Otte et al., 2007; Shidrang et al., 2016; Bazgir et al., 2017; Heydari-Guran and Ghasidian, 2017). Beyond the Zagros foothills, several open-air sites in stratigraphic context have been recently discovered in the northern and western edges of the Iranian central plateau, as well as the central Alborz (e.g., see Berillon et al., 2007; Berillon and Asgari Khaneghah, 2016; Conard et al., 2009; Heydari-Guran et al., 2014; Vahdati Nasab and Hashemi, 2016; Nasab et al., 2013; Vahdati Nasab et al., 2019). Notwithstanding this abundant archaeological evidence, the debate suffers from a lack of chronological data for this area.

### 3.2.1 Geomorphological and stratigraphic setting

The Palaeolithic site of Mirak lies in a dissected plain (53°25'53" E; 35°28'10" N; ca 1,035 m a.s.l.), which extends from the southern part of the Alborz Mountains to the margin of the central desert (Dasht-e kavir) (Fig. 3.1). In this area, Holocene nebkhas (i.e. shadow dunes; mounds) are located in a Pleistocene alluvial pediment (see Jamet and Akhavan Kharazian in Berillon et al. 2017 and Kharazian Akhavan et al. 2018 for details; synthesis in Vahdati Nasab et al. 2019). Mound n. 8 was selected for excavation due to the high concentration of archaeological material findings both on the surface and also inside the debris of one illegal pit (henceforth named S2) dug by pot hunters on the mound in recent times. Our coring results as well as the stratigraphic record of the pit S2 led to opening of three main trenches in the northern, eastern and southern slopes of the mound (Berillon et al., 2017; Vahdati Nasab et al., 2019). Figs. 3.2 and 3.3 show the synthetic stratigraphy based on sedimentological observations. The upper part of the northern stratigraphy (ca 4 m) exhibits calcareous aeolian sands (units 0 to 3) due to Holocene windblown activity. The windblown deposits are reduced in the eastern stratigraphy (ca 1.5 m). The lower part of the synthetic stratigraphy exhibits an alluvial sequence composed of silty clay deposits (units 4, 6 & 8) with very fine intercalated sands (units 5 & 7). Considering the whole lithofacies, we identified at least three alluvial palaeosoils (marsh environment) separated by shallow-water deposits. No channel geometry was observed directly to explain sand bedding. However, the geomorphological position of mound no. 8 downstream of an alluviated pediment indicates an old anastomosed system dominated by rills and sheet washing processes.

#### 3.2.1.1 In situ archaeological assemblages

Three main trenches have been excavated in the northern, eastern and southern slopes of the mound no. 8 with excavation areas of 19 $m^2$, 12 $m^2$ and 5 $m^2$ respectively; as well as a 1/4 $m^2$

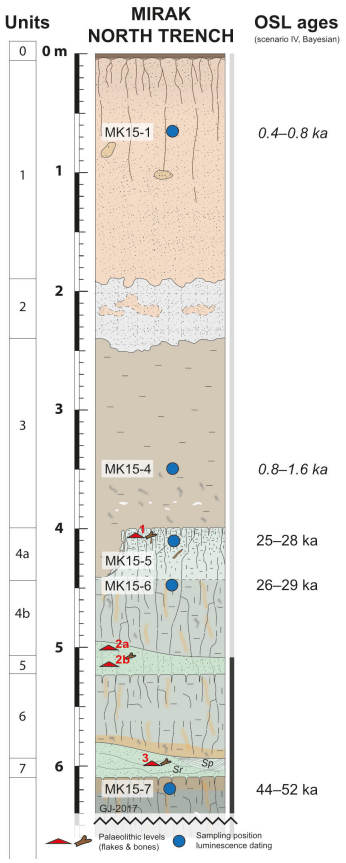


Figure 3.2: Synthetic stratigraphic record for the north trench in Mirak (the age of the samples Mk15-1 and Mk15-4 were calculated using the frequentist approach. Figure redrawn with modifications from Vahdati Nasab et al. (2019).

at the bottom of the pit S2 (Berillon et al., 2017; Vahdati Nasab et al., 2019) (see Fig. 3.9). The stratigraphic logs of the northern and eastern sections are shown in Figs. 3.2 and 3.3.

The archaeological assemblage in Mirak consists mostly of lithic artefacts, which are spread extensively over the surface and within the *in situ* deposits. Indeed, considerable numbers of in situ artefacts were recorded during the three seasons of excavations in Mirak (in total 2,709 pieces); they were mainly discovered in the three main areas of excavations (northern, southern and eastern trenches) as well as in the lowest part of the S2.

In the east trench where the main excavation was carried out, three distinct in situ assemblages have been identified and their vertical distributions are displayed in Fig. 3.3. Typo-technological investigations indicated that the lower assemblage (level 3) mainly corresponds to Middle Palaeolithic characteristics, while the intermediate assemblage (level 2) shows mixed characteristics of Upper and Middle Palaeolithic. However, this level is spread over a depth of 50 cm and may be divided into two sublevels. The upper assemblage (level 1) has evident Upper Palaeolithic

affinities although only represented by a few artefacts (see Vahdati Nasab et al., 2019, for details).

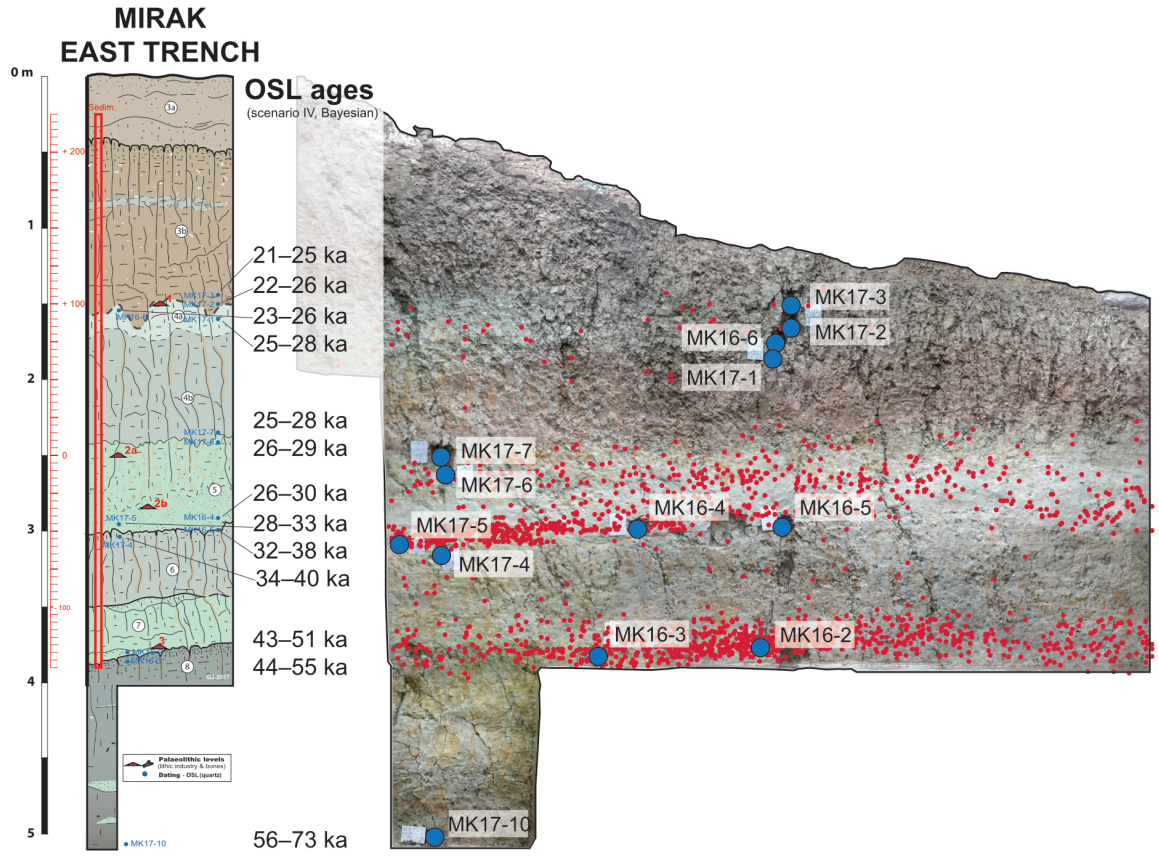


Figure 3.3: Synthetic stratigraphic record for the east trench, plus 2D dispersion of the coordinated archaeological findings and the location of luminescence samples in the east trench. Stratigraphic sketches by G. Jamet; 2D picture and projection by G. Berillon).

## 3.3 Material and methods

### 3.3.1 Sampling

The sediment sampling for Mirak was carried out during three field campaigns between 2015 and 2017. Each year, a series of sediment samples, in total 20, were extracted for OSL dating using opaque tubes hammered into the stratigraphic sections (Figs. 3.2 and 3.3).

In 2015, five sediment samples were taken from the north trench. The first two samples were recovered from the top of the mound, Mk15-1 from the vegetated surface (unit 1) and Mk15-4 downwards from the wind-blown deposits (unit 3) on the top of the Palaeolithic layers. Additionally, Mk15-5 was sampled from unit 4a containing the Upper Palaeolithic assemblage, while

Mk15-6 was taken from unit 4b. Mk15-7 originated from unit 8 beneath the Middle Palaeolithic level 3. An additional sample, Mk15-8, was extracted from pit S2 attributable to the sedimentological unit 6.

In 2016, five luminescence samples were taken from the eastern trench and one from the southern ditch. In the eastern trench, sampling started from unit 4a, which contains Upper Palaeolithic artefacts (Mk16-6). The next sample (Mk16-4) came from the bottom of unit 5, which includes an intermediate archaeological layer featuring artefacts with mixing characteristics attributable to both, the Upper and Middle Palaeolithic, periods. Mk16-5 originated from the archaeologically-sterile unit 6. Finally, two samples were extracted from the bottom of unit 7 (Mk16-2) and from top of unit 8 (Mk16-3) framing the layer which contains Middle Palaeolithic assemblage. Additionally, one sample was taken from corresponding geological unit 6 from the south trench (Mk16-1).

In 2017, a last series of samples were taken again from the east trench. The purpose of this sampling was not only to access the lowest unit of the mound, but also to detail the chronological study to obtain a better understanding of the Palaeolithic settlements. We took two samples from unit 3b (Mk17-2 and Mk17-3) from the top of Upper Palaeolithic archaeological layer and one sample from the bottom of the same layer in the geological unit 4a (Mk17-1). Then sample Mk17-7 was taken from the bottom of geological unit 4b. We continued by taking two samples from the top and bottom of the unit 5 containing intermediate assemblage (Mk17-6 and Mk17-5) and one sample from the very top of unit 6 (Mk17-4). Finally, the last sample (Mk17-10) was taken from the lowest excavated unit 8.

### 3.3.2 Sample preparation

The samples were prepared using routine procedures for luminescence dating (e.g., Preusser et al., 2008). Subdued orange (ca 589 nm, sodium vapour lamp) light conditions prevented unwanted loss of the luminescence signal during sample preparation. Wet sieving was carried out to extract grains between 80 $\mu$m and 140 $\mu$m, which is the dominant grain-size fraction according to grain size analyses. HCl (10 %) and $H_2O_2$ (30 %) were used to eliminate carbonates and organic materials, respectively. To separate quartz and feldspar grains, lithium heteropolytungstates (LST) heavy-liquid based density separation was applied (density 2.62 g cm$^{-3}$). The quartz fraction was treated with HF (40 %) for 40 min, not only to remove any probable feldspar contamination, but also to minimize the luminescence signal induced by $\alpha$ particles. To separate K-feldspar grains from the Na-feldspar grains we employed another separation with LST (2.58 g cm$^{-3}$). The K-feldspar grains were etched with HF (10 %) for 10 min to remove the outer part of the grains believed to be affected by $\alpha$-particles. The last samples were taken from the eastern trench (Mk17-1 to Mk17-10) for which we planned to carry out the measurements only on the quartz fraction. These sediments were not treated with LST, but were soaked in HF

(40 %) for 40 min to remove all feldspar grains and purify quartz. Finally, the grains were rinsed in HCl (15 %) overnight to remove Ca-fluorides and were sieved with the smaller-sized meshes to remove fragmented grains (e.g., Porat et al., 2015).

### 3.3.3 Instrumentation

Luminescence measurements were carried out on four luminescence readers: Two Freiberg Instruments *lexsyg SMART* TL/OSL systems (S1 and S2) (Richter et al., 2015) and two Freiberg Instruments *lexsyg research* readers (L1 and L2) (ca 15 % of the measurements) (Richter et al., 2013). The readers were equipped with a $^{90}Sr/^{90}Y$- source delivering ca 11 Gy min$^{-1}$ (S1) and ca 9 Gy min$^{-1}$ (S2) on the *SMART* systems, and 7 Gy min$^{-1}$ (L1) and 3 Gy min$^{-1}$ (L2) on *lexsyg research* system. Each system was calibrated for coarse-grain quartz on stainless steel cups using Risø calibration quartz batch 90 (Hansen et al., 2015). For measuring the equivalent dose of the quartz grains, we employed S1, S2 and L1 (we used green stimulation in S1 and S2 and blue stimulation in L1). S1 and S2 were equipped with ten green LEDs (525 $\Delta$ 20 nm, max. 70 mW cm$^{-2}$) and five infrared LEDs (850 $\Delta$ 3 nm, max. 300 mW cm$^{-2}$), set to 40 mW cm$^{-2}$ (green) and 100 mW cm$^{-2}$ (infrared) during continuous wave (CW) stimulation. OSL was detected through a UV filter set (Schott BG 3, 3 mm and Delta BP 365/50EX; green-OSL) in front of a Hamamatsu H7360-02 photomultiplier tube (PMT). L1 was equipped with five blue LEDs (458 $\Delta$ 3 nm, max. 100 mW cm$^{-2}$) and five infrared LEDs (850 $\Delta$ 3 nm, max. 300 mW cm$^{-2}$). It was set to 40 mW cm$^{-2}$ (blue) and 130 mW cm$^{-2}$ (infrared) during continuous wave (CW) stimulation. A UV-filter set (Schott BG 3, 3 mm and Delta BP 365/50 EX) was used for signal detection. For measuring the equivalent doses of K-feldspar, systems S2, L1 and L2 were employed. L1 and L2 were equipped with five infrared LEDs (850 $\Delta$ 3 nm, max. 300 mW cm$^{-2}$) set to 130 mW cm$^{-2}$ (infrared) during continuous wave (CW) stimulation. S2 was equipped with five infrared LEDs (850 $\Delta$ 3 nm, max. 300 mW cm$^{-2}$) set to 100 mW cm$^{-2}$ during continuous wave (CW) stimulation. Luminescence was detected through a blue-violet filter combination (Schott BG 39, 3 mm and AHF-BL HC 414/46 (S1), Schott BG 39, 3 mm and Chroma D410/30x (L1), Schott BG 39, 3 mm and AHF-ET 405/20) for L2 in front of a Hamamatsu H7360-02 photomultiplier tube (PMT). Several hundred grains, either quartz or feldspar, were mounted on stainless-steel cups using silicon oil and a mask of diameter 5 mm (medium size). We measured up to 15 aliquots per sample for the feldspar and up to 40 aliquots for the quartz fractions.

### 3.3.4 Dose rate determination

Energy is stored in minerals such as quartz and feldspar due to natural ionising radiation in terms of $\alpha$-, $\beta$-particles, and $\gamma$-photons as well as cosmic-rays (Aitken, 1985). In this study, the size of the grains lies between 80 $\mu$m and 140 $\mu$m. We assume that the outer rim of the grains, which was affected by $\alpha$-particles, was removed by the HF etching. Hence, the $\alpha$-dose rate contribution is

assumed negligible. Furthermore, the dose rate absorbed by the natural dosimeters (quartz and feldspar grains) consists of two parts: the internal dose rate due to the activity of radionuclides inside the dosimeters and the external dose rate induced by the activity of the radionuclides outside the natural dosimeters.

#### 3.3.4.1 Internal dose rate

The concentration of radionuclides inside the quartz grains is low in comparison to the environmental radionuclides concentrations. For our samples, we considered an internal dose rate of $0.06 \pm 0.03\,\mathrm{Gy\,ka^{-1}}$, following (Mejdahl, 1987). The internal dose-rate of K-feldspar grains was calculated based on a potassium content of $12.5 \pm 0.5\,\%$ (Huntley and Baril, 1997). The conversion factors after Guérin et al. (2011) were applied, and the self-dose fraction was taken from Guérin et al. (2012), which resulted in an internal dose rate of $0.39 \pm 0.06\,\mathrm{Gy\,ka^{-1}}$ for samples (Mk15-1 to MK15-8) and $0.42 \pm 0.04\,\mathrm{Gy\,ka^{-1}}$ for the rest of the samples (Mk16-1 to Mk16-6 as well as Mk17-1 to Mk17-10) due to the corresponding grain size of 80–140 $\mu$m and 100–140 $\mu$m, respectively.

#### 3.3.4.2 External dose rate

The main sources for external $\beta$ and $\gamma$-radiation are radionuclides decay of $^{40}$K, $^{232}$Th, and $^{238}$U series. High-resolution, low background $\gamma$-ray spectrometry was employed to measure the concentrations (Guibert and Schvoerer, 1991). Therefore, the sediment was first dried to measure the remaining water content. The water content estimated for each sample, ranging from $2 \pm 1\,\%$ to $19 \pm 8\,\%$, was used to correct the dose rate accordingly. The value for sample Mk16-2 was $5 \pm 3\,\%$; thus, it seems to be underestimated in comparison with other values obtained for the bottom of the east trench. Hence, for the final age calculation of this sample, we used an average water content of $10 \pm 5\,\%$ (Table 3.1). In general, the values of the water content for the samples from the top to the middle of the east trench (with the average of 3 %) were smaller than the values for samples from the top to the middle of the north trench (with an average of 8 %). The sediment thickness on the top of the samples from the north trench is much higher (more than 3 m from the surface) except for Mk15-1 (the uppermost sample) compared to the east trench (more than 1 m from the surface) (see Figs. 3.2 and 3.3). As a result, evaporation can be seen as a reason why water content values for samples from the east trench are smaller than corresponding samples from the north trench. Vegetation on the top of the mound in the north trench can be a reason why the water content for the uppermost sample Mk15-1 in north trench was larger (9 %) compared to the average of 6 %. The water content values increased from ca 3 %–6 % for samples Mk16-5 and Mk17-4 in the middle of the east trench and finally for the last sample (Mk17-10) at the bottom of the east trench, this value reached to 19 %. Furthermore, probably there is recent stream activity under the mound, which must exist close to the north

and east sections; however, there was no strict evidence of a stream except for the pit S2 (gravels and sands with crossbedding). Due to a low energy system (alluvial pediment), any channel is generally confined with short-term activity and very often altered.

To determine the radionuclides concentrations inside the sediment samples first they were dried. Then, following Martin (2015), and Tribolo et al. (2017), we considered that the true $\beta$-dose rate is mostly reflected in sediments with diameters $< 2$ mm and the one that is calculated from the fraction $< 1$ cm. This is because of the ca 2 mm stopping power range of $\beta$-particles in sediments and the self-absorption of coarser minerals. In our case, the fraction $> 2$ mm represented a negligible amount compared to the $< 2$ mm (grain-size analysis did not show grains larger than ca 500 $\mu$m). Therefore, its contribution can be neglected and this double, more complex calculation for the 2 mm to 1 cm fraction was actually not needed. Then the dried samples were crushed following sieving using a mesh size of 2 mm and packed into sealed plastic boxes to avoid the loss of radon. In the following, the crushed and sealed samples were stored over a minimum of four weeks to ensure a radioactive equilibrium between $^{226}$Rn and its daughter nuclides (e.g., Guibert and Schvoerer, 1991) before running the measurements. The concentrations of the radionuclides obtained by $\gamma$-ray spectrometry were converted to $\beta$-dose rates using the conversion factors by Guérin et al. (2011). The $\beta$-dose rates were then corrected for the intrinsic attenuation due to the grain size of the quartz and feldspar grains after Guérin et al. (2012). The effect of HF etching, as well as the effect of moisture on $\beta$-dose rates, were corrected after Nathan (2010) and Nathan and Mauz (2008), respectively. The concentration of the U, Th and K contents are shown in Table 3.1. The concentrations of K and Th for entire samples fall between 1.26 % and 2.32 % and 4.67 ppm to 12.45 ppm, respectively. Besides, the concentrations of U determined from the top of the chain range from 1.80 ppm to 3.28 ppm. The concentration derived from the bottom of the chain lies between 1.75 ppm and 9.42 ppm (this high U concentration belongs to sample Mk15-8 from the pit S2, if we exclude this value, then the highest value would be 4.30 ppm (from Mk17-4)). The disequilibrium in the U chain is discussed below. The external $\beta$-dose rates for entire sample range from 1.20 Gy ka$^{-1}$ to 2.10 Gy ka$^{-1}$. They contribute 55 % to 59 % to the total dose rate.

Table 3.1: Environmental dose rates with internal dose rates for the quartz grains of $0.06 \pm 0.03$ Gy Gy ka$^{-1}$ and $0.39 \pm 0.06$ Gy ka$^{-1}$ for K-feldspar grains (Mk15-1 to Mk15-8) and $0.42 \pm 0.04$ Gy ka$^{-1}$ for the rest of the samples (details see Sec. 3.3.4.1)

| **SAMPLE** | **K** | $\sigma$ | $\mathbf{U}_{pre-Ra}$ | $\sigma$ | $\mathbf{U}_{post-Ra}$ | $\sigma$ | **Th** | $\sigma$ | **W.** | $\sigma$ | $\dot{D}_{\beta}$ | $\sigma$ | $\dot{D}_{\gamma}$ | $\sigma$ | $\dot{D}_{cosm.}$ | $\sigma$ | $\dot{D}_{Q}$ | $\sigma$ | $\dot{D}_{FS}$ | $\sigma$ |
|---|---|---|---|---|---|---|---|---|---|---|---|---|---|---|---|---|---|---|---|---|
| | [ %] | | [ppm] | | [ppm] | | [ppm] | | [ %] | | [Gy ka$^{-1}$] | | [Gy ka$^{-1}$] | | [Gy ka$^{-1}$] | | [Gy ka$^{-1}$] | | [Gy ka$^{-1}$] | |
| Mk15-1 | 1.26 | 0.01 | 1.91 | 0.06 | 2.10 | 0.02 | 4.67 | 0.04 | 9 | 4 | 1.20 | 0.04 | 0.70 | 0.02 | 0.22 | 0.02 | 2.18 | 0.05 | 2.51 | 0.07 |
| Mk15-4 | 1.41 | 0.02 | 2.02 | 0.08 | 2.37 | 0.02 | 5.18 | 0.05 | 6 | 3 | 1.37 | 0.03 | 0.80 | 0.01 | 0.16 | 0.02 | 2.39 | 0.05 | 2.72 | 0.07 |
| Mk15-5 | 2.16 | 0.02 | 2.27 | 0.09 | 2.60 | 0.02 | 8.76 | 0.08 | 9 | 4 | 1.96 | 0.06 | 1.13 | 0.03 | 0.15 | 0.02 | 3.29 | 0.07 | 3.62 | 0.09 |
| Mk15-6 | 2.06 | 0.03 | 2.07 | 0.17 | 4.00 | 0.05 | 9.36 | 0.12 | 6 | 3 | 1.97 | 0.05 | 1.21 | 0.02 | 0.14 | 0.02 | 3.37 | 0.06 | 3.70 | 0.08 |
| Mk15-7 | 2.10 | 0.02 | 2.31 | 0.06 | 2.89 | 0.02 | 9.25 | 0.06 | 13 | 5 | 1.87 | 0.08 | 1.12 | 0.03 | 0.12 | 0.02 | 3.16 | 0.09 | 3.49 | 0.10 |
| Mk15-8 | 1.81 | 0.02 | 2.57 | 0.12 | 9.42 | 0.06 | 7.08 | 0.07 | 4 | 1 | 2.04 | 0.03 | 1.39 | 0.02 | 0.20 | 0.02 | 3.69 | 0.05 | 4.02 | 0.07 |
| Mk16-1 | 1.72 | 0.02 | 2.05 | 0.07 | 1.75 | 0.02 | 6.68 | 0.05 | 2 | 1 | 1.65 | 0.02 | 0.92 | 0.01 | 0.16 | 0.02 | 2.78 | 0.04 | 3.14 | 0.05 |
| Mk16-2 | 1.73 | 0.02 | 1.93 | 0.09 | 1.95 | 0.02 | 6.93 | 0.07 | 10 | 5 | 1.53 | 0.07 | 0.88 | 0.03 | 0.16 | 0.02 | 2.63 | 0.08 | 2.99 | 0.08 |
| Mk16-3 | 2.24 | 0.02 | 2.42 | 0.09 | 2.94 | 0.02 | 9.41 | 0.08 | 13 | 5 | 1.94 | 0.08 | 1.16 | 0.04 | 0.16 | 0.02 | 3.32 | 0.10 | 3.68 | 0.10 |
| Mk16-4 | 1.66 | 0.02 | 1.98 | 0.08 | 2.41 | 0.02 | 6.49 | 0.06 | 2 | 1 | 1.65 | 0.02 | 0.97 | 0.01 | 0.17 | 0.02 | 2.84 | 0.04 | 3.20 | 0.05 |
| Mk16-5 | 1.97 | 0.02 | 2.19 | 0.08 | 2.78 | 0.02 | 7.08 | 0.06 | 6 | 3 | 1.83 | 0.04 | 1.06 | 0.02 | 0.17 | 0.02 | 3.12 | 0.06 | 3.48 | 0.06 |
| Mk16-6 | 2.18 | 0.02 | 2.24 | 0.10 | 3.39 | 0.03 | 9.15 | 0.08 | 4 | 2 | 2.08 | 0.04 | 1.23 | 0.02 | 0.20 | 0.02 | 3.57 | 0.05 | 3.93 | 0.06 |
| Mk17-1 | 2.07 | 0.04 | 2.39 | 0.19 | 2.24 | 0.04 | 8.55 | 0.12 | 2 | 1 | 2.01 | 0.03 | 1.15 | 0.01 | 0.20 | 0.02 | 3.42 | 0.05 | | |
| Mk17-2 | 2.10 | 0.03 | 2.44 | 0.16 | 2.32 | 0.03 | 8.62 | 0.10 | 3 | 1 | 2.02 | 0.03 | 1.16 | 0.01 | 0.20 | 0.02 | 3.44 | 0.05 | | |
| Mk17-3 | 2.12 | 0.03 | 2.41 | 0.17 | 2.80 | 0.04 | 8.78 | 0.11 | 2 | 1 | 2.10 | 0.03 | 1.24 | 0.01 | 0.20 | 0.02 | 3.60 | 0.05 | | |
| Mk17-4 | 1.87 | 0.03 | 1.80 | 0.19 | 4.30 | 0.06 | 7.01 | 0.12 | 6 | 2 | 1.77 | 0.05 | 1.06 | 0.02 | 0.17 | 0.02 | 3.05 | 0.06 | | |
| Mk17-5 | 1.60 | 0.03 | 2.14 | 0.15 | 3.13 | 0.04 | 6.14 | 0.09 | 3 | 1 | 1.61 | 0.03 | 0.96 | 0.01 | 0.17 | 0.02 | 2.79 | 0.05 | | |
| Mk17-6 | 1.83 | 0.03 | 2.30 | 0.18 | 2.45 | 0.04 | 7.34 | 0.11 | 3 | 1 | 1.80 | 0.03 | 1.05 | 0.01 | 0.18 | 0.02 | 3.09 | 0.05 | | |
| Mk17-7 | 2.03 | 0.04 | 2.38 | 0.19 | 2.79 | 0.04 | 8.26 | 0.12 | 4 | 1 | 1.97 | 0.04 | 1.16 | 0.02 | 0.18 | 0.02 | 3.37 | 0.05 | | |
| Mk17-10 | 2.32 | 0.04 | 3.28 | 0.22 | 2.60 | 0.04 | 12.45 | 0.15 | 19 | 8 | 1.95 | 0.11 | 1.20 | 0.05 | 0.14 | 0.02 | 3.35 | 0.13 | | |

W. = Water content | Q = quartz | FS = feldspar

The $\gamma$-dose rate was calculated from K, Th and U concentrations using conversion factors by Guérin et al. (2011) and correction for water content after Guérin and Mercier (2012). The $\gamma$-dose rates fall between 0.70 Gy ka$^{-1}$ to 1.39 Gy ka$^{-1}$ and they contribute around 35 % of the total dose rate (Table 3.1).

Finally, the cosmic-dose rate was calculated using the `calc_CosmicDoseRate()` function available in the R (R Core Team, 2019) package 'Luminescence' (Kreutzer et al., 2012, 2019) applying the approach after Prescott and Stephan (1982) and Prescott and Hutton (1994). For calculating the total dose rate ($\dot{D}$), we used a self-written *MS Excel*$^{TM}$ sheet (results were compared against *DRAC*, Durcan et al. 2015). The final dose rates for quartz grains range from 2.18 Gy ka$^{-1}$ to 3.69 Gy ka$^{-1}$; correspondingly for K-feldspar grains it lies between 2.51 Gy ka$^{-1}$ to 4.02 Gy ka$^{-1}$ (Table 3.1).

#### 3.3.4.3 Radioactive disequilibria

Radioactive disequilibria in the decay chain of U can be problematic for dating since they may imply dose-rate changes, while the basic requirement of the age equation is dose rate stability. Substantial disequilibria can be caused, e.g., by leaching of U and Ra (due to the chemical mobility of the U and Ra) (Aitken, 1985), and the influx of $^{210}$Pb through ground and rainwater and loss of Rn (Guibert et al., 2009). The equivalent $^{238}$U content is estimated from three different parts of the decay chain, where a possibility for a disequilibrium exists: first, from the initial part of the chain, by calculating the value from $^{234}$Th, $^{234\mathrm{m}}$Pa and $^{234}$U emissions; second, immediately after $^{226}$Ra (by considering $^{214}$Pb and $^{214}$Bi) and finally after $^{210}$Pb. Fig. 3.4 shows the ratio of $^{238}$U concentrations from the top and the bottom of the U-series divided by $^{232}$Th, which is chemically immobile (Guibert et al., 2009). Explicitly, the equivalent $^{238}$U concentrations, which were derived from the bottom of the decay chain, were about 1.5–3.7 times larger in comparison with values estimated from the top for five samples (MK15-6, MK15-8, MK16-6, MK17-4, and MK17-5). These findings represent disequilibria in the U-series. Since Ra is soluble and chemically active, accumulation of Ra could be a reason for these disequilibria. We herein assume that these disequilibria developed gradually during burial time. As a result, the average of the effective $^{238}$U concentrations estimated from the top and the bottom (average uptake scenario) is considered instead of the preliminary effective $^{238}$U concentration from the bottom of the chain and applied to these samples. Applying the average-uptake scenario results in older ages (in comparison to a non-average scenario); the highest impacts are observed for samples Mk17-5 and Mk15-8 for which the ages increased by 7 % to 16 %. The ages of the rest of the samples increased between 3 % and 4 %.

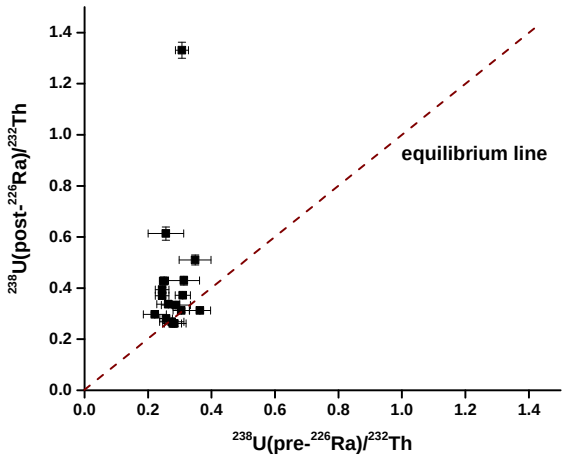


Figure 3.4: Evaluation of the disequilibrium in the decay chain of $^{238}$U. The ratio of $^{238}$U (post-$^{226}$Ra)/$^{232}$Th and $^{238}$U (pre-$^{226}$Ra)/$^{232}$Th is shown for all the samples. The ratios for most of the samples are close to the equilibrium line except MK15–6, MK15–8, MK16–6, MK17-4, and MK17-5.

### 3.3.5 Luminescence signal measurements

#### 3.3.5.1 Quartz UV signal

We applied the single aliquot regenerative (SAR) dose protocol (Murray and Wintle, 2000) to determine the equivalent dose ($D_e$). The protocol parameters for the Mirak samples were obtained from conventional tests such as examining the presence of a fast decaying signal component, preheat plateau and dose-recovery tests Wintle and Murray (2006). OSL signal measurements were started with samples MK15-1 and Mk15-4. However, these two samples were attributed to a Holocene period with their $D_e$s varying around 1 Gy–3 Gy, respectively. Due to the low luminescence signal intensity of these two samples, blue-OSL was preferred to improve the signal to noise ratio, and these settings were also used for the rest of the samples taken in 2015 (MK15-5, MK15-6, MK15-7 and MK15-8). Meanwhile, we carried out further luminescence tests (see Sec. 3.3.5.2 and Sec. 3.7.3), which indicated a possible, but unwanted, medium component contribution to the OSL signal. This led us to perform all subsequent measurements with green stimulated luminescence (GSL). A few GSL measurements were also repeated for samples MK15–5, MK15–6, MK15–7 and MK15-8 and the final equivalent dose is the average of blue and green stimulation (see below for a discussion). For blue-OSL we used initial channels 1–4 (0.64 s) for the signal and subtracted early background using channels 5–15 (1.6 s).

#### 3.3.5.2 Testing the fast component

Quartz OSL signals usually consist of several first-order kinetic exponential components, which are linked to specific electron traps (e.g., McKeever, 1991; Chen et al., 1991; Bailey, 2001). The so-called fast component has the advantage of being easily bleachable in natural environments and is believed to be suitable for the SAR protocol. Therefore, the first step was to test whether our samples show a dominant fast component. We first compared the Mirak OSL signal with a signal from 'calibration quartz', which is known to be dominated by a fast component (Fig. 3.10). Besides, we used linearly modulated OSL (LM-OSL) (Bulur, 1996) to deconvolve individual signal components. The LM-OSL results and details of our investigation are shown in the supplementary material (Figs. 3.11 and 3.12). The results indicated that the Mirak samples contain a medium component in addition to the fast and several slow components. However, the medium component may exhibit unwanted luminescence characteristics (Wintle and Murray, 2006; Bailey, 2010); thus, it should be separated from the OSL signal. Singarayer and Bailey (2004) showed that the photoionization cross-sections of the fast and medium components depend on the wavelength. The ratio of $\sigma_{fast}/\sigma_{medium}$ decreases significantly by reducing the stimulation wavelength from 590 nm to 375 nm. Therefore, we decided to stimulate our samples with green light (525 nm) instead of blue light (470 nm) to increase the above-mentioned ratio. Increasing the ratio results in detecting more photons from the fast component in the first channels of the shine-down curve in comparison to the medium component. Hence, we can substantially reduce potential medium component contamination and in- crease the probability of detecting more photons from the fast component. The OSL signal was measured at 125 °C for 40 s following a preheat at 260 °C for 10 s. The test dose was measured following a cut-heat at 220 °C.

Additionally, for 30 aliquots of one sample (Mk17-6), we tested the dependence of the $D_e$ on the signal integration times (Fig. 3.13), to determine whether our choice for the signal integral may have biased the final $D_e$. Figure 3.13 illustrates that an appropriate channel integration (believed to be represented by a plateau) varies from one sample to another. Therefore, we determined the individual $D_e$ values for each aliquot using the best channel integral, which lies in the plateau. Then, we calculated the average of all individual $D_e$s, which were determined using various channel integrations. We compared this obtained average with the average of all individual $D_e$ determined using only 1–45 channel. This comparison shows that, although the individual $D_e$ may vary with channel integral, the overall averages (when various channel integrations were used compared to when only 1–45 channel was applied to aliquots) are indistinguishable within 1 % of unity. This finding justified our applied signal channel range for GSL of 1–45 (7.2 s) with the background 280–399 (19.2 s).

#### 3.3.5.3 SAR protocol parameters

The SAR protocol was applied to determine the $D_e$ for multi-grain aliquots of quartz. Five regenerative points, approximately 31 Gy, 61 Gy, 122 Gy, 245 Gy and 490 Gy, were used to construct the dose-response curves. The test dose was set to 31 Gy. The recuperation ratio after delivering a zero dose was always below 5 %. The first regenerative dose after the recuperation test was used to check the efficiency of correction for sensitivity change (recycling ratio). The recycling ratio was not taken into account as a rejection criterion following Guérin et al. (2015) and Heydari and Guérin (2018), however, they were almost within $2\sigma$. Moreover, we calculated the average of the recycling ratio for each sample; the minimum and the maximum were $0.85 \pm 0.07$ and $1.02 \pm 0.12$, respectively. The possibility of a contamination with feldspar was examined by applying the IR depletion ratio test Duller (2003). This ratio was within 10 % of unity for all samples. Therefore, we found no significant evidence for a feldspar contamination of our quartz samples. Typical TL curves, GSL shine-down curves, and corresponding dose-response curves are shown for sample Mk17-1 as an example in Fig. 3.14.

The preheat temperature was varied in order to check the independency of the $D_e$ from this parameter (preheat plateau test). The result of a typical preheat plateau for one sample (Mk16-1) is shown in Fig. 3.14a. Each point represents the average $D_e$s of six aliquots for the temperature ranges from 220 °C to 280 °C (20 °C steps). We selected 260 °C as the preheat temperature for the SAR protocol since it was located in the middle of the plateau.

Additionally, we performed a dose-recovery test on six aliquots of sample Mk15-5 (Fig. 3.13b). The aliquots were bleached for 100 s with a blue light at room temperature in the reader to empty the natural luminescence signal. This was followed by a 10,000 s pause that allows the decay of the 110 °C peak (Wintle and Murray, 2006). The samples were then bleached for a second time to deplete charges in the fast component related trap, potentially transferred from the shallow 110 °C trap during the pause. Finally, samples received a $\beta$-dose of 111 Gy (close to the expected equivalent doses), and the SAR protocol was applied. The mean recovered dose based on the measurement of six aliquots was $100 \pm 5$ Gy. The dose-recovery ratio was $0.90 \pm 0.04$, which was consistent with the set 10 % offset from unity acceptance criteria and therefore validated the chosen SAR protocol parameters. We assumed similar behaviour for the rest of the samples; thus, we applied the SAR protocol with the same parameters to all samples.

For the conventional data analysis, we employed the software *Analyst* (Duller, 2015, v.453) for determining the $D_e$. An exponential plus linear function was used for the dose-response curve fitting. Selection criteria for the aliquot were based only on the relative uncertainty of the first (natural) test signal, fixed to $< 20$ %, following Guérin et al. (2015). We calculated the arithmetic mean to determine the palaeodose and the standard error of the mean for representing the uncertainty on each $D_e$ (Table 3.2). Except for $D_e$s of samples M15-1 and Mk15-4 that are less than 3 Gy, the determined palaeodoses for the rest of the samples lay between 76 Gy and

216 Gy (Table 3.2).

For the feldspar samples, the $pIRIR_{290}$ protocol (Thomsen et al. 2008; protocol settings after Buylaert et al. 2012) was applied to five samples from the east trench, one sample from the south trench, as well as five samples from the north trench and one sample from the pit S2. Typical TL curves, infrared light stimulated shine-down curves, and corresponding dose-response curve from the $pIRIR_{290}$ signal are shown for sample Mk16-4 as an example in Fig. 3.16. Following quartz data treatments, herein the $D_e$s were determined using the arithmetic mean, and their uncertainties showed based on standard error of the mean. Except for the samples Mk15-1 and Mk15-4 for which the determined $D_e$s are less than 8 Gy, the $D_e$s of the rest of the samples fall between 113 Gy and 454 Gy (Table 3.2). Abanico plots for illustrating the distribution of the $D_e$ and their uncertainties for one sample (Mk16-3) are provided for both GSL on quartz and $pIRIR_{290}$ on feldspar (Fig. 3.17).

Table 3.2: The estimated luminescence ages based on the frequentist approach.

| **SAMPLE** | *Quartz* | | | | *Feldspar* | | | |
|---|---|---|---|---|---|---|---|---|
| | $D_e$ | $\sigma$ | **Age** | $\sigma$ | $D_e$ | $\sigma$ | **Age** | $\sigma$ |
| | [Gy] | | [ka] | | [Gy] | | [ka] | |
| Mk15-1 | 1.2 | 0.2 | 0.6 | 0.1 | 4.4 | 0.3 | 1.7 | 0.1 |
| Mk15-4 | 2.9 | 0.4 | 1.2 | 0.2 | 7.6 | 0.3 | 2.8 | 0.1 |
| Mk15-5 | 92 | 4 | 28 | 1 | 118 | 4 | 32 | 2 |
| Mk15-6 | 95 | 6 | 28 | 2 | 116 | 3 | 31 | 1 |
| Mk15-7 | 159 | 6 | 50 | 3 | 249 | 9 | 71 | 4 |
| Mk15-8 | 135 | 6 | 37 | 2 | 197 | 4 | 49 | 2 |
| Mk16-1 | 114 | 6 | 41 | 2 | 179 | 9 | 57 | 3 |
| Mk16-2 | 123 | 4 | 47 | 2 | 193 | 8 | 65 | 3 |
| Mk16-3 | 156 | 11 | 47 | 4 | 454 | 52 | 123 | 15 |
| Mk16-4 | 76 | 3 | 27 | 1 | 144 | 10 | 45 | 3 |
| Mk16-5 | 110 | 5 | 35 | 2 | 258 | 52 | 74 | 15 |
| Mk16-6 | 77 | 4 | 21 | 1 | 113 | 3 | 29 | 1 |
| Mk17-1 | 96 | 3 | 28 | 1 | - | - | - | - |
| Mk17-2 | 83 | 4 | 24 | 1 | - | - | - | - |
| Mk17-3 | 84 | 3 | 23 | 1 | - | - | - | - |
| Mk17-4 | 110 | 3 | 36 | 1 | - | - | - | - |
| Mk17-5 | 84 | 4 | 30 | 2 | - | - | - | - |
| Mk17-6 | 77 | 3 | 25 | 1 | - | - | - | - |
| Mk17-7 | 90 | 3 | 27 | 1 | - | - | - | - |
| Mk17-10 | 216 | 12 | 64 | 5 | - | - | - | - |

### 3.3.6 Bayesian chronology using 'BayLum'

The chosen data representation may bring the question of: *To which extent the arithmetic mean is a reliable representative while the scatter in the precision of each individual aliquot is not negligible (see Fig. 3.17)*? To consider properly the analytical uncertainty of each individual $D_e$ to our final $D_e$ for the frequentist approach (it is inherent for the Bayesian modelling), we recalculated the average of individual $D_e$s based on a concept presented as Average Dose Model (ADM; see Guérin et al. 2017. The approach calculates the standard error of the $D_e$ using bootstrapping, considering an intrinsic overdispersion deduced from dose recovery experiments (here 9 %). Table 3.7.3 shows the result of the ADM for all the 18 samples, which were the same samples as used for the Bayesian analysis. A comparison of the arithmetic average and ADM results showed excellent consistency between the two approaches. This means that the variation of the individual standard errors has a negligible effect on the results.

The Bayesian modelling was carried out using the R (R Core Team, 2019) package 'BayLum' (Philippe et al., 2019; Christophe et al., 2019). For the calculation process, we used a multi-core workstation where subfolders were created containing the required input information, i.e. BIN/BINX-files, the reader dose rate, the environmental dose rate, as well as the position of the selected aliquots. The function `AgeS_Computation()` was applied to provide the chronology for several samples, including information on the stratigraphic order. For our study, the dose-response curves were fitted with an exponential plus linear equation through the option `LIN_fit = TRUE`. Then the argument `distribution = c('gaussian')` was used to assume a Gaussian distribution for estimation the palaeodose for each sample (based on the study by Heydari and Guérin 2018). The argument `priorAge` allowed including pre-knowledge about ages of the sample before running the measurements.

The stratigraphic order can be imposed on the data by calling the function `StratiConstraints()`. The function called `create_ThetaMatrix()` helps to express and address the systematic shared uncertainties between the samples. After determining the Bayesian chronology, the `plot_Scatterplots()` function can be used to create bivariate plots of age densities for every two samples. These plots illustrate the correlation between samples caused by the shared systematic uncertainties. The applied R script, as well as the convergence plots from the Monto-Carlo Markov Chain (MCMC) sampler are provided in the supplementary material (Sec. 3.7.6.2 and Sec. 3.7.6.3). To reach convergence, 4,000,000 iterations were employed on the thirteen samples of the eastern trench. Although calculations were run on a local multi-core workstation, depending on the setting, each calculation took roughly a week.

#### 3.3.6.1 Theta matrix

To address shared systematic uncertainty, 'BayLum' applies the basic statistical concept of a covariance matrix in the form of a so-called Theta ($\Theta$) matrix. Diagonal elements of the matrix

refer to the systematic and individual (statistical) uncertainty mainly on the dose-rate estimation as well as the systematic uncertainty on the determined palaeodose of each sample and non-diagonal elements of this matrix refer to the systematic uncertainty shared between two samples, or in other words, it shows the correlation between them (Combès and Philippe, 2017).

Systematic uncertainties for our study are dominated by uncertainties in the concentration of U, K and Th (which are used for calibration of the $\gamma$-ray spectrometers), the uncertainty on the internal-dose rate (the same value is applied to all samples) as well as the un- certainty on the $\beta$-source dose rate in the OSL reader. We detail the background of the Theta ($\Theta$) matrix and how it can be created in 'BayLum' after Combès and Philippe (2017) for readers not familiar with this topic in the supplement (see Sec. 3.7.5). A dedicated function to create the Theta matrix in R `create_ThetaMatrix()`) was written for this study and is now part of 'BayLum'.

## 3.4 Results

### 3.4.1 Comparison of quartz and feldspar ages derived by the frequentist approach

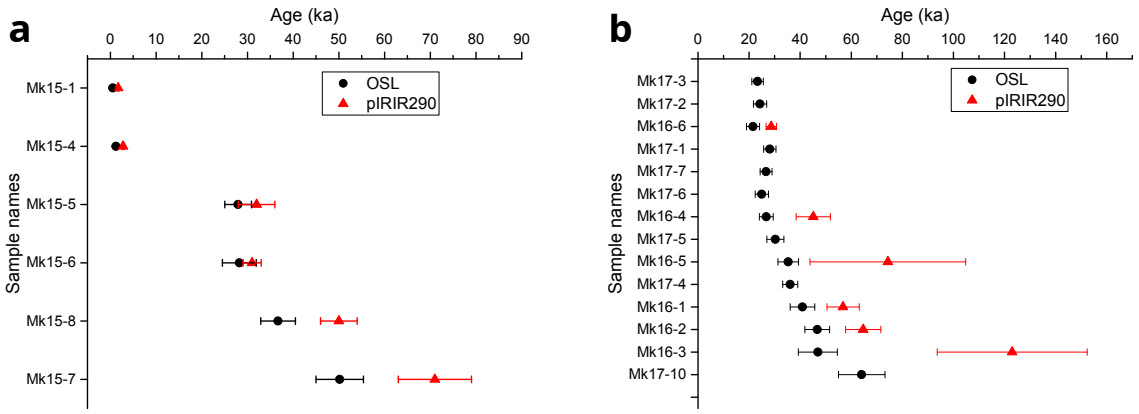


Figure 3.5: Comparison of quartz OSL ages with $pIRIR_{290}$ ages from the north (left plot) (except Mk15-8 from pit S2) and the east (right) sector (except Mk 16–1 from the south trench). All ages are quoted with $2\sigma$ uncertainty. The quartz and feldspar ages increase with depth. The discrepancy between the two ages is significant for Mk16-3 (right figure).

Figs. 3.5a and 3.5b show the ages determined with the frequentist statistic from feldspar and quartz for the north and the east trenches respectively within $2\sigma$ uncertainty (95 % confidence interval). Both, quartz and feldspar ages, increase with depth. However, the feldspar ages are older than the quartz ages. The top of the north trench starts with the quartz ages of samples Mk15-1 and Mk15-4 (0.4–0.8 ka and 0.8–1.6 ka). The quartz ages of samples Mk15-5 and Mk15-

6 (25–31 ka, 24–32 ka) overlap with the corresponding feldspar ages of 29–36 ka and 29–34 ka. The feldspar ages determined from samples Mk15-8 and Mk15-7 (46–52 ka, 64–78 ka) are significantly older than the associated quartz ages (33–41 ka, 44–56 ka). The quartz ages from the east trench start from the top with sample Mk17-3, 21–26 ka, and increase gradually with depth, ending up with sample Mk17-10, which represents the oldest age of the whole sequence, at 55–74 ka. Here also the feldspar ages are older than the quartz ages. The feldspar ages for samples Mk16-6, Mk16-4, Mk16-1 (the only sample from the south trench) and Mk16-2 are between 30 % and 70 % older than the quartz ages. The feldspar ages of samples Mk16- 5 and Mk16-3 are not only two times older than the quartz ages, but also the dispersion between the aliquots is much higher than for the rest of the $pIRIR_{290}$ ages. An Abanico plot (Dietze et al., 2016) is used to illustrate the dispersion in quartz and feldspar $D_e$ distributions for sample Mk16-3, as an example (Fig. 3.17).

This discrepancy between the quartz and feldspar ages may be explained by the different bleaching rates of the OSL quartz in com- parison to the $pIRIR_{290}$ signal (∼100 s vs ∼1,000 s; Murray et al. 2012). We know that the geological units 4 down to 8 are part of an alluvial deposit. Units 4, 6 and 8, in particular, have repetitively experienced flood events. The turbidity of the water during the flood may have caused insufficient bleaching of the feldspar grains on the top of the, potentially, short light exposure due to the high transport energy. The observed discrepancies between the feldspar ages and the quartz ages especially for samples Mk16-5 and Mk16-3, which were taken from units 6 and 8 may be attributable to such rapid sediment transport process. Guérin et al. (2015) reported a similar observation where feldspar grains suffer from insufficient bleaching, but quartz grains were believed to be bleached completely, showing age consistency with the $^{14}C$ age control. Here we do not have any independent age control. Consequently, we cannot rule out partial bleaching of the quartz samples, leaving the possibility that our quartz ages might be overestimated. However, an overestimation of the feldspar ages is more likely.

### 3.4.2 Unravelling the Bayesian chronology

Bayesian modelling was applied on samples from the east trench. The aim of this investigation was to test different options available in 'BayLum' package to our dataset and compare and discuss the obtained chronologies to highlight the effect of these options. We defined four modelling scenarios. In scenario I, we ran the Bayesian model without considering any stratigraphic constraints and without any input for the Theta matrix. Henceforth, we call this scenario the simplistic Bayesian model (Fig. 3.6a). In scenario II, we added the correlation between samples, i.e. taking the Theta matrix into account (Fig. 3.6b). Contrary, in scenario III the Bayesian model was applied to the samples considering the stratigraphic constraints, but without any inference on the correlation between the samples (no Theta matrix; Fig. 3.6c). Finally, in scenario IV, we considered the stratigraphic order in conjunction with the Theta matrix to address the corre-

lation between the samples (Fig. 3.6d). We plotted the frequentist chronology alongside the four Bayesian chronology scenarios (Fig. 3.6a–3.6d). The estimated ages are quoted in a 95 % confidence interval for the frequentist approach and a 95 % credible interval for the Bayesian approach. The point in the credible interval (Fig. 3.6) corresponds to the highest probability density (HPD) estimation, i.e. the Bayes estimate for the Bayesian approach and the point in the middle of the confidence interval corresponds to the average of the distribution in the frequentist approach.

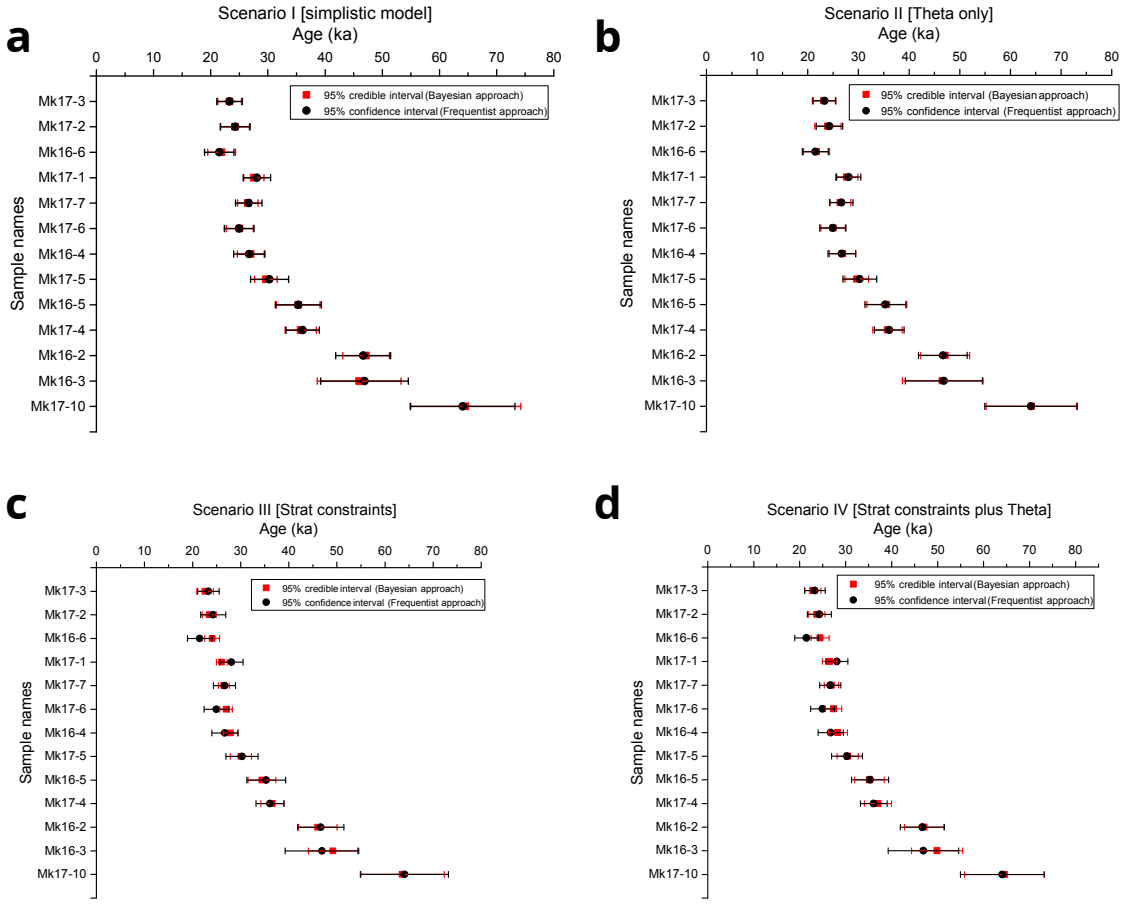


Figure 3.6: Comparison of the different Bayesian and the frequentist chronologies for the 13 quartz samples from the east trench. Top left: Simplistic Bayesian model (for definition, see main text). Top right: Bayesian chronology considering Theta matrix only (for definition, see the main text and the supplementary material). Bottom left: Bayesian chronology imposing the stratigraphic order. Bottom right: Bayesian chronology imposing the stratigraphic order and applying the Theta matrix, which addresses systematic shared errors.

#### 3.4.2.1 Scenario I

The results of the simplistic Bayesian model do not indicate significant discrepancies for most of the samples compared to the obtained frequentist approach (Fig. 3.6a). The average in the frequentist approach and the HPD in Bayesian do not differ by more than 2 % while the uncertainties of the Bayesian estimates are reduced compared to the frequentist estimates. This uncertainty reduction is significant for samples Mk17-1 and Mk17-5 (reduction by 26 % and 41 %, respectively).

#### 3.4.2.2 Scenario II

Figure 3.6b shows almost complete agreement between the frequentist chronology and the Bayesian model when the Theta matrix (only) is considered. The only exception is sample Mk17-5 for which the Bayesian model leads to ca 30 % reduction in the credible interval in comparison with the confidence interval.

#### 3.4.2.3 Scenario III

Figure 3.6c presents the Bayesian chronology applying the stratigraphic constraint with no consideration of the correlations between the dose rates or equivalent dose estimates. The most striking observation is the significant reduction of the uncertainty for the Bayesian estimates. We observed reductions of 24 %–53 % in uncertainty for the set of samples located at the beginning of the sequence (Mk17-3 to Mk 16-5). At the bottom of the sequence, sample Mk16-3 showed a 33 % uncertainty reduction. There appears to be no significant change between Bayesian and frequentist ages: the Bayesian HPDs for samples Mk17-3, Mk17-2, Mk17-1 and Mk16-5 were between 3 % and 7 % younger than the corresponding averages, while, on the contrary, Bayesian HPDs of samples Mk16-6, Mk17-6, Mk16-4 and Mk16-3 were 4 %–11 % older in comparison to the frequentist averages.

#### 3.4.2.4 Scenario IV

The last plot (Fig. 3.6d), which refers to the application of the stratigraphic order and correlation between samples (Theta matrix) results in a reduced credible interval from 5 % (Mk17-10) up to a maximum of 33 % (Mk17-1) compared to the confidence intervals. Moreover, for five samples (out of 13), the Bayesian ages moved towards the older ages (up to 14 %) in comparison to the frequentist ages. The Bayesian age for one sample (Mk17-1) is younger than the frequentist age by 6 %. For the rest of the samples, the Bayesian ages render almost the same ages as the frequentist approach.

#### 3.4.2.5 Further results

In this section, we provide a visual perception to better illustrate (1) the correlation between samples due to the systematic shared error as well as (2) the effect of stratigraphic order on the sample age. The package 'BayLum' allows to create correlation plots (here bivariate plots) for each two samples to illustrate the correlation between their ages. Each point (in the figure interpolated as hexagons, to allow a better visual perception) corresponds to the estimated ages for two samples as sampled from the MCMC. Here we present three groups of bivariate plots corresponding to scenario I, III and IV. For simplicity, we show only five samples from the east trench (in the stratigraphic order from Mk17-3 to Mk17-7). A complete version of this plot is available in the supplementary material (Figs. 3.20–3.22). Figure 3.7a shows the results after applying the simplistic Bayesian model (scenario I). Mk17-3 is the youngest sample and Mk17-7 is the oldest one. The symmetric shape of the distribution for each of the two samples is almost present for all the plots, which indicates no specific correlation between the samples, and which is in line with the idea of not considering the Theta matrix. Figure 3.7b is related to Fig. 3.6c where the stratigraphic constraints affect the final chronology, but neither the correlation within the dose-rate data nor within the equivalent-dose data (scenario III) were considered. For some of the plots, we observed a truncation in the top-left corner letting the distribution appear asymmetric. For instance, the bivariate plots of two ages like Mk17-3/Mk17-2, Mk17-2/Mk16-6, Mk17-1/Mk17-7 and Mk17-3/Mk16-6 are truncated. These truncations are caused by overlapping age intervals of all the two mentioned samples. The part of the distribution that does not satisfy the stratigraphic order is truncated. The last bivariate plots are displayed in Fig. 3.7c, where both, the stratigraphic correlations and the correlations on the systematic errors are considered (scenario IV). In this figure, all bivariate plots appear graphically in a prolate shape, showing a similar truncation to the one observed in Fig. 3.7b due to the effect of stratigraphic constraints. The prolate shapes illustrate the positive correlation between each two samples because of the effect of systematic shared error, which is considered in scenario IV (Theta matrix was taken into account).

## 3.5 Discussion

### 3.5.1 Improvement of the age precision

Besides the rough comparison between frequentist chronology and different Bayesian modelling scenarios in the previous section, here we present the kernel density distributions of the relative uncertainties for all scenarios to visualise the changes in the obtained age uncertainties (Fig. 3.8). All these distributions (except for scenario II) illustrate uncertainties smaller for the Bayesian scenarios than with the frequentist approach, as observed in Sec. 3.4 Moreover, the

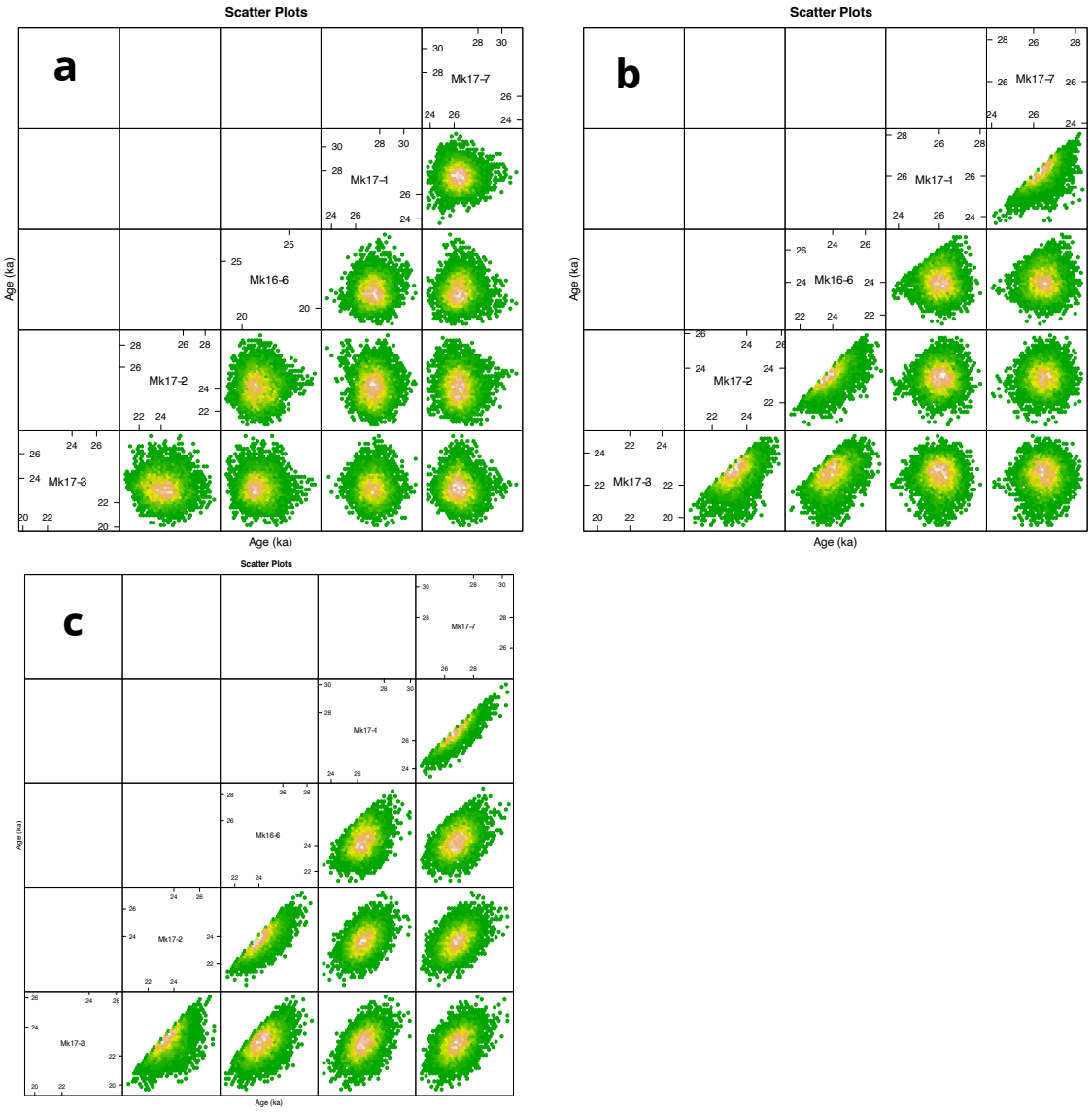


Figure 3.7: Example of scatter plots (here so-called hexagon plots) for samples Mk17–3, MK-17-2, Mk16-6, Mk17-1 and Mk17-7. The full plots are shown in Figs. 3.20–3.22. The figures illustrate the probability densities of the age estimations for two samples for which the hexagons bin the estimated ages of two samples. (a) The bivariate plots of probability densities age estimations for the simplistic Bayesian model. (b) Applying the stratigraphic constraints. (c) Applying stratigraphic constraints and modelling systematic error with the Theta matrix. In this last figure, a positive correlation is observed for each plot, which reflects the shared systematic errors. The top left corner truncation in each square illustrates the effect of stratigraphic constraints.

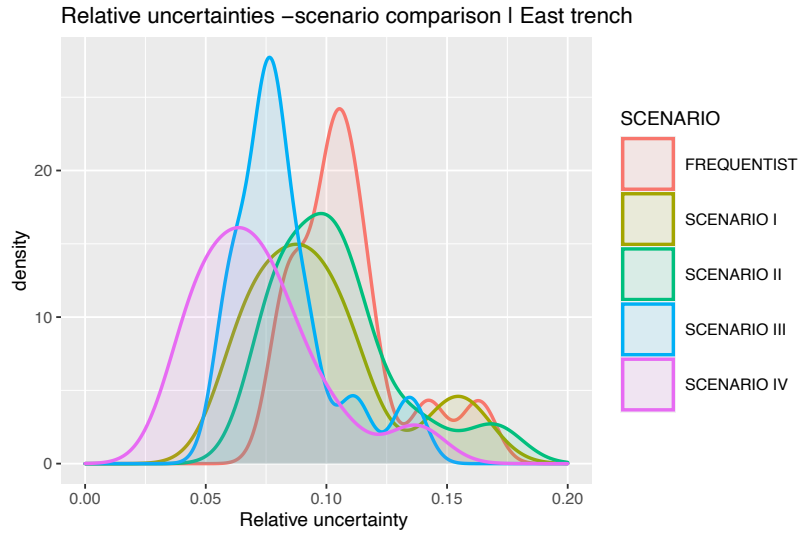


Figure 3.8: Kernel density plots comparing relative age uncertainties for the applied modelling scenarios. Here shown are the results for the east trench.

Table 3.3: Test results Welch one-sided paired $t$-test for relative uncertainty distribution

| **DATASET** | **SCENARIO** | ***t-value*** | **Df** | ***p-value*** |
|---|---|---|---|---|
| East trench | SCENARIO I | -3.347 | 12 | 2.91E-03* |
| East trench | SCENARIO II | -1.732 | 12 | 5.45E-02 |
| East trench | SCENARIO III | -6.709 | 12 | 1.08E-05* |
| East trench | SCENARIO IV | -7.442 | 12 | 3.91E-06* |

** Statistically significant to a significance value of 0.01*

*$H_0$: this scenario has similar or larger mean than the frequentist results (identical or lower precision)*

*$H_A$: this scenario has a lower mean than the frequentist results (higher precision)*

two models that employ stratigraphic constraints (scenarios III and IV) show the lowest relative uncertainty in comparison to the frequentist results. To determine whether these results are also statistically significant, we performed a one-sided paired Welch $t$-test with the results listed in Table 3.5.1. For a significance level of 0.01, all scenarios except scenario II exhibit that the uncertainty distribution has a statistically lesser mean than the frequentist results, i.e. the OSL ages calculated with 'BayLum' are more precise than those calculated with the conventional approach. Although, the rough comparison between the Bayesian and frequentist chronology for scenario I appeared to not to be considerable (see Sec. 3.4.2.1).

With regard to the initially formulated objective (2) (see Sec. 3.1) of our work, it appears that we must reject $H_0$. Thus, applying Bayesian models results in a chronology distinguishable from the frequentist approach. Nevertheless, this conclusion alone allows no statement about the best suitability of a particular scenario and why results differ between the scenarios.

### 3.5.2 Bayesian chronology: stratigraphic order and the correlation between samples

While the different scenarios were proposed in order to unravel the effect of stratigraphic constraints and age correlations, it must be emphasized that scenario III, while it shows the best improvement of the precision, is inappropriate for discussing the final chronology because it does not consider the existing correlation between the data (Fig. 3.7c). For example, the plot with samples Mk17-1 and Mk17-7 shows a strong positive correlation, i.e. if the age of sample Mk17-1 becomes older, the age of sample Mk17-7 is likely to get older likewise. However, this correlation is not observed in Fig. 3.7b, since scenario III does not take into account correlations between the data. The Bayesian model in that scenario treats all of the errors as random. Therefore, particularly when the ages of the two successive (in the stratigraphy) samples overlap one another, the model reduces the uncertainty to satisfy the stratigraphic order. In other words, such a model has the highest impact in the absence of systematic shared uncertainty where samples do not correlate. Consequently, to address properly the effect of the stratigraphic order for our data (which includes systematic shared uncertainties), the Theta matrix should be applied and scenario III cannot be considered. However, if the systematic shared error is added to the result of this scenario, then the result can be considered following (Rhodes et al., 2003), who suggested adding the relative systematic shared uncertainty in quadrature to calculate the final standard error of the age as the square root of its sum.

### 3.5.3 Bayesian chronology: effect of stratigraphic order and the question of age accuracy

It was shown that scenarios III and IV result in a considerable reduction in age uncertainties in comparison with the results obtained using the frequentist approach. Both Bayesian models take the stratigraphic order into account. Figure 3.6c and d display that the maximum reduction in the uncertainties is observed for samples Mk16-6 to Mk16-4 where confidence intervals overlap one another. The frequentist age of sample Mk16-6 does not follow the stratigraphic order, but when the stratigraphic order applies, the credible interval shifts towards the older part of the corresponding frequentist interval to satisfy the imposed ordering. Consequently, the rest of the samples from Mk17-1 to Mk16-4 which roughly place between 24 ka and 29 ka should follow this ordering; thus, the credible intervals decrease significantly in both scenarios. Rhodes et al. (2003) already mentioned that Bayesian modelling might lead to substantial improvements in the precision where the sampling resolution is high enough, so that ages overlap each other. Contrary, if the age intervals do not overlap, the Bayesian chronology considering the stratigraphic order does not render results more precise than the frequentist chronology (see for example the Bayesian ages of samples Mk16-2 and Mk17-10 in Fig. 3.6c and 3.6d). Moreover, Figs. 3.6c

and 3.6d show that part of the obtained frequentist-age intervals are 'discarded' when the stratigraphic order is imposed. For instance, for sample Mk17-6, more than 50 % of the uncertainty interval is 'eliminated' pushing the credible interval out of the average of the frequentist model. The same pattern is observed for Mk16-6, where the Bayesian age shifts by 11 % towards an older age. The estimated credible interval does not overlap the first part of the frequentist confidence interval and results in a smaller uncertainty (38 % reduction) in comparison with the frequentist approach. This shift towards older ages almost affects the entire dataset; thus, result in the ages, which are older or younger than the frequentist ages (see Mk16-4, Mk17-4, Mk16-3). Therefore, stratigraphic constraints should be applied with caution since they affect all age estimates within a sequence. In other words, here, it is not only the question of precision, but also the question of accuracy that matters when the application of such a model is attempted. Therefore, the stratigraphic order of the samples should be well known and well established before being applied. Misinterpretations have a strong effect on the Bayesian ages and can result in over or underestimated ages.

### 3.5.4 Technical issues

The ideal way to address systematic uncertainty with Bayesian modelling is a rigorous experimental design, using one well-known instrument each, for estimation of the palaeodose and the dose rate. However, experimental reality proofs differently. For our measurements, which were carried out over more than two years, different OSL readers were employed (Freiberg Instruments *lexsyg SMART* and *lexsyg research* readers, see above) limited by the technical availability of the machines. The systematic uncertainty from the source-dose rate of the OSL readers varies typically between 2 % and 3 %, or even more (see discussion in Tribolo et al. 2019). However, it is also not clear whether the source dose-rate uncertainty affects the entire ages toward one direction (higher or lower value). It can result in higher doses in one machine but lower in another. Nevertheless, in our case, the systematic errors are correlated since we used the same calibration standard for the calibration of the radioactive sources in the OSL readers.

Furthermore, it should be noted that variations of the systematic error could also occur if only one machine was used. For our modelling, we applied a 2 % systematic uncertainty, and we provided the Theta matrix based on that value. Additionally, we also provide the Theta matrix with 3 % uncertainty on the source-dose rate (OSL reader) and compare the Bayesian chronology of both (2 % vs. 3 %; see supplement Fig. 3.24 and Tables 3.5–3.6). Our results suggest that both values, for our samples and our assumptions, result in plots indistinguishable from each other and the minor differences are likely being introduced by the stochastic process itself, which indicates that the application of our modelling was generally justified. Similarly, we employed two different $\gamma$-ray spectrometers in our lab to estimate the radionuclide concentration. However, we consider the differences in the systematic errors between both systems negligible

in particular due to the used identical material for the calibration of those spectrometers.

### 3.5.5 Further remarks

The entire dataset from the Late Pleistocene geological units consist of thirteen samples from the east trench, three samples from the north trench, one sample from the southern trench, and finally, one sample from the pit S2. Since the stratigraphic relationship between the different trenches is not consistent, we applied Bayesian models separately to the samples from the east and the north trenches; the later results are shown in the supplementary material (Fig. 3.18). Our observation showed that the Bayesian model in scenario IV results in a more precise chronology compared to the frequentist model. For the final archaeological age interpretation, we present and discuss the results from scenario IV alongside the frequentist chronology.

### 3.5.6 The obtained chronology in the prehistoric context

One of our aims for this study was to provide a chronology for the Upper, Intermediate and Middle Palaeolithic assemblages in the open- air site of Mirak. The Bayesian and the frequentist ages of sample Mk15-5 from the north trench, which originated from the Upper Palaeolithic assemblage layer (level 1; geological unit 4a), resulted in 25–28 ka and 25–31 ka, respectively. In the east trench, four samples (Mk17-3, Mk17-2, Mk16-6, Mk17-1) were taken from the layer containing the Upper Palaeolithic assemblage (level 1; geological units 3a and 4a). The Bayesian ages of these samples were (21–25, 22–26, 23–26 and 25–28) ka while the frequentist results gave (21–26, 22–27, 19–24 and 26–30) ka. Hence, the Upper Palaeolithic occupation of Mirak is defined by the samples dating between 21 ka and 28 ka (95 % credible interval, Bayesian approach) and 19–31 ka (95 % confidence interval, frequentist approach). The geographical nearest Upper Palaeolithic site to Mirak for which an absolute chronology is available is Garm Roud 2. This site is located in the northern foothills of the Alborz Mountains in the Mazandaran Province (Berillon et al., 2007; Berillon and Asgari Khaneghah, 2016). Radiocarbon dating results for the site of Garm Roud 2 yielded 28–35 cal. ka BP (Antoine et al., 2016) which seems to be slightly older than Bayesian and frequentist chronology for the Upper Palaeolithic layer of Mirak; although the frequentist age interval overlap with the determined age interval of the site of Garm Roud 2. However, the Bayesian approach leads to a more precise chronology in comparison to the frequentist approach. Interestingly, our results from Mirak, like those for the site of Garm Roud 2, exhibit ages for the Upper Palaeolithic that are younger than the reported ages of the same period for the Zagros region. Indeed, $^{14}$C dating has been applied on the Upper Palaeolithic period of various sites, such as Shanidar cave in the north of Zagros foothills which resulted in 29–40 cal. ka BP (original data: Solecki 1963; Hole and Flannery, 1968; recalculated data: Becerra-Valdivia et al. 2017; Ghasidian et al. 2019). $^{14}$C dating was also applied for the kaldar

cave in central Zagros (Bazgir et al. 2017; 37–54 cal. ka BP), Yafteh cave in the west-central Zagros (Otte et al. 2011; 29–42 cal. ka BP), and Ghār-e Boof in the southern Zagros (Conard and Ghasidian 2011; Ghasidian 2014; Becerra-Valdivia et al. 2017; 35–42 cal. ka BP). The geographical locations of the mentioned sites are shown in Fig. 3.1B. The temporal period, engulfing all of these four age ranges is around 35–40 cal. ka BP, which renders an earlier Upper Palaeolithic occupation than presumed for Mirak 21–28 ka. However, the chronology of Mirak aligns better with the chronology of Garm Roud 2 (north of Alborz). Although, it is worth mentioning that the concentration of the lithic artefacts attributable to the Upper Palaeolithic period is very scarce in Mirak, the younger Upper Palaeolithic chronologies for the central Alborz region (Mirak and Garm Roud 2) in comparison with the chronologies of Upper Palaeolithic assemblages in the Zagros echo some temporal differences between the two areas, which may be also translated into cultural variabilities (Berillon et al., 2007; Chevrier, 2016; Vahdati Nasab et al., 2019).

The intermediate assemblage (level 2, east trench; Fig. 3.3) appears to be spread over two sub-layers in Mirak, which raises the question of the existence of two distinct assemblages. Indeed, the preliminary study of the lithic material of this layer highlighted a mix of Upper and Middle Palaeolithic affinities that potentially characterise a transitional phase likely related to early Aurignacian industries of the Zagros (Vahdati Nasab et al., 2019). One issue was to know, based on a refined chronology, whether these apparent sub-layers correspond to two distinct occupations; and if so, our interpretation of this apparently mix assemblage should be reconsidered. The Bayesian and the frequentist ages of sample Mk17-7 (sub-layer 1, geological unit 4 b) resulted in 25–28 ka and 24–29 ka. The Bayesian and the frequentist ages of sample Mk17-6 refer to sub-layer 1 (geological unit 5), resulting in 26–29 ka and 22–28 ka, respectively. Moreover, the ages of Mk16-4 and Mk17-5, which were taken from the sub-layer 2 (geological unit 5), yield 26–30 ka and 28–33 ka for the Bayesian, and 24–29 ka and 27–34 ka for the frequentist model. The Bayesian ages of samples Mk16-5 and sample Mk17-4 from the geological unit 6, just below the sub-layer 2, resulted in 32–38 ka and 34–40 ka while the frequentist ages yielded 31–39 ka and 33–39 ka.

In summary, the Bayesian age for the sub-layer 2 in (95 % credible interval) frames 26–33 ka and the frequentist age results in 24–34 ka (95 % confidence interval). Here again the Bayesian approach leads to smaller uncertainties in comparison to the frequentist approach providing a more precise age. Moreover, the Bayesian age for sub-layer 1, 26–29 ka agrees to the 26–30 ka (sample Mk16-4) in sub-layer 2. Therefore, it appears likely that the two sub-layers relate more or less to one another and should be considered as a single archaeological assemblage; this interpretation reinforces the hypothesis of the existence in Mirak of an intermediate phase between Middle and Upper Palaeolithic periods (Vahdati Nasab et al., 2019), which may be

seen as transitional. However, this finding does not indicate an occupation by a single group of people. The MIS 3 is a period with millennial-scale fluctuations in climatic-environmental regime at global and regional scales (e.g., Bond, 1997; Dansgaard et al., 1993; Heinrich, 1988; Wolff et al., 2010; Mehterian et al., 2017; Vlaminck, 2018) and thus, the site may have been frequently abandoned and reoccupied in millennial and even centennial scales (Hashemi et al., 2018). In addition, the results for the intermediate layer indicate that, despite some cultural differences, this layer features a close chronology with that of the layer 1 allocated to the Upper Palaeolithic 21–28 ka. Interestingly, the Bayesian age of 28–33 ka, which is the oldest age from sub-layer 2, agrees with the age of 28–35 cal. ka BP for the Upper Palaeolithic assemblages of the open-air site of Garm Roud 2. Our results thus imply that the chronological interval of 26–33 ka (comprising sub-layers 1 and 2) in Mirak is most likely an original cultural entity in the region with subsequent and sub-contemporaneous cultures, some with clear Upper Palaeolithic affinities (Mirak layer 1 and Garm Roud 2) and some with mixed characteristics featuring likely a transitional entity (Mirak layer 2).

Finally, the Bayesian ages for samples Mk16-2 and Mk16-3, which were taken from the layers that contain the Middle Palaeolithic assemblage (archaeological layer 3; end of unit 7 and beginning of unit 8 in the sedimentological log), resulted in 43–51 ka and 44–55 ka, respectively, while the frequentist ages for these two samples exhibited 42–51 ka and 39–55 ka. Here again, the Bayesian modelling provides ages more precise than the frequentist ages. The determined ages for the Middle Palaeolithic layer of the site Mirak align with the period of Middle-Upper Palaeolithic transition in Shanidar 39–49 cal. ka BP (Becerra-Valdivia et al., 2017) as well as with the Neanderthal occupation layer in the Shanidar Cave, which was dated to ca 46–60 cal. ka BP (Becerra-Valdivia et al., 2017; Solecki and Solecki, 1993). However, this age-range is close to the temporal limit of $^{14}$C dating and, thus, should be treated cautiously. Our results strengthen the idea of a cultural context that is highly complex in the area, with the potential contemporaneity of Middle and Upper Palaeolithic cultures in some parts of the region (Iranian Plateau) during MIS3 to MIS2 (age-boundaries according to Lisiecki and Raymo 2005); a hypothesis that needs further investigations and the one which implies the likely contemporaneous presence of both Neanderthals and modern humans in the region (see Zeitoun, 2016).

## 3.6 Conclusions

We applied and tested various Bayesian modelling scenarios to the chronological samples taken from the east and the north trenches of the open-air Palaeolithic site of Mirak and presented the results of each model. Additionally, we provided the first complete numerical chronology from the Late Holocene 0.8–1.6 ka (samples Mk15-1 and Mk15- 4) to Late Pleistocene 56–73 ka (Bayesian age of the oldest sample Mk17-10) for the site of Mirak in Iran. We conclude that:

- Our study suggests that Bayesian modelling generally results in a statistically significant improvement of the age precision (except scenario II), which discards our initially formulated $H_0$ (scenario I and scenario IV). The best improvement was achieved when the uncertainty of the samples overlap one another (scenario IV). However, applying a stratigraphic relationship to the model has a strong impact on the final ages; therefore, for such a case the stratigraphic ordering should be understood clearly. Otherwise it leads to age under- or over-estimations.

- Although providing the Theta matrix addresses systematic shared errors, in the absence of independent chronologies, with a higher temporal resolution than luminescence dating (e.g., $^{14}$C dating), it does not result in improved chronological precision and the obtained result is almost indistinguishable from the frequentist approach (scenario II).

- The Bayesian chronology for the Upper Palaeolithic occupation of the site of Mirak was attributed to 21–28 ka. The Bayesian chronology for the intermediate layer, provided the age range of 26–29 ka for sub-layer 1 and 26–33 ka for the sub-layer 2. Therefore, based on our chronology, it is highly probable that the two distinct sub- layers can be considered as a one individual layer with the age of 26–33 ka. The Bayesian chronology for the Middle Palaeolithic assemblage resulted in 43–55 ka.

In summary, based on our observations, it appears that the advantages of Bayesian modelling have the strongest impact when a stratigraphic order is applied to the samples for which age uncertainties overlap. Hence, in the absence of explicit stratigraphic constraints, applying the frequentist approach may be favoured compared to the time-consuming and error-prone Bayesian modelling (over several days on a multi-core workstation). However, it should be mentioned that for this study, we did not access $^{14}$C dating as an independent age control of the site. Such a combination can be the topic of future work. Although Bayesian modelling provides more precise ages compared to ages obtained by the frequentist approach, in a prehistoric context of this study, the determined ages from both approaches lead to a similar interpretation. Both approaches provided valuable chronological evidence that Late Pleistocene humans frequently used the site of Mirak during MIS 3 and 2. However, fluctuations in climatic-environmental characteristics on continental and regional scales likely impacted the site of Mirak (e.g., oscillations between arid and semi-arid landscapes; Dennell 2017). Therefore, human groups most likely lived in the region in a temporally-discontinuous fashion. Further investigation is needed to shed light on the issue of millennial- and larger-scale fluctuations in climate and their impacts on regions such as the Iranian central plateau during Late Pleistocene.

## Acknowledgements

We are thankful to Frank Preusser and one anonymous reviewer. This work was financed by the LaScArBx LabEx supported by the ANR - n° ANR-10-LABX-52 and was performed in the framework of the PhD thesis of MH.

Chantal Tribolo is thanked for her constructive comments on an earlier version of the manuscript. We would like to thank the Research Center for Cultural Heritage and Tourism of Iran (RICHT) and the Ira- nian Center for Archaeological Research (ICAR) for granting the permit for conducting the Joint Iranian and French Project at Mirak, and authorizing the exportation of the OSL samples for analysis. We thank the Office of International Affairs at the RICHT for facilitating the VISA- granting process for the non-Iranian collaborators. We are greatly indebted to Mr. Khajeh Beidokhti, the director of the Iranian Cultural Heritage Organization (ICHO) office in Semnan Province at the time and his colleagues for providing logistics and comfort to conduct the field- work. The fieldwork and geological analyses have been co-funded by the office of governor of Semnan, the French ministry of Europe and Foreign Affair (MEAE) and the UMR7194 CNRS-MNHN-UPVD (Paris); we are very grateful to them. Special thanks go to the field crew in alphabetical order: Alieh Abdollahi, Mahkameh Abolfathi, Laya Alinia, Benoit Chevrier, Nasim Feizi, Mozhgan Jayez, Mahyar Khademi, Ashghar Nateghi, Mona Oryat, Soroush Razi, Robabeh Sadeghinejad, Yashar Sadeghi, Sanaz Shirvani, Mohammad Javad Shoaee, and Marzieh Zareh Khalili.

## 3.7 Supplement

### 3.7.1 The site of Mirak

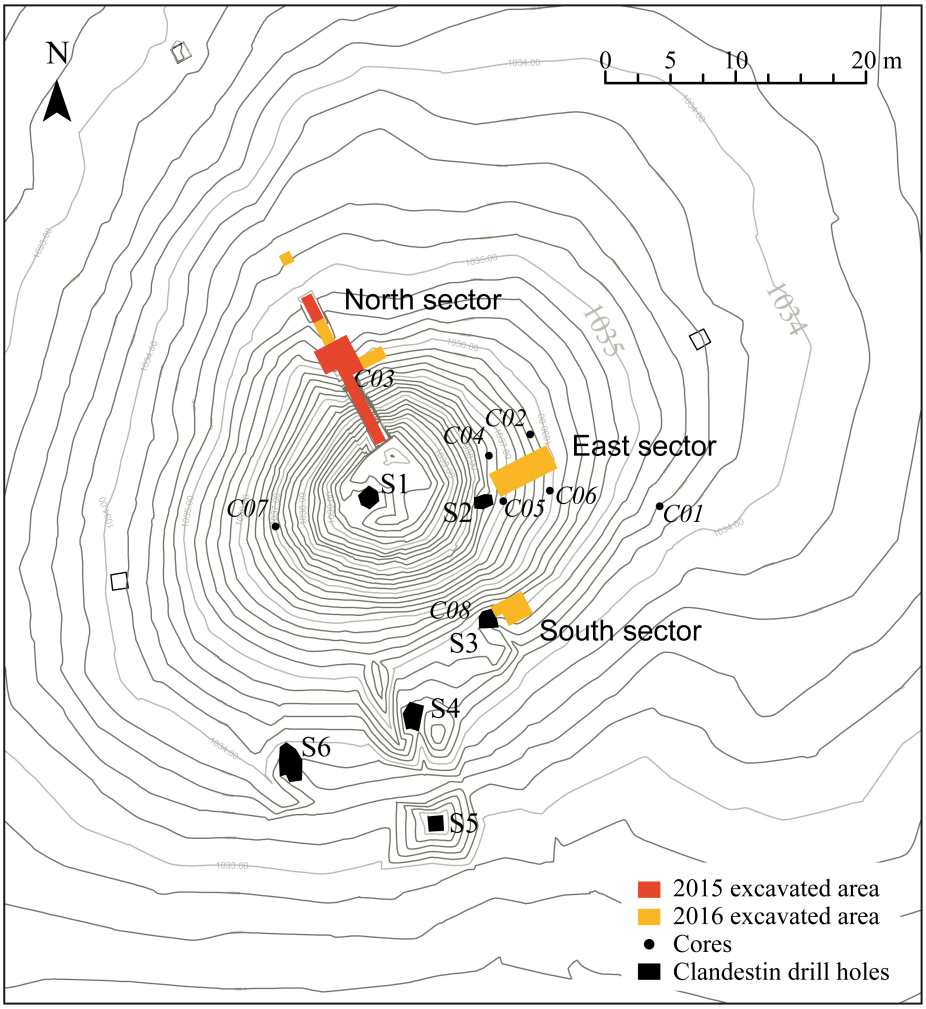


Figure 3.9: The topographic map of site Mirak (mound n. 8) redrawn from Vahdati Nasab et al. (2019). The plan view shows the excavated area including the north, east and south trench as well as the location of the illegal pits.

### 3.7.2 Testing the fast component

A routine and straightforward way to check the presence of a fast OSL component is a signal comparison against a calibration quartz sample with a known fast component dominated OSL signal. To test the Mirak sample, we used Risø calibration quartz (batch 90, Hansen et al., 2015). The OSL signals of the sample (Mk15-7) and of the calibration quartz were first measured using

blue continuous-wave (CW) light stimulation at 458 nm and then transformed into a pseudo linearly modulated OSL (pLM-OSL) curve after Bos and Wallinga (2012). Both curves are shown in Fig. 3.9. The figure illustrates an acceptable match in the first part of the two signal curves, which indicates a dominant fast component in the investigated sample.

However, the last part of the investigated signal does not match the curve of calibration quartz, indicating the presence of other signal components, which cannot be identified without further analyses. Therefore, we used a linearly modulated OSL method (LM-OSL) (Bulur, 1996) to deconvolve individual signal components. In this method, the stimulation intensity is ramped linearly, which induces a sequential release of electrons from traps. Then the signal requires mathematical fitting methods (e.g., Choi et al., 2006) to decompose the sum signal curve into specific signal components. The experiment was done using a *lexsyg research* reader (Richter et al., 2013). For technical reasons, for this experiment we used blue laser diodes (458 nm, see above) in conjunction with a Hoya U340 + AHF BrightLine HC 340/26 interference filter for signal detection. The maximum stimulation power was set to 60 mW $cm^{-2}$ and ramped over 15,005 s. he first-order kinetics deconvolution uses nonlinear least-squares methods provided through the function `fit_LMCurve()` from the **R** (R Core Team, 2019) package 'Luminescence' package (Kreutzer et al., 2012, 2019).

Quartz signal component parameters, such as the photoionization cross-section ($\sigma$ in $cm^2$) (Choi et al., 2006) were determined for sample Mk15-7. Exemplary, LM-OSL results and signal deconvolutions are shown in Fig. 3.10 (natural and regenerated). The obtained photoionization cross-sections (ca $7.0 \times 10^{-18}$ $cm^2$ to $7.3 \times 10^{-18}$ $cm^2$ and ca $7.3 \times 10^{-19}$ $cm^2$ to $9.6 \times 10^{-19}$ $cm^2$) generally appear to correspond to the fast and medium component categorisation after Singarayer and Bailey (2003) and Jain et al. (2003). Other components are shown in the plot, but are of no further relevance for our work. However, their (Singarayer and Bailey, 2003; Jain et al., 2003) photoionisation cross-sections range around $10^{-17}$ $cm^2$ for the fast and $10^{-18}$ $cm^2$ for the medium component. For our samples, this would indicate that the signal is dominated by non-fast components only, which appears to be very unlikely. More likely seemed to be that our measurement system results in different photoionisation cross-section values, e.g., due to the used laser diodes (non-optimal signal ramp) and the main detection window centred around 340 nm. To verify our results, we repeated LM-OSL experiment for the natural signal for a fast-component dominated calibration quartz sample (Risø calibration quartz, batch 90; Hansen et al. 2015). The results in Fig. 3.12 confirm that the fast component, using our system, calculates with $7.3 \times 10^{-18}$ $cm^2$ also for the calibration quartz. This confirms that the Mirak sample is dominated by a fast component, however, it also shows (Fig. 3.10) a medium component which is believed to cause an unwanted luminescence behaviour (Wintle and Murray, 2006) and should thus be subtracted from the OSL signal.

For the final equivalent dose ($D_e$) measurements, following Bailey et al. (2011), we decided to

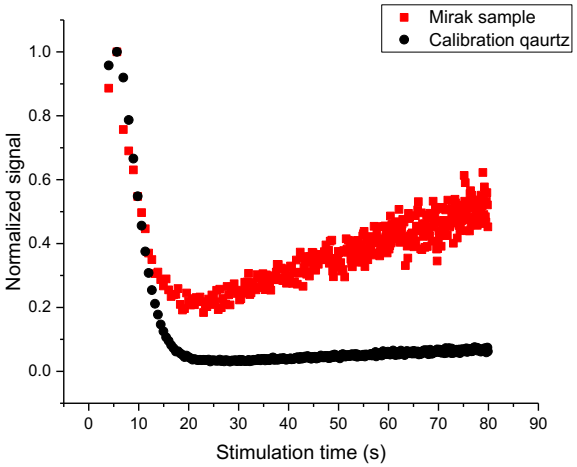


Figure 3.10: Signal comparison of the pseudo LM-OSL (Bulur, 2000) signal of Mirak with a pseudo LM-OSL signal from a 'calibration quartz' sample. The initiated part of both curves match, which indicates the presence of fast component in Mirak samples. Contrary, the later part seem to reveal slower signal components.

measure all samples with green-light stimulated OSL to better separate fast and medium component. According to Singarayer and Bailey (2003), the photoionization cross-sections of fast and medium components differ significantly when stimulated in the green wavelength range (peak ca 532 nm).

### 3.7.3 Additional luminescence results

### 3.7.4 Bayesian modelling output

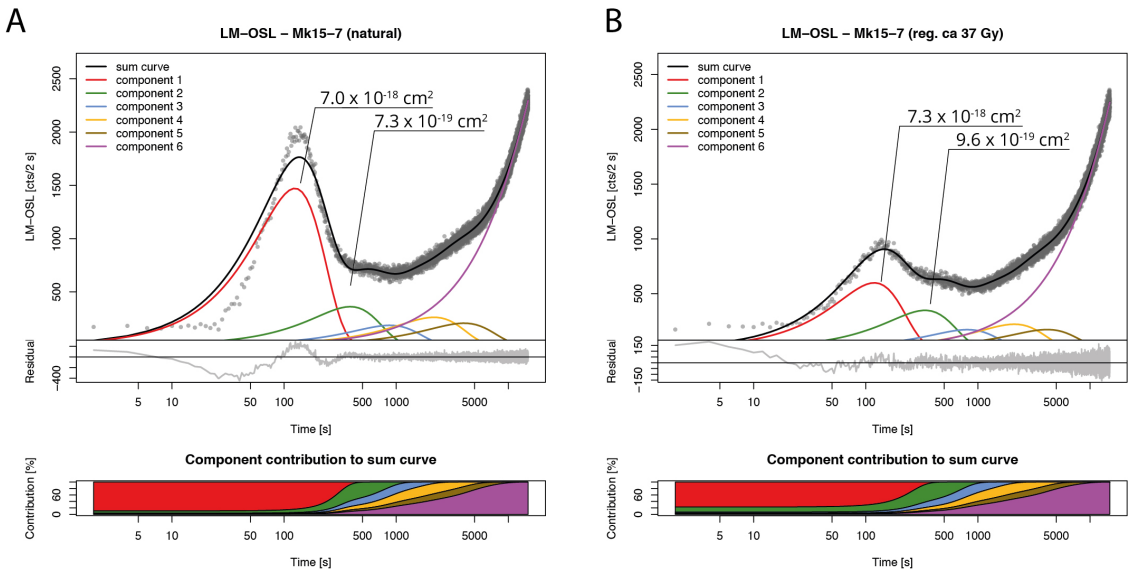


Figure 3.11: LM-OSL signal deconvolution of one Mirak sample. The function `fitt_LMCurve()` from the 'Luminescence' package (Kreutzer et al., 2012, 2019) used to determine the signal parameters such as the photoionization cross-section ($\sigma$ in cm$^2$). (A) Shows the LM-OSL results for the natural signal, while (B) shows the LM-OSL results for the regenerated signal. The photoionization cross-sections are given in the figures for the fast and the medium component. For further details see text.

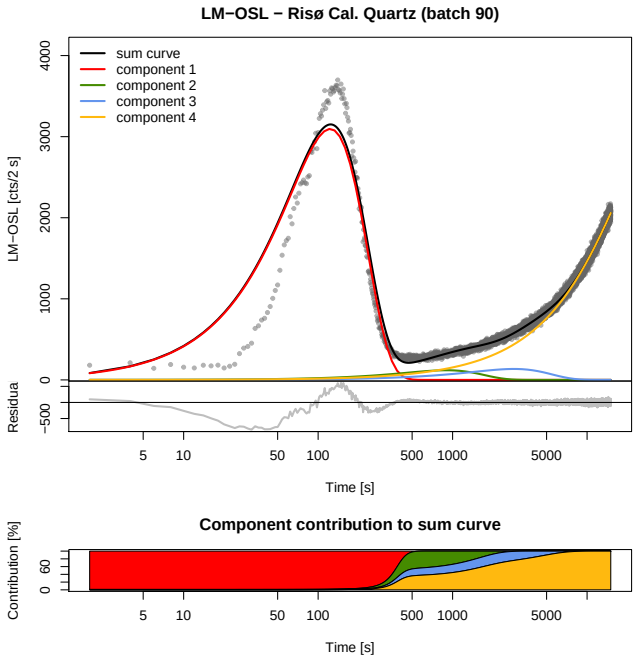


Figure 3.12: Example LM-OSL signal deconvolution for one aliquot from Risø calibration quartz (batch 90). The red-cure indicates the fast component with a corresponding photoionization cross-section of $7.3 \times 10^{-18}\,\mathrm{cm}^2$. This value is similar to the believed fast component in the Mirak samples shown in Fig. 3.10.

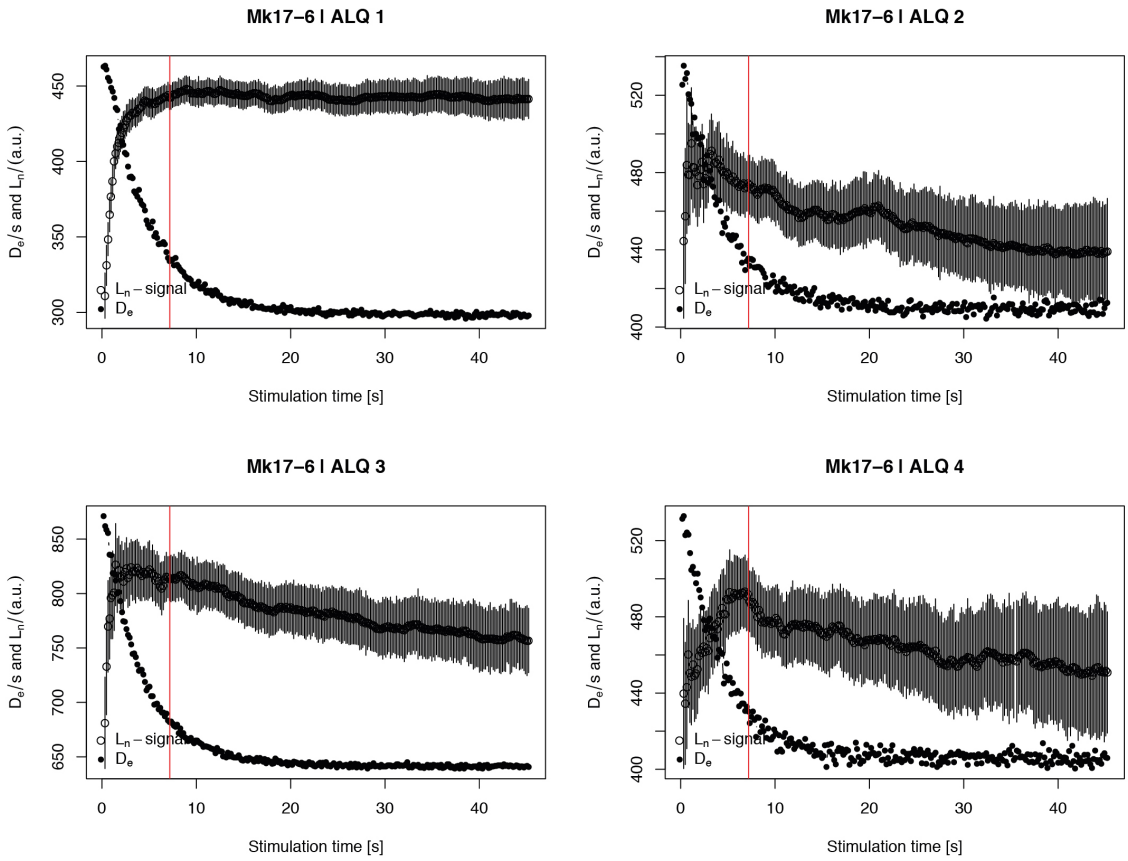


Figure 3.13: Adaptation of the $D_e(t)$ plot visualisation after Bailey et al. (2003) for sample Mk17-6. Shown are four aliquots out of 30. Each plot shows the GSL $D_e$ as a function of the signal integration limit, which here was sequentially expanded. For example, the first point shows the $D_e$ with its uncertainty for a signal integral based on channels 1–2, the second $D_e$ uses the integral of channels 1–3 and so on. For all plots, the background integral remained unchanged (channels 280–399). The vertical red line indicates the signal integral (channels 1–45, 7.2 s) chosen for the final $D_e$ estimation. The plots display a large variety of the $D_e$s as a function of the signal integral. While the $D_e$ would vary significantly for one aliquot if the signal integral changes, further tests (not shown) with signal integrals 1–20, 1–45, 1–60 showed that the resulting mean $D_e$ over all aliquots remains similar within $< 1\,\%$ of unity. These findings justify the selected channel integral of 1–45 for the final $D_e$ calculation. The discussion of the nature of the here observed $D_e$ patterns is beyond the scope of our contribution, but our findings might of interest to others. The analysis was carried out with the function `plot_DetPlot()` from the R package 'Luminescence'.

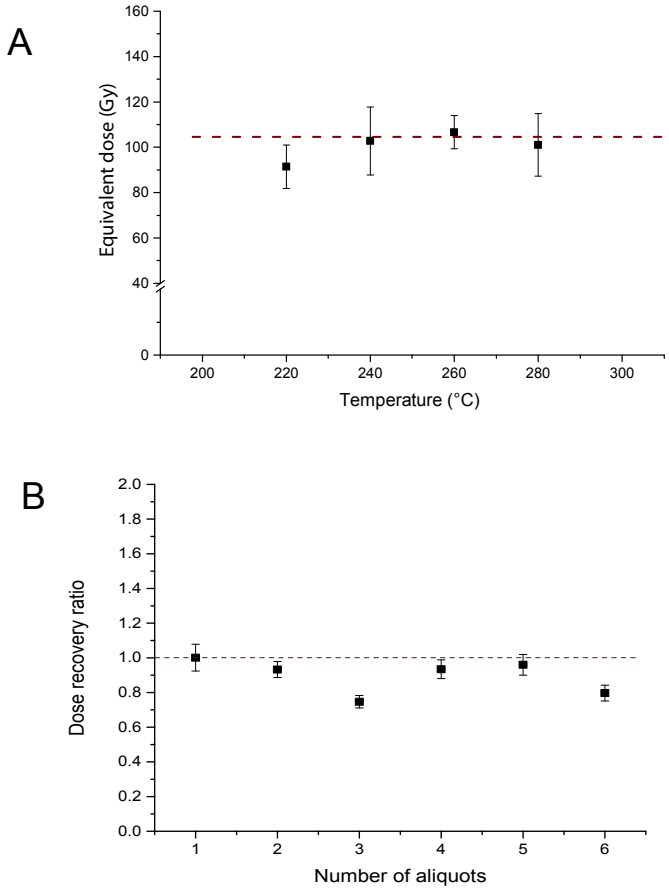


Figure 3.14: The results of the preheat-plateau test of sample Mk16-1 (A) and the dose-recovery test of sample Mk15-5 (B).

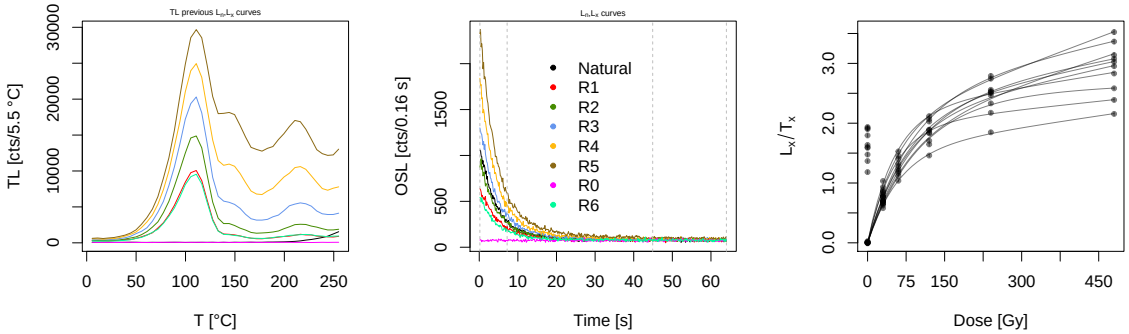


Figure 3.15: Typical TL preheat curves (left), green stimulated shine-down curves (middle) and typical dose-response curve (right) of sample Mk17-1.

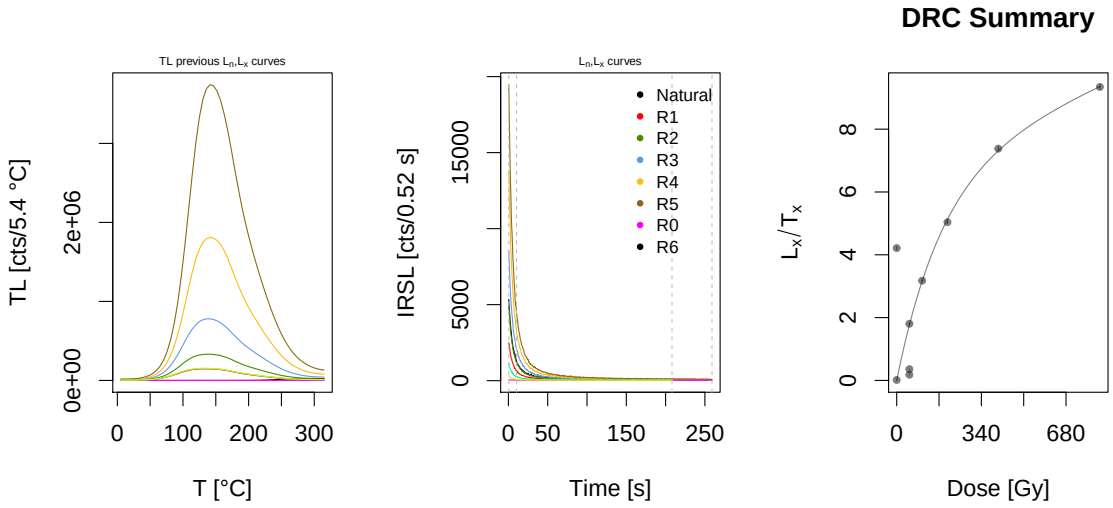


Figure 3.16: Typical TL preheat curves (left), infrared light stimulated shine-down curves (middle), and typical dose-response curves (right) of sample Mk16-4.

Table 3.4: Comparison of $D_e$ values derived by calculating the arithmetic average vs. the standard error of the mean and by applying the average dose model (Guérin et al., 2017), which takes the individual standard errors into account. The discrepancy between the results of two approaches is negligible.

| **Sample** | **Average** (Gy) | **SE** (Gy) | **ADM** (Gy) | **SE** (Gy) |
|---|---|---|---|---|
| Mk15-5 | 92 | 4 | 92 | 4 |
| Mk15-6 | 95 | 6 | 94 | 6 |
| Mk15-7 | 159 | 6 | 155 | 6 |
| Mk15-8 | 135 | 6 | 133 | 5 |
| Mk16-1 | 114 | 6 | 113 | 6 |
| Mk16-2 | 123 | 4 | 125 | 3 |
| Mk16-3 | 156 | 11 | 158 | 11 |
| Mk16-4 | 76 | 3 | 75 | 3 |
| Mk16-5 | 110 | 5 | 108 | 6 |
| Mk16-6 | 77 | 4 | 76 | 4 |
| Mk17-1 | 96 | 3 | 95 | 3 |
| Mk17-2 | 83 | 4 | 84 | 4 |
| Mk17-3 | 84 | 3 | 83 | 4 |
| Mk17-4 | 110 | 3 | 110 | 3 |
| Mk17-5 | 84 | 4 | 84 | 4 |
| Mk17-6 | 77 | 3 | 77 | 4 |
| Mk17-7 | 90 | 3 | 89 | 3 |
| Mk17-10 | 216 | 12 | 210 | 12 |

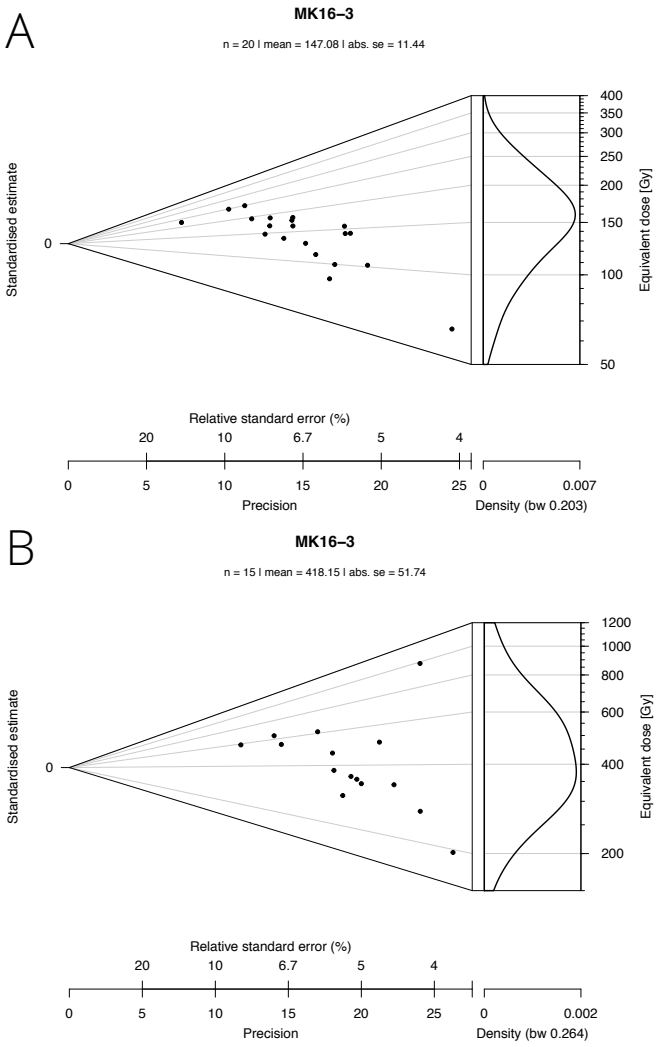


Figure 3.17: Abanico (Dietze et al., 2016) plots illustrating the $D_e$ distributions of sample Mk16-3 (A) using green OSL and infrared light stimulation (B).

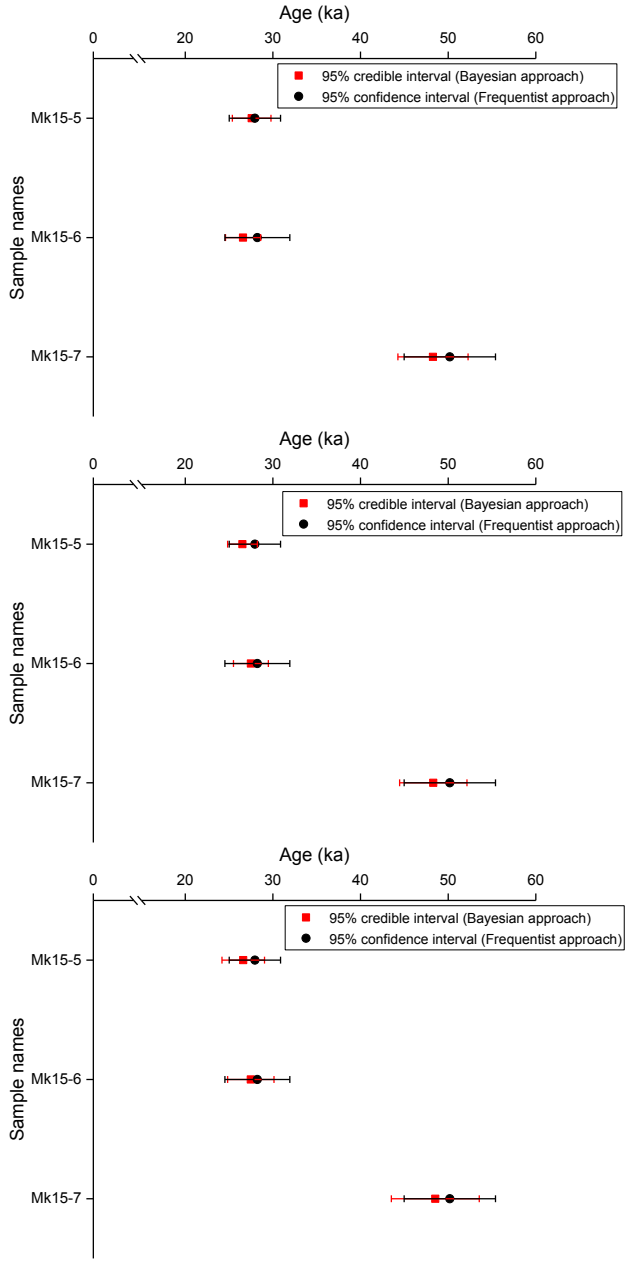


Figure 3.18: Comparing the Bayesian and frequentist chronology for three samples from the north trench for three different scenarios. Top: Simplistic Bayesian model in the explicit stratigraphy. Middle: Bayesian chronology imposing the stratigraphy order. Bottom: Bayesian chronology imposing the stratigraphy order and applying the $\Theta$ matrix. Please note that this results have not been further considered for the final age interpretation.

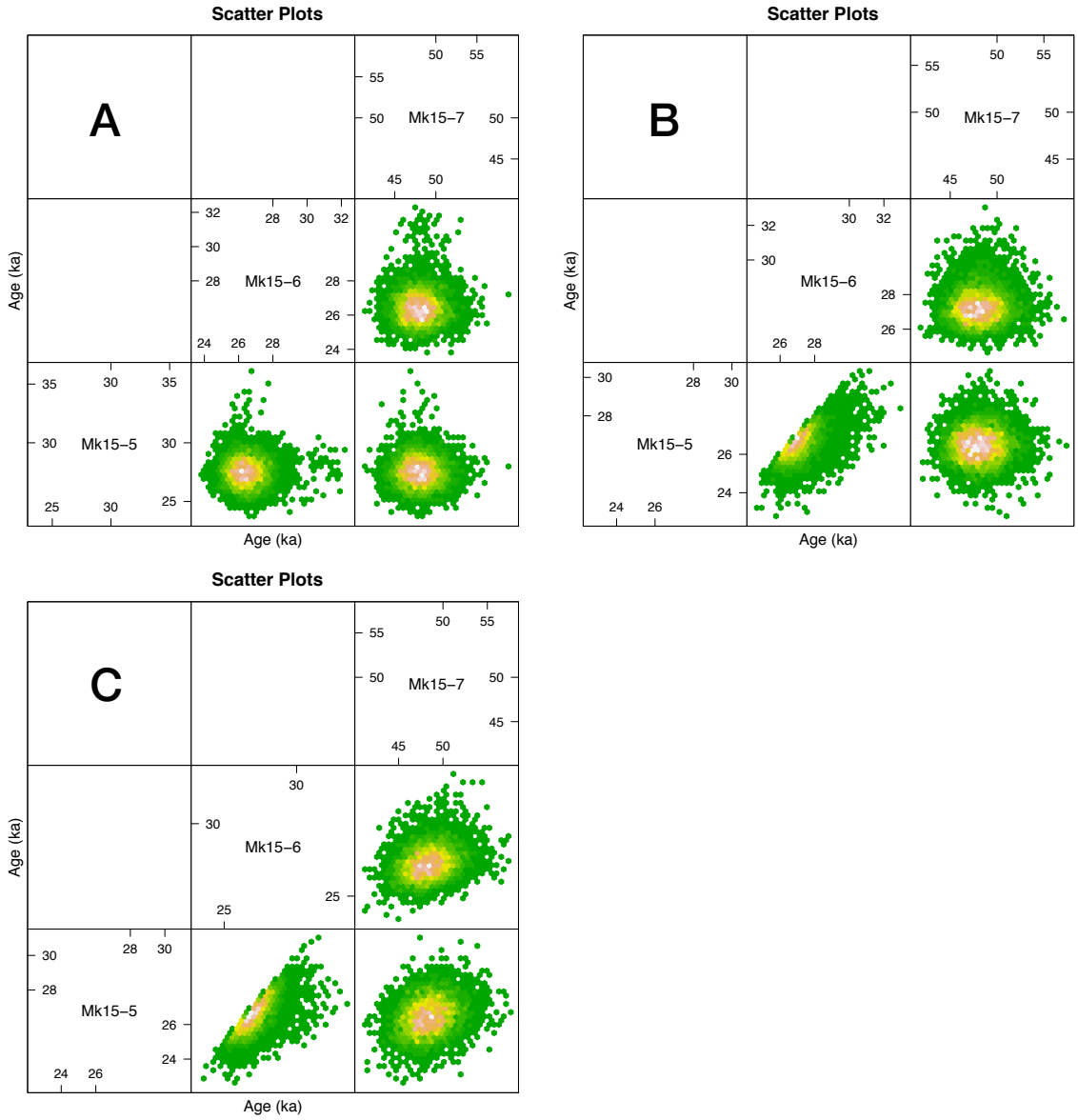


Figure 3.19: The bivariate plots of probability densities age estimation of two samples for which the hexagons correspond to the estimated ages of two samples. (A) Bivariate plots for the simplistic Bayesian modelling, (B) stratigraphy ordered model and (C) stratigraphy order model and $\Theta$ matrix. Samples show results from the north trench, which had been tested, but not further considered in the main text due to the different stimulation wavelengths used.

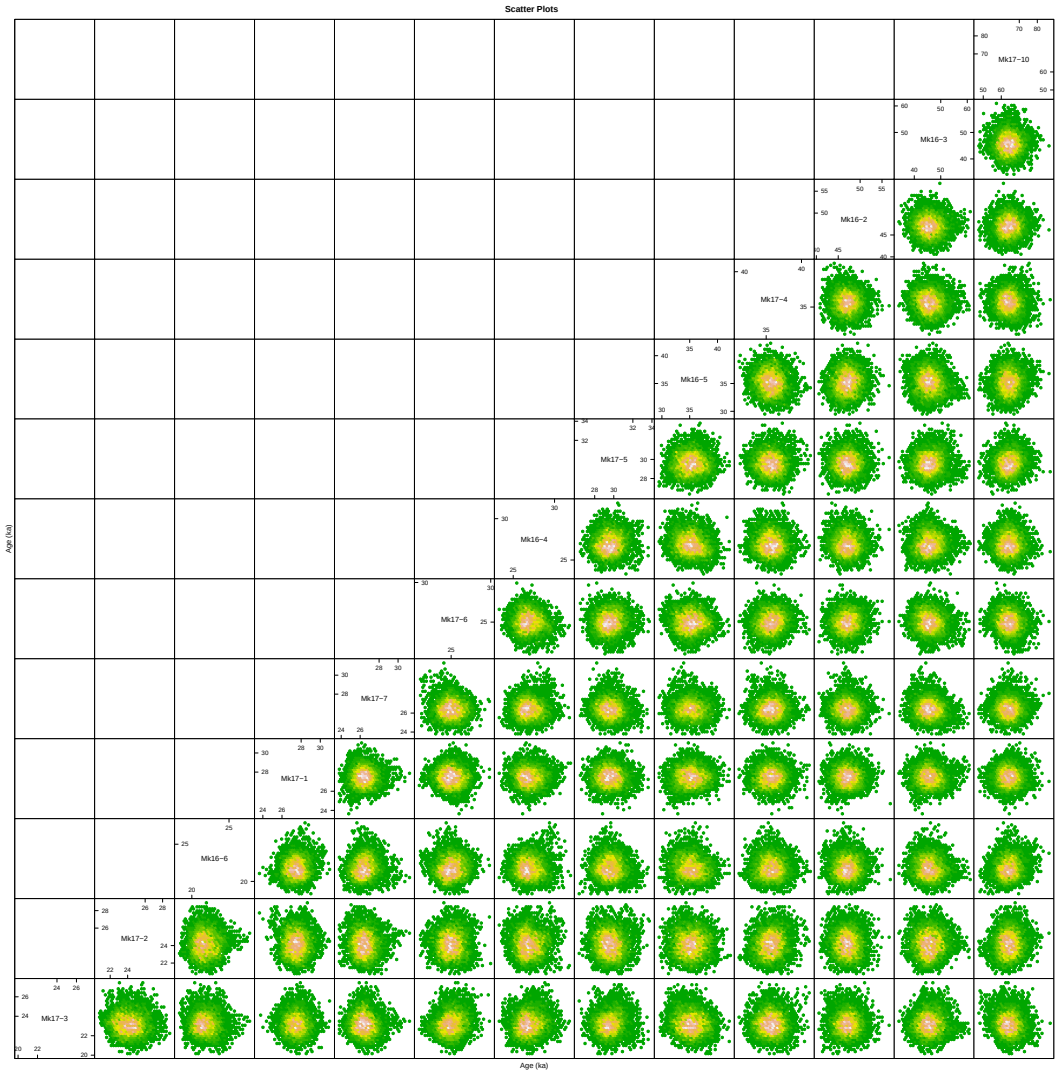


Figure 3.20: The complete bivariate plots of probability densities age estimation of 13 samples from the east trench for the simplistic model.

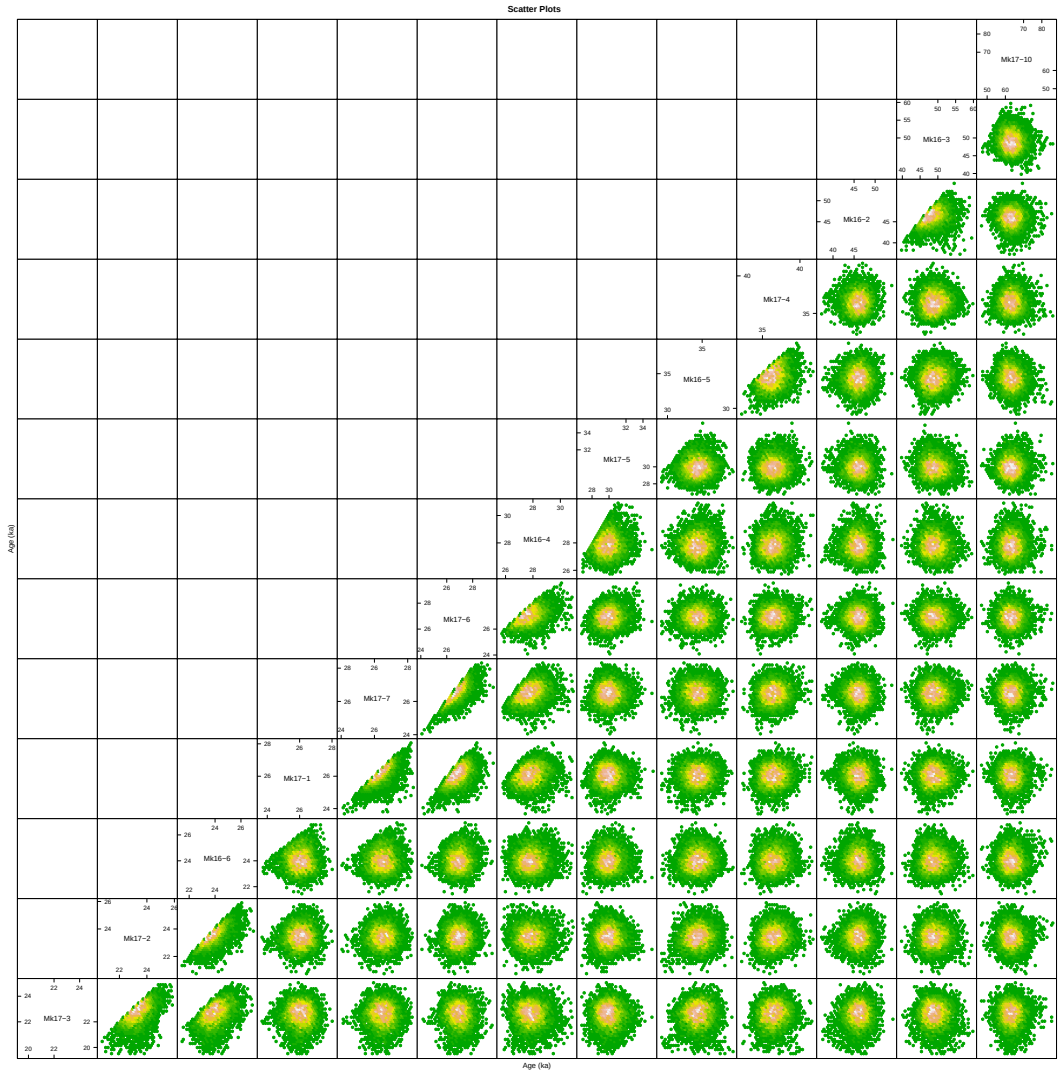


Figure 3.21: The complete bivariate plots of probability densities age estimation of 13 samples from the east trench for the model including the stratigraphic order.

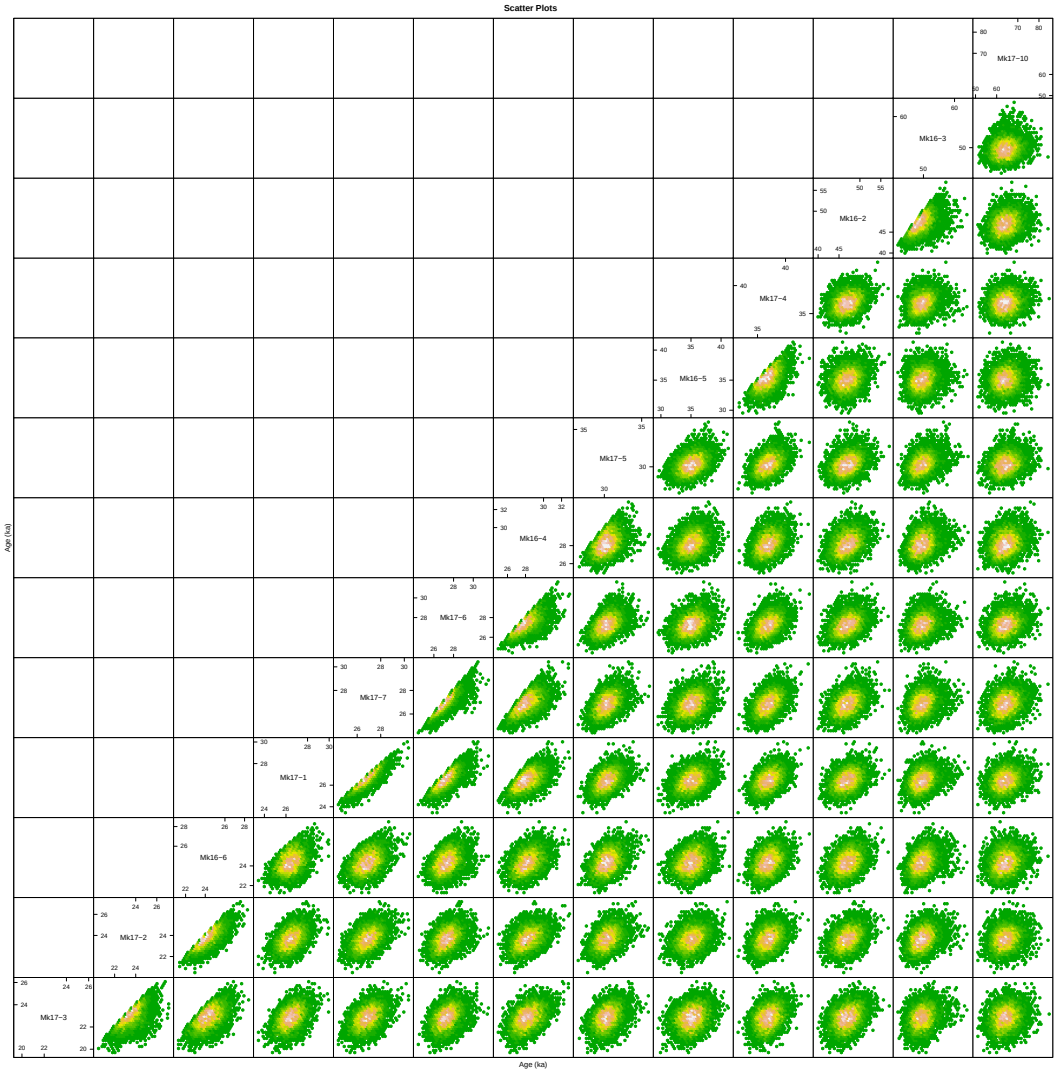


Figure 3.22: The complete bivariate plots of probability densities age estimation of 13 samples from the east trench for the model including the stratigraphic order and the Θ matrix.

### 3.7.5 Theta matrix creation

The Theta matrix ($\Theta$) is created from the covariance matrix ($\Sigma$) which is described in Combès and Philippe (2017). Here we use the implantation of $\Theta$, addressing different sources of uncertainty in luminescence dating. Below, we repeat a minor part of the equations to explain $\Theta$ and its implementation in the 'BayLum' package. For full details we refer to Combès and Philippe (2017). Imagine we have a series of samples belonging to one site for which we have measured the environmental-dose rate ($\dot{d}_i$, in Gy ka$^{-1}$) and the palaeodose ($D_i$, in Gy) to calculate the age $A_i = \frac{D_i}{\dot{d}_i}$. To address shared systematic uncertainty, 'BayLum' applies the basic statistical concept of a covariance matrix, here denoted $\Sigma$. The covariance matrix ($\Sigma$) satisfies Eq. 3.1 where $\mathcal{N}$ refers to a Gaussian distribution of those ages.

$$(D_1, ..., D_n) \sim \mathcal{N}((A_1\dot{d}_1, ..., A_n\dot{d}_n), \Sigma) \tag{3.1}$$

Diagonal elements (Eq. 3.2) refer to the systematic and individual uncertainty for each sample and non-diagonal elements (Eq. 3.3) of this matrix refer to the systematic uncertainty shared between two samples, or in other words, it shows the correlation between them. These elements are:

$$\Sigma_{i,i} = A_i^2(\sigma_{\dot{d},i}^2 + a_i^2\sigma_{\dot{d},c}^2) \tag{3.2}$$

$$\Sigma_{i,j} = A_iA_j\alpha_i\alpha_j\sigma_{\dot{d},c}^2 \tag{3.3}$$

for which $\alpha_i$ and $\alpha_j$ refer to the extent of being affected by systematic uncertainty, $\sigma_{\dot{d},i}$ is the individual statistical uncertainty (here expressed as the standard deviation) and $\sigma_{\dot{d},c}$ refers to the instrumental systematic uncertainty.

We also have another source of systematic uncertainty, which arises from the $\beta$-source calibration of our luminescence reader, named $\alpha_{lab}$. This value is determined based on the relative standard deviation deduced from the scatter of the aliquots using a particular reader as well as the gamma-irradiation uncertainty of the given dose of the calibration quartz. Then Eqs. 3.2 and 3.3 can be written as

$$\Sigma_{i,i} = A_i^2(\sigma_{\dot{d},i}^2 + \alpha_i^2\sigma_{\dot{d},c}^2 + \dot{d}_i^2\sigma_{lab}^2) \tag{3.4}$$

$$\Sigma_{i,j} = A_iA_j(\alpha_i\alpha_j\sigma_{\dot{d},c}^2 + \dot{d}_i\dot{d}_j\sigma_{lab}^2) \tag{3.5}$$

If we remove the ages ($A_i^2$) and $A_iA_j$) from the equations, the new matrix is called $\Theta$ which should be created to account for systematic uncertainty in 'BayLum'. The diagonal and non-

diagonal elements of Θ are:

$$\Theta_{i,i} = (\alpha^2_{\dot{d},i} + \alpha^2_i \sigma^2_{\dot{d},c} + \dot{d}^2_i \sigma^2_{lab}) \tag{3.6}$$

$$\Theta_{i,j} = (\alpha_i \alpha_j \sigma^2_{\dot{d},c} + \dot{d}_i \dot{d}_j \sigma^2_{lab}) \tag{3.7}$$

The source of the uncertainty on the dose rate, which we, for our study, consider mainly dominated by uncertainty in the concentration of U, K and Th, arise from the calibration of the $\gamma$-ray spectrometers ($\sigma^2_{U,cal}$, $\sigma^2_{K,cal}$, $\sigma^2_{Th,cal}$), including counting statistic uncertainty on their calibration curves. Then there is individual uncertainty on each sample measured curves ($\sigma^2_{U_i^{stat}}$, $\sigma^2_{K_i^{stat}}$, $\sigma^2_{Th_i^{stat}}$). Additionally, the uncertainty on the internal dose rate ($\sigma^2_{internal}$), is also considered a potential source of a systematic error since it affects age determinations of samples in the same direction. It is being said that $\alpha_i$ refers to the degree of influence by systematic uncertainty, corresponding to the amount of $\beta$- and $\gamma$-dose rate (simply spoken: the higher the $\beta$- or $\gamma$-dose rate the higher the relative systematic uncertainty). On the other hand, the uncertainty on the internal dose rate is the same for all samples and is therefore similarly applied to all samples. As a result, the diagonal element can be written as Eq. 3.8:

$$\begin{aligned}\Theta_{i,i} = \dot{d}^2_{\beta_i,U}(\sigma^2_{U,cal} + \sigma^2_{U_i^{stat}}) + \dot{d}^2_{\beta_i,K}(\sigma^2_{K,cal} + \sigma^2_{K_i^{stat}}) + \dot{d}^2_{\beta_i,Th}(\sigma^2_{Th,cal} + \sigma^2_{Th_i^{stat}}) + \\ \dot{d}^2_{\gamma_i,U}(\sigma^2_{U,cal} + \sigma^2_{U_i^{stat}}) + \dot{d}^2_{\gamma_i,K}(\sigma^2_{K,cal} + \sigma^2_{K_i^{stat}}) + \dot{d}^2_{\gamma_i,Th}(\sigma^2_{Th,cal} + \sigma^2_{Th_i^{stat}}) + \\ \sigma^2_{internal} + \dot{d}^2_i \sigma^2_{lab}\end{aligned} \tag{3.8}$$

The systematic and individual uncertainty for each sample can be written as $\sigma^2_{\dot{d}_i}$ which is the variance of the uncertainty in the measured final dose rate. So simply we can rewrite Eq. 3.8 to:

$$\Theta_{i,i} = \sigma^2_{\dot{d}_i} + \dot{d}^2_i \sigma^2_{lab} \tag{3.9}$$

In addition, non-diagonal yields as Eq. 3.9.

$$\begin{aligned}\Theta_{i,j} = \dot{d}_{\beta_{i,U}} \dot{d}_{\beta_{j,U}} \sigma^2_{U,cal} + \dot{d}_{\beta_{i,K}} \dot{d}_{\beta_{j,K}} \sigma^2_{K,cal} + \dot{d}_{\beta_{i,Th}} \dot{d}_{\beta_{j,Th}} \sigma^2_{Th,cal} + \\ \dot{d}_{\gamma_{i,U}} \dot{d}_{\gamma_{j,U}} \sigma^2_{U,cal} + \dot{d}_{\gamma_{i,K}} \dot{d}_{\gamma_{j,K}} \sigma^2_{K,cal} + \dot{d}_{\gamma_{i,Th}} \dot{d}_{\gamma_{j,Th}} \sigma^2_{Th,cal} + \\ \dot{d}_i \dot{d}_j \sigma^2_{lab}\end{aligned} \tag{3.10}$$

Θ, as implemented in 'BayLum', is based on Eqs. 3.7 and 3.8. The input is the relative standard deviation of the concentration of U, K and Th, the absolute standard deviation of the internal dose rate, and relative standard deviation of the $\beta$-source calibration of the reader ($^{90}$Sr/$^{90}$Y

$\beta$-source dose rate). The $\beta$-dose rate and $\gamma$-dose rate should be separated for each sample in a CSV-file. Then the function `create_ThetaMatrix()` can create a corresponded $\Theta$ matrix (cf. Sec. S4.1 for the applied **R** code).

It should be noted that the function can be also used explicitly for addressing other sources of uncertainty associated with different ways of estimating the dose rate, such as *in situ* $\gamma$-ray measurements, however the details are beyond the scope of our manuscript.

### 3.7.6 Bayesian R code and additional output graphs

#### 3.7.6.1 Theta matrix

Below we quote the code we used to create the Θ matrix using using the function `create_ThetaMatrix()` from the **R** package 'BayLum' (Philippe et al., 2019; Christophe et al., 2019) in version 0.1.4.9000-37 (package versions under development can be found under `https://github.com/crp2a/BayLum`). Two example matrices are tabulated below the code.

Listing 3.1: The code used to create the Theta matrix

```
## load package
library(BayLum)

## create template CSV-file for Theta matrix and to be filled
## with a conventional spreadsheet program
create_ThetaMatrix(output_file = "Input_Theta_matrix-18_samples.csv")

## import filled template and create Theta matrix
Theta <-
  create_ThetaMatrix(
    input = "Input_Theta_matrix-18_samples.csv",
    output_file = "Output_Theta_matrix-18_samples.csv" ,
    sigma_s = c(
      s_betaK = 0.01,
      s_betaU = 0.007,
      s_betaTh = 0.006,
      s_gammaK = 0.01,
      s_gammaU = 0.007,
      s_gammaTh = 0.006,
      s_gammaDR = 0.05,
      s_CAL = 0.02,
      s_intDR = 0.03
    )
  )
```

Table 3.5: Created Theta matrix with 2% systematic uncertainty on the source of OSL reader.

| X1 | X2 | X3 | X4 | X5 | X6 | X7 | X8 | X9 | X10 | X11 | X12 | X13 |
|---|---|---|---|---|---|---|---|---|---|---|---|---|
| 0.00756 | 0.00613 | 0.00633 | 0.00610 | 0.00602 | 0.00559 | 0.00521 | 0.00514 | 0.00565 | 0.00554 | 0.00490 | 0.00595 | 0.00602 |
| 0.00613 | 0.00732 | 0.00609 | 0.00587 | 0.00579 | 0.00539 | 0.00502 | 0.00495 | 0.00544 | 0.00534 | 0.00472 | 0.00572 | 0.00579 |
| 0.00633 | 0.00609 | 0.00796 | 0.00606 | 0.00598 | 0.00555 | 0.00518 | 0.00510 | 0.00561 | 0.00550 | 0.00486 | 0.00591 | 0.00598 |
| 0.00610 | 0.00587 | 0.00606 | 0.00723 | 0.00576 | 0.00536 | 0.00500 | 0.00493 | 0.00541 | 0.00531 | 0.00470 | 0.00570 | 0.00576 |
| 0.00602 | 0.00579 | 0.00598 | 0.00576 | 0.00756 | 0.00529 | 0.00493 | 0.00486 | 0.00534 | 0.00524 | 0.00464 | 0.00562 | 0.00569 |
| 0.00559 | 0.00539 | 0.00555 | 0.00536 | 0.00529 | 0.00616 | 0.00460 | 0.00453 | 0.00497 | 0.00488 | 0.00433 | 0.00523 | 0.00529 |
| 0.00521 | 0.00502 | 0.00518 | 0.00500 | 0.00493 | 0.00460 | 0.00487 | 0.00424 | 0.00464 | 0.00456 | 0.00405 | 0.00488 | 0.00493 |
| 0.00514 | 0.00495 | 0.00510 | 0.00493 | 0.00486 | 0.00453 | 0.00424 | 0.00526 | 0.00457 | 0.00449 | 0.00399 | 0.00481 | 0.00486 |
| 0.00565 | 0.00544 | 0.00561 | 0.00541 | 0.00534 | 0.00497 | 0.00464 | 0.00457 | 0.00732 | 0.00492 | 0.00436 | 0.00528 | 0.00534 |
| 0.00554 | 0.00534 | 0.00550 | 0.00531 | 0.00524 | 0.00488 | 0.00456 | 0.00449 | 0.00492 | 0.00749 | 0.00429 | 0.00518 | 0.00524 |
| 0.00490 | 0.00472 | 0.00486 | 0.00470 | 0.00464 | 0.00433 | 0.00405 | 0.00399 | 0.00436 | 0.00429 | 0.00900 | 0.00459 | 0.00464 |
| 0.00595 | 0.00572 | 0.00591 | 0.00570 | 0.00562 | 0.00523 | 0.00488 | 0.00481 | 0.00528 | 0.00518 | 0.00459 | 0.01384 | 0.00562 |
| 0.00602 | 0.00579 | 0.00598 | 0.00576 | 0.00569 | 0.00529 | 0.00493 | 0.00486 | 0.00534 | 0.00524 | 0.00464 | 0.00562 | 0.02161 |

Table 3.6: Created Theta matrix with 3% systematic uncertainty on the source of OSL reader.

| X1 | X2 | X3 | X4 | X5 | X6 | X7 | X8 | X9 | X10 | X11 | X12 | X13 |
|---|---|---|---|---|---|---|---|---|---|---|---|---|
| 0.01404 | 0.01232 | 0.01276 | 0.01225 | 0.01208 | 0.01115 | 0.01033 | 0.01016 | 0.01126 | 0.01104 | 0.00963 | 0.01192 | 0.01209 |
| 0.01232 | 0.01323 | 0.01222 | 0.01174 | 0.01158 | 0.01069 | 0.00990 | 0.00975 | 0.01079 | 0.01058 | 0.00923 | 0.01143 | 0.01159 |
| 0.01276 | 0.01222 | 0.01433 | 0.01216 | 0.01198 | 0.01106 | 0.01024 | 0.01008 | 0.01117 | 0.01095 | 0.00955 | 0.01183 | 0.01199 |
| 0.01225 | 0.01174 | 0.01216 | 0.01307 | 0.01151 | 0.01063 | 0.00985 | 0.00969 | 0.01074 | 0.01053 | 0.00919 | 0.01137 | 0.01152 |
| 0.01208 | 0.01158 | 0.01198 | 0.01151 | 0.01322 | 0.01048 | 0.00971 | 0.00956 | 0.01058 | 0.01038 | 0.00906 | 0.01120 | 0.01136 |
| 0.01115 | 0.01069 | 0.01106 | 0.01063 | 0.01048 | 0.01093 | 0.00898 | 0.00884 | 0.00978 | 0.00959 | 0.00838 | 0.01035 | 0.01049 |
| 0.01033 | 0.00990 | 0.01024 | 0.00985 | 0.00971 | 0.00898 | 0.00890 | 0.00820 | 0.00906 | 0.00889 | 0.00778 | 0.00959 | 0.00972 |
| 0.01016 | 0.00975 | 0.01008 | 0.00969 | 0.00956 | 0.00884 | 0.00820 | 0.00916 | 0.00892 | 0.00875 | 0.00766 | 0.00944 | 0.00957 |
| 0.01126 | 0.01079 | 0.01117 | 0.01074 | 0.01058 | 0.00978 | 0.00906 | 0.00892 | 0.01218 | 0.00968 | 0.00846 | 0.01045 | 0.01059 |
| 0.01104 | 0.01058 | 0.01095 | 0.01053 | 0.01038 | 0.00959 | 0.00889 | 0.00875 | 0.00968 | 0.01215 | 0.00830 | 0.01024 | 0.01038 |
| 0.00963 | 0.00923 | 0.00955 | 0.00919 | 0.00906 | 0.00838 | 0.00778 | 0.00766 | 0.00846 | 0.00830 | 0.01245 | 0.00894 | 0.00906 |
| 0.01192 | 0.01143 | 0.01183 | 0.01137 | 0.01120 | 0.01035 | 0.00959 | 0.00944 | 0.01045 | 0.01024 | 0.00894 | 0.01934 | 0.01121 |
| 0.01209 | 0.01159 | 0.01199 | 0.01152 | 0.01136 | 0.01049 | 0.00972 | 0.00957 | 0.01059 | 0.01038 | 0.00906 | 0.01121 | 0.02729 |

#### 3.7.6.2 Bayesian modelling code

Listing 3.2: Full Bayesian chronology

```
# clear workspace
rm(list = ls())

## load package
library(BayLum)

## set working directory
setwd("~/Mirak/Bayesian/")

## set sample names
Names <-
  c(
    "Mk17-3",
    "Mk17-2",
    "Mk16-6",
    "Mk17-1",
    "Mk17-7",
    "Mk17-6",
    "Mk16-4",
    "Mk17-5",
    "Mk16-5",
    "Mk17-4",
    "Mk16-2",
    "Mk16-3",
    "Mk17-10"
  )


DATA_OSL1 <- Generate_DataFile_MG(
  Path = c("Mk17-3/"),
  FolderNames = c("D1"),
  Nb_sample = 1,
  BinPerSample = rep(1, Nb_sample = 1)
)

DATA_OSL2 <- Generate_DataFile_MG(
  Path = c("Mk17-2/"),
  FolderNames = c("D1"),
  Nb_sample = 1,
  BinPerSample = rep(1, Nb_sample = 1)
)

DATA_OSL3 <- Generate_DataFile_MG(
  Path = c("Mk16-6/"),
  FolderNames = c("D1", "D2"),
  Nb_sample = 1,
  BinPerSample = rep(2, Nb_sample = 1)
)

```

```
DATA_OSL4 <- Generate_DataFile_MG(
  Path = c("Mk17-1/"),
  FolderNames = c("D1"),
  Nb_sample = 1,
  BinPerSample = rep(1, Nb_sample = 1)
)

DATA_OSL5 <- Generate_DataFile_MG(
  Path = c("Mk17-7/"),
  FolderNames = c("D1"),
  Nb_sample = 1,
  BinPerSample = rep(1, Nb_sample = 1)
)

DATA_OSL6 <- Generate_DataFile_MG(
  Path = c("Mk17-6/"),
  FolderNames = c("D1"),
  Nb_sample = 1,
  BinPerSample = rep(1, Nb_sample = 1)
)

DATA_OSL7 <- Generate_DataFile_MG(
  Path = c("Mk16-4/"),
  FolderNames = c("D1", "D2"),
  Nb_sample = 1,
  BinPerSample = rep(2, Nb_sample = 1)
)

DATA_OSL8 <- Generate_DataFile_MG(
  Path = c("Mk17-5/"),
  FolderNames = c("D1"),
  Nb_sample = 1,
  BinPerSample = rep(1, Nb_sample = 1)
)

DATA_OSL9 <- Generate_DataFile_MG(
  Path = c("Mk16-5/"),
  FolderNames = c("D1", "D2"),
  Nb_sample = 1,
  BinPerSample = rep(2, Nb_sample = 1)
)

DATA_OSL10 <- Generate_DataFile_MG(
  Path = c("Mk17-4/"),
  FolderNames = c("D1"),
  Nb_sample = 1,
  BinPerSample = rep(1, Nb_sample = 1)
)

DATA_OSL11 <- Generate_DataFile_MG(
  Path = c("Mk16-2/"),
  FolderNames = c("D1", "D2"),
  Nb_sample = 1,
```

```
  BinPerSample = rep(2, Nb_sample = 1)
)

DATA_OSL12 <- Generate_DataFile_MG(
  Path = c("Mk16-3/"),
  FolderNames = c("D1", "D2"),
  Nb_sample = 1,
  BinPerSample = rep(2, Nb_sample = 1)
)

DATA_OSL13 <- Generate_DataFile_MG(
  Path = c("Mk17-10/"),
  FolderNames = c("D1"),
  Nb_sample = 1,
  BinPerSample = rep(1, Nb_sample = 1)
)

## combine DataFiles to produce DATA
DATA <- combine_DataFiles(
  DATA_OSL1,
  DATA_OSL2,
  DATA_OSL3,
  DATA_OSL4,
  DATA_OSL5,
  DATA_OSL6,
  DATA_OSL7,
  DATA_OSL8,
  DATA_OSL9,
  DATA_OSL10,
  DATA_OSL11,
  DATA_OSL12,
  DATA_OSL13
)

## get number of samples
Nb_sample <- length(Names)

##Age calculation in stratigraphic constraints
SC <- SC_Ordered(Nb_sample = Nb_sample)

SC <- matrix(data = 0, ncol = Nb_sample, nrow = 14)
SC[1, ] <- c(1, 1, 1, 1, 1, 1, 1, 1, 1, 1, 1, 1, 1)
SC[2, ] <- c(0, 1, 1, 1, 1, 1, 1, 1, 1, 1, 1, 1, 1)
SC[3, ] <- c(0, 0, 1, 1, 1, 1, 1, 1, 1, 1, 1, 1, 1)
SC[4, ] <- c(0, 0, 0, 1, 1, 1, 1, 1, 1, 1, 1, 1, 1)
SC[5, ] <- c(0, 0, 0, 0, 1, 1, 1, 1, 1, 1, 1, 1, 1)
SC[6, ] <- c(0, 0, 0, 0, 0, 1, 1, 1, 1, 1, 1, 1, 1)
SC[7, ] <- c(0, 0, 0, 0, 0, 0, 1, 1, 1, 1, 1, 1, 1)
SC[8, ] <- c(0, 0, 0, 0, 0, 0, 0, 1, 1, 1, 1, 1, 1)
SC[9, ] <- c(0, 0, 0, 0, 0, 0, 0, 0, 1, 1, 1, 1, 1)
SC[10, ] <- c(0, 0, 0, 0, 0, 0, 0, 0, 0, 1, 1, 1, 1)
SC[11, ] <- c(0, 0, 0, 0, 0, 0, 0, 0, 0, 0, 1, 1, 1)
SC[12, ] <- c(0, 0, 0, 0, 0, 0, 0, 0, 0, 0, 0, 1, 1)
```

```
SC[13, ] <- c(0, 0, 0, 0, 0, 0, 0, 0, 0, 0, 0, 0, 1)
SC[14, ] <- c(0, 0, 0, 0, 0, 0, 0, 0, 0, 0, 0, 0, 0)

## Age calculation considering Theta matrix
PathCM <- c("")
Theta <- paste0(PathCM, "Theta.csv")
errorMatrix <- read.csv(Theta, sep = ",")
Theta <- as.matrix(errorMatrix)

## Full Bayesian chronology
## (comment / uncomment lines to try different scenarios)
A <-
  AgeS_Computation(
    DATA,
    SampleNames = Names,
    Nb_sample = 13,
    PriorAge = c(10, 40, 10, 40, 10, 40, 20, 40, 20, 40, 20, 40,  20, 40,
                 20, 50, 20, 60, 20, 60, 30, 70, 30, 70, 40, 92),
    BinPerSample = c(1, 1, 2, 1, 1, 1, 2, 1, 2, 1, 2, 2, 1),
    SavePdf = TRUE,
    OutputFileName = c("Theta"),
    OutputFilePath = c("Bayesian_Output/"),
    SaveEstimates = TRUE,
    OutputTableName = c("Theta"),
    OutputTablePath = c("Bayesian_Output/"),
    ## THETA = Theta,
    ## sepTHETA = c(","),
    StratiConstraints = SC,
    sepSC = c(","),
    LIN_fit = TRUE,
    Origin_fit = TRUE,
    distribution = c("gaussian"),
    Iter = 4000000,
    t = 5,
    n.chains = 3
    ##jags_method = "rjparallel",
    ##max.time="2h"
  )

## return scatter plots
plot_Scatterplots(
  object = A$Sampling,
  variables = c("A"),
  sample_names = Names,
  sample_selection = c(1:13)
)
```

### 3.7.6.3 MCMC output examples

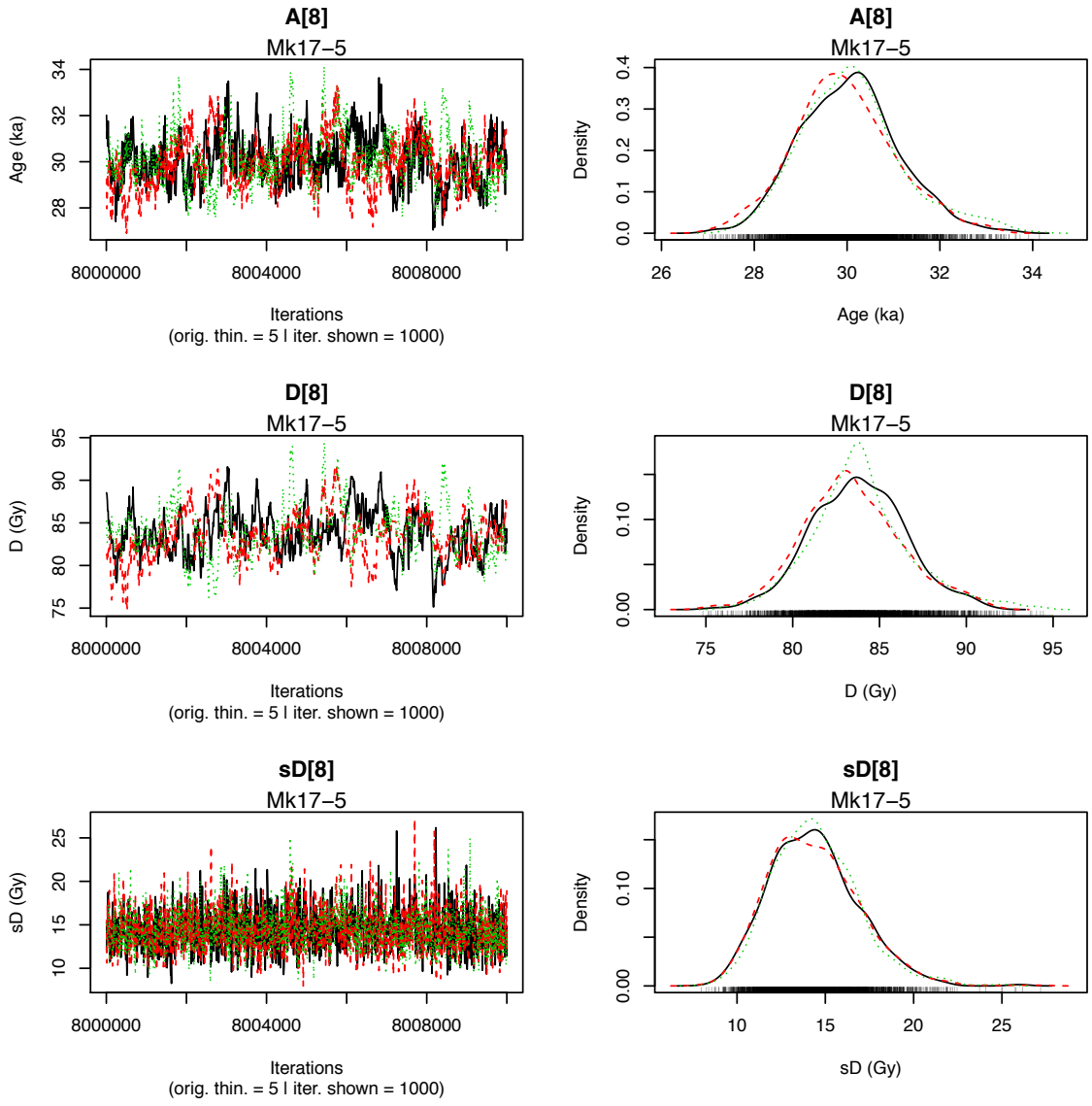


Figure 3.23: Example MCMC plots for sample Mk17-5 from the east trench.

#### 3.7.6.4 Additional age comparison (East trench)

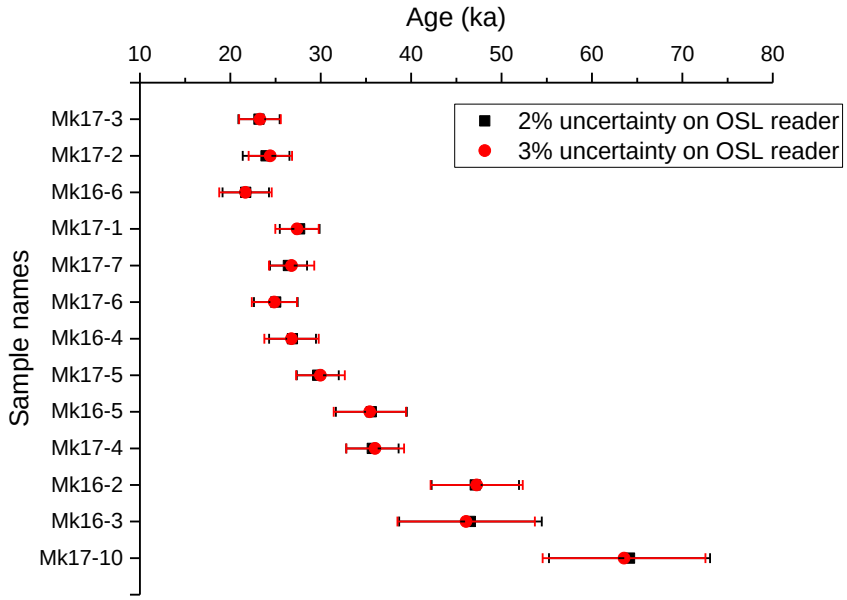


Figure 3.24: Comparison the Bayesian chronology of the East trench considering Theta matrix only, which is created with 2 % and 3 % systematic uncertainty on the source-dose rate of the OSL reader.

## Study II: References

Aitken, M. J.: Thermoluminescence dating, Studies in archaeological science, Academic Press, 1985.

Antoine, P., Bahain, J. J., Ghaleb, B., and Mercier, N.: The chronostratigraphic framework at Garm roud, in: Garm Roud. A Hunting Place in Iran, Upper Palaeolithic, edited by Berillon, G. and Asgari Khanegah, A., pp. 49–55, Editions IFRI & @rchéo-éditions (French- English-Persian), 2016.

Bailey, R. M.: Towards a general kinetic model for optically and thermally stimulated luminescence of quartz, Radiation Measurements, 33, 17–45, 2001.

Bailey, R. M.: Direct measurement of the fast component of quartz optically stimulated luminescence and implications for the accuracy of optical dating, Quaternary Geochronology, 5, 559–568, 2010.

Bailey, R. M., Singarayer, J. S., Ward, S., and Stokes, S.: Identification of partial resetting using De as a function of illumination time, Radiation Measurements, 37, 511–518, 2003.

Bailey, R. M., Yukihara, E. G., and McKeever, S. W. S.: Separation of quartz optically stimulated luminescence components using green (525 nm) stimulation, Radiation Measurements, 46, 643–648, 2011.

Bazgir, B., Ollé, A., Tumung, L., Becerra-Valdivia, L., Douka, K., Higham, T., van der Made, J., Picin, A., Saladié, P., López-García, J. M., Blain, H.-A., Allue, E., Fernández-García, M., Rey-Rodríguez, I., Arceredillo, D., Bahrololoumi, F., Azimi, M., Otte, M., and Carbonell, E.: Understanding the emergence of modern humans and the disappearance of Neanderthals: Insights from Kaldar Cave (Khorramabad Valley, Western Iran), Scientific Reports, 7, 525–16, 2017.

Becerra-Valdivia, L., Douka, K., Comeskey, D., Bazgir, B., Conard, N. J., Marean, C. W., Ollé, A., Otte, M., Tumung, L., Zeidi, M., and Higham, T. F. G.: Chronometric investigations of the Middle to Upper Paleolithic transition in the Zagros Mountains using AMS radiocarbon dating and Bayesian age modelling, Journal of Human Evolution, 109, 57–69, 2017.

Berillon, G. and Asgari Khaneghah, A., eds.: Garm Roud. A Hunting Place in Iran, Upper Palaeolithic, Editions IFRI & @rchéo-éditions (French- English-Persian), 2016.

Berillon, G., Khaneghah, A. A., Antoine, P., Bahain, J.-J., Chevrier, B., Zeitoun, V., Aminzadeh, N., Beheshti, M., Chanzanagh, H. E., and Nochadi, S.: Discovery of new open-air Paleolithic localities in Central Alborz, Northern Iran, Journal of Human Evolution, 52, 380–387, 2007.

Berillon, G., Nasab, H. V., Asgari Khaneghah, A., Jamet, G., Akhavan, M., Guérin, G., Heydari, M., Anvari, Z., Auguste, P., Bonilauri, S., Chevrier, B., Zeitoun, V., Mohammadkhani, K., Hashemi, M., Jayez, M., and Darvishi, J.: *Fouille du site Mirak 8:* Rapport Annuel. Programme Paléoanthropologique Franco-Iranien (FIPP), Tech. rep., 2017.

Biglari, F.: Recent Finds of Paleolithic Period from Bisitun, Central Western Zagros Mountains, Iranian Journal of Archaeology and History, 28, 50–60, 2001.

Bond, G.: A Pervasive Millennial-Scale Cycle in North Atlantic Holocene and Glacial Climates, Science, 278, 1257–1266, 1997.

Bos, A. J. J. and Wallinga, J.: How to visualize quartz OSL signal components, Radiation Measurements, 47, 752–758, 2012.

Buck, C. E. and Meson, B.: On being a goodBayesian, World Archaeology, 47, 567–584, 2015.

Buck, C. E. and Millard, A. R.: Tools for Constructing Chronologies - Crossing Disciplinary Boundaries, vol. 177 of *Lecture Notes in Statistics*, Springer, 2004.

Bulur, E.: An Alternative Technique For Optically Stimulated Luminescence (OSL) Experiment, Radiation Measurements, 26, 701–709, 1996.

Bulur, E.: A simple transformation for converting CW-OSL curves to LM-OSL curves, Radiation Measurements, 32, 141–145, 2000.

Buylaert, J. P., Jain, M., Murray, A. S., Thomsen, K. J., Thiel, C., and Sohbati, R.: A robust feldspar luminescence dating method for Middle and Late Pleistocene sediments, Boreas, 41, 435–451, 2012.

Carlin, B. P. and Louis, T. A.: Bayes and Empirical Bayes Methods for Data Analysis , Chapman & Hall/CRC, 2nd edn., 2000.

Chen, R., Kirsh, Y., and Townsend, P. D.: Models for the sensitization of thermoluminescence in silica fibres, International Journal of Radiation Applications and Instrumentation. Part D. Nuclear Tracks and Radiation Measurements, 18, 13–17, 1991.

Chevrier, B.: The lithic assemblage from Gram Roud, in: Garm Roud. A Hunting Place in Iran, Upper Palaeolithic, edited by Berillon, G. and Asgari Khaneghah, A., pp. 63–69, Editions IFRI & @rchéo-éditions (French- English-Persian), 2016.

Choi, J. H., Duller, G. A. T., and Wintle, A. G.: Analysis of quartz LM-OSL curves, Ancient TL, 24, 9–20, 2006.

Christophe, C., Philippe, A., Kreutzer, S., and Guérin, G.: BayLum: Chronological Bayesian Models Integrating Optically Stimulated Luminescence and Radiocarbon Age Dating, CRAN, Version: 0.1.4, URL `https://cran.r-project.org/package=BayLum`, http://github.com/crp2a/BayLum, 2019.

Combès, B. and Philippe, A.: Bayesian analysis of individual and systematic multiplicative errors for estimating ages with stratigraphic constraints in optically stimulated luminescence dating, Quaternary Geochronology, 39, 24–34, 2017.

Combès, B., Philippe, A., Lanos, P., Mercier, N., Tribolo, C., Guérin, G., Guibert, P., and Lahaye, C.: A Bayesian central equivalent dose model for optically stimulated luminescence dating, Quaternary Geochronology, 28, 62–70, 2015.

Conard, N. J. and Ghasidian, E.: The Rostamian cultural group and thetaxonomy of the Iranian Upper Paleolithic, in: Between Sand and Sea. The Archaeology and Human Ecology of Southwestern Asia, edited by Conard, N. J., Drechsler, P., and Morales, A., pp. 33–52, Kerns Verlag, Tübingen,Germany, 2011.

Conard, N. J., Ghasidian, E., and Heydari-Guran, S.: The open-air Late Paleolithic site of Bardia and the Paleolithic occupation of the Galeh Gusheh sand dunes, Esfahan province, Iran, in: Iran Paleolithic, Le Paléolithique d'Iran, edited by Otte, M., Biglari, F., and Jaubert, J., pp. 141–154, Bar International Series, 2009.

Dansgaard, W., Johnsen, S. J., Clausen, H. B., Dahl-Jensen, D., Gundestrup, N. S., Hammer, C. U., Hvidberg, C. S., Steffensen, J. P., Sveinbjörnsdottir, A. E., Jouzel, J., and Bond, G.: Evidence for general instability of past climate from a 250-kyr ice-core record, Nature, 364, 218–220, 1993.

Dennell, R.: Human Colonization of Asia in the Late Pleistocene: The History of an Invasive Species, Current Anthropology, 58, S383–S396, 2017.

Dibble, H. L.: The Mousterian Industry from Bisitun Cave (Iran), Paléorient, 10, 23–34, 1984.

Dietze, M., Kreutzer, S., Burow, C., Fuchs, M. C., Fischer, M., and Schmidt, C.: The abanico plot: visualising chronometric data with individual standard errors, Quaternary Geochronology, 31, 12–18, 2016.

Duller, G. A. T.: Distinguishing quartz and feldspar in single grain luminescence measurements, Radiation Measurements, 37, 161–165, 2003.

Duller, G. A. T.: The Analyst software package for luminescence data: overview and recent improvements , Ancient TL, 33, 35–42, 2015.

Durcan, J. A., King, G. E., and Duller, G. A. T.: DRAC: Dose Rate and Age Calculator for trapped charge dating, Quaternary Geochronology, 28, 54–61, 2015.

Gelman, A., Carlin, J. B., Stern, H. S., Dunson, D. B., Vehtari, A., and Rubin, D. B.: Bayesian Data Analysis, Third Edition, CRC Press, 2013.

Ghasidian, E.: The Early Upper Paleolithic Occupation at Ghār-e Boof Cave: A Reconstruction of Cultural Tradition in the Southern Zagros Mountains of Iran, Kerns Verlag, Tübingen, 2014.

Ghasidian, E., Heydari-Guran, S., and Mirazón Lahr, M.: Upper Paleolithic cultural diversity in the Iranian Zagros Mountains and the expansion of modern humans into Eurasia, Journal of Human Evolution, 132, 101–118, 2019.

Guérin, G. and Mercier, N.: Preliminary insight into dose deposition processes in sedimentary media on a scale of single grains: Monte Carlo modelling of the effect of water on the gamma dose rate, Radiation Measurements, 47, 541–547, 2012.

Guérin, G., Mercier, N., and Adamiec, G.: Dose-rate conversion factors: update, Ancient TL, 29, 5–9, 2011.

Guérin, G., Mercier, N., Nathan, R., Adamiec, G., and Lefrais, Y.: On the use of the infinite matrix assumption and associated concepts: A critical review, Radiation Measurements, 47, 778–785, 2012.

Guérin, G., Frouin, M., Talamo, S., Aldeias, V., Bruxelles, L., Chiotti, L., Dibble, H. L., Goldberg, P., Hublin, J.-J., Jain, M., Lahaye, C., Madelaine, S., Maureille, B., McPherron, S. J. P., Mercier, N., Murray, A. S., Sandgathe, D., Steele, T. E., Thomsen, K. J., and Turq, A.: A multi-method luminescence dating of the Palaeolithic sequence of La Ferrassie based on new excavations adjacent to the La Ferrassie 1 and 2 skeletons, Journal of Archaeological Science, 58, 147–166, 2015.

Guérin, G., Christophe, C., Philippe, A., Murray, A. S., Thomsen, K. J., Tribolo, C., Urbanova, P., Jain, M., Guibert, P., Mercier, N., Kreutzer, S., and Lahaye, C.: Absorbed dose, equivalent dose, measured dose rates, and implications for OSL age estimates: Introducing the Average Dose Model, Quaternary Geochronology, 41, 1–32, 2017.

Guibert, P. and Schvoerer, M.: TL dating: Low background gamma spectrometry as a tool for the determination of the annual dose, International Journal of Radiation Applications and Instrumentation. Part D. Nuclear Tracks and Radiation Measurements, 18, 231–238, 1991.

Guibert, P., Lahaye, C., and Bechtel, F.: The importance of U-series disequilibrium of sediments in luminescence dating: A case study at the Roc de Marsal Cave (Dordogne, France), Radiation Measurements, 44, 223–231, 2009.

Hansen, V., Murray, A., Buylaert, J.-P., Yeo, E.-Y., and Thomsen, K.: A new irradiated quartz for beta source calibration, Radiation Measurements, 81, 123–127, 2015.

Hashemi, M., Vahdati Nasab, H., Berillon, G., Jamet, G., Azizi, Q., Jayez, M., Guérin, G., Heydari, M., Kharazian Akhavan, M., Nateghi, A., and Abdollahi, A.: The late Pleistocene in the northern fringes of Iranian central desert and the formation of archaeological sites; case study: Mirak, Semnan, Quater. J. Iran, 3, 405–430, 2018.

Heinrich, H.: Origin and Consequences of Cyclic Ice Rafting in the Northeast Atlantic Ocean During the Past 130,000 Years, Quaternary Research, 29, 142–152, 1988.

Heydari, M. and Guérin, G.: OSL signal saturation and dose rate variability: Investigating the behaviour of different statistical models, Radiation Measurements, 120, 96–103, 2018.

Heydari-Guran, S. and Ghasidian, E.: The MUP Zagros Project: tracking the Middle–Upper Palaeolithic transition in the Kermanshah region, west-central Zagros, Iran, Antiquity, 91, 40–7, 2017.

Heydari-Guran, S., Ghasidian, E., and Conard, N.: Middle Paleolithic settlements on the Iranian Central plateau, in: Settlement Dynamics of the Middle Paleolithic and Middle Stone Age, edited by Conard, N. and Delagnes, A., pp. 171–203, Tübingen Publication in Prehistory, 2014.

Huntley, D. J. and Baril, M. R.: The K content of the K-feldspars being measured in optical dating or in the thermoluminescence dating, Ancient TL, 15, 11–13, 1997.

Huntley, D. J., Godfrey-Smith, D. I., and Thewalt, M. L. W.: Optical dating of sediments, Nature, 313, 105–107, 1985.

Huntriss, A.: A Bayesian analysis of luminescence dating , Ph.D. thesis, University of Durham, URL `http://etheses.dur.ac.uk/2928/1/2928-759.pdf?UkUDh:CyT`, 2008.

Jain, M., Murray, A. S., and Bøtter-Jensen, L.: Characterisation of blue-light stimulated luminescence components in different quartz samples: implications for dose measurement, Radiation Measurements, 37, 441–449, 2003.

Kharazian Akhavan, M., Jamet, G., Puaud, S., Heydari, M., Guérin, G., Hashemi, M., Vahdati Nasab, H., and Berillon, G.: The geoarchaeological study of Paleolithic open-air site of Mirak (Semnan, Iran) using sedimentological and physical-chemical analysis, Quater. J. Iran, 4, 273–290, 2018.

Kreutzer, S., Schmidt, C., Fuchs, M. C., Dietze, M., Fischer, M., and Fuchs, M.: Introducing an R package for luminescence dating analysis, Ancient TL, 30, 1–8, 2012.

Kreutzer, S., Burow, C., Dietze, M., Fuchs, M. C., Schmidt, C., Fischer, M., and Friedrich, J.: Luminescence: Comprehensive Luminescence Dating Data Analysis, URL `https://CRAN.R-project.org/package=Luminescence`, r package version 0.8.5, 2019.

Lahaye, C., Guérin, G., Gluchy, M., Hatté, C., Fontugne, M., Clemente-Conte, I., Santos, J. C., Villagran, X. S., Da Costa, A., Borges, C., Guidon, N., and Boëda, E.: Another site, same old song: The Pleistocene-Holocene archaeological sequence of Toca da Janela da Barra do Antonião-North, Piauí, Brazil, Quaternary Geochronology, 49, 223–229, 2019.

Liritzis, I., Singhvi, A. K., Feathers, J. K., Wagner, G. A., Kadereit, A., Zacharias, N., and Li, S.-H.: Luminescence Dating in Archaeology, Anthropology, and Geoarchaeology, SpringerBriefs in Earth System Sciences, Springer International Publishing, Heidelberg, 2013.

Lisiecki, L. E. and Raymo, M. E.: A Pliocene-Pleistocene stack of 57 globally distributed benthic $\delta\ ^{18}$O records, Paleoceanography, 20, 1–17, 2005.

Martin, L.: Caractérisation et modélisation d'objets archéologiques en vue de leur datation par des méthodes paléo-dosimétriques. Simulation des paramètres dosimétriques sous Geant4., Ph.D. thesis, Université Bordeaux Montaigne, 2015.

McKeever, S. W. S.: Mechanisms of thermoluminescence production: Some problems and a few answers?, International Journal of Radiation Applications and Instrumentation. Part D. Nuclear Tracks and Radiation Measurements, 18, 5–12, 1991.

Mehterian, S., Pourmand, A., Sharifi, A., Lahijani, H. A. K., Naderi, M., and Swart, P. K.: Speleothem records of glacial/interglacial climate from Iran forewarn of future Water Availability in the interior of the Middle East, Quaternary Science Reviews, 164, 187–198, 2017.

Mejdahl, V.: Internal radioactivity in quartz and feldspar grains, Ancient TL, 5, 10–17, 1987.

Mercier, N., Kreutzer, S., Christophe, C., Guérin, G., Guibert, P., Lahaye, C., Lanos, P., Philippe, A., and Tribolo, C.: Bayesian statistics in luminescence dating: The 'baSAR'-model and its implementation in the R package 'Luminescence', Ancient TL, 34, 14–21, 2016.

Murray, A. S. and Wintle, A. G.: Luminescence dating of quartz using an improved single-aliquot regenerative-dose protocol, Radiation Measurements, 32, 57–73, 2000.

Murray, A. S., Thomsen, K. J., Masuda, N., Buylaert, J. P., and Jain, M.: Identifying well-bleached quartz using the different bleaching rates of quartz and feldspar luminescence signals, Radiation Measurements, 47, 688–695, 2012.

Nasab, H. V., Clark, G. A., and Torkamandi, S.: Late Pleistocene dispersal corridors across the Iranian Plateau: A case study from Mirak, a Middle Paleolithic site on the northern edge of the Iranian Central desert (Dasht-e Kavir), Quaternary International, 300, 267–281, 2013.

Nathan, R. P.: Numerical modelling of environmental dose rate and its application to trapped-charge dating, Ph.D. thesis, St Hugh's College, Oxford, URL https://ora.ox.ac.uk/objects/ora:6421, 2010.

Nathan, R. P. and Mauz, B.: On the dose-rate estimate of carbonate-rich sediments for trapped charge dating, Radiation Measurements, 43, 14–25, 2008.

Okladnikow, A. P.: Investigations of the mousterian site and the neanderthal burial at the teshik-tash grotto, south Uzbekistan (central Asia), in: Teshik Tash Paleolithic Man, edited by Gremiatsky, M. A. and Nesturkh, M. F., pp. 7–85, Moscow State University, Moscow, 1949.

Olszewski, D. I. and Dibble, H. L.: The Zagros Aurignacian, Current Anthropology, 35, 68–75, 1994.

Orton, C., Buck, C. E., Cavanagh, W. G., and Litton, C. D.: Bayesian Approach to Interpreting Archaeological Data, American Journal of Archaeology, 102, 187–3, 1998.

Otte, M., Biglari, F., Flas, D., Shidrang, S., Zwyns, N., Mashkour, M., Naderi, R., Mohaseb, A., Hashemi, N., Darvish, J., and Radu, V.: The Aurignacian in the Zagros region: new research at Yafteh Cave, Lorestan, Iran, Antiquity, 81, 82–96, 2007.

Otte, M., Shidrang, S., Zwyns, N., and Flas, D.: New radiocarbon dates for the Zagros Aurignacian from Yafteh cave, Iran, Journal of Human Evolution, 61, 340–346, 2011.

Philippe, A., Guérin, G., and Kreutzer, S.: BayLum - An R package for Bayesian analysis of OSL ages: An introduction, Quaternary Geochronology, 49, 16–24, 2019.

Porat, N., Faerstein, G., Medialdea, A., and Murray, A. S.: Re-examination of common extraction and purification methods of quartz and feldspar for luminescence dating, Ancient TL, 33, 22–30, 2015.

Prescott, J. R. and Hutton, J. T.: Cosmic ray contributions to dose rates for luminescence and ESR dating: Large depths and long-term time variations, Radiation Measurements, 23, 497–500, 1994.

Prescott, J. R. and Stephan, L. G.: The contribution of cosmic radiation to the environmental dose for thermoluminescence dating. Latitude, altitude and depth dependences, PACT 3 - Revue du Réseau Européen de Sciences et Techniques appliquées au Patrimoine Culturel, pp. 17–25, 1982.

Preusser, F., Degering, D., Fuchs, M., Hilgers, A., Kadereit, A., Klasen, N., Krbetschek, M. R., Richter, D., and Spencer, J. Q. G.: Luminescence dating: basics, methods and applications, Eiszeitalter und Gegenwart (Quaternary Science Journal), 57, 95–149, 2008.

R Core Team: R: A Language and Environment for Statistical Computing, Vienna, Austria, URL https://r-project.org, 2019.

Rezvani, H.: Settlement patterns of prehistoric cultures in Semnan Province, in: 32 Articles in Memory of E. Negahban, edited by Alizadeh, A., Majidzadeh, Y., and Malek Shahmirzadi, S., pp. 7–19, Tehran University Press, Tehran, 1990.

Rezvani, H. and Vahdati Nasab, H.: A major paleolithic open site at Mirak, Semnan province, Iran, Antiquity Project Gallery, 84, 2010.

Rhodes, E. J., Bronk Ramsey, C., Outram, Z., Batt, C., Willis, L., Dockrill, S., and Bond, J.: Bayesian methods applied to the interpretation of multiple OSL dates: high precision sediment ages from Old Scatness Broch excavations, Shetland Isles, Quaternary Science Reviews, 22, 1231–1244, 2003.

Richter, D., Richter, A., and Dornich, K.: lexsyg — a new system for luminescence research, Geochronometria, 40, 220–228, 2013.

Richter, D., Richter, A., and Dornich, K.: Lexsyg smart — a luminescence detection system for dosimetry, material research and dating application, Geochronometria, 42, 202–209, 2015.

Roberts, R. G., Jacobs, Z., Li, B., Jankowski, N. R., Cunningham, A. C., and Rosenfeld, A. B.: Optical dating in archaeology: thirty years in retrospect and grand challenges for the future, Journal of Archaeological Science, 56, 41–60, 2015.

Shidrang, S., Biglari, F., Bordes, J. G., and Jaubert, J.: Continuity and Change in the Late Pleistocene Lithic Industries of the Central Zagros: A Typo-Technological Analysis of Lithic Assemblages from Ghar-e Khar Cave, Bisotun, Iran, Archaeology, Ethnology & Anthropology of Eurasia, 44, 27–38, 2016.

Singarayer, J. and Bailey, R. M.: Component-resolved bleaching spectra of quartz optically stimulated luminescence: preliminary results and implications for dating, Radiation Measurements, 38, 111–118, 2004.

Singarayer, J. S. and Bailey, R. M.: Further investigations of the quartz optically stimulated luminescence components using linear modulation, Radiation Measurements, 37, 451–458, 2003.

Solecki, R. S.: Shanidar Cave, A Palaeolithic Site in Northern Iraq, Smithsonian Institution Annual Report for 1954, pp. 389–425, 1955.

Solecki, R. S.: The Baradostian Industry and the Upper Palaeolithic in the Near East, Ph.D. thesis, Columbia University, 1958.

Solecki, R. S.: Prehistory in Shanidar Valley, Northern Iraq: Fresh insights into Near Eastern prehistory from the Middle Paleolithic to the Proto-Neolithic are obtained, Science, 139, 179–193, 1963.

Solecki, R. S. and Solecki, R. L.: The pointed tools from the Mousterian occupations of Shanidar Cave, northern Iraq, in: The Paleolithic Prehistory of the Zagros-Taurus, pp. 119–146, The University Museum of Archaeology and Anthropology. University of Pennsylvania, Philadelphia, 1993.

Thomsen, K. J., Murray, A. S., Jain, M., and Bøtter-Jensen, L.: Laboratory fading rates of various luminescence signals from feldspar-rich sediment extracts, Radiation Measurements, 43, 1474–1486, 2008.

Tribolo, C., Asrat, A., Bahain, J.-J., Chapon, C., Douville, E., Fragnol, C., Hernandez, M., Hovers, E., Leplongeon, A., Martin, L., Pleurdeau, D., Pearson, O., Puaud, S., and Assefa, Z.: Across the Gap: Geochronological and Sedimentological Analyses from the Late Pleistocene-Holocene Sequence of Goda Buticha, Southeastern Ethiopia, PLOS ONE, 12, e0169 418, 2017.

Tribolo, C., Kreutzer, S., and Mercier, N.: How reliable are our beta-source calibrations?, Ancient TL, 37, 1–10, 2019.

Trinkaus, E.: The Shanidar Neandertals, Academic press, 1983.

Trinkaus, E. and Biglari, F.: Middle Paleolithic Human Remains from Bisitun Cave, Iran, Paléorient, 32, 105–111, 2006.

Vahdati Nasab, H. and Hashemi, M.: Playas and Middle Paleolithic settlement of the Iranian Central Desert: The discovery of the Chah-e Jam Middle Paleolithic site, Quaternary International, 408, 140–152, 2016.

Vahdati Nasab, H., Berillon, G., Jamet, G., Hashemi, M., Jayez, M., Khaksar, S., Anvari, Z., Guérin, G., Heydari, M., Akhavan Kharazian, M., Puaud, S., Bonilauri, S., Zeitoun, V., Sévêque, N., Darvishi Khatooni, J., and Asgari Khaneghah, A.: The open-air Paleolithic site of Mirak, northern edge of the Iranian Central Desert (Semnan, Iran): Evidence of repeatedhuman occupations during the late Pleistocene, Comptes Rendus Palevol, 18, 465–478, 2019.

Vlaminck, S.: Northeastern Iranian Loess and its Palaeoclimatic Implications, Ph.D. thesis, Faculty of Mathematics and Natural Sciences, University of Cologne, 2018.

Wintle, A. G. and Murray, A. S.: A review of quartz optically stimulated luminescence characteristics and their relevance in single-aliquot regeneration dating protocols, Radiation Measurements, 41, 369–391, 2006.

Wolff, E. W., Chappellaz, J., Blunier, T., Rasmussen, S. O., and Svensson, A.: Millennial-scale variability during the last glacial: The ice core record, Quaternary Science Reviews, 29, 2828–2838, 2010.

Zanolli, C., Biglari, F., Mashkour, M., Abdi, K., Monchot, H., Debue, K., Mazurier, A., Bayle, P., Le Luyer, M., Rougier, H., Trinkaus, E., and Macchiarelli, R.: A Neanderthal from the Central Western Zagros, Iran. Structural reassessment of the Wezmeh 1 maxillary premolar, Journal of Human Evolution, 135, 102 643–12, 2019.

Zeitoun, V.: Where palaeoanthropology and prehistory meet, in: Garm Roud. A Hunting Place in Iran, Upper Palaeolithic, edited by Berillon, G. and Asgari Khaneghah, A., pp. 101–110, Editions IFRI & @rchéo-éditions (French- English-Persian), 2016.

Zink, A.: A coarse Bayesian approach to evaluate luminescence ages, Geochronometria, 40, 90–100, 2013.

Zink, A. J. C.: Bayesian analysis of luminescence measurements, Radiation Measurements, 81, 71–77, 2015.

# 4 Study III

Journal of Human Evolution 151 (2021) 102926

Contents lists available at ScienceDirect

Journal of Human Evolution

journal homepage: www.elsevier.com/locate/jhevol

# Bayesian luminescence dating at Ghār-e Boof, Iran, provides a new chronology for Middle and Upper Paleolithic in the southern Zagros

Maryam Heydari [a, *], Guillaume Guérin [a], Mohsen Zeidi [b, c], Nicholas J. Conard [b, c]

[a] IRAMAT-CRP2A, UMR 5060, CNRS-Université Bordeaux Montaigne, Maison de l'Archéologie, 33607, Pessac Cedex, France
[b] Department of Early Prehistory and Quaternary Ecology, University of Tübingen, Germany
[c] Senckenberg Centre for Human Evolution and Palaeoenvironment, University of Tübingen, Germany

Maryam Heydari[1,*], Guillaume Guérin[1], Mohsen Zeidi[2,3], Nicholas J. Conard[2,3]

*corresponding author: mariheyd@gmail.com

**Journal of Human Evolution**

Year: 2021, Volume: 151, Pages: 102926

- published -

https://doi.org/10.1016/j.jhevol.2020.102926

## Abstract

Ghār-e Boof is a Paleolithic cave site in Iran well known for its rich early Upper Paleolithic Rostamian assemblages. The site is located on the edge of the Dasht-e Rostam plain in the southern Zagros. Recent excavations by the members of the Tübingen-Iranian Stone Age Research Project at Ghār-e Boof also recovered well-stratified Middle Paleolithic assemblages. Here, we provide the first detailed luminescence chronology for the Middle and Upper Paleolithic of the site. More generally, our work is the first luminescence chronology for a Middle and Upper Paleolithic site in the Zagros Mountains region in Iran. The luminescence ages for the Upper Paleolithicof Ghār-e Boof agree with published $^{14}$C dates.We applied Bayesian models specifically designed for luminescence dating using the R package 'BayLum' to incorporate the well-established stratigraphic constraints, as well as the published $^{14}$C ages with our optically stimulated luminescence (OSL) ages to improve the precision of the chronological framework. The Bayesian chronology shows a significantly improved precision of the OSL ages in particular for the upper part of the sequence where $^{14}$C ages were available. The Bayesian OSL ages for the Rostamian horizons, archaeological horizon (AH) III (a-b-c), and AH IV, fall in the range of 37–42 ka (68 % credible interval [CI]). Moreover, we determined a series of dates between 45 ka and 81 ka (68 % CI) for the Middle Paleolithic strata from AH IVd to AH VI. Our results point to a demographic shift in the populations responsible for the Middle Paleolithic and the Rostamian within three millennia. This major techno- logical change accompanied by the rise of symbolic artifacts such as personal ornaments, may or may not reflect a replacement of Neanderthals by modern humans. While we are confident that the Rostamian was made by modern humans, available information does not allow us to be sure who made the local Middle Paleolithic.

## 4.1 Introduction

### 4.1.1 Aims of this study

Chronological studies are an integral part of Paleolithic research to track human evolution over time. Numerous Middle and Upper Paleolithic sites were dated to establish a chronology for the dispersal of anatomically modern humans (AMHs) from Africa to- ward central Asia, in particular in the Levant (e.g., O Bar-Yosef, 2001; Shea, 2003, 2010; Grün et al., 2005; Trinkaus, 2005; Meignen, 2012; Nishiaki and Akazawa, 2018). However, further toward the east, in the vast region of the Zagros Mountains, we still lack reliable chronologies, which hampers a better understanding of the rich archaeological record of the region (Smith, 1986; Shidrang et al., 2016). While fossils of AMH are known in the Zagros Mountains (e.g., site of Wezmeh: Trinkaus et al. 2008; site of Warwasi: Tsanova 2013), they have been poorly dated.

The Zagros Mountains have been the focus of Paleolithic studies for decades, not only to unravel the Middle and the Upper Paleo- lithic cultures of this region but also to decipher occupational discontinuity or transition documented in the region (e.g., Biglari, 2001; Jaubert et al., 2006; Conard and Ghasidian, 2011; Shidrang et al., 2016; Heydari-Guran and Ghasidian, 2017; Bazgir et al., 2017).

The few dated stratigraphic sequences in the Zagros Mountains rely on $^{14}$C dating. Shanidar cave, with its rich history of study, provided radiometric ages for the Baradostian cultural group (Solecki, 1963; Hole and Flannery, 1968; Solecki and Solecki, 1993; Becerra-Valdivia et al., 2017). Moreover, in addition to the radio- carbon sequence at Ghār-e-Boof (Conard and Ghasidian, 2011; Baines et al., 2014; Becerra-Valdivia et al., 2017), $^{14}$C dating was also applied at two sites, the Yafteh Cave (Otte et al., 2011) and the Kaldar Cave (Bazgir et al., 2017), located in the Central Zagros, to determine ages for the Upper Paleolithic in Zagros. Nevertheless, despite the few successful applications of $^{14}$C dating, the temporal range is technically limited to the early Upper Paleolithic or very late Middle Paleolithic period (ca 50 ka; Higham, 2011).

In this study, we present a new chronology for the site of Ghār-e Boof located at the south of the Zagros Mountains, obtained by luminescence dating. The site has yielded both Middle and the Upper Paleolithic assemblages (Conard and Ghasidian, 2011; Bretzke and Conard, 2017; Conard and Zeidi, 2019; Zeidi and Conard, 2019). It is situated close to a probable passage of AMH, arriving from Africa through the south of the Iranian plateau, according to various dispersal models (Mellars, 2006; Petraglia et al., 2010; Rosenberg et al., 2011; Boivin et al., 2013; Nasab et al., 2013).

The site of Ghār-e Boof has been excavated and studied since 2006 in the framework of the Tübingen-Iranian Stone Age Research Project (TISARP). The rich and distinctive lamellar early Upper Paleolithic assemblage found during the excavation at Ghār-e Boof and during surveys at 88 sites in the Dasht-e Rostam alone stands in remarkable contrast to the Baradostian and

the so-called Zagros Aurignacian. This led Conard and Ghasidian (2011) to define a new industry named the Rostamian, after the Dasht-e Rostam Plains (Conard et al., 2013). The Upper Paleolithic sequence of the site was already dated with $^{14}$C dating in several earlier studies (Conard and Ghasidian, 2011; Baines et al., 2014; Becerra-Valdivia et al., 2017). These results were refined using Bayesian modeling, leading to the earliest Upper Paleolithic settlement between 41,950 and 39,850 cal. BP (68 % credible interval [CI]; Becerra-Valdivia et al. 2017). Ghasidian's doctoral research resulted in detailed presentations of the cultural sequence of the Rostamian from Ghār-e Boof (Ghasidian, 2014; Ghasidian et al., 2017) based on the first two seasons of excavation in 2006 and 2007. Fieldwork by the TISARP team in 2015 and 2017 extended the stratigraphic sequence to bedrock and uncovered multiple Middle Paleolithic find horizons (Bretzke and Conard, 2017; Conard and Zeidi, 2019; Zeidi and Conard, 2019).

Below, we provide details of the luminescence dating for the Middle and Upper Paleolithic sequence of the site, and we compare the obtained luminescence ages of the Upper Paleolithic with those available $^{14}$C ages. We present the first luminescence-based chronology for the Middle Paleolithic period in the south of the Zagros Mountains. Moreover, our study goes beyond a simple Middle and Upper Paleolithic luminescence chronology for the Zagros Mountains: we also deployed Bayesian modeling as implemented in the R (R Core Team, 2019) package 'BayLum' (Combès et al., 2015; Combès and Philippe, 2017; Philippe et al., 2019) to incorporate all available chronological data (optically stimulated luminescence [OSL] and $^{14}$C ages) for the site of Ghār-e Boof, to render a precise chronology covering both the Middle and the Upper Paleolithic periods. The advantages of such incorporation in Bayesian School will be discussed.

### 4.1.2 Environmental setting

The Dasht-e Rostam region is located in the south of the Zagros Mountains in the northwest of the Fars Province. The province stretches mainly across the Zagros Folded belt. Most of the eleva- tions of this belt comprised parallel limestone anticlines, which are generally oriented from northwest to southeast (Brookes, 1989; Stöcklin and Navabi, 1973). The topography of this area is diverse with various geomorphological features such as mountains ranging from 700 m to 2500 m a.s.l., valleys, rivers, and plains (Heydari-Guran, 2014). The area is known to be semiarid to arid, but the presence of the permanent Fahlian River (Fig. 4.1) alongside more than 50 springs and seasonal rivers, such as Shiv and Solak form a local wetland (Heydari-Guran, 2014). The climate of this region belongs to the mild temperature zone (Bobek, 1968; Ganji, 1968).

The geological context in this area comprises the Miocene to the Quaternary, and the Jurassic to the Oligocene (Heydari-Guran, 2014). The rocks of this region are mainly composed of limestone, dolomite, and argillaceous limestone, which is a normal pattern for the Zagros Mountains (Motiei, 1993).

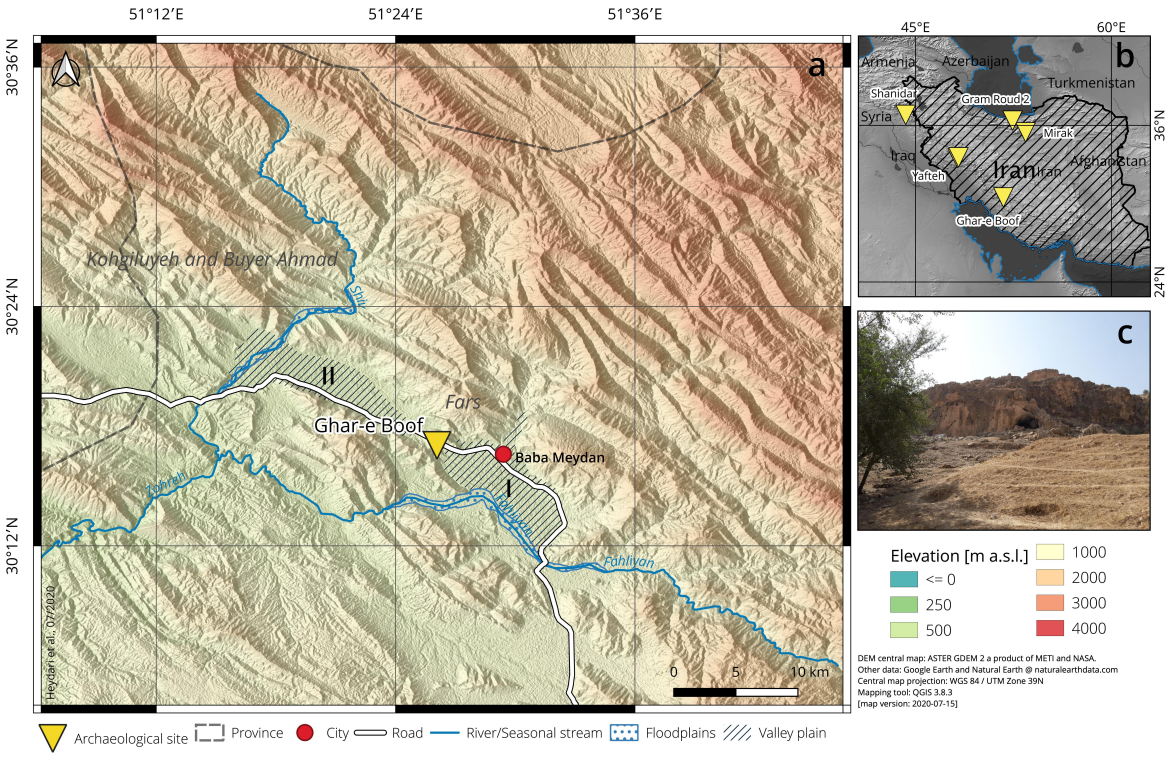


Figure 4.1: a) Dasht-e Rostam region; the dashed areas show Dasht-e Rostam I and Dasht-e Rostam II, the site of Ghār-e Boof is located at the microhabitat of Yagheh Sangar. b) Location of the Paleolithic sites in the region, as mentioned in the text. (c) Photo of the site of Ghār-e Boof.

Members of the TISARP conducted survey in the Dasht-e Rostam and identified numerous Paleolithic sites in the form of open-air sites, rock shelters, and caves. Study of these lithic artifacts assemblages showed that they mainly originate from the Upper Paleolithic (Conard and Ghasidian, 2011; Heydari-Guran, 2014). According to the distribution of the discovered lithic artifacts from the surface, the region was classified into divided small zones (microhabitats; Heydari-Guran 2014). One of those zones, which exhibits the highest concentration of lithic artifacts, is the Yagheh Sangar corridor. The pass is situated in the middle of the Dasht-e Rostam, and it connects plains of Dasht-e Rostam I and Dasht-e Rostam II (Fig. 4.1). This corridor encompasses several caves, rock shelters, and open-air sites, which contains ca 33 % of the known Paleolithic sites in the Dasht-e Rostam plains (Heydari-Guran, 2014). The cave of Ghār-e Boof, which is located at an altitude of 905 m a.s.l., 40 m above the valley bottom, is one of these Paleolithic sites, in the center of the Yagheh Sangar corridor.

The area inside of the cave is ca 60 $m^2$, with a ceiling height of ca 8 m (Fig. 4.1). The Fahlian River is located 5 km at the south of the cave, and the seasonal Solak stream is situated within 200 m at the northeast of the cave. Several large boulders at the entrance of the cave protect the

deposited sediments inside the cave from being washed away by erosional processes (Conard and Ghasidian, 2011; Ghasidian, 2014). These preserved sediments distinguish the site of Ghār-e Boof from the other Paleolithic sites in the region, providing a unique potential for further systematic investigations. Surface studies yielded 436 lithic artifacts, categorized by the presence of flakes, blade and, especially, bladelets and bladelet cores (Conard and Ghasidian, 2011; Ghasidian, 2014). The chert from the Fahlian River was the main source of raw material for producing lithic artifacts.

In the following, the observed layers are identified based on geological horizons (GHs) and archaeological horizons (AHs). Besides, both GH and AH refer to identical layers but were investigated using different approaches.

#### 4.1.2.1 Stratigraphy

The overall sequence at Ghār-e Boof is comprised of nearly 6 m of well-stratified deposits. The GHs 1 and 2 at the top of the profile are associated with the Holocene. GH 2 encompasses two sublayers (GH 2a and GH 2b). The bottom of GH 2 (GH 2b) contains limestone cobbles with sizes from 5 to 25 cm in the north and the center of the profile (western wall; Fig. 4.2). These cobbles separate the Holocene layers from the Pleistocene layers, which start from GH 3 onward (Ghasidian, 2014).

GH 3, with thicknesses ranging from 10 cm to 65 cm in different parts of the cave, often contains ashy silt sediments with colors from yellow-brown to light gray. Fragments of limestone are pre- sent in this layer. Sublayers GH 3a and GH 3b underlay GH 3 with a thickness of ca 15 cm and ca 60 cm, comprised medium brown ashy silt and dark brown silt, respectively. Both sublayers contain abundant lithic artifacts, faunal remains and pieces of charcoal. Continuing downward, GH 4 consists of yellow-gray silt with a thickness of ca 15 cm. The density of limestone fragments in this layer is higher than in GH 3. GH 4a with a thickness of ca 30 cm, is characterized by a mixture of light yellow-brown silt and limestone fragments smaller than 5 cm. GH 4b, that is darker in color than GH 4a, and contains light brown silt and pieces of limestone in lower concentration than GH 4a. Finally, GH 5 and GH 6, which correspond to about 2.5 m of deposits overlying the bedrock (Fig. 4.2), comprised light brown to gray silty sediments with a large amount of limestone clasts (Conard and Zeidi, 2019; Zeidi and Conard, 2019).

#### 4.1.2.2 Archaeological findings

The AH I and AH II contain ceramic and pottery sherds, which are attributed to the historical period (Conard and Ghasidian, 2011). AH III yielded the richest archaeological materials, not only because of the high concentration of lithic artifacts but also because of fragmented but well-preserved animal bones. The botanical remains preserve what appears to be an exceptional record of early dietary plant use during the Rostamian (Baines et al., 2014). The lithic artifacts

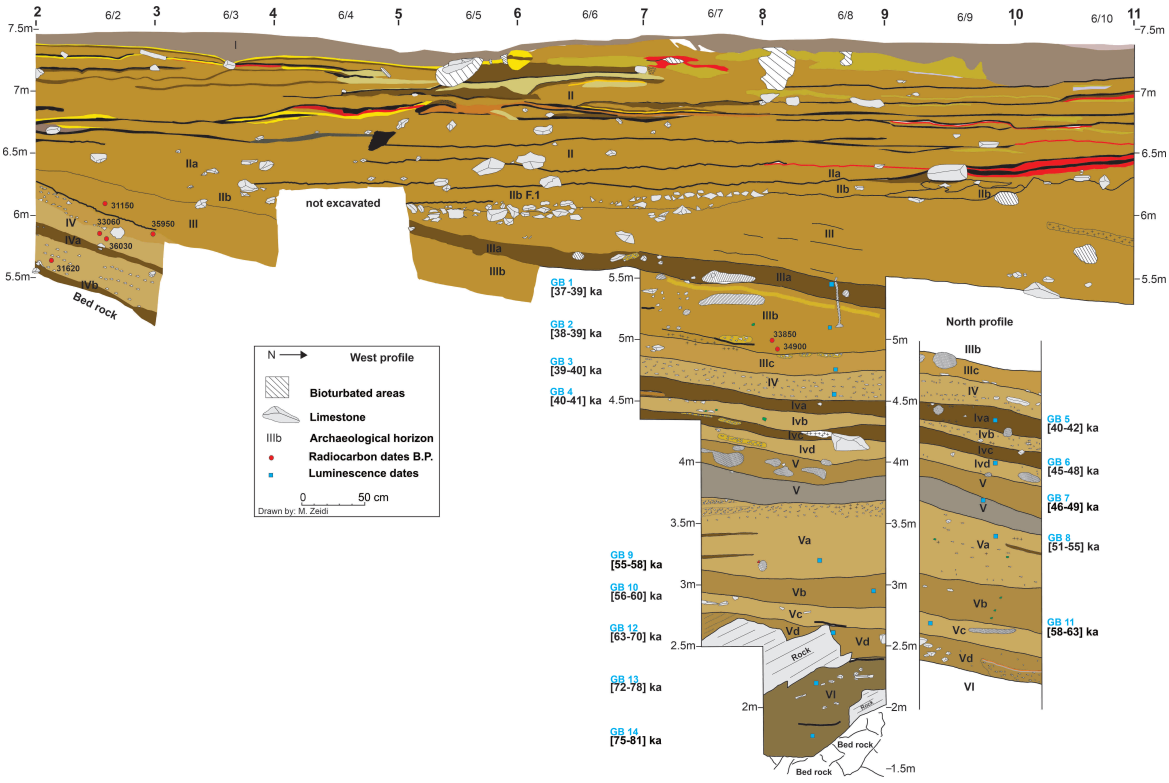


Figure 4.2: Synthetic stratigraphic sections of the western and northern walls of the site of Ghār-e Boof. Locations of the luminescence samples alongside the Bayesian ages estimated in this study, as well as the $^{14}$C dates published in Conard and Ghasidian (2011); Baines et al. (2014); Becerra-Valdivia et al. (2017) are shown.

from AH III, which are rich in bladelets and tools made on bladelets, make Ghār-e Boof the type locality for the Rostamian (Conard and Ghasidian, 2011; Conard et al., 2013; Ghasidian, 2014). Moreover, many perforated shells of various species from AH II b to AH IV were used as personal ornaments (Conard and Ghasidian, 2011; Ghasidian, 2014; Conard and Zeidi, 2019).

The concentrations of lithic artifacts in the Middle Paleolithic strata of AH IVd to AH VI are low compared with the extremely rich Rostamian deposits. These layers also contain large amounts of charred botanical remains as well as faunal remains that are currently under study. The Middle Paleolithic assemblages excavated in 2015 and 2017 have thus far only been published in preliminary reports (Bretzke and Conard, 2017; Conard and Zeidi, 2019; Zeidi and Conard, 2019).

## 4.2 Material and methods

### 4.2.1 Sampling

Fourteen sediment samples were taken from the western and northern walls (Fig. 4.2) starting from AH IIIa on top of the sequence to AH VI right above the bedrock. To protect the stability of the profile, we avoided hammering and collected the samples in opaque bags at night using orange light. For the sampling, first, we cleaned each sampling location and removed a sediment layer of ca 5 cm to avoid sampling weathered sediments subject to recent long-term exposition to light and air. Then, we collected the sediments by digging into the profile.

### 4.2.2 Sample preparation

Sample preparations were carried out following commonly accepted luminescence sample preparation procedures (Preusser et al., 2008) under subdued orange light conditions appropriate for luminescence dating (sodium vapor lamp, ca 589 nm). Wet sieving was performed to extract grains between 41 $\mu$m and 60 $\mu$m. We have selected this grain size because it represents the dominant fraction of the material available in (relative) abundance, and the fraction could be prepared in a reasonable amount of time. The samples were then treated with HCl (10 % and 35 %) to dissolve carbonates until no more reaction was observed. The samples were then treated with $H_2O_2$ (30 %) for one week to eliminate organic materials. Then, we divided the prepared sediments into two groups: group 1 was treated using HCl (35 %) at 65 °C for 3 h to remove iron coating. We retained this part of the so-prepared samples (polymineral) for infrared stimulated luminescence (IRSL) measurements. Group 2 was soaked with a mixture of 90 % hexafluorosilicic acid ($H_2SiF_6$, 37 %) plus 10 % nitric acid ($HNO_3$ 68 %; cf. Frayret et al. 2006 for the procedure) for one week to obtain purified quartz grains. This procedure was followed by another wash in HCl (15 %) overnight to remove remaining calcium fluorides. Finally, wet sieving was applied again to discard any remaining grains from the mineral group of feldspar, as well as removing any aggregated quartz with the size of less than 41 $\mu$m. The amount of quartz grains for sample GB12 was negligible. Therefore, we could not perform any measurements on quartz for this particular sample.

### 4.2.3 Instrumentation and source calibration

OSL (Huntley et al., 1985) and IRSL (Hütt et al., 1988) were carried out on two Freiberg Instruments *lexsyg SMART* TL/OSL systems (Richter et al., 2015). For estimation of the equivalent dose ($D_e$) of the quartz grains, we used a system equipped with five blue LEDs (458 D 10 nm, maximum 70 mW cm$^{-2}$) and five infrared LEDs (850 D 3 nm, maximum 300 mW cm$^{-2}$). The stimulation power was set to 40 mW cm$^{-2}$ for blue and 100 mW cm$^{-2}$ for infrared during con-

tinuous wave (CW) stimulation. For estimating the $D_e$ of the polymineral grain, we employed another system, equipped with ten green LEDs (525 D 20 nm, maximum 70 mW cm$^{-2}$) and five infrared LEDs (850 D 3 nm, maximum 300 mW cm$^{-2}$) set to 100 mW cm$^{-2}$ (infrared) during CW stimulation. The heating rate for TL signal measurements for both blue-OSL and IRSL measurements was 5 °C/s. Luminescence was detected through a UV filter set for blue-OSL measurements (Schott BG 3, 3 mm and Delta BP 365/50 EX) and a blue-violet filter combination for IRSL measurements (Schott BG 39, 3 mm and AHF-BL HC 414/46 and Schott NG 11, 1 mm) in front of a Hamamatsu H7360-02 photomultiplier tube. The two readers were equipped with a $^{90}$Sr/$^{90}$Y-source, which were specifically calibrated for our samples grain size (41–60 $\mu$m). We used grains from sample GB4 for calibration with quartz grains, as well as calibration with polymineral fraction. The samples were first bleached following a dose recovery test (see Section 4.2.4) and then were irradiated with an external $^{137}$Cs $\gamma$-source (Valladas, 1978) in the laboratory of Gif-sur-Yvette (Laboratoire des Sciences du Climat et de l'Environnement). The quartz grains and the polymineral both received a gamma-dose of ca 53 Gy. We measured the given dose using a single aliquot regenerative (SAR) dose protocol (Murray and Wintle, 2000) with the same setup as for our measurements. The result showed that the two luminescence readers delivered ca 8.5 Gy min$^{-1}$ (reader used for the quartz measurements) and ca 10 Gy min$^{-1}$ (polymineral) to grains of 41–60 $\mu$m.

Several hundred grains, either quartz or polymineral, were mounted on the stainless steel cups using silicon oil and a mask of diameter 1 mm (small size). We measured 30 aliquots per sample for the quartz grains and 15–16 for the polymineral fractions.

For additional radiofluorescence (RF) test measurements in Bordeaux, we applied the system used by Frouin et al. (2017). RF spectrometry measurements were carried out on the *lexsyg research* (Richter et al., 2013) system of the Lux laboratory at the Université du Quebec à Montréal. The system is similar to the system in Bordeaux but equipped with an Andor SR-163 spectrograph in conjunction with an Andor DU420A-OE CCD camera connected via a glass fiber to the measurement position. The system was wavelength calibrated, and efficiency calibration relied on technical data relayed by the manufacturer.

### 4.2.4 Luminescence signal measurements

We measured luminescence signals of the quartz and polymineral fraction to determine the corresponding equivalent doses. These procedures enable us to compare the final obtained ages from different minerals and protocols and increase the confidence in the luminescence chronology for Ghār-e Boof.

#### 4.2.4.1 Quartz optically stimulated luminescence

We applied a SAR protocol to the quartz samples to determine the equivalent doses ($D_e$s). Quartz blue-OSL signal (detected in the UV wavelength) consists of several signal components (Bailey et al., 1997). However, the SAR protocol is preferentially employed for the fast decaying signal component, the so-called fast component, bleachable within a few seconds (Wintle and Murray, 2006). Therefore, the first step of measurement was to verify whether quartz samples of the site of Ghār-e Boof were dominated by the fast decaying component or not. We compared one sample from the site (GB10) with the calibration quartz (Risø, batch 90; Hansen et al. 2015), which is known to be dominated by the fast component, using blue CW- OSL, and the corresponding luminescence signals were measured in the UV. Both signals were then transformed into the pseudo-linearly modulated-OSL, following Bos and Wallinga (2012) for results see Section 4.3.1.

The OSL signal was measured at 125 °C for 40 s following a preheat for 10 s. The test dose was measured following a cut-heat. We employed the *Analyst* software v.4.53 (Duller, 2015) for determining the equivalent doses ($D_e$s). Regenerative dose points were set at (22, 44, 88, 176, 352) Gy following a test dose of 22 Gy for regeneration dose 1 to 5 (R1 to R5). We calculated the signal intensity based on the initial 0.2 s of stimulation, and the back- ground was estimated from the last 10 s. An exponential plus linear function was used for fitting the dose-response curves. After delivering the largest regenerative dose point in the SAR sequence (R5), the samples were given a zero dose (R6) to measure the potential effect of charge transfer due to the previous irradiation or stimulation (Wintle and Murray, 2006). After recuperation, the first regenerative point cycle was repeated (R7) to check the efficiency of correction for sensitivity changes. To account for the possibility of potential contamination of the quartz grains by feldspars, we applied an IR depletion ratio test (Duller, 2003) administrating the same dose as for the first regenerative dose at the end of each SAR cycle (R8).

To monitor a dependency of the $D_e$ upon the preheat temperature, the preheat plateau test was carried out for sample GB4. The minimum preheat temperature was set to 200 °C, then increased by 20 °C at each step to reach a final temperature of 300 °C. We kept the difference between the preheat and the cut-heat temperature constant at 40 °C.

Additional dose recovery tests were performed on samples GB4 and GB8. The natural signals were first bleached for 100 s in a solar simulator, and then the procedure was followed by a pause of 3 h before the samples were bleached again for another 100 s to eliminate potential charge transfer from the shallow traps into the main trap (325 °C trap). Samples GB4 and GB8 were received doses of 57 Gy and 67 Gy (close to their paleodose), respectively, using the $\beta$-source inside the luminescence reader, then the given doses were measured using the SAR protocol.

#### 4.2.4.2 Polymineral fraction and the infrared stimulated luminescence

Feldspar has been extensively used in luminescence dating. Stimulation of this mineral with an infrared wavelength produces the IRSL signal (Hütt et al., 1988), usually measured in the blue-violet wavelength range, which has several advantages over the quartz OSL signal measured in the UV. The IRSL signal saturates at higher doses compared to the quartz OSL, which leads to the extension of the dating range limitation. Moreover, IRSL signal of potassium feldspar is brighter and usually resulting in lower statistical uncertainties (e.g., Li and Li, 2011). However, IRSL signal suffers from athermal fading (e.g., Wintle, 1973; Spooner, 1992), e.g., an unwanted loss of the signal of interest. To overcome this problem, several concepts have been proposed either to correct for fading (e.g., Huntley and Lamothe, 2001) or to use signals with a lower rate of fading (Thomsen et al., 2008, 2011; Thiel et al., 2011). These investigations showed that an elevated temperature IRSL signal displays low or even negligible fading (Thomsen et al., 2011; Li and Li, 2011). These concepts resulted in a series of measurement protocols measuring the IRSL signal at elevated temperatures, e.g., 290 °C following IRSL at 50 °C, the so-called post-IR IRSL 290 °C ($pIRIR_{290}$) protocol (Buylaert et al., 2012). The $pIRIR_{290}$ signal is believed not to require any fading correction for the doses 400 Gy (Li and Li, 2012; Zhang and Li, 2020). Hence, this signal was measured for all of the samples using the protocol proposed by Buylaert et al. (2012). The setting of this protocol is listed Table 4.9.

First, dose recovery tests were carried out on two samples: one sample from the top of the sequence (GB1) and the other one from the bottom of the sequence (GB14). The samples were first bleached for 72 h in a solar simulator then the residual doses were measured, which were 3 Gy for sample GB1 and 4 Gy for sample GB14. Subsequently, samples GB1 and GB14 received doses of 65 Gy and 124 Gy using $\beta$-source inside the luminescence reader, then the given doses were measured using the $pIRIR_{290}$ protocol. The residual doses were subtracted from the measured doses.

### 4.2.5 Dose rates

Energy available to luminescence dating is stored in natural minerals (e.g., quartz) mainly due to the emission of $\alpha$- and $\beta$-particles, as well as $\gamma$-photons from natural radionuclides in the surrounding sediment along with dose contributions from high-energetic cosmic rays (Aitken, 1985). In addition, radionuclides inside potassium feldspar and quartz grains result in an internal dose rate contribution. However, the internal dose rate of quartz grains is often negligible in comparison with the internal dose rate of potassium feldspar grains (Mejdahl, 1987; Huntley and Baril, 1997).

The main sources of external radioactivity are nuclides of the U and Th decay chain, as well as K. For our study, the concentration of these radioelements was determined using high-resolution,

low- level background $\gamma$-ray spectrometry (Guibert and Schvoerer, 1991). We assumed that the true $\beta$-dose rate arose from sediment with the grain size less than 2 mm and between 2 mm and 1 cm after Martin (2015); Tribolo et al. (2017). For our samples, however, the amount of sediment between 2 mm and 1 cm was negligible compared to the fraction of less than 2 mm. Thus, the sediment samples were first sieved using a mesh size of 2 mm; then the smaller size fraction was packed and sealed in boxes of 12 $cm^3$. Storage time of at least four weeks ensured a radioactive equilibrium between $^{222}$Rn and its daughters (Guibert and Schvoerer, 1991). The obtained equivalent concentrations of U, Th, and K were converted to dose rates using the factors tabulated by Guérin et al. (2011). The attenuation of $\alpha$ and $\beta$ particles was corrected after Guérin et al. (2012). We applied $\alpha$-efficiency values ($a$-values) of $0.03 \pm 0.01$ after Mauz et al. (2006) to calculate the $\alpha$-dose rate for the quartz grains. For the polymineral fractions, we calculated the average $\alpha$-efficiency and its standard deviation ($0.093 \pm 0.013$) from values reported for $pIRIR_{290}$ in Schmidt et al. (2018).

Based on a granulometric analysis (see Fig. 4.9 as an example) and derived pore volume data, we approximated that a value of $15 \pm 6$ % would best represent the past water content. This value was increased to $20 \pm 8$ % for the last two samples (GB13 and GB14), which were taken from GH 6 because of markedly higher water content observed at this particular layer. The uncertainty on water content was set to 40 %; this relatively large value was chosen to cover a wider range of water content values. To correct dose rates for the water content, we applied values tabulated in Aitken (1985); Nathan and Mauz (2008); Guérin and Mercier (2012) for $\alpha$ and $\beta$ particles, and $\gamma$ photons, respectively.

The internal dose rate for the quartz grains was calculated using nuclide concentration values from Vandenberghe et al. (2008). For feldspar grains in the polymineral fractions, we assumed an internal K concentration of $10 \pm 2$ % after Smedley et al. (2012), and accordingly, we estimated the internal dose rate (Rb was taken into account with a concentration of $370 \pm 74$ ppm following Mejdahl 1987) using the conversion factors from Guérin et al. (2011) and corrected for the self-dose fraction after Guérin et al. (2012).

The *in situ* $\gamma$-dose rate was measured for nine samples (GB1 to GB9) using $Al_2O_3$:C chips following the procedure of Kreutzer et al. (2018). The chips were heated to 350 °C for 10 min before being dispatched. Each aluminum tube contained three chips. The tubes stayed in the sediment over 720 days (within 5 cm horizontal distance from the location of the corresponding sample). For samples GB10 to GB14, the $\gamma$-dose rates were derived from radionuclide concentrations of K, U, and Th obtained by $\gamma$-ray spectrometry (see Sec. 4.2.7).

The cosmic-dose rates were calculated after Prescott and Stephan (1982) and Prescott and Hutton (1994). For the calculation, we used a self-written *Microsoft Excel™* sheet. It was designed to estimate the cosmic-dose rate from four different directions, two sections from the cave entrance and two other sections form the rear of the cave. For each section, the cosmic-

dose rate was estimated based on nine subsections (in the spherical coordinate system from 0° to 10°, 10° to 20°, to finally 80° to 90°). We then summed the dose rate estimated from each 10° representing the dose rate of each section. The final dose rate is the sum of the dose rate from all four sections. For estimating the overall uncertainty, we have used 10 % after Prescott and Hutton (1994) on the final dose rate estimation. To calculate the total dose rate ($\dot{D}$), we used a self-written *Microsoft Excel*$^{TM}$.

### 4.2.6 Radioactive disequilibrium

Equilibrium in the U decay chain is an underlying fundamental assumption to estimate the dose rate. However, due to the mobility of some of the radionuclides in a particular environmental setting, radioactive disequilibria can be observed. Typical sources of radioactive disequilibria are: (1) $^{234}$U (preferentially over $^{238}$U) can form water-soluble oxidation compound (Krbetschek et al., 1994) that might be transferred and accumulated in other layers; (2) Ra is soluble and chemically active, and can be leached; (3) entrance of soluble $^{210}$Pb in soil water; and (4) loss of $^{222}$Rn (gas) due to large pores. One of the typical ways to monitor the possibility of disequilibria in $^{238}$U decay chain is to estimate the effective $^{238}$U content from the top of the chain (pre-$^{226}$Ra) and from the bottom (post-$^{226}$Ra), which accounts for the potential high chemical mobility of $^{226}$Ra (Guibert et al., 2009). To better illustrate the probable radioactive disequilibrium in the $^{238}$U decay chain, the effective $^{238}$U concentrations from the top and the bottom of the U-series were normalized to $^{232}$Th, which is believed to be chemically immobile, to provide a better indicator of radionuclides movement in $^{238}$U following the approach after Guibert et al. (2009). The figure is shown in the results section.

### 4.2.7 Combining quartz ages with the radiocarbon ages in 'BayLum'

The R (R Core Team, 2019) package 'BayLum' provides an environment for Bayesian data analysis in luminescence dating (Philippe et al. 2019; Christophe et al. 2019; for an application see; Heydari et al. 2020). However, 'BayLum' is also capable of combining available chronological information, in particular, stratigraphic constraints and $^{14}$C dates with OSL ages to improve luminescence chronologies. This may be considered as the most important advantage of performing data analysis in a Bayesian framework (although gains in precision and accuracy have already been demonstrated when using the models implemented in 'BayLum'; Heydari and Guérin 2018) since it had the potential to lead to more precise chronologies (e.g., Rhodes et al., 2003; Millard, 2006; Guérin et al., 2015). Integrating OSL ages with $^{14}$C dates for one specific site in 'BayLum' can reduce the effect of shared systematic errors between the OSL ages. Systematic errors affecting series of OSL ages can be modeled using the concept of the covariance matrix, which is named $\Theta$ matrix in 'BayLum' (Combès and Philippe, 2017). The uncertainty on the calibration of the $\gamma$-ray spectrometer, for estimating $\beta$- and $\gamma$-dose rate, as well as the uncertainty on the

$\beta$-source of the luminescence reader are the main sources of uncertainty inserted into the theta matrix for our study (for full implementation see Heydari et al. 2020). However, for 11 of 13 quartz samples we used *in situ* $\gamma$-dose rate measurements while for the two last samples, we used values derived from $\gamma$-ray spectrometry (see Sec. 4.4.2). We did not consider the systematic source of uncertainty for the $\alpha$-dose rate due to its low contribution compared to the total external dose rate (see Sec. 4.3.2).

The input for running the model in 'BayLum' is raw data in the form of BIN/BINX-files and the associated information such as channel integrals, the dose rate of the luminescence reader and the environmental dose rate. We assumed that the Gaussian distribution is a representative model to illustrate the equivalent doses (Guérin et al., 2017; Heydari and Guérin, 2018). The uncalibrated $^{14}$C ages with the corresponding uncertainty published in Conard and Ghasidian (2011); Baines et al. (2014); Becerra-Valdivia et al. (2017) were also combined with the OSL ages and calibrated using *IntCal13* (Reimer et al., 2016). For all calculations, the stratigraphic order constrained the modeling.

## 4.3 Results

### 4.3.1 Equivalent doses

#### 4.3.1.1 Quartz equivalent doses

The results of transformed signals into the pseudo-linearly modulated-OSL from the calibration quartz and sample GB10 are shown in Fig. 4.10. The perfect match of the two curves indicates that the fast signal component dominates the quartz of the samples of Ghār-e Boof.

In the SAR protocol, the normalized recuperation signal to the natural signal was always less than 5 % for our samples. The recycling ratio (R7/R1) was less than one, and the average of these ratios for our samples ranged from $0.82 \pm 0.00$ (for sample GB7) to $0.87 \pm 0.02$ (for sample GB6). The averages of these ratios for all samples are listed in Table 4.6. The average of the IR depletion ratios (R8/R7) for each sample ranged from $0.977 \pm 0.008$ to $0.991 \pm 0.003$. These results indicate that the quartz samples were not contaminated with feldspar.

Typical dose-response curves and luminescence signals from quartz are shown in Fig. 4.3a as examples. We have also illustrated the TL curves from blue-OSL to visualize the preheat.

The result of the preheat measurements is shown in Fig. 4.11; each point represents the average of $D_e$ after measuring 5 aliquots. The figure illustrates a plateau from 220 °C to 260 °C, indicating that these temperatures can be used for preheat. We selected a preheat temperature of 260 °C for our measurements. The dose recovery ratio resulted in $1.12 \pm 0.04$ and $1.12 \pm 0.05$ (average of three measured aliquots). We tried to modify the preheat and the cut-heat temperatures to improve the dose recovery ratio and found that a preheat temperature of 280 °C

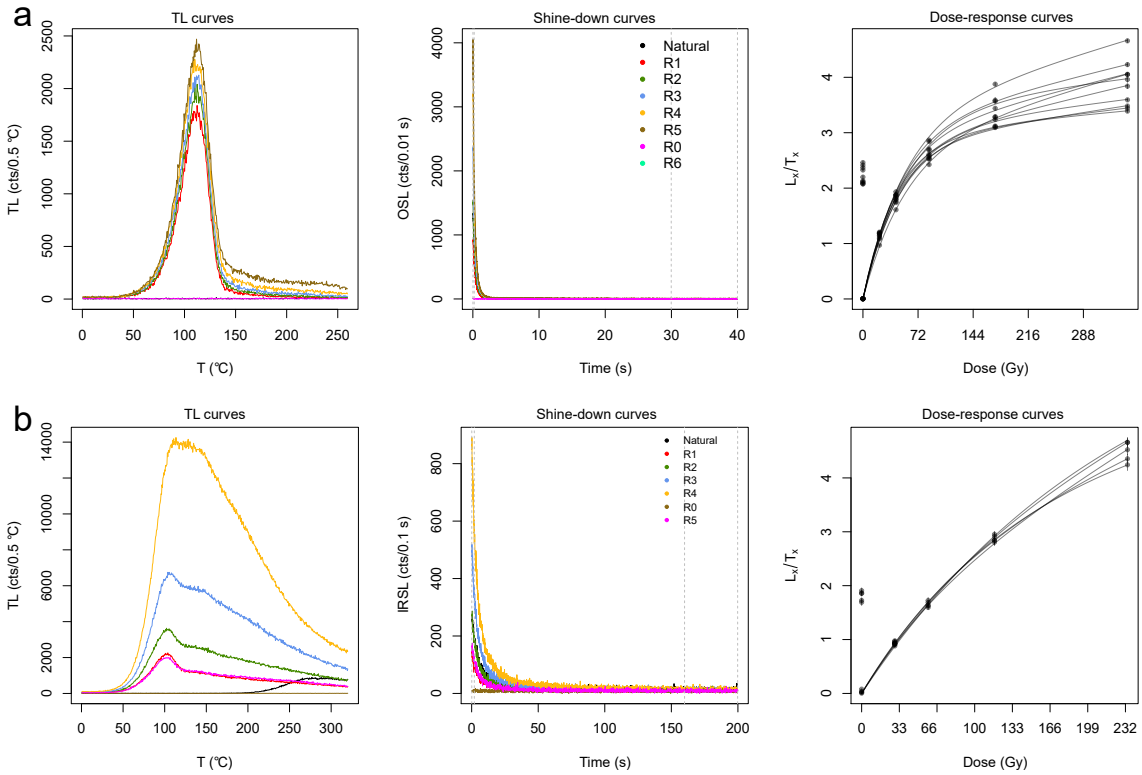


Figure 4.3: TL curves, shine-down curves and typical dose-response curves of samples GB1 for both quartz (a) and polymineral fraction (b). Abbreviations: TL = thermoluminescence; OSL = optically stimulated luminescence; IRSL = infrared stimulated luminescence.

and test dose cut-heat of 260 °C (henceforth 280–260 °C) led to the best dose recovery ratios of $1.01 \pm 0.01$ and $1.00 \pm 0.03$ for GB4 and GB8 (average of three measured aliquots). We also performed a preheat plateau test for this protocol on sample GB8. The preheat varied from 220 °C to 280 °C with the cut-heat set to 20 °C less than the preheat at each step.

The result of this preheat test is shown in Fig. 4.12. This figure illustrates that the measured $D_e$ using the 280–260 °C protocol appears not to be located in the plateau. Therefore, we continued our measurement using 260–220 °C protocol. However, we determined the equivalent doses using the 280–260 °C protocol for three samples GB1, GB4, and GB8 and divided the obtained $D_e$ from the 260–220 °C protocol to the corresponding $D_e$ obtained from the 280–260 °C protocol. The ratios were $1.00 \pm 0.03$, $1.00 \pm 0.03$, and $1.01 \pm 0.03$ for samples GB1, GB4, and GB8 respectively, i.e., indistinguishable from unity. Therefore, we concluded that for our samples, the dose recovery test is not a good representative to test the suitability of the SAR protocol parameters. This observation is in agreement with Guérin et al. (2015), who concluded that dose recovery might not be a strong indicator of the accuracy of the measurement protocol settings.

#### 4.3.1.2 Polymineral equivalent doses

We obtained dose recovery ratios of $0.99 \pm 0.02$ for sample GB1 and $0.97 \pm 0.3$ (average of three measured aliquots) for sample GB14 and thus within 10 % of unity. The proportions of the test dose to the given dose were 44 % for sample GB1 and 23 % for sample GB14. These results agree with the findings by Colarossi et al. (2017), who suggested that the ratio of the test dose to the given dose in the $pIRIR_{290}$ signal should not be less than 15 %. Besides the average of recycling ratios for our samples here ranged from $0.99 \pm 0.06$ (for sample GB6) to $1.05 \pm 0.01$ (for sample GB5). Contrary to quartz samples, recycling ratios for polymineral were within 5 % of unity. The average of the recycling ratios (for consistency with blue-OSL measurements) for all samples are summarized in Table 4.6.

Typical dose-response curves and luminescence signals from sample GB1 are shown in Fig. 4.3b as examples. We have also illustrated the TL curves from $pIRIR_{290}$ to visualize the preheat.

#### 4.3.1.3 Scatter in the equivalent dose distributions

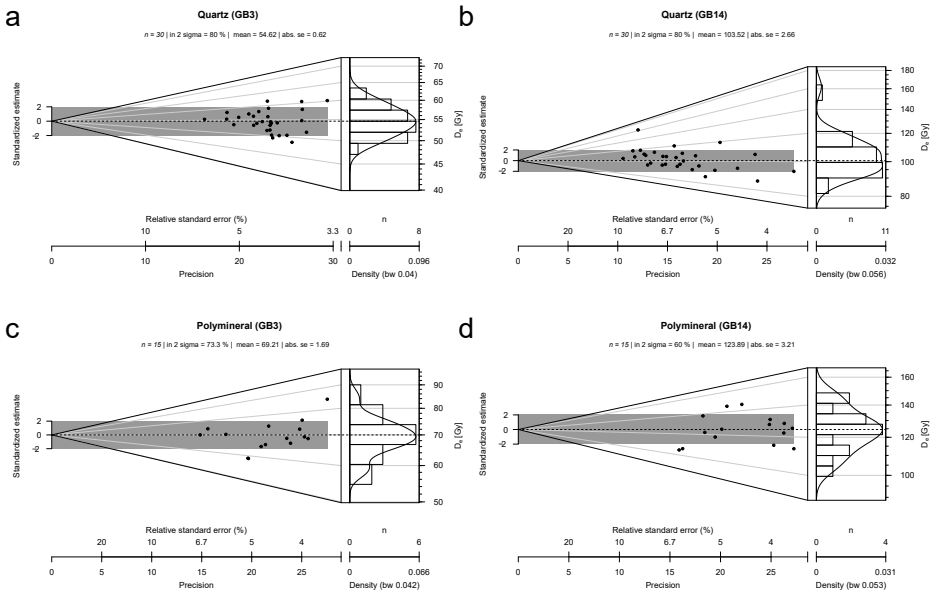


Figure 4.4: Equivalent dose distributions of samples GB3 and GB14 as examples from the quartz (a, b) and polymineral fractions (c, d). The final equivalent doses are determined based on arithmetic average, and the uncertainty is estimated according to the standard error of the mean. Abbreviations: $D_e$ = equivalent dose; n = number of aliquots; `abs.se` = absolute standard error.

The distributions of the $D_e$ for both, quartz and polymineral, are exemplarily displayed for samples GB3 and GB14 as Abanico plots (Dietze et al., 2016) in Fig. 4.4. The $D_e$ distributions for all samples are provided in the Figs. 4.13 and 4.14. In addition, we calculated the overdispersion

Table 4.1: The radionuclide concentration derived by $\gamma$-ray spectrometry.

| Sample | K | $\sigma$ | $U_{pre\text{-}Ra}$ | $\sigma$ | $U_{post\text{-}Ra}$ | $\sigma$ | Th | $\sigma$ |
|---|---|---|---|---|---|---|---|---|
| | [%] | | [ppm] | | [ppm] | | [ppm] | |
| GB1 | 1.01 | 0.02 | 1.51 | 0.11 | 1.33 | 0.03 | 2.80 | 0.06 |
| GB2 | 0.84 | 0.02 | 1.49 | 0.10 | 1.23 | 0.03 | 2.49 | 0.06 |
| GB3 | 0.84 | 0.02 | 1.66 | 0.09 | 1.68 | 0.03 | 2.58 | 0.05 |
| GB4 | 0.73 | 0.02 | 2.30 | 0.10 | 1.64 | 0.03 | 2.54 | 0.06 |
| GB5 | 0.75 | 0.02 | 2.23 | 0.11 | 2.01 | 0.03 | 2.47 | 0.06 |
| GB6 | 0.61 | 0.02 | 1.96 | 0.10 | 1.89 | 0.03 | 2.47 | 0.05 |
| GB7 | 0.61 | 0.02 | 2.48 | 0.11 | 1.30 | 0.03 | 2.19 | 0.06 |
| GB8 | 0.59 | 0.02 | 2.08 | 0.09 | 1.95 | 0.03 | 2.26 | 0.05 |
| GB9 | 0.56 | 0.02 | 2.26 | 0.10 | 2.06 | 0.03 | 2.24 | 0.05 |
| GB10 | 0.62 | 0.02 | 2.43 | 0.10 | 1.82 | 0.03 | 2.31 | 0.05 |
| GB11 | 0.49 | 0.01 | 2.24 | 0.09 | 2.15 | 0.03 | 1.96 | 0.04 |
| GB12 | 0.38 | 0.01 | 2.13 | 0.09 | 2.06 | 0.03 | 1.68 | 0.04 |
| GB13 | 0.40 | 0.01 | 2.59 | 0.09 | 1.99 | 0.03 | 1.70 | 0.04 |
| GB14 | 0.64 | 0.02 | 2.89 | 0.12 | 2.44 | 0.04 | 2.58 | 0.06 |

Abbreviation: $\sigma$ = error-propagated uncertainty.

for each $D_e$ distribution (Table 4.6) after Galbraith et al. (1999). The $D_e$s are quoted as arithmetic average ± the standard error of the mean. The $D_e$s of the quartz grains and polymineral fractions ranged from 55 ± 1 Gy to 104 ± 3 Gy and from 65 ± 2 Gy to 124 ± 3 Gy, respectively (Table 4.3.5).

To justify the use of the arithmetic average for calculating the central dose, despite observing the scatter within aliquots (Fig. 4.4; for complete version see Figs. 4.13 and 4.14), we have, in addition, calculated the central dose using the average dose model (ADM) after Guérin et al. (2017). In this model, the uncertainty on each $D_e$ is considered in the final central dose. These results are listed in Table 4.6. This table shows that the arithmetic average and the ADM lead to almost identical results. Thus, the arithmetic average is an appropriate measure for this data set despite the observed scattering between aliquots.

### 4.3.2 Dose rates

The equivalent concentrations of U, Th, and K, as well as the calculated external and total dose rates, are shown in Tables 4.3.2 and 4.3.2, respectively. The internal dose rates for quartz and polymineral grains were estimated using *DRAC* v.1.2 (Durcan et al., 2015) and resulted in $0.01 \pm 0.00\,\mathrm{Gy\,ka^{-1}}$ and $0.18 \pm 0.04\,\mathrm{Gy\,ka^{-1}}$. The external $\alpha$-dose rates varied between $0.04 \pm 0.01\,\mathrm{Gy\,ka^{-1}}$ and $0.06 \pm 0.01\,\mathrm{Gy\,ka^{-1}}$ for the quartz grains and between $0.13 \pm 0.02\,\mathrm{Gy\,ka^{-1}}$ and $0.20 \pm 0.03\,\mathrm{Gy\,ka^{-1}}$ for the polymineral fractions. The external $\beta$-dose rates ranged from $0.53 \pm 0.02\,\mathrm{Gy\,ka^{-1}}$ to $0.89 \pm 0.05\,\mathrm{Gy\,ka^{-1}}$. The *in situ* $\gamma$-dose rate for samples GB1 to GB9 varied between $0.40 \pm 0.03\,\mathrm{Gy\,ka^{-1}}$ to $0.49 \pm 0.03\,\mathrm{Gy\,ka^{-1}}$, which is in good agreement within uncertainties with the corresponding $\gamma$-dose rates derived by laboratory $\gamma$-ray spectrometry, which ranged from $0.35 \pm 0.01\,\mathrm{Gy\,ka^{-1}}$ to $0.47 \pm 0.02\,\mathrm{Gy\,ka^{-1}}$ (for samples GB1 to GB14). The final

Table 4.2: The determined environmental dose rates.

| **Sample** | $\dot{D}_{Q_\alpha}$ [Gy ka$^{-1}$] | $\sigma$ | $\dot{D}_{KF_\alpha}$ [Gy ka$^{-1}$] | $\sigma$ | $\dot{D}_\beta$ [Gy ka$^{-1}$] | $\sigma$ | $\dot{D}_\gamma$ [Gy ka$^{-1}$] | $\sigma$ | $\dot{D}_{\gamma_{in\ situ}}$ [Gy ka$^{-1}$] | $\sigma$ | $\dot{D}_{cosm.}$ [Gy ka$^{-1}$] | $\sigma$ | $\dot{D}_{Q_{total}}$ [Gy ka$^{-1}$] | $\sigma$ | $\dot{D}_{PM_{total}}$ [Gy ka$^{-1}$] | $\sigma$ |
|---|---|---|---|---|---|---|---|---|---|---|---|---|---|---|---|---|
| GB1 | 0.04 | 0.01 | 0.14 | 0.02 | 0.89 | 0.05 | 0.46 | 0.02 | 0.49 | 0.03 | 0.11 | 0.01 | 1.55 | 0.06 | 1.81 | 0.07 |
| GB2 | 0.04 | 0.01 | 0.13 | 0.02 | 0.77 | 0.04 | 0.41 | 0.02 | 0.42 | 0.02 | 0.10 | 0.01 | 1.34 | 0.04 | 1.60 | 0.06 |
| GB3 | 0.05 | 0.01 | 0.15 | 0.02 | 0.80 | 0.04 | 0.44 | 0.02 | 0.44 | 0.02 | 0.10 | 0.01 | 1.40 | 0.04 | 1.67 | 0.06 |
| GB4 | 0.05 | 0.01 | 0.17 | 0.02 | 0.77 | 0.04 | 0.45 | 0.02 | 0.46 | 0.01 | 0.10 | 0.01 | 1.39 | 0.04 | 1.67 | 0.06 |
| GB5 | 0.06 | 0.01 | 0.17 | 0.03 | 0.80 | 0.04 | 0.45 | 0.02 | 0.46 | 0.02 | 0.10 | 0.01 | 1.42 | 0.04 | 1.71 | 0.06 |
| GB6 | 0.05 | 0.01 | 0.16 | 0.02 | 0.68 | 0.03 | 0.41 | 0.01 | 0.43 | 0.01 | 0.09 | 0.01 | 1.26 | 0.03 | 1.54 | 0.06 |
| GB7 | 0.05 | 0.01 | 0.15 | 0.02 | 0.67 | 0.03 | 0.40 | 0.02 | 0.40 | 0.03 | 0.09 | 0.01 | 1.23 | 0.05 | 1.50 | 0.07 |
| GB8 | 0.05 | 0.01 | 0.16 | 0.02 | 0.67 | 0.03 | 0.40 | 0.01 | 0.42 | 0.01 | 0.09 | 0.01 | 1.24 | 0.03 | 1.52 | 0.06 |
| GB9 | 0.05 | 0.01 | 0.17 | 0.03 | 0.67 | 0.03 | 0.41 | 0.02 | 0.40 | 0.03 | 0.09 | 0.01 | 1.22 | 0.05 | 1.51 | 0.07 |
| GB10 | 0.05 | 0.01 | 0.17 | 0.03 | 0.71 | 0.03 | 0.43 | 0.02 | - | - | 0.08 | 0.01 | 1.25 | 0.05 | 1.57 | 0.06 |
| GB11 | 0.05 | 0.01 | 0.17 | 0.03 | 0.62 | 0.03 | 0.39 | 0.01 | - | - | 0.08 | 0.01 | 1.16 | 0.04 | 1.43 | 0.06 |
| GB12 | 0.05 | 0.01 | 0.16 | 0.03 | 0.53 | 0.02 | 0.35 | 0.01 | - | - | 0.08 | 0.01 | 1.02 | 0.03 | 1.29 | 0.05 |
| GB13 | 0.05 | 0.01 | 0.16 | 0.03 | 0.54 | 0.03 | 0.36 | 0.02 | - | - | 0.08 | 0.01 | 1.04 | 0.04 | 1.31 | 0.06 |
| GB14 | 0.06 | 0.01 | 0.20 | 0.03 | 0.75 | 0.04 | 0.47 | 0.02 | - | - | 0.08 | 0.01 | 1.38 | 0.05 | 1.68 | 0.07 |

Abbreviations: Q = quartz; PM = polymineral; $\sigma$ = error propagated uncertainty; $\dot{D}$ = estimated dose rate.

dose rate for the quartz grains ranged from $1.02 \pm 0.03$ Gy ka$^{-1}$ to $1.55 \pm 0.06$ Gy ka$^{-1}$ and correspondingly for potassium feldspar ranged from $1.29 \pm 0.05$ Gy ka$^{-1}$ to $1.81 \pm 0.07$ Gy ka$^{-1}$.

To address figuratively possible radioactive disequilibria, we plotted the ratio of effective U concentration derived from the top of the chain (pre-$^{226}$Ra), as well as from the bottom of the chain (post-$^{226}$Ra) divided by $^{232}$Th as it was mentioned in Sec. 4.3.2. In Fig. 4.5 5, most of the samples lie close to the equilibrium line. However, the effective $^{238}$U concentrations estimated from the top of the chain are higher (from ca 1.2 times to a maximum of 1.9 times) than the corresponding contents from the bottom of the chain for samples GB2, GB4, GB7, GB10, GB13, and GB14. Unfortunately, it is not straightforward to distinguish whether the source of disequilibria can be attributed to the top or to the bottom of the U chain. Hence, we decided to calculate the average of the effective $^{238}$U from the top and the bottom of the chain for samples GB2, GB4, GB7, GB10, GB13, and GB14 and presented the dose rate according to the average. However, if we assumed that the disequilibria happened recently in the top of the chain then considering the lower effective U concentration from the bottom, would lead to older ages, by 1 % up to 7 %. Likewise calculating the ages from the effective U concentration from the top of U chain compared with the average would lead to younger ages, by 1 % up to 6 %. However, these differences do not have a significant effect on the overall Paleolithic interpretation.

### 4.3.3 Quartz and polymineral ages

Blue-OSL ages from the quartz samples alongside pIRIR$_{290}$ ages from the polymineral samples within their standard errors (68 % confidence interval) are shown in Fig. 4.6. The figure also presents the calibrated $^{14}$C ages after Baines et al. (2014) and Becerra-Valdivia et al. (2017)

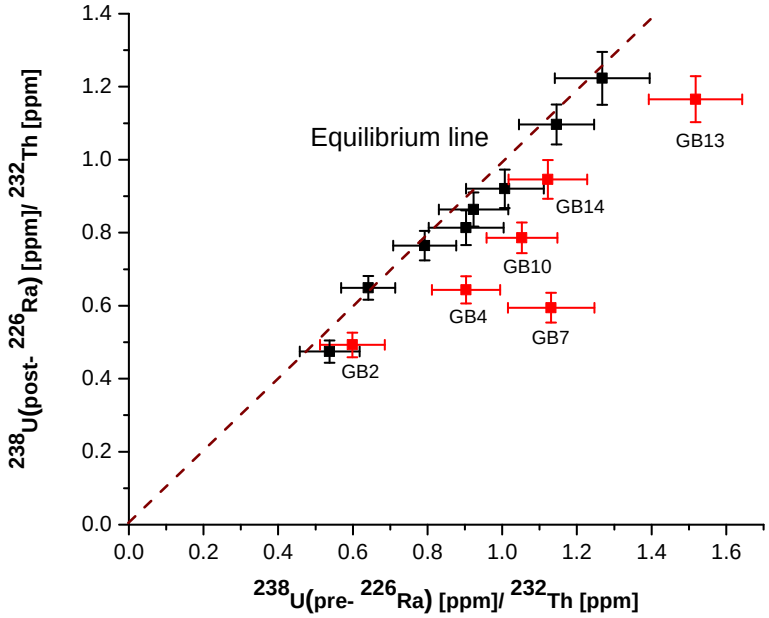


Figure 4.5: Radioactive disequilibrium check for the $^{238}$U decay chain. The ratios of $^{238}$U (post-$^{226}$Ra)/$^{232}$Th and $^{238}$U (pre-$^{226}$Ra)/$^{232}$Th for the entire samples are shown. Most of the samples lie close to the equilibrium line except for samples GB2, GB4, GB7, GB10, GB13, and GB14 (they are color-coded in red). For these samples, averages of the top (pre-$^{226}$Ra) and the bottom (post-$^{226}$Ra) of the $^{238}$U decay chain were used to determine the dose rates.

the calibrated ages are taken from Ghasidian et al. (2019). We split those ages into two groups associated with the year of their publication: $^{14}$C (2014) and $^{14}$C (2017) in the legend of Fig. 4.6. The names of archaeological layers in which the samples were taken are displayed next to each sample's name. At first glance, a perfect agreement between the quartz ages and the polymineral ages is observed for almost the entire sample set. Both quartz and polymineral ages smoothly increase with depth. Moreover, the $^{14}$C ages agree with the luminescence ages from the top of the sequence.

### 4.3.4 Infrared RF tests on the polymineral fraction

We employed infrared RF (IR-RF; Trautmann et al. 1998, 1999) using the protocol suggested by Frouin et al. (2017) on two poly- mineral samples (GB2 and GB14). Unfortunately, the determined $D_e$s significantly overestimated those values obtained with the pIRIR$_{290}$ protocol (values not shown). To rule out insufficient luminescence signal bleaching as a potential (but here unlikely) cause for this overestimation, we additionally recorded RF spectra (see Fig. 4.15 as an

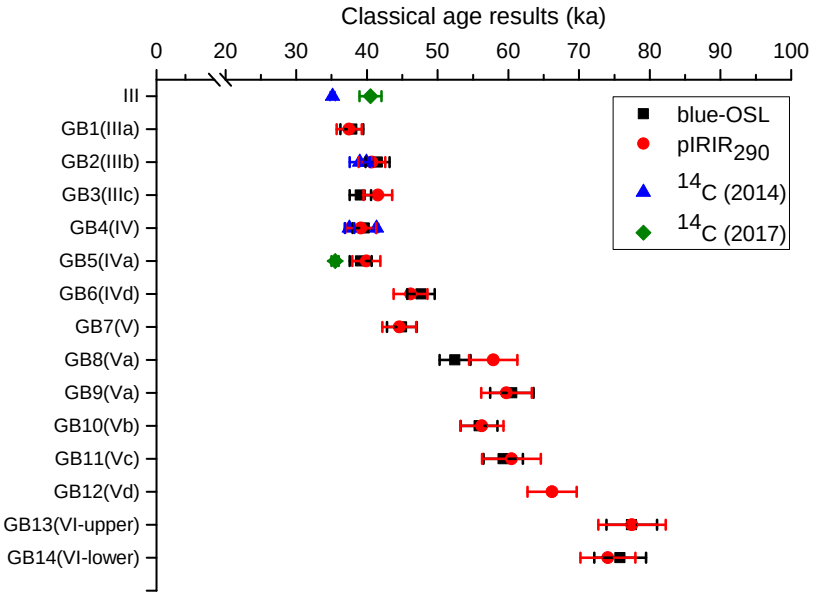


Figure 4.6: Results of the quartz OSL ages and $pIRIR_{290}$ ages of the polymineral fractions within 68 % confidence interval. The quartz and polymineral ages overlap one another, and they gradually increase with depth. The $^{14}C$ ages (2014) were taken from Conard and Ghasidian (2011) and Baines et al. (2014), while the $^{14}C$ ages (2017) were taken from Becerra-Valdivia et al. (2017). Abbreviations: OSL = optically stimulated luminescence; $pIRIR_{290}$ = post-infrared infrared stimulated luminescence at 290 °C.

example for sample GB2) using again the protocol by Frouin et al. (2017). These measurements revealed that the RF spectra are dominated by a strong red emission, while the relevant IR emission here is not distinguishable from background noise, i.e., the polymineral samples from Ghār-e Boof are unsuitable for IR-RF dating; thus, this approach was not further followed-up.

### 4.3.5 Bayesian ages

Figure 4.7 illustrates the result of quartz ages combined with the $^{14}C$ dates using 'BayLum'. We did not have OSL samples from AH III; thus the OSL ages start from sublayers IIIa, IIIb, and IIIc, which resulted in 37–39 ka (68 % CI) following 40–41 ka and 40e42 ka corresponding to the sublayers AH IV and AH IVa. Combining the OSL ages with $^{14}C$ dates resulted in 35–42 ka for AH III to AH IV (and sublayer IVa). Afterward, the Middle Paleolithic ages started from sample GB6 with the age of 45–48 ka, continuing to the oldest sample of the sequence GB14 with the age of 75–81 ka. The convergence of the Markov chain Monte Carlo (MCMC) along with the age probability density are plotted for sample GB4 in Fig. 4.16 as an example. The Bayesian process

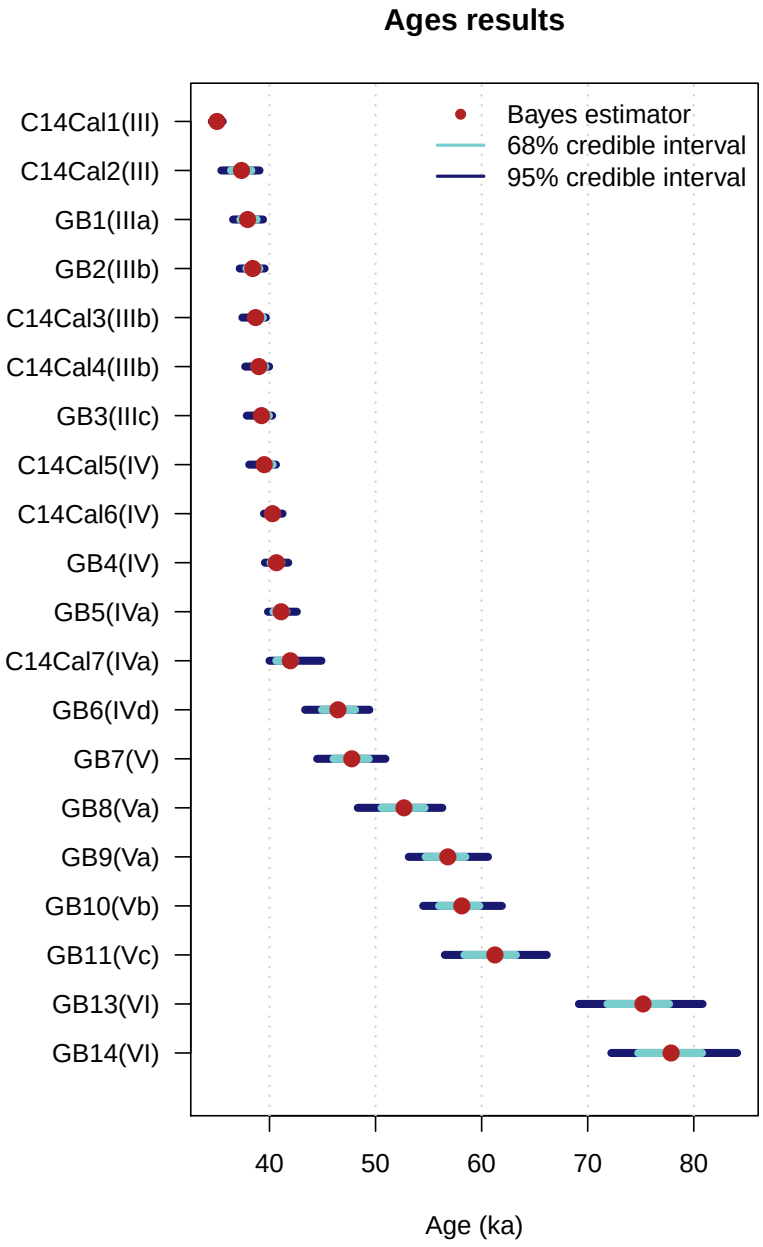


Figure 4.7: Bayesian age plot. It illustrates the estimated Bayesian optically stimulated luminescence (OSL) ages and the calibrated $^{14}$C dates using the R package 'BayLum'. The $^{14}$C dates were taken from Conard and Ghasidian (2011); Baines et al. (2014); Becerra-Valdivia et al. (2017). The Bayesian model addresses the shared systematic error between samples, and it also includes stratigraphic constraints.

Table 4.3: The equivalent dose and corresponding ages in the classical approach..

| **Samle** | $D_{e_{blue-OSL}}$ | $\sigma$ | **Age**$_{blue-OSL}$ | $\sigma$ | $D_{e_{pIRIR_{290}}}$ | $\sigma$ | **Age**$_{pIRIR_{290}}$ | $\sigma$ |
|---|---|---|---|---|---|---|---|---|
| GB1 | 59 | 1 | 38 | 2 | 68 | 1 | 37 | 2 |
| GB2 | 55 | 1 | 42 | 2 | 65 | 1 | 41 | 2 |
| GB3 | 55 | 1 | 39 | 2 | 69 | 2 | 42 | 2 |
| GB4 | 55 | 1 | 40 | 2 | 65 | 2 | 39 | 2 |
| GB5 | 55 | 1 | 39 | 2 | 68 | 2 | 40 | 2 |
| GB6 | 60 | 1 | 48 | 2 | 71 | 2 | 46 | 2 |
| GB7 | 55 | 1 | 45 | 2 | 67 | 2 | 45 | 2 |
| GB8 | 65 | 2 | 52 | 2 | 88 | 4 | 58 | 4 |
| GB9 | 74 | 2 | 61 | 3 | 90 | 3 | 60 | 3 |
| GB10 | 70 | 1 | 56 | 3 | 88 | 3 | 56 | 3 |
| GB11 | 69 | 1 | 59 | 3 | 87 | 5 | 60 | 4 |
| GB12 | - | - | - | - | 86 | 2 | 66 | 3 |
| GB13 | 80 | 2 | 77 | 4 | 102 | 4 | 77 | 5 |
| GB14 | 104 | 3 | 76 | 4 | 124 | 3 | 74 | 4 |

Abbreviations: $D_e$ = equivalent dose; SEM = standard error of the mean; $\sigma$ = error propagated uncertainty; Q = quartz; PM = polymineral.

converged after 4,000,000 iterations.

## 4.4 Discussion

### 4.4.1 Reliability of luminescence ages

The OSL age results derived from the quartz grains are in good agreement with the pIRIR$_{290}$ ages from the polymineral fractions. The only exception was observed for sample GB8, for which the average of the confidence interval of the pIRIR$_{290}$ represents an age ca 10 % older than for quartz. A residual dose (hard bleachable signal) might be a reason for the older age of the polymineral compared to the quartz age. The measured residual doses for two samples of GB1 and GB14 were less than 4 Gy and, hence, not significant in comparison with the equivalent doses of 68 Gy and 124 Gy. However, there is no indication that laboratory bleaching is equivalent to the natural bleaching before sediment deposition. The residual doses obtained in our study agree with values published in Buylaert et al. (2012) considering well-bleached samples. The excellent agreement between the quartz ages in comparison with the corresponding polymineral ages suggests that the quartz and potassium feldspar grains in the polymineral were sufficiently bleached (Murray et al., 2012).

The probable critical point regarding the blue-OSL ages might be the poor recycling ratio (up to 13–18 % lower than unity). These values are lower than what is usually accepted (within 10 % of unity) as a standard criterion (Wintle and Murray, 2006). However, here the good match between blue-OSL ages with pIRIR$_{290}$ ages (on top of a good agreement with $^{14}$C results) gives confidence on the accuracy of these ages. To see the dependency of estimated $D_e$ on the

recycling ratio, in addition, we categorized the $D_e$ distribution of each sample (for six randomly selected samples, GB1, GB3, GB5, GB8, GB10, GB14) based on their recycling ratios into two groups: group 1 with recycling ratios less than its average alongside group 2 with recycling ratios larger than its average. The results listed in Table 4.14, indicate no difference between the $D_e$ of group 1 and 2 for samples GB5 and GB8. The discrepancies between the $D_e$ of two groups corresponding to GB10 and GB14 are negligible. Yet, the $D_e$ differences observed for samples GB1 and GB3 are more noticeable compared with the other samples; however, within uncertainties, they agree with one another. More importantly, the $D_e$s calculated from both groups for GB1 and GB3 show no correlation between low or high recycling ratio and the smaller or larger $D_e$. We, therefore, conclude that for our samples, neither low nor high recycling ratios result in significant $D_e$ underestimation or overestimation.

Besides, it appears that the $^{14}$C ages published in Baines et al. (2014) agree more with the OSL ages in comparison with the two ages published in Becerra-Valdivia et al. (2017). These $^{14}$C ages increase gradually with depth and provide the same pattern as for the OSL ages. For layer III (the first layer in the plot) it appears that the age of Baines et al. (2014) (calibrated from Ghasidian et al. 2019) is more consistent with the luminescence ages and it is likely that the $^{14}$C age of layer III (Becerra-Valdivia et al., 2017) is slightly older. Besides, the age of IVa (Becerra-Valdivia et al., 2017) appears to be younger in comparison with luminescence ages. Finally, the good match of the two distinctly obtained series of luminescence ages (quartz and polymineral), and the consistency with the $^{14}$C ages provides reasonable confidence in the chronology for the top of the sequence. For ages in the lower profile, OSL and $pIRIR_{290}$ ages agree with each other and are stratigraphically consistent.

### 4.4.2 The Bayesian approach toward more precise ages

In Sec. 4.3.5, we combined the OSL ages with the available $^{14}$C ages (Conard and Ghasidian, 2011; Baines et al., 2014; Becerra-Valdivia et al., 2017) to build up the Bayesian chronology using the R package 'BayLum'. The correlation between OSL samples due to shared systematic error mainly produced by calibrating the instruments, was addressed by creating a theta matrix. For all OSL dating measurements (both the equivalent dose and the dose rate), the same instruments were used except for estimating the $\gamma$-dose rate. We noticed that the $\gamma$-dose rate of samples GB10 and GB11 ($0.43 \pm 0.02\,\mathrm{Gy\,ka^{-1}}$ and $0.39 \pm 0.01\,\mathrm{Gy\,ka^{-1}}$, respectively) deduced from laboratory measurements agreed with the *in situ* $\gamma$-dose rate of sample GB9 ($0.40 \pm 0.03\,\mathrm{Gy\,ka^{-1}}$), which is in close location to samples GB10 and GB11 in the profile with *in situ* $\gamma$-dose rate available (Fig. 4.2). Therefore, for these two samples, we have used the *in situ* $\gamma$-dose rate of sample GB9. We provided one theta matrix considering (1) the uncertainties of *in situ* $\gamma$-dose rates for samples GB1 to GB11, and (2) the uncertainties of $\gamma$-ray spectrometry for samples GB13 and GB14. We did not use the *in situ* $\gamma$-dose rate of sample GB9 for samples GB13 and GB14 at the bottom since

the environmental situation is completely different with the rest of samples due to presence of large rocks in AH VI and being close to the bedrock (Fig. 4.2).

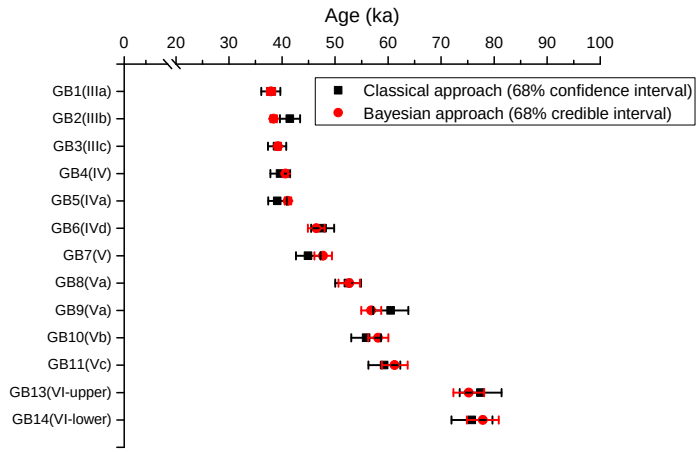


Figure 4.8: Comparison of the quartz optically stimulated luminescence (OSL) ages derived from Bayesian modeling and the classical approach. As illustrated applying stratigraphic constraints and incorporating the $^{14}$C dates play fundamental roles in reducing the uncertainties at the top of the age sequence. However, even at the bottom where age intervals overlap one another, the Bayesian uncertainties are smaller than the corresponding classical approach.

Comparing Bayesian chronology in Fig. 4.7 with the classical quartz ages in Fig. 4.6 shows that the Bayesian age intervals were considerably reduced, especially for the top of the sequence where $^{14}$C ages are available. To better illustrate the improvement of the uncertainty in the Bayesian chronology, in Fig. 4.8 we show classical quartz ages from Sec. 4.3.3 and the Bayesian quartz ages (Sec. 4.3.5). The CIs created by the Bayesian approach are considerably smaller than those confidence intervals of the classical approach. These reductions are significant (from 57 % to a maximum of 73 %), where $^{14}$C ages are combined with the OSL ages (from GB1 to GB4). Our results show that combining OSL ages with $^{14}$C ages in the Bayesian modeling when stratigraphic constraints were also included indeed result in more precise chronologies. However, for GB6 to GB14, where no $^{14}$C ages were available, Bayesian modeling provides more precise ages by reducing the uncertainties (from 17 % to a maximum of 40 %). Heydari et al. (2020) observed similar improvements in the precision of the Bayesian chronology by including stratigraphic ordering even where only OSL ages are involved. In that study, the authors emphasized the effect of applied stratigraphic constraints leading to a reduction of overall uncertainty where samples' age intervals overlap one another. In our study, the stratigraphic order also plays a role, in particular for samples GB1 to GB4, where their age intervals overlap. However, the other reason

for the uncertainty reduction is the integration of the $^{14}$C ages as independent ages, since such combination, corrects the effect of systematic errors in OSL dating and resulted in ages that are more precise.

Moreover, the result of the Bayesian chronology ended up with ages younger (such as GB2 and GB9) and older (such as GB7, GB10 and GB11) than the corresponding ages produced by the classical approach of data analysis to satisfy the stratigraphic constraints. Besides, applying stratigraphic constraints for samples GB13 and GB14, which belong to one layer, results in a younger age for sample GB13 and older age for GB14. On the other hand, the classical ages show that the age of GB14 is slightly younger than GB13. As a result, it can be concluded that applying stratigraphic ordering might lead to underestimated or overestimated ages when age intervals overlap. Here we believe that this discrepancy is not critical since the Bayesian ages overlap and they statistically are not distinguishable.

### 4.4.3 The obtained chronology in its Paleolithic context

Ghār-e Boof is mainly recognized for its rich Upper Paleolithic assemblages based on bladelet production named Rostamian tradition Conard and Ghasidian (2011); Ghasidian (2014); Ghasidian et al. (2017). The richest horizon linked to the Rostamin tradition is AH III. The Bayesian OSL results for sublayers IIIa, IIIb, and IIIc suggest that the producers of Rostamian tradition likely occupied the site of Ghār-e Boof between 37 ka and 39 ka (68 % CI). The obtained Bayesian chronology using both OSL ages and $^{14}$C dates resulted in 35–42 ka for AH III to AH IV (also sublayer IVa). Moreover, the result of Bayesian modeling only for $^{14}$C published in Becerra-Valdivia et al. (2017) yielded the age of 41,950–39,850 cal. BP (in 68 % CI), which corresponds to the beginnings of the Upper Paleolithic period for the site and for the Zagros as a whole. These results agree with the Bayesian OSL ages of the AH IV and AH IVa of 40–42 ka.

Sublayers AH IVc and AH IVd have low find densities and cannot at present be attributed with confidence to either the Middle or the Upper Paleolithic. Although Arjeneh point and perforated shells were observed in AH IV to AH IVb, which we attribute to the Upper Paleolithic, they are missing in AH IVc and AH IVd. As a result, the age of AH IVd 45–48 ka may be considered to represent the period between Middle Paleolithic and the Rostamian at Ghār-e Boof.

In summary, the Bayesian OSL ages determined for the Upper Paleolithic sequence of the site from AH IIIa to AH IVa resulted in ages of 37–42 ka (68 % CI). This range agrees with the chronology for the Upper Paleolithic of the Shanidar cave in the north of Zagros which is in ca 29–40 cal ka BP (original data: Solecki 1963; Hole and Flannery 1968, recalculated data: Becerra-Valdivia et al. 2017). This result is also in agreement with the Upper Paleolithic chronology provided for the site of Yafteh associated with the Baradostian cultural group (Otte et al. 2011; ca 29–42 cal. ka BP). Aside from the controversial ages for the early Upper Paleolithic of the Kaldar cave with the range of ca 37–54 cal. ka BP Bazgir et al. (2017), the results from Ghār-e

Boof are consistent with the Upper Paleolithic chronology known elsewhere in the Zagros.

In general, the chronology for the Upper Paleolithic part of the site of Ghār-e Boof, similar to other sites mentioned in the Zagros Mountains, seems to be older than the chronology provided for the Paleolithic sites located in the north of central Iranian desert. For instance, the site of Garm roud 2, which is situated in the north of the Alborz Mountains region, suggests an Upper Paleolithic settlement between 28 cal. ka BP and 35 cal. ka BP (Berillon et al., 2007; Antoine et al., 2016). Moreover, the Bayesian OSL dating for the Upper Paleolithic sequence of the open-air site of Mirak (Nasab et al., 2019) resulted in 21–28 ka (Heydari et al., 2020).

The Bayesian OSL chronology of the Middle Paleolithic for AH V results in the range of 46–49 ka. Below, for samples taken from AH Va, in the western and the northern wall, the Bayesian ages result in 51–55 ka and 55–58 ka. The age results for sublayers AH Vb and AH Vc encompass the range of 56–60 ka and 58–63 ka. The two Bayesian ages for the last layer AH VI from the top and the bottom exhibited 72–78 ka and 75–81 ka. In summary, the chronology of the archaeological layers containing Middle Paleolithic assemblages shows a wide range of 45–81 ka, starting with the range of 72–81 ka and continuing to the very late Middle Paleolithic 45–46 ka. The Middle Paleolithic deposits at Ghār-e Boof (AH IVd to AH VI) are not as rich as the Rostamian part of the sequence. Although the Middle Paleolithic assemblages have not yet been published in detail, we argue that there is no continuity observed between the Middle Paleolithic and the bladelet assemblages of the Upper Paleolithic at Ghār-e Boof (Bretzke and Conard, 2017; Conard and Zeidi, 2019). The much lower density of the Middle Paleolithic assemblages appears to reflect sporadic, short-term occupations characterized by diverse scrapers and a dominance of flake production. These assemblages stand in stark contrast to the rich unidirectional bladelet production during the Rostamian. Also the rich record of personal ornaments, including numerous perforated shells and a perforated incisor of an ungulate (Conard and Ghasidian, 2011; Conard and Zeidi, 2019), is thus far limited to the Rostamian deposits. We hypothesize that the Rostamian appeared due to the presence of a new group of AMH in the region. This population was likely different from the humans who created the relatively sparse Middle Paleolithic record from period pre- ceding the Rostamian. For the moment, we do not know which human species were responsible for Middle Paleolithic assem- blages recovered from Ghār-e Boof. This being said, to date, the evidence available from sites in the Zagros including Bisitun Cave, Shanidar, and Wezmeh suggest that Neanderthals were often responsible for making Middle Paleolithic assemblages (Coon, 1951; Solecki, 1963; Trinkaus, 1983; Zanolli et al., 2019) . On the other hand, the complex record of human fossils dating to the Late Middle Pleistocene and Upper Pleistocene in southwestern Asia as a whole points to a long history of early modern humans in the macroregion and warns against rushing to hasty conclusions in the absence of human skeletal remains (Hershkovitz et al., 2018).

In summary, our study shows that Ghār-e Boof was occupied intensely during MIS (Marine Iso-

tope Stage) 3 (after Lisiecki and Raymo, 2005) near the beginning of the Upper Paleolithic. The site was occupied during MIS 3, MIS 4, and MIS 5a by the makers of the Middle Paleolithic assemblages. Although many questions remain open, it is worth mentioning that the new Middle Paleolithic chronology for the site of Ghār-e Boof represents the first reliable absolute chronology for the Middle Paleolithic of the southern Zagros. Due to the unique location of Ghār-e Boof, and the likely association of the Rostamian with modern humans, our chronology provides insights into dispersal routes of early modern humans from Africa toward central Asia through the south of the Iranian Plateau. To decipher the full picture in the southern Zagros, more archaeological fieldwork and paleochronological studies are needed in the future.

## 4.5 Conclusion

We have presented a luminescence chronology based on quartz and the polymineral for the Middle and Upper Paleolithic sequences of the site of Ghār-e Boof. Our investigation showed that the $pIRIR_{290}$ ages for the polymineral fractions are in good agreement with the blue-OSL ages of the quartz grains. In addition, previously published $^{14}C$ ages for the Upper Paleolithic part of the cave agree with the luminescence ages. We then applied Bayesian modeling, specifically designed for luminescence dating on blue-OSL quartz signals using the R package 'BayLum', which enabled us to incorporate published $^{14}C$ ages and the well-established stratigraphic constraints to further improve the precision of the chronology. The obtained Bayesian ages resulted in a significantly improved precision by reducing the age uncertainties. The Bayesian ages of the Upper Paleolithic sequence of the cave for AH IIIa to IVa produced ages of 37–42 ka (68 % CI). This result is in agreement with the chronology based on $^{14}C$ (Conard and Ghasidian, 2011; Baines et al., 2014; Becerra-Valdivia et al., 2017).

The chronology obtained for the Middle Paleolithic sequence of the cave in AH IVd to AH VI resulted in a wide age range of 45–81 ka (68 % CI). This work provides a solid luminescence-based chronology for the Middle Paleolithic period in Iran. Moreover, the Bayesian OSL chronology for the site of Ghār-e Boof is the first complete luminescence dating of the Middle and the Upper Paleolithic periods in the Zagros Mountain region in Iran. The radical change in material culture between the Middle Paleolithic and Rostamian Upper Paleolithic occupations at Ghār-e Boof almost certainly documents the occupation of the site by different groups of humans during MIS 3, MIS 4 and MIS 5a. While we have good reasons to hypothesize that the Rostamian assemblages were left by AMH, both Neanderthals and modern humans remain plausible candidates as the makers of the sites Middle Paleolithic assemblages. Regardless of the specific identity of these populations, the chronostratigraphic sequence from Ghār-e Boof points to a shift between the Middle Paleolithic and Rostamian demographic groups within three millennia.

## Acknowledgements

This work is part of the Ph.D. Dissertation of M.H. financed by the Laboratoire d'Excellence Sciences archéologiques $D_e$ Bordeaux (LaScArBx), a programme supported by the Agence Nationale de la Recherche (ANR) - n° ANR-10-LABX-52. We are grateful to David Alba, associate editor, and three anonymous reviewers for providing constructive feedback that improved our manuscript. Sebastian Kreutzer is thanked for creating the map and running the IR-RF tests on the spectrometer system at the Lux laboratory at the Université du Quebec à Montréal (Canada). We are grateful to Michel Lamothe for giving us access to his equipment for the IR-RF tests. Chantal Tribolo is thanked for her constructive comments on an earlier version of the manuscript. Hélène Valladas is thanked for irradiating two samples at the laboratory of Gif-sur-Yvette (Laboratoire des Sciences du Climat et de l'Environnement). We are grateful to Mohammad Beheshti, the former head of research center at Iran Cultural Heritage, Handicrafts and Tourism Organization (ICHHTO), Hamideh Choubak, the former head of Iranian Center for Archaeological Research (ICAR), Monireh Kholghi, the head of international section at ICHHTO, Alireza Sardari, Ahmad Chaichi, Siamak Sarlak, Mohammad Mortezaei, Hana Bah- rani Pour, and Fatemeh Farshi Jalali, at ICAR for facilitating this work and providing the necessary permits. We are also grateful to Mosayeb Amiri, the head of ICHHTO in Fars and Maghamat Mah- moudi, the head of the cultural heritage office of Rostam County for their help and facilitating the work. We thank Rasoul Boroujeni and Kourosh Alamdari, our Iranian representatives, the field crew especially Saman Hamzavi for their work in as members of the excavation team and for their important contribution to the lab work. The excavation was funded by the Deutsche Forschungsgemeinschaft (DFG) grant CO 226/30-1.

## 4.6 Supplement

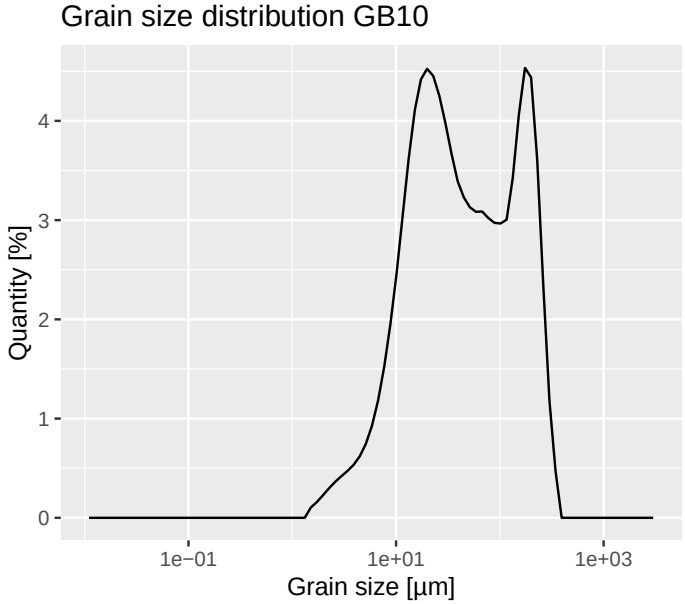


Figure 4.9: Exemplary grain size distribution for sample GB10. Although the distribution indicates a bimodal grain size distribution, the coarser size was not observed in significant abundance during sample preparation, and it was likely the result of conglomerates.

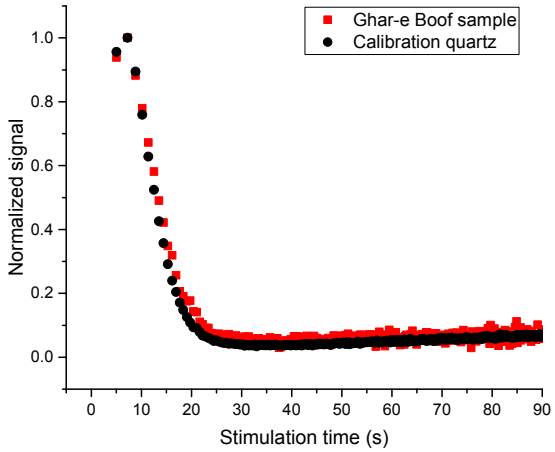


Figure 4.10: Comparison of the OSL signal of Ghār-e Boof (GB10) with the OSL signal from a calibration quartz sample. The perfect match of the two signals indicates a fast decaying signal component domination of the OSL signal from Ghār-e Boof.

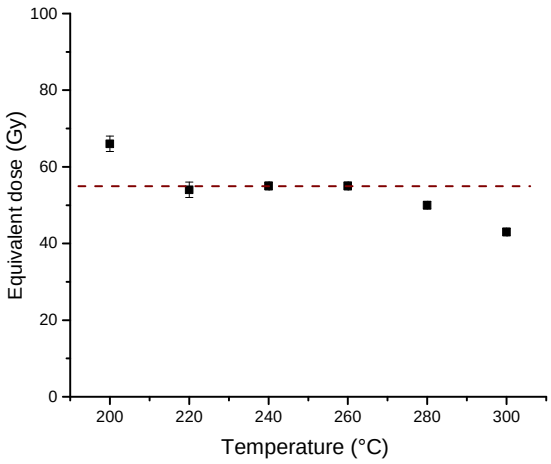


Figure 4.11: The result of the preheat plateau test for sample GB4. We selected 260 °C for the preheat temperature, which is located in the plateau. The dashed line represents the average of the entire measured equivalent doses in the test.

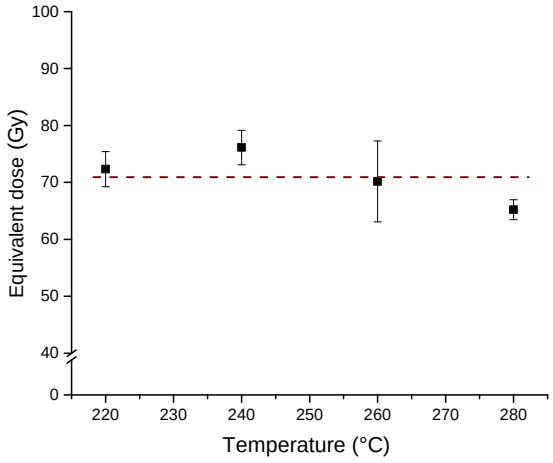


Figure 4.12: The result of preheat plateau test for sample GB8. The preheat temperature of 280 °C appears to be situated under the plateau (as for sample GB 4 Fig. S4.11).

Table 4.4: The post-IR IRSL 290 °C protocol after Buylaert et al. (2012).

| # | STEP | OBSERVATION |
|---|---|---|
| 1 | Irradiation (regenerative dose) | |
| 2 | Thermal treatment (preheat 320 °C) | |
| 3 | IRSL stimulation (for 200 s at 50 °C) | |
| 4 | IRSL stimulation (for 200 s at 290 °C) | $L_n$, $L_x$ |
| 5 | Irradiation (test-dose) | |
| 6 | Thermal treatment (preheat 320 °C) | |
| 7 | IRSL stimulation (for 200 s at 50 °C) | |
| 8 | IRSL stimulation (for 200 s at 290 °C) | $T_n$, $T_x$ |
| 9 | IRSL stimulation (for 200 s at 325 °C) | |

Abbreviations: post-IR IRSL 290 °C = post-infrared stimulated luminescence at 290 °C
$L_n$ = measured natural dose; $L_x$ = measured regenerative dose
$T_n$ = measured natural test dose; $T_x$ = measured regenerative test dose

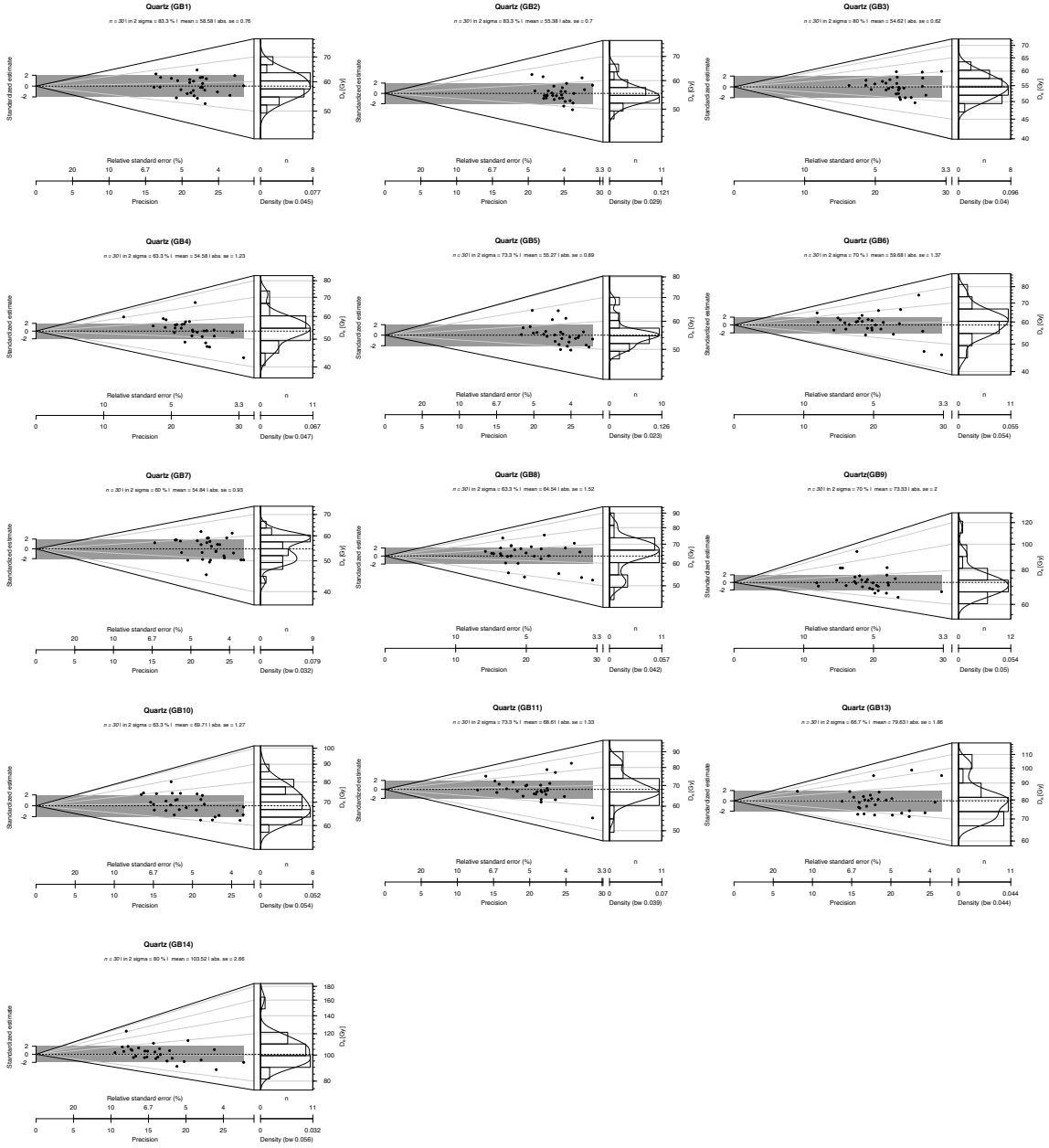


Figure 4.13: Equivalent dose distributions of all quartz samples. Abbreviations: `n` = number of the measured aliquots for each sample; `abs.se` = absolute standard error.

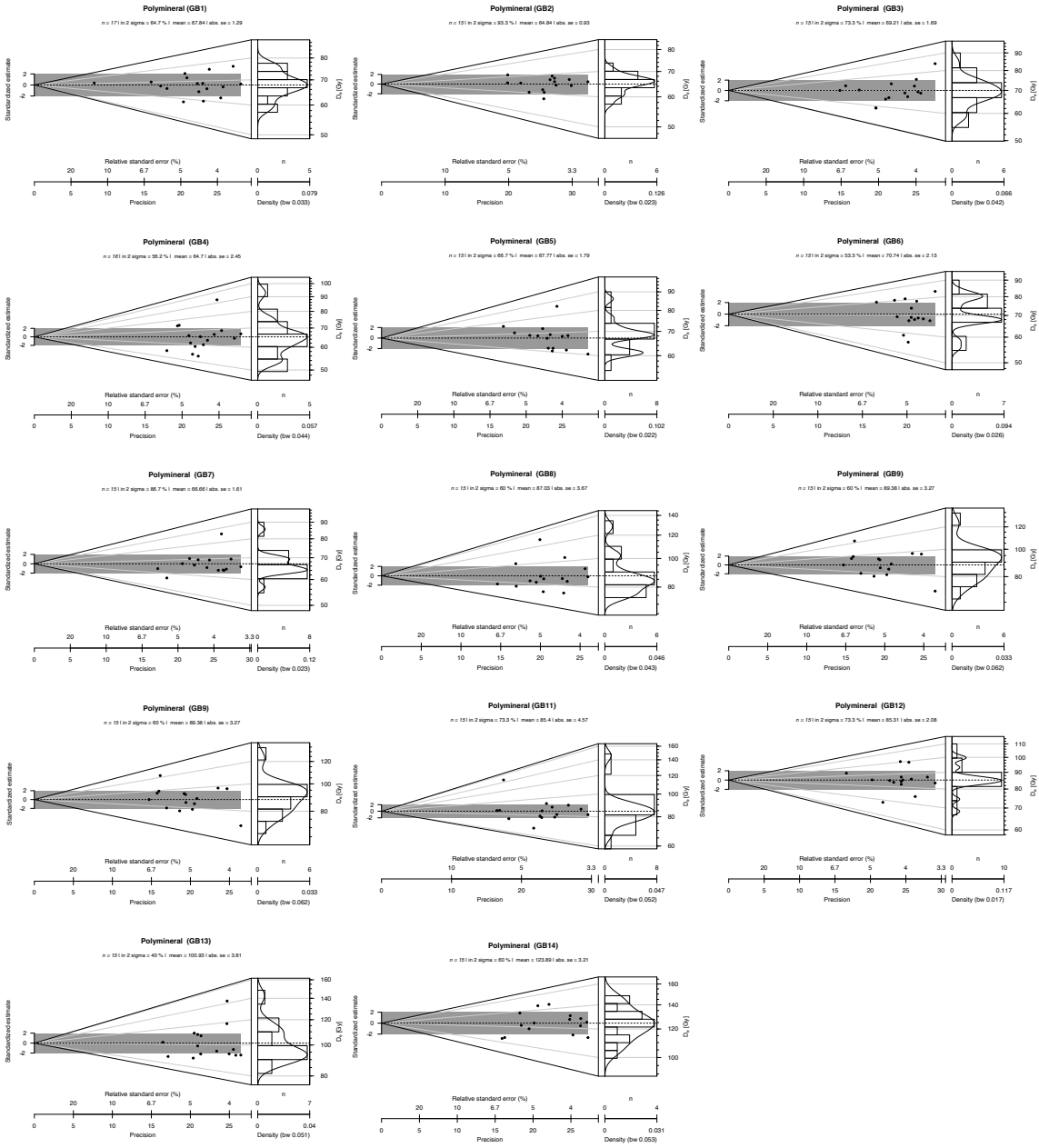


Figure 4.14: Equivalent dose distributions of all polymineral samples. Abbreviations: `n` = number of the measured aliquots for each sample; `abs.se` = absolute standard error.

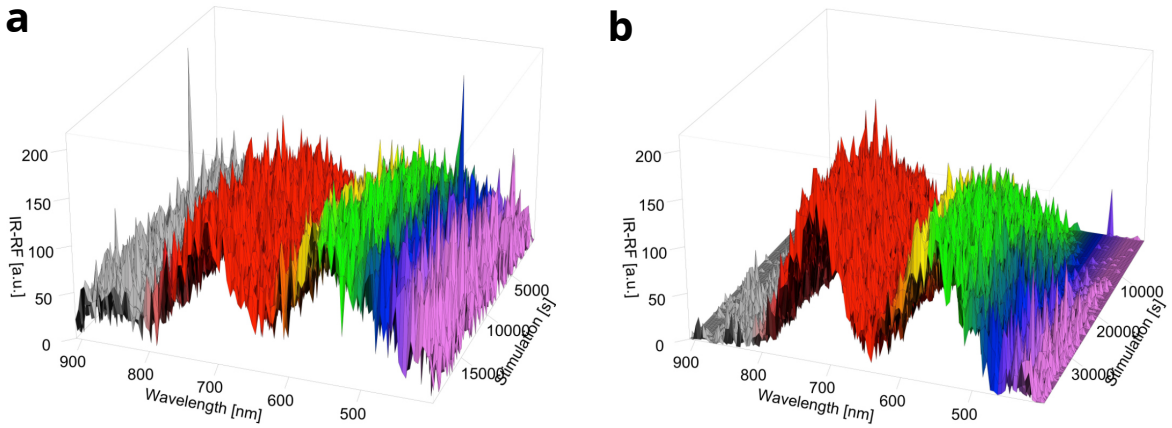


Figure 4.15: Radiofluorescence spectra measured for sample GB2: a) natural spectra; b) regenerative spectra. The spectra show that the relevant signal in the IR wavelength range is basically not existing and largely biased by a peak in the red wavelength region.

Table 4.5: The average of the obtained recycling ratio for all quartz samples.

| SAMPLES | RECYLING RATIO | SEM |
|---|---|---|
| GB1 | 0.83 | 0.00 |
| GB2 | 0.83 | 0.00 |
| GB3 | 0.84 | 0.01 |
| GB4 | 0.83 | 0.01 |
| GB5 | 0.82 | 0.00 |
| GB6 | 0.87 | 0.02 |
| GB7 | 0.82 | 0.00 |
| GB8 | 0.85 | 0.01 |
| GB9 | 0.85 | 0.01 |
| GB10 | 0.85 | 0.01 |
| GB11 | 0.85 | 0.01 |
| GB12 | - | - |
| GB13 | 0.84 | 0.01 |
| GB14 | 0.84 | 0.01 |

Abbreviation: SEM = standard error of the mean.

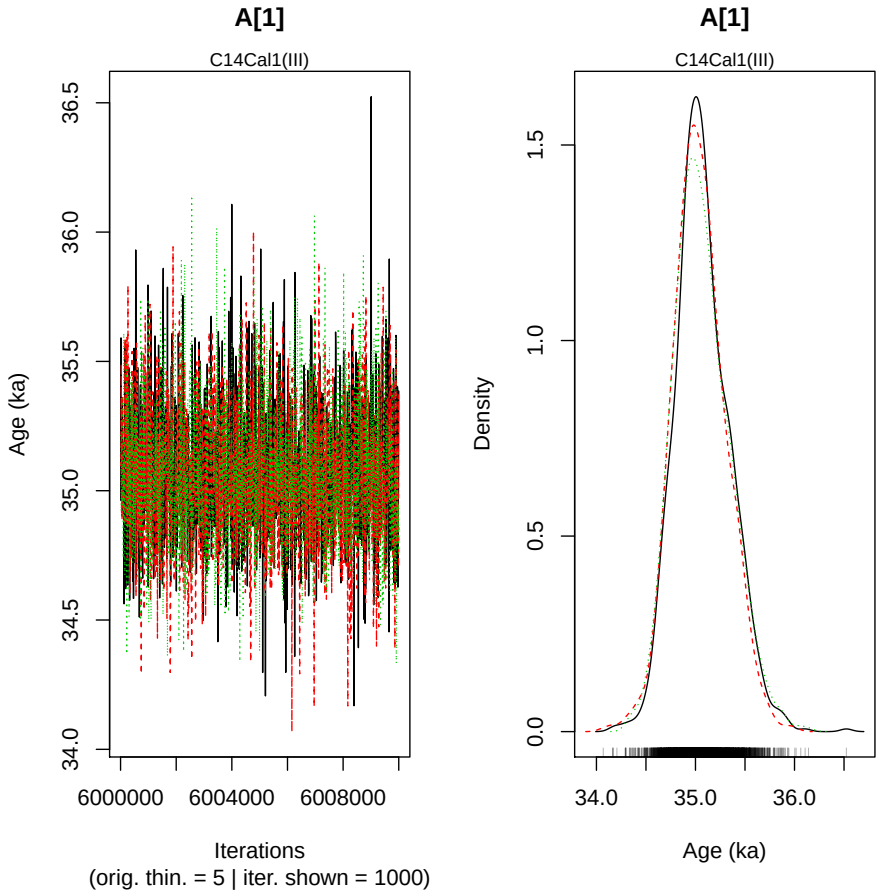


Figure 4.16: Example Markov Chain Monte Carlo (MCMC) convergence plot (left) and age density distribution plot (right) example for sample GB4.

Table 4.6: The average of the obtained recycling ratio for all polymineral samples.

| SAMPLES | RECYLING RATIO | SEM |
|---|---|---|
| GB1 | 1.03 | 0.01 |
| GB2 | 1.05 | 0.01 |
| GB3 | 1.04 | 0.01 |
| GB4 | 1.04 | 0.01 |
| GB5 | 1.05 | 0.01 |
| GB6 | 0.99 | 0.06 |
| GB7 | 1.04 | 0.01 |
| GB8 | 1.04 | 0.01 |
| GB9 | 1.03 | 0.01 |
| GB10 | 1.03 | 0.01 |
| GB11 | 1.04 | 0.01 |
| GB12 | 1.03 | 0.01 |
| GB13 | 1.04 | 0.01 |
| GB14 | 1.02 | 0.01 |

Abbreviation: SEM = standard error of the mean.

Table 4.7: The estimated overdispersion for all quartz and polymineral samples in this study after Galbraith et al. (1999).

| SAMPLES | QUARTZ | | POLYMINERAL | |
|---|---|---|---|---|
| | OD (%) | SE | OD (%) | SE |
| GB1 | 5 | 1 | 6 | 2 |
| GB2 | 5 | 1 | 3 | 1 |
| GB3 | 5 | 1 | 8 | 2 |
| GB4 | 11 | 2 | 13 | 3 |
| GB5 | 7 | 1 | 8 | 2 |
| GB6 | 11 | 2 | 10 | 2 |
| GB7 | 8 | 1 | 7 | 2 |
| GB8 | 12 | 2 | 13 | 3 |
| GB9 | 12 | 2 | 12 | 3 |
| GB10 | 8 | 1 | 11 | 2 |
| GB11 | 9 | 2 | 15 | 3 |
| GB12 | - | - | 8 | 2 |
| GB13 | 10 | 2 | 12 | 3 |
| GB14 | 10 | 2 | 8 | 2 |

Abbreviations: OD = overdispersion in percentage.

Table 4.8: The calculated central dose using Average Dose Model (ADM) after Guérin et al. (2017) and the estimated arithmetic average for both quartz and polymineral samples.

| SAMPLE | QUARTZ | | | | POLYMINERAL | | | |
|---|---|---|---|---|---|---|---|---|
| | ADM (Gy) | SE | Arithmetic average (Gy) | SEM | ADM (Gy) | SE | Arithmetic average (Gy) | SEM |
| GB1 | 59 | 1 | 59 | 1 | 68 | 1 | 68 | 1 |
| GB2 | 55 | 1 | 55 | 1 | 65 | 1 | 65 | 1 |
| GB3 | 55 | 1 | 55 | 1 | 70 | 2 | 69 | 2 |
| GB4 | 55 | 1 | 55 | 1 | 65 | 2 | 65 | 2 |
| GB5 | 55 | 1 | 55 | 1 | 68 | 2 | 68 | 2 |
| GB6 | 60 | 1 | 60 | 1 | 71 | 2 | 71 | 2 |
| GB7 | 55 | 1 | 55 | 1 | 67 | 1 | 67 | 2 |
| GB8 | 65 | 1 | 65 | 2 | 88 | 3 | 88 | 4 |
| GB9 | 74 | 2 | 74 | 2 | 90 | 3 | 90 | 3 |
| GB10 | 69 | 1 | 70 | 1 | 88 | 3 | 88 | 3 |
| GB11 | 69 | 1 | 69 | 1 | 86 | 4 | 87 | 5 |
| GB12 | - | - | - | - | 86 | 2 | 86 | 2 |
| GB13 | 80 | 2 | 80 | 2 | 102 | 4 | 102 | 4 |
| GB14 | 103 | 3 | 104 | 3 | 125 | 3 | 124 | 3 |

Abbreviation: SEM = standard error of the mean.

Table 4.9: Investigating the correlation between the $D_e$ and recycling ratio. The $D_e$ distributions for six samples are divided into two groups: group1 with recycling ratio smaller than the average (showing with $< D_e$ (Gy)) and group 2 with recycling ratio larger than the average (showing with $> D_e$ (Gy)).

| SAMPLE | $<D_e$ (Gy) | SEM | n | $>D_e$ (Gy) | SEM | n | $D_e$ (Gy) | SEM |
|---|---|---|---|---|---|---|---|---|
| GB1 | 60 | 1 | 16 | 57 | 1 | 14 | 59 | 1 |
| GB3 | 53 | 1 | 15 | 56 | 1 | 15 | 55 | 1 |
| GB5 | 55 | 1 | 11 | 55 | 1 | 19 | 55 | 1 |
| GB8 | 65 | 2 | 12 | 65 | 2 | 18 | 65 | 2 |
| GB10 | 69 | 2 | 13 | 71 | 2 | 17 | 70 | 1 |
| GB14 | 104 | 4 | 16 | 105 | 4 | 14 | 104 | 3 |

Abbreviations: $D_e$ = equivalent dose, n = number of measured aliquots.
SEM = standard error of the mean.

## Study III: References


Aitken, M. J.: Thermoluminescence dating, Studies in archaeological science, Academic Press, 1985.

Antoine, P., Bahain, J. J., Ghaleb, B., and Mercier, N.: The chronostratigraphic framework at Garm roud, in: Garm Roud. A Hunting Place in Iran, Upper Palaeolithic, edited by Berillon, G. and Asgari Khanegah, A., pp. 49–55, Editions IFRI & rchéo-éditions (French- English-Persian), 2016.

Bailey, R. M., Smith, B. W., and Rhodes, E. J.: Partial Bleaching and the decay from characteristics of quartz OSL, Radiation Measurements, 27, 123–136, 1997.

Baines, J. A., Riehl, S., Conard, N., and Zeidi-Kulehparcheh, M.: Upper Palaeolithic archaeobotany of Ghar-e Boof cave, Iran: a case study in site disturbance and methodology, Archaeological and Anthropological Sciences, 7, 245–256, 2014.

Bazgir, B., Ollé, A., Tumung, L., Becerra-Valdivia, L., Douka, K., Higham, T., van der Made, J., Picin, A., Saladié, P., López-García, J. M., Blain, H.-A., Allue, E., Fernández-García, M., Rey-Rodríguez, I., Arceredillo, D., Bahrololoumi, F., Azimi, M., Otte, M., and Carbonell, E.: Understanding the emergence of modern humans and the disappearance of Neanderthals: Insights from Kaldar Cave (Khorramabad Valley, Western Iran), Scientific Reports, 7, 525–16, 2017.

Becerra-Valdivia, L., Douka, K., Comeskey, D., Bazgir, B., Conard, N. J., Marean, C. W., Ollé, A., Otte, M., Tumung, L., Zeidi, M., and Higham, T. F. G.: Chronometric investigations of the Middle to Upper Paleolithic transition in the Zagros Mountains using AMS radiocarbon dating and Bayesian age modelling, Journal of Human Evolution, 109, 57–69, 2017.

Berillon, G., Asgari Khaneghah, A., Antoine, P., Bahain, J.-J., Chevrier, B., Zeitoun, V., Aminzadeh, N., Beheshti, M., Chanzanagh, H. E., and Nochadi, S.: Discovery of new open-air Paleolithic localities in Central Alborz, Northern Iran, Journal of Human Evolution, 52, 380–387, 2007.

Biglari, F.: Recent Finds of Paleolithic Period from Bisitun, Central Western Zagros Mountains, Iranian Journal of Archaeology and History, 28, 50–60, 2001.

Bobek, H.: Vegetation, in: The Cambridge History of Iran, edited by Fisher, W. B., pp. 280–293, Cambridge University Press, Cambridge, 1968.

Boivin, N., Fuller, D. Q., Dennell, R., Allaby, R., and Petraglia, M. D.: Human dispersal across diverse environments of Asia during the Upper Pleistocene, Quaternary International, 300, 32–47, 2013.

Bos, A. J. J. and Wallinga, J.: How to visualize quartz OSL signal components, Radiation Measurements, 47, 752–758, 2012.

Bretzke, K. and Conard, N. J.: Not Just a Crossroad: Population Dynamics and Changing Material Culture in Southwestern Asia during the Late Pleistocene, Current Anthropology, 58, S449–S462, 2017.

Brookes, I. A.: The physical geography, geomorphology, and Late Quaternary history of the Mahidasht project area, Qara Su Basin, central west Iran, vol. 1, Royal Ontario Museum, Toronto, 1989.

Buylaert, J. P., Jain, M., Murray, A. S., Thomsen, K. J., Thiel, C., and Sohbati, R.: A robust feldspar luminescence dating method for Middle and Late Pleistocene sediments, Boreas, 41, 435–451, 2012.

Christophe, C., Philippe, A., Kreutzer, S., and Guérin, G.: BayLum: Chronological Bayesian Models Integrating Optically Stimulated Luminescence and Radiocarbon Age Dating, CRAN, Version: 0.1.4, URL `https://cran.r-project.org/package=BayLum`, http://github.com/crp2a/BayLum, 2019.

Colarossi, D., Duller, G. A. T., and Roberts, H. M.: Exploring the behaviour of luminescence signals from feldspars: Implications for the single aliquot regenerative dose protocol, Radiation Measurements, 109, 35–44, 2017.

Combès, B. and Philippe, A.: Bayesian analysis of individual and systematic multiplicative errors for estimating ages with stratigraphic constraints in optically stimulated luminescence dating, Quaternary Geochronology, 39, 24–34, 2017.

Combès, B., Philippe, A., Lanos, P., Mercier, N., Tribolo, C., Guérin, G., Guibert, P., and Lahaye, C.: A Bayesian central equivalent dose model for optically stimulated luminescence dating, Quaternary Geochronology, 28, 62–70, 2015.

Conard, N. J. and Ghasidian, E.: The Rostamian cultural group and thetaxonomy of the Iranian Upper Paleolithic, in: Between Sand and Sea. The Archaeology and Human Ecology of Southwestern Asia, edited by Conard, N. J., Drechsler, P., and Morales, A., pp. 33–52, Kerns Verlag, Tübingen, Germany, 2011.

Conard, N. J. and Zeidi, M.: New research on the Paleolithic occupation of Ghar-e Boof, Fars Province, Archaeology, Journal of the Iranian Center for Archaeological Research, 2, 7–16, 2019.

Conard, N. J., Ghasidian, E., and Heydari-Guran, S.: The Paleolithic of Iran, in: The Oxford Handbook of Ancient Iran, edited by Potts, D. T., pp. 29–48, Oxford University Press, 2013.

Coon, C. S.: Cave explorations in Iran, 1949., University Museum, University of Pennsylvania, Philadelphia, 1951.

Dietze, M., Kreutzer, S., Burow, C., Fuchs, M. C., Fischer, M., and Schmidt, C.: The abanico plot: visualising chronometric data with individual standard errors, Quaternary Geochronology, 31, 12–18, 2016.

Duller, G. A. T.: Distinguishing quartz and feldspar in single grain luminescence measurements, Radiation Measurements, 37, 161–165, 2003.

Duller, G. A. T.: The Analyst software package for luminescence data: overview and recent improvements , Ancient TL, 33, 35–42, 2015.

Durcan, J. A., King, G. E., and Duller, G. A. T.: DRAC: Dose Rate and Age Calculator for trapped charge dating, Quaternary Geochronology, 28, 54–61, 2015.

Frayret, J., Castetbon, A., Trouve, G., and Potin-Gautier, M.: Solubility of (NH4)2SiF6, K2SiF6 and Na2SiF6 in acidic solutions, Chemical Physics Letters, 427, 356–364, 2006.

Frouin, M., Huot, S., Kreutzer, S., Lahaye, C., Lamothe, M., Philippe, A., and Mercier, N.: An improved radiofluorescence single-aliquot regenerative dose protocol for K-feldspars, Quaternary Geochronology, 38, 13–24, 2017.

Galbraith, R. F., Roberts, R. G., Laslett, G. M., Yoshida, H., and Olley, J. M.: Optical dating of single and multiple grains of Quartz from Jinmium Rock Shelter, Northern Australia: Part I, Experimental design and statistical models, Archaeometry, 41, 339–364, 1999.

Ganji, M. H.: Climate, in: The Cambridge History of Iran, edited by Fisher, W. B., pp. 212–249, Cambridge University Press, Cambridge, 1968.

Ghasidian, E.: The Early Upper Paleolithic Occupation at Ghār-e Boof Cave: A Reconstruction of Cultural Tradition in the Southern Zagros Mountains of Iran, Kerns Verlag, Tübingen, 2014.

Ghasidian, E., Bretzke, K., and Conard, N. J.: Excavations at Ghār-e Boof in the Fars Province of Iran and its bearing on models for the evolution of the Upper Palaeolithic in the Zagros Mountains, Journal of Anthropological Archaeology, 47, 33–49, 2017.

Ghasidian, E., Heydari-Guran, S., and Mirazón Lahr, M.: Upper Paleolithic cultural diversity in the Iranian Zagros Mountains and the expansion of modern humans into Eurasia, Journal of Human Evolution, 132, 101–118, 2019.

Grün, R., Stringer, C., McDermott, F., Nathan, R., Porat, N., Robertson, S., Taylor, L., Mortimer, G., Eggins, S., and McCulloch, M.: U-series and ESR analyses of bones and teeth relating to the human burials from Skhul, Journal of Human Evolution, 49, 316–334, 2005.

Guérin, G. and Mercier, N.: Preliminary insight into dose deposition processes in sedimentary media on a scale of single grains: Monte Carlo modelling of the effect of water on the gamma dose rate, Radiation Measurements, 47, 541–547, 2012.

Guérin, G., Mercier, N., and Adamiec, G.: Dose-rate conversion factors: update, Ancient TL, 29, 5–9, 2011.

Guérin, G., Mercier, N., Nathan, R., Adamiec, G., and Lefrais, Y.: On the use of the infinite matrix assumption and associated concepts: A critical review, Radiation Measurements, 47, 778–785, 2012.

Guérin, G., Combès, B., Lahaye, C., Thomsen, K. J., Tribolo, C., Urbanova, P., Guibert, P., Mercier, N., and Valladas, H.: Testing the accuracy of a Bayesian central-dose model for single-grain OSL, using known-age samples, Radiation Measurements, 81, 62–70, 2015.

Guérin, G., Christophe, C., Philippe, A., Murray, A. S., Thomsen, K. J., Tribolo, C., Urbanova, P., Jain, M., Guibert, P., Mercier, N., Kreutzer, S., and Lahaye, C.: Absorbed dose, equivalent dose, measured dose rates, and implications for OSL age estimates: Introducing the Average Dose Model, Quaternary Geochronology, 41, 1–32, 2017.

Guibert, P. and Schvoerer, M.: TL dating: Low background gamma spectrometry as a tool for the determination of the annual dose, International Journal of Radiation Applications and Instrumentation. Part D. Nuclear Tracks and Radiation Measurements, 18, 231–238, 1991.

Guibert, P., Lahaye, C., and Bechtel, F.: The importance of U-series disequilibrium of sediments in luminescence dating: A case study at the Roc de Marsal Cave (Dordogne, France), Radiation Measurements, 44, 223–231, 2009.

Hansen, V., Murray, A., Buylaert, J.-P., Yeo, E.-Y., and Thomsen, K.: A new irradiated quartz for beta source calibration, Radiation Measurements, 81, 123–127, 2015.

Hershkovitz, I., Weber, G. W., Quam, R., Duval, M., Grün, R., Kinsley, L., Ayalon, A., Bar-Matthews, M., Valladas, H., Mercier, N., Arsuaga, J. L., Martinón-Torres, M., Bermúdez de Castro, J. M., Fornai, C., Martín-Francés, L., Sarig, R., May, H., Krenn, V. A., Slon, V., Rodríguez, L., García, R., Lorenzo, C., Carretero, J. M., Frumkin, A., Shahack-Gross, R., Bar-Yosef Mayer, D. E., Cui, Y., Wu, X., Peled, N., Groman-Yaroslavski, I., Weissbrod, L., Yeshurun, R., Tsatskin, A., Zaidner, Y., and Weinstein-Evron, M.: The earliest modern humans outside Africa, Science, 359, 456–459, 2018.

Heydari, M. and Guérin, G.: OSL signal saturation and dose rate variability: Investigating the behaviour of different statistical models, Radiation Measurements, 120, 96–103, 2018.

Heydari, M., Guérin, G., Kreutzer, S., Jamet, G., Kharazian, M. A., Hashemi, M., Nasab, H. V., and Berillon, G.: Do Bayesian methods lead to more precise chronologies? 'BayLum' and a first OSL-based chronology for the Palaeolithic open-air site of Mirak (Iran), Quaternary Geochronology, 59, 101 082, 2020.

Heydari-Guran, S.: Paleolithic Landscapes of Iran, Archaeopress, Oxford, 2014.

Heydari-Guran, S. and Ghasidian, E.: The MUP Zagros Project: tracking the Middle–Upper Palaeolithic transition in the Kermanshah region, west-central Zagros, Iran, Antiquity Project Gallery, 91, 40–7, 2017.

Higham, T.: European Middle and Upper Palaeolithic radiocarbon dates are often older than they look: problems with previous dates and some remedies, Antiquity Project Gallery, 85, 235–249, 2011.

Hole, F. and Flannery, K. V.: The Prehistory of Southwestern Iran: A Preliminary Report, Proceedings of the Prehistoric Society, 33, 147–206, 1968.

Huntley, D. J. and Baril, M. R.: The K content of the K-feldspars being measured in optical dating or in the thermoluminescence dating, Ancient TL, 15, 11–13, 1997.

Huntley, D. J. and Lamothe, M.: Ubiquity of anomalous fading in K-feldspars and the measurement and correction for it in optical dating, Canadian Journal of Earth Sciences, 38, 1093–1106, 2001.

Huntley, D. J., Godfrey-Smith, D. I., and Thewalt, M. L. W.: Optical dating of sediments, Nature, 313, 105–107, 1985.

Hütt, G., Jaek, I., and Tchonka, J.: Optical dating: K-Feldspars optical response stimulation spectra, Quaternary Science Reviews, 7, 381–385, 1988.

Jaubert, J., Biglari, F., Bordes, J.-G., Bruxelles, L., Mourre, V., Shidrang, S., Naderi, R., and Alipour, S.: New Research on Paleolithic of Iran: Preliminary Report of 2004 Iranian-French Joint Mission, Archaeological Reports, 4, 17–26, 2006.

Krbetschek, M. R., Rieser, U., Zöller, L., and Heinicke, J.: Radioactive disequilibria in palaeodosimetric dating of sediments, Radiation Measurements, 23, 485–489, 1994.

Kreutzer, S., Martin, L., Guérin, G., Tribolo, C., Selva, P., and Mercier, N.: Environmental Dose Rate Determination Using a Passive Dosimeter: Techniques and Workflow for alpha-$Al_2O_3$:C Chips, Geochronometria, 45, 56–67, 2018.

Li, B. and Li, S.-H.: Luminescence dating of K-feldspar from sediments: A protocol without anomalous fading correction, Quaternary Geochronology, 6, 468–479, 2011.

Li, B. and Li, S.-H.: A reply to the comments by Thomsen et al. on “Luminescence dating of K-feldspar from sediments: A protocol without anomalous fading correction”, Quaternary Geochronology, 8, 49–51, 2012.

Lisiecki, L. E. and Raymo, M. E.: A Pliocene-Pleistocene stack of 57 globally distributed benthic $\delta\ ^{18}$O records, Paleoceanography, 20, 1–17, 2005.

Martin, L.: Caractérisation et modélisation d’objets archéologiques en vue de leur datation par des méthodes paléo-dosimétriques. Simulation des paramètres dosimétriques sous Geant4., Ph.D. thesis, Université Bordeaux Montaigne, 2015.

Mauz, B., Packman, S. C., and Lang, A.: The alpha effectiveness in silt-sized quartz: New data obtained by single and multiple aliquot protocols, Ancient TL, 24, 47–52, 2006.

Meignen, L.: Levantine Perspectives on the Middle to Upper Paleolithic “Transition”, Archaeology, Ethnology & Anthropology of Eurasia, 40, 12–21, 2012.

Mejdahl, V.: Internal radioactivity in quartz and feldspar grains, Ancient TL, 5, 10–17, 1987.

Mellars, P.: Why did modern human populations disperse from Africa ca. 60,000 years ago? A new model, Proceedings of the National Academy of Sciences, 103, 9381–9386, 2006.

Millard, A. R.: Bayesian analysis of ESR dates, with application to Border Cave, Quaternary Geochronology, 1, 159–166, 2006.

Motiei, H.: Stratigraphy of Zagros. Treatise on the Geology of Iran, Ministry of Mines and Metals, Geological Survey of Iran, 1, 281–289, 1993.

Murray, A. S. and Wintle, A. G.: Luminescence dating of quartz using an improved single-aliquot regenerative-dose protocol, Radiation Measurements, 32, 57–73, 2000.

Murray, A. S., Thomsen, K. J., Masuda, N., Buylaert, J. P., and Jain, M.: Identifying well-bleached quartz using the different bleaching rates of quartz and feldspar luminescence signals, Radiation Measurements, 47, 688–695, 2012.

Nasab, H. V., Clark, G. A., and Torkamandi, S.: Late Pleistocene dispersal corridors across the Iranian Plateau: A case study from Mirak, a Middle Paleolithic site on the northern edge of the Iranian Central desert (Dasht-e Kavir), Quaternary International, 300, 267–281, 2013.

Nasab, H. V., Berillon, G., Jamet, G., Hashemi, M., Jayez, M., Khaksar, S., Anvari, Z., Guérin, G., Heydari, M., Kharazian, M. A., Puaud, S., Bonilauri, S., Zeitoun, V., Sévêque, N., Khatooni, J. D., and Asgari Khaneghah, A.: The open-air Paleolithic site of Mirak, northern edge of the Iranian Central Desert (Semnan, Iran): Evidence of repeated human occupations during the late Pleistocene, Comptes Rendus Palevol, 18, 465–478, 2019.

Nathan, R. P. and Mauz, B.: On the dose-rate estimate of carbonate-rich sediments for trapped charge dating, Radiation Measurements, 43, 14–25, 2008.

Nishiaki, Y. and Akazawa, T.: Archeological Issues in the Middle and Upper Paleolithic of the Levant and Its Neighboring Regions, in: The Middle and Upper Paleolithic Archeology of the Levant and Beyond, edited by Nishiaki, Y. and Akazawa, T., pp. 133–156, Springer Singapore, Singapore, 2018.

O Bar-Yosef, L. M.: The Chronology of the Levantine Middle Palaeolithic Period in Retrospect, Bulletins et mémoires de la Société dAnthropologie de Paris, 13, 269–289, 2001.

Otte, M., Shidrang, S., Zwyns, N., and Flas, D.: New radiocarbon dates for the Zagros Aurignacian from Yafteh cave, Iran, Journal of Human Evolution, 61, 340–346, 2011.

Petraglia, M. D., Haslam, M., Fuller, D. Q., Boivin, N., and Clarkson, C.: Out of Africa: new hypotheses and evidence for the dispersal of Homo sapiensalong the Indian Ocean rim, Annals of Human Biology, 37, 288–311, 2010.

Philippe, A., Guérin, G., and Kreutzer, S.: BayLum - An R package for Bayesian analysis of OSL ages: An introduction, Quaternary Geochronology, 49, 16–24, 2019.

Prescott, J. R. and Hutton, J. T.: Cosmic ray contributions to dose rates for luminescence and ESR dating: Large depths and long-term time variations, Radiation Measurements, 23, 497–500, 1994.

Prescott, J. R. and Stephan, L. G.: The contribution of cosmic radiation to the environmental dose for thermoluminescence dating. Latitude, altitude and depth dependences, PACT 3 - Revue du Réseau Européen de Sciences et Techniques appliquées au Patrimoine Culturel, pp. 17–25, 1982.

Preusser, F., Degering, D., Fuchs, M., Hilgers, A., Kadereit, A., Klasen, N., Krbetschek, M. R., Richter, D., and Spencer, J. Q. G.: Luminescence dating: basics, methods and applications, Eiszeitalter und Gegenwart (Quaternary Science Journal), 57, 95–149, 2008.

R Core Team: R: A Language and Environment for Statistical Computing, Vienna, Austria, URL `https://r-project.org`, 2019.

Reimer, P. J., Bard, E., Bayliss, A., Beck, J. W., Blackwell, P. G., Ramsey, C. B., Buck, C. E., Cheng, H., Edwards, R. L., Friedrich, M., Grootes, P. M., Guilderson, T. P., Haflidason, H., Hajdas, I., Hatté, C., Heaton, T. J., Hoffmann, D. L., Hogg, A. G., Hughen, K. A., Kaiser, K. F., Kromer, B., Manning, S. W., Niu, M., Reimer, R. W., Richards, D. A., Scott, E. M., Southon, J. R., Staff, R. A., Turney, C. S. M., and van der Plicht, J.: IntCal13 and Marine13 Radiocarbon Age Calibration Curves 0–50,000 Years cal BP, Radiocarbon, 55, 1869–1887, 2016.

Rhodes, E. J., Bronk Ramsey, C., Outram, Z., Batt, C., Willis, L., Dockrill, S., and Bond, J.: Bayesian methods applied to the interpretation of multiple OSL dates: high precision sediment ages from Old Scatness Broch excavations, Shetland Isles, Quaternary Science Reviews, 22, 1231–1244, 2003.

Richter, D., Richter, A., and Dornich, K.: lexsyg — a new system for luminescence research, Geochronometria, 40, 220–228, 2013.

Richter, D., Richter, A., and Dornich, K.: Lexsyg smart — a luminescence detection system for dosimetry, material research and dating application, Geochronometria, 42, 202–209, 2015.

Rosenberg, T. M., Preusser, F., Fleitmann, D., Schwalb, A., Penkman, K., Schmid, T. W., Al-Shanti, M. A., Kadi, K., and Matter, A.: Humid periods in southern Arabia: Windows of opportunity for modern human dispersal, Geology, 39, 1115–1118, 2011.

Schmidt, C., Bösken, J., and Kolb, T.: Is there a common alpha-efficiency in polymineral samples measured by various infrared stimulated luminescence protocols?, Geochronometria, 45, 160–172, 2018.

Shea, J. J.: The Middle Paleolithic of the East Mediterranean Levant, Journal of World Prehistory, 17, 313–394, 2003.

Shea, J. J.: Neanderthals and Homo sapiens in the Levant, in: South-Eastern Mediterranean Peoples Between 130,000 and 10,000 Years Ago, edited by Garcea, E. A. A., pp. 126–143, Oxbow Books, 2010.

Shidrang, S., Biglari, F., Bordes, J. G., and Jaubert, J.: Continuity and Change in the Late Pleistocene Lithic Industries of the Central Zagros: A Typo-Technological Analysis of Lithic Assemblages from Ghar-E Khar Cave, Bisotun, Iran, Archaeology, Ethnology & Anthropology of Eurasia, 44, 27–38, 2016.

Smedley, R. K., Duller, G. A. T., Pearce, N. J. G., and Roberts, H. M.: Determining the K-content of single-grains of feldspar for luminescence dating, Radiation Measurements, 47, 790–796, 2012.

Smith, P. E. L.: Paleolithic archaeology in Iran, The American Institute of Iranian Studies Monograph 1, Philadelphia (PA): The University Museum, 1986.

Solecki, R. S.: Prehistory in Shanidar Valley, Northern Iraq: Fresh insights into Near Eastern prehistory from the Middle Paleolithic to the Proto-Neolithic are obtained, Science, 139, 179–193, 1963.

Solecki, R. S. and Solecki, R. L.: The pointed tools from the Mousterian occupations of Shanidar Cave, northern Iraq, in: The Paleolithic Prehistory of the Zagros-Taurus, pp. 119–146, The University Museum of Archaeology and Anthropology. University of Pennsylvania, Philadelphia, 1993.

Spooner, N. A.: Optical dating: Preliminary results on the anomalous fading of luminescence from feldspars, Quaternary Science Reviews, 11, 139–145, 1992.

Stöcklin, J. and Navabi, M. H.: Tectonic Map of Iran, Iran Geological Survey, Tehran, 1973.

Thiel, C., Buylaert, J. P., Murray, A., Terhorst, B., Hofer, I., Tsukamoto, S., and Frechen, M.: Luminescence dating of the Stratzing loess profile (Austria) - Testing the potential of an elevated temperature post-IR IRSL protocol, Quaternary International, 234, 23–31, 2011.

Thomsen, K., Murray, A., and Jain, M.: Stability of IRSL signals from sedimentary K-feldspar samples, Geochronometria, 38, 1–13, 2011.

Thomsen, K. J., Murray, A. S., Jain, M., and Bøtter-Jensen, L.: Laboratory fading rates of various luminescence signals from feldspar-rich sediment extracts, Radiation Measurements, 43, 1474–1486, 2008.

Trautmann, T., Krbetschek, M. R., Dietrich, A., and Stolz, W.: Investigations of feldspar radioluminescence: potential for a new dating technique, Radiation Measurements, 29, 421–425, 1998.

Trautmann, T., Krbetschek, M. R., Dietrich, A., and Stolz, W.: Feldspar radioluminescence: a new dating method and its physical background, Journal of Luminescence, 85, 45–58, 1999.

Tribolo, C., Asrat, A., Bahain, J.-J., Chapon, C., Douville, E., Fragnol, C., Hernandez, M., Hovers, E., Leplongeon, A., Martin, L., Pleurdeau, D., Pearson, O., Puaud, S., and Assefa, Z.: Across the Gap: Geochronological and Sedimentological Analyses from the Late Pleistocene-Holocene Sequence of Goda Buticha, Southeastern Ethiopia, PLOS ONE, 12, e0169 418, 2017.

Trinkaus, E.: The Shanidar Neandertals, Academic press, 1983.

Trinkaus, E.: Early Modern Humans, Annual Review of Anthropology, 34, 207–230, 2005.

Trinkaus, E., Biglari, F., Mashkour, M., Monchot, H., Reyss, J.-L., Rougier, H., Heydari, S., and Abdi, K.: Late Pleistocene human remains from Wezmeh Cave, western Iran, American Journal of Physical Anthropology, 135, 371–378, 2008.

Tsanova, T.: The beginning of the Upper Paleolithic in the Iranian Zagros. A taphonomic approach and techno-economic comparison of Early Baradostian assemblages from Warwasi and Yafteh (Iran), Journal of Human Evolution, 65, 39–64, 2013.

Valladas, G.: A gamma ray irradiator, PACT 3 - Revue du Réseau Européen de Sciences et Techniques appliquées au Patrimoine Culturel, pp. 439–442, 1978.

Vandenberghe, D., De Corte, F., Buylaert, J. P., Kučera, J., and Van den haute, P.: On the internal radioactivity in quartz, Radiation Measurements, 43, 771–775, 2008.

Wintle, A. G.: Anomalous Fading of Thermoluminescence in Mineral Samples, Nature, 245, 143–144, 1973.

Wintle, A. G. and Murray, A. S.: A review of quartz optically stimulated luminescence characteristics and their relevance in single-aliquot regeneration dating protocols, Radiation Measurements, 41, 369–391, 2006.

Zanolli, C., Biglari, F., Mashkour, M., Abdi, K., Monchot, H., Debue, K., Mazurier, A., Bayle, P., Le Luyer, M., Rougier, H., Trinkaus, E., and Macchiarelli, R.: A Neanderthal from the Central Western Zagros, Iran. Structural reassessment of the Wezmeh 1 maxillary premolar, Journal of Human Evolution, 135, 102 643–12, 2019.

Zeidi, M. and Conard, N. J.: The forth season report of survey at Ghār-e Boof in city of Rostam at Fars Province, th Annual Symposium of the Iranian Archaeology, in Persian, 234–238, 2019.

Zhang, J. and Li, S.-H.: Review of the Post-IR IRSL Dating Protocols of K-Feldspar, Methods and Protocols, 3, 7–19, 2020.

# 5 Study IV

# Preliminary luminescence dating results Bawa Yawan (Iran)

Maryam Heydari[1]

[1]IRAMAT-CRP2A, UMR 5060, CNRS-Université Bordeaux Montaigne, Pessac, France

*corresponding author: mariheyd@gmail.com

- under preparation -

## 5.1 Introduction

Bawa Yawan rock shelter is located in Kermanshah Province at western central Zagros (Fig. 5.1). The dating study was started to unravel the presence of Neanderthals and AMH in the Middle to Upper Palaeolithic period in Kermanshah (Heydari-Guran and Ghasidian, 2017). The first investigations revealed Palaeolithic assemblages from Middle to Upper as well as Epipalaeolithic period (Heydari-Guran and Ghasidian, 2019). The geomorphological research identified six geological units, starting from the modern soil (unit 1) on the top to the last discovered unit so far, unit 6. Geological unit 2 contains Upper and Epipalaeolithic assemblages. The top of the unit is associated with the Epipalaeolithic industry and bottom is related to the Upper Palaeolithic assemblages. Geological unit 3 shows a sparse number of Upper Palaeolithic tools on the top, which were replaced by Middle Palaeolithic tools at the end of this unit. Geological unit 4 encompasses scattered Middle Palaeolithic assemblages.

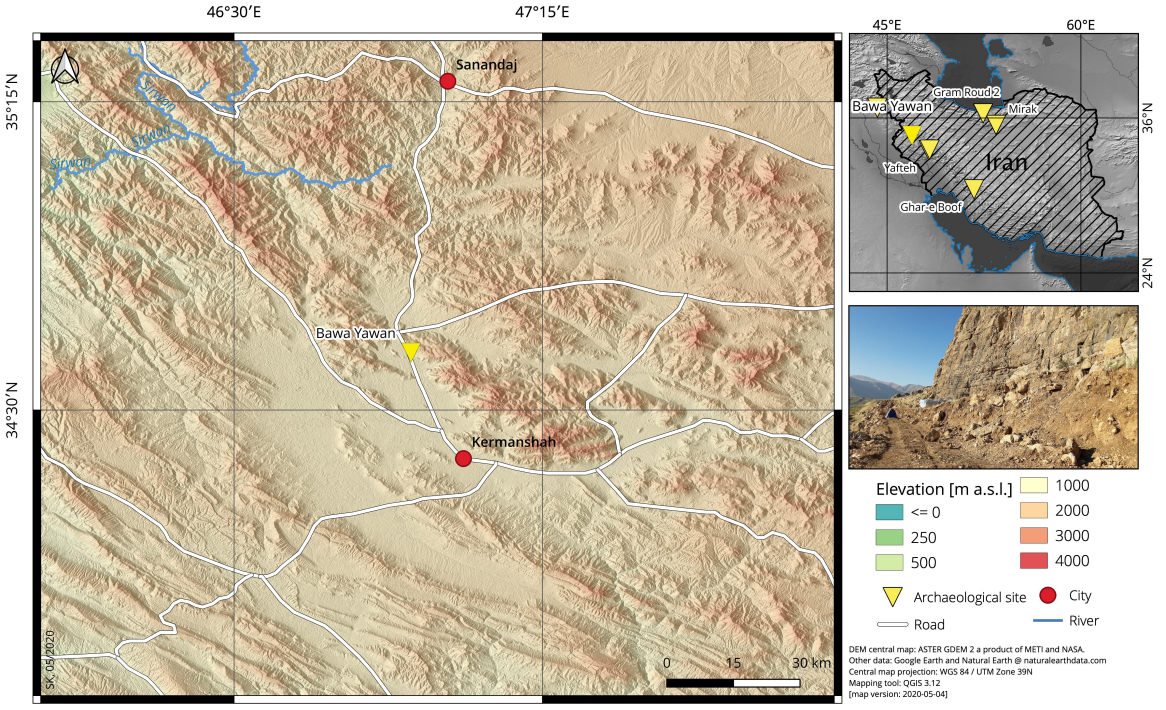


Figure 5.1: Study area of Bawa Yawan. Central map showing the site close to the city Kermanshah. The upper-right map provides an overview map. The photo shows Bawa Yawan in the landscape on the north-eastern valley terrace.

Geological unit 5, however, contains rich Middle Palaeolithic assemblage. The discovery of remains of Neanderthal teeth are the most significant achievements of this excavation, which was found at the beginning of geological unit 5 (Heydari-Guran and Ghasidian, 2019). To provide a luminescence chronology two series of samples were taken from the site. The first six samples

were taken in 2017 by our collaboration partners and sent to the lab. Unfortunately, the preliminary results did not seem promising since they did not follow the stratigraphic order of the site. Therefore, another six samples were taken during a field trip to Iran in November 2018. Only the results of this this campaign are reported here. Since the geological unit 1 encompasses modern soil, we started sampling from unit 2. Afterwards, we continued by sampling from unit 3, unit 4 and unit 5. Two samples were taken from geological unit 6, one from the bottom of the profile and the other vertically extracted from the surface, which was planned to be discovered in the next excavation season. Fig. 5.1 showed the location of luminescence sediment sample in the site.

## 5.2 Material and methods

### 5.2.1 Sampling

In November 2018, six sediment samples were taken from a sediment profile of Palaeolithic site of Bawa Yawan. Six geological units were identified in the site. The first unit on the top, consisted of modern soil and was not considered for OSL dating. The first sample was taken from geological unit 2 from the outcrop, outside of the trench (sample BY1; for simplicity, henceforth samples names are preceded by "BY" for Bawa Yawan). Samples BY2, BY3 and BY4 were taken inside the trench from geological units 3, 4 and 5. The two last samples, BY5 and BY6, originated from unit 6, one from the profile and the other from the bed of the trench. The sample identifiers BY1 to BY6 correspond to field numbers OSL45 to OSL50 (see Fig. B4)

### 5.2.2 Sample preparation

Sample preparations were carried-out under subdued orange light conditions, appropriate for luminescence dating samples (sodium vapour lamp, ca 589 nm). Wet sieving was performed to extract grains between 20 $\mu$m to 41 $\mu$m. The samples were then treated with HCl (10 %) until no more reaction was observed and then soaked in HCl (35 %) for one hour to dissolve remaining carbonates. The samples were then rinsed in $H_2O_2$ (30 %) for 48 hours to eliminate organic materials. We kept a part of the so prepared samples (polymineral) for infrared light stimulated luminescence (IRSL) measurements. The other part was soaked with a mixture of hexafluorosilicic acid ($H_2SiF_6$, 37 %) plus Nitric acid ($HNO_3$, 68 %) (a combination of 90 % of hexafluorosilicic acid plus 10 % of nitric acid), for one week to obtain purified quartz grains. This procedure was followed by another wash in HCl (15 %) overnight to remove Ca-fluorides. Finally, wet sieving was applied again to discard grains largely smaller than the target grain size.

### 5.2.3 Instrumentation and source calibration

Luminescence measurements were carried out on two Freiberg Instruments *lexsyg SMART TL/OSL* systems Richter et al. (2015) at the IRAMAT-CRP2A. The system used for the $D_e$ estimation of the quartz grains facilitated five blue LEDs (458 Δ 10 nm, max. 70 mW cm$^{-2}$) and five infrared LEDs (850 Δ 3 nm, max. 300 mW cm$^{-2}$). The power densities were set to 40 mW cm$^{-2}$ (blue) and 100 mW cm$^{-2}$ (infrared) during continuous wave (CW) stimulation and luminescence was detected through a UV filter set (Schott BG 3, 3mm and Delta BP 365/50 EX) in front of a Hamamatsu H7360-02 photomultiplier tube (PMT). For the$D_e$ estimation of the polymineral fraction, the system used facilitated five infrared LEDs (850 Δ 3 nm, max. 300 mW cm$^{-2}$) which were set to 100 mW cm$^{-2}$ (infrared) during continuous wave (CW) stimulation. Luminescence was detected using a Schott BG 3, 3 mm in conjunction with an AHF-BL HC 414/46 and a Schott NG 11, 1 mm filter.

Both readers (called S1 and S2) were equipped with a $^{90}$Sr/$^{90}$Y-source delivering and 10.14 Gy min$^{-1}$ (S1) and ca 8.88 Gy min$^{-1}$ (S2), calibrated for coarse-grain quartz on stainless steel cups using Risø calibration quartz (batch 90, Hansen et al. 2015). Additionally, we specifically calibrated the radiation-sources for our samples due to the small grain size (20–41 $\mu$m). Therefore, we used grains from sample BY3 for the calibration with the polymineral material and sample BY4 for the calibration with the quartz grains. The samples were first bleached following the procedure of dose-recovery test (see below) and then irradiated with an external $^{137}$Cs $\gamma$-source in the laboratory of Gif-sur-Yvette (Laboratoire des Sciences du Climat et de l'Environnement, France). The samples received doses of 106 Gy and 212 Gy, respectively. We measured the given dose using a SAR protocol with the same set up as for our measurements (see below). The result showed that the luminescence readers S2 and S1 delivered ca 8.34 Gy min$^{-1}$ and 10.80 Gy min$^{-1}$ on quartz and polymineral grains from the grain size fraction 20–41 $\mu$m. For the measurements, several hundred grains, either quartz or feldspar, were mounted on the stainless-steel cups using silicon (1 mm spray mask). We measured 19–25 aliquots per sample for the feldspar and 39–40 aliquots for the quartz fractions.

### 5.2.4 Luminescence measurements

The quartz samples were measured using the single aliquot regenerative dose (SAR) (Murray and Wintle, 2000). To check whether the OSL signal was dominated by a so-called fast decaying signal component the OSL signal of one sample of the site (BY2) was compared with the signal of a calibration quartz (Hansen et al., 2015) after Bos and Wallinga (2012). The result of this comparison is shown in Fig. 5.2; the perfect matching in both signals indicates that the OSL signal of the site of Bawa Yawan is dominated by a fast decaying signal component and thus appropriate for the SAR protocol.

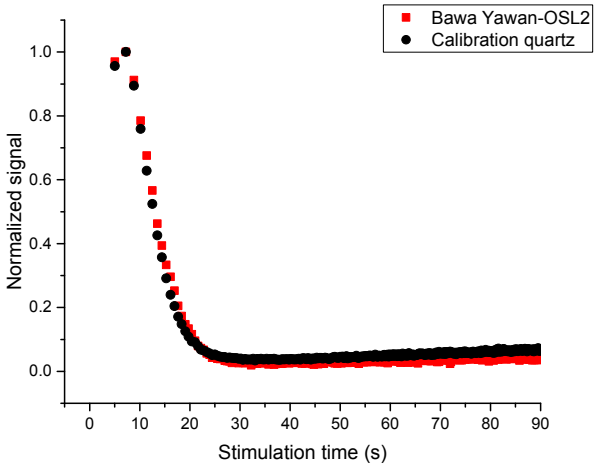


Figure 5.2: Signal comparison of the 'calibration quartz' and of Bawa Yawan (BY2). The perfect matching of both signals indicates that the OSL signal of the site of Bawa Yawan is dominated by a fast decaying signal component.

The dependency of the $D_e$ on the preheat temperature was checked by performing the preheat-plateau test on three samples (BY1, BY2 and BY5). The results are shown in Fig. 5.3. Each point represents the average of the $D_e$ for five aliquots for the temperature ranges of 220 °C to 280 °C (20 °C increments). The cut-heat was set always 20 °C less than the corresponding preheat temperature in each step. We finally selected 260 °C as a preheat temperature and 240 °C as the cut-heat temperature for our measurements since they seem to be form a plateau in this temperature region (Fig. 5.3).

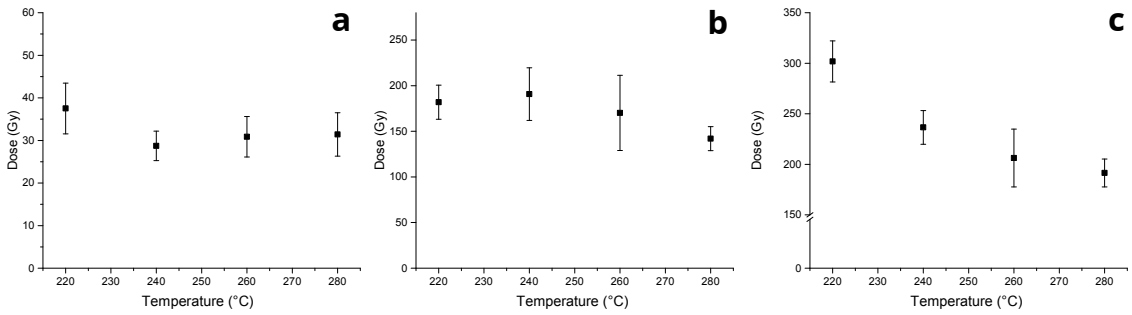


Figure 5.3: Results of the preheat-plateau test of samples BY1 (top), BY 2(bottom-left) and BY5 (bottom right). The Preheat temperature of 260 °C and the cut heat temperature of 240 °C appeared to form a plateau in all three tests and we used them as parameters in the SAR protocol.

Additionally, we performed a dose-recovery test on three samples by measuring between six to nine aliquots for samples BY1, BY2 and BY5. The aliquots first were bleached for 100 s inside a Hönle UVACUBE 400 solar stimulator to deplete the natural luminescence signal. This step was followed by a 10,000 s pause that allows the decay of the 110 °C peak (Wintle and Murray, 2006). Then, the samples were bleached for a second time to deplete charges in the fast component, potentially transferred from the shallow 110 °C trap during the pause. Finally, samples BY1, BY2 and BY5 received a $\beta$-dose of 33 Gy, 149 Gy and 219 Gy (close to the expected $D_e$) inside the OSL reader and the SAR protocol was applied to them to test whether the given dose can be satisfying recovered. The dose-recovery ratios (i.e. ratio between the obtained and given doses) for samples BY1, BY2, and BY5 resulted in $1.05 \pm 0.02$, $1.01 \pm 0.04$ and $1.04 \pm 0.04$ which were consistent with unity. Thus, they validated the chosen SAR protocol parameters. We assumed similar behaviour for the rest of the three samples. Therefore, we applied the SAR protocol with the same parameters to all samples. The OSL signal was measured at 125 °C for 40 s following preheat at 260 °C for 10 s. The test dose was measured following a cut heat at 240 °C. For the blue OSL we used initial channels 1–2 (0.2 s) for the signal and subtracted late background using channels 300–400 (10 s). The SAR protocol was applied to multi-grain aliquots of quartz to determine the equivalent dose. Four regenerative points, approximately 56 Gy, 112 Gy, 224 Gy, 449 Gy, were used to construct the dose-response curves for sample BY2 to BY6, with a test dose of 56 Gy. A different setup was used for BY 1 due to its lower $D_e$ compared to other samples (BY2 to BY6) following 14 Gy, 28 Gy, 56 Gy, 112 Gy, with a test dose of 14 Gy. A single exponential plus linear equation was used to fit the dose-response curves, which were forced through the origin. The recuperation ratio after delivering a zero dose was always below 5 %. The first regenerative dose after the recuperation test was used to check the efficiency of correction for sensitivity change (recycling ratio). The recycling ratio was not taken into account as a rejection criterion following Thomsen et al. (2016) and (Guérin et al., 2015). However, we calculated the average of recycling ratio for each sample; the minimum and the maximum were $0.90 \pm 0.05$ and $0.95 \pm 0.01$, indicating its consistency within 10 % of unity (Murray and Wintle, 2000). The possibility of contamination by feldspar was examined by applying the IR depletion ratio test (Duller, 2003). This ratio was within 10 % of unity for all samples. Therefore, no significant evidence for feldspar contamination was observed. Typical TL curves, blue stimulated shine-down curves, and corresponding dose-response curves are shown for sample BY3 as an example (Fig. 5.4). The palaeodoses and their uncertainties are quoted as arithmetic mean and the standard error of the mean, which lead to $33 \pm 1$ Gy, $147 \pm 3$ Gy, $179 \pm 11$ Gy, $179 \pm 7$ Gy, $225 \pm 7$ Gy, $232 \pm 9$ Gy, for samples BY1 to BY6.

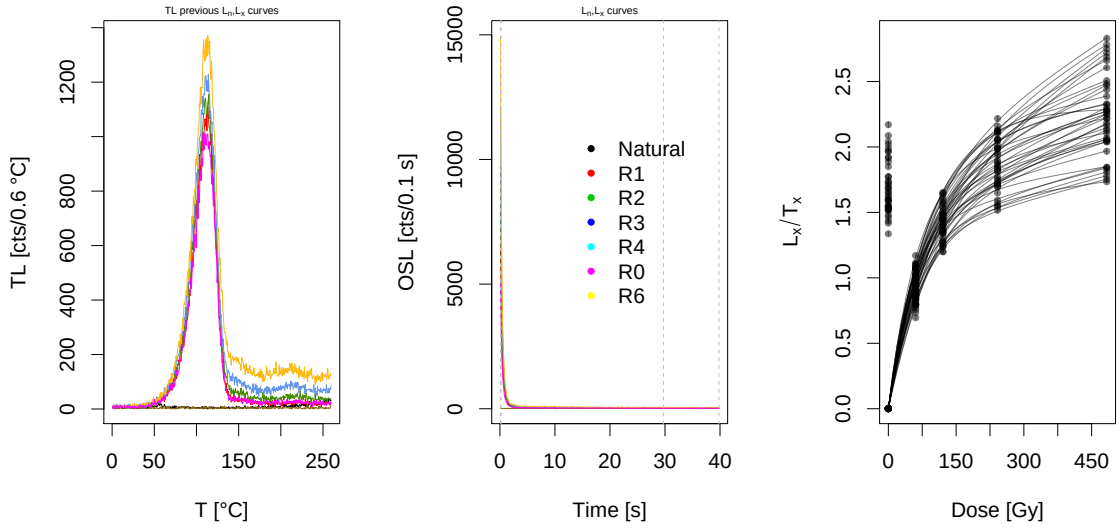


Figure 5.4: Typical TL preheat curves (left), blue stimulated shine-down curves (middle) and typical dose-response curves (right) of sample BY3.

#### 5.2.4.1 OSL signal saturation

Blue-OSL, measured in the UV wavelength, saturates at relatively low dose around 150–200 Gy (Wintle and Murray, 2006). Although here, we have used a single exponential plus linear function for fitting the dose-response curves which do not saturate. However, we additionally measured $D_0$ values. The $D_0$ values is the curvature parameter of the dose-response curves when a single saturating exponential function of the form $L/T = A(1 - exp(-D/D_0))$ is used. Those measurements were carried-out for samples BY5 and BY6 (each three aliquots). We built-up dose-response curves using regenerative points ranging from 35 Gy to 1,181 Gy (in total 11 points). The results are shown in Fig. 5.5. The $D_0$ values for BY5 and BY6 were 137 Gy and 126 Gy, respectively. For both samples, the determined palaeodoses are lower than two times the obtained $D_0$ values, justifying the accuracy of the determined palaeodoses after Wintle and Murray (2006). Besides, the dose recovery ratio of sample BY5 also confirmed that the given dose could be recovered sufficiently. However, we used Bayesian modelling for calculating the palaeodose, which is in or close to the saturation level after Heydari and Guérin (2018). For the modelling, a Gaussian distribution was used for determining the palaeodoses, which result in $149 \pm 3$ Gy, $164 \pm 6$ Gy, $175 \pm 5$ Gy, and $210 \pm 7$ Gy, $221 \pm 8$ Gy. For consistency, the palaeodose of BY1 was also calculated using Bayesian modelling, which yielded $34 \pm 1$ Gy. The obtained palaeodoses from Bayesian and non-Bayesian agree within uncertainties. *However, in the following we provide the final ages considering the Bayesian palaeodoses only*.

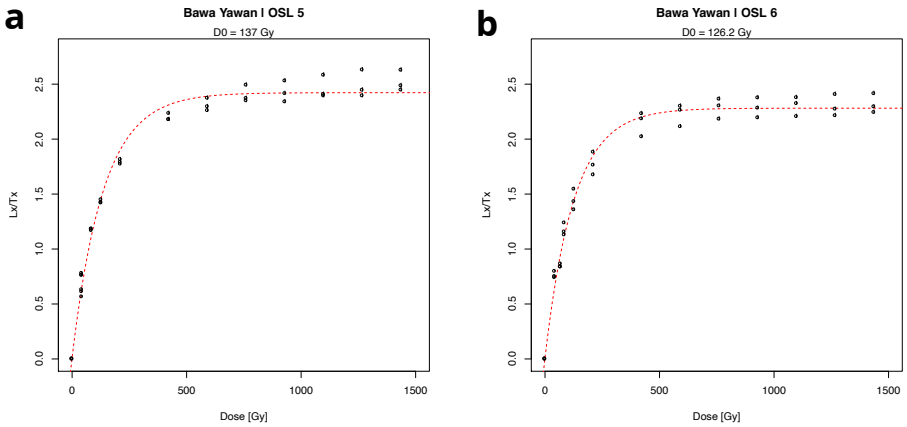


Figure 5.5: High-dose dose-response curves using 11 regenerative points and to estimate $D_0$ values for samples BY5 (left) and sample BY6 (right). The experiment was repeated for three aliquots each.

### 5.2.5 Feldspar measurements

To measure the polymineral fraction we applied the post-IR IRSL (Thomsen et al., 2008) approach, which applies a sequence of IRSL measurements at elevated temperatures. The post-IR IRSL signal at 290 °C ($pIRIR_{290}$) signal is believed to be free from considerable anomalous fading (cf. Buylaert et al., 2012) and hence this protocol was applied to the samples using the same settings as in (cf. Buylaert et al., 2012). First, dose-recovery tests were carried out on three samples (BY1, BY2, and BY5) after measuring the residual doses. The samples were bleached for 72 hours in the solar simulator then the residual doses were measured, resulting in 6 Gy for BY1, 8 Gy for samples BY2 and BY5. The samples received doses of 43 Gy, 170 Gy and 256 Gy, respectively inside the OSL reader and then the given dose was measured using the $pIRIR_{290}$ protocol. Test doses of 18 Gy and 64 Gy were used for sample BY1 and for samples BY2 and BY5, respectively. The results of the first dose-recovery tests were $0.87 \pm 0.07$, $0.91 \pm 0.02$ and $0.88 \pm 0.02$ after subtracting the residual dose for samples BY1, BY2 and BY5 respectively. We then tried to modify the protocol by varying the test-dose values (Colarossi et al., 2017) in order to, potentially, improve the dose-recovery ratios between 0.90 and 1.1 (Wintle and Murray, 2006). We increased the value of the test dose for two samples (BY2 and BY5) by selecting 85 Gy and 128 Gy, which resulted in dose-recovery ratios of $0.78 \pm 0.03$ and $0.83 \pm 0.04$, respectively. We also reduced the value of the test dose for one sample (BY2) to 43 Gy, which leaded to $0.86 \pm 0.07$. Therefore, we selected the first protocol settings for our final measurements, which provided the most satisfactory result in comparison with the two others protocols. Typical TL curves, infrared light stimulated shine-down curves, and corresponding dose-response curves are shown for sample BY3 as an example (Fig. 5.6)

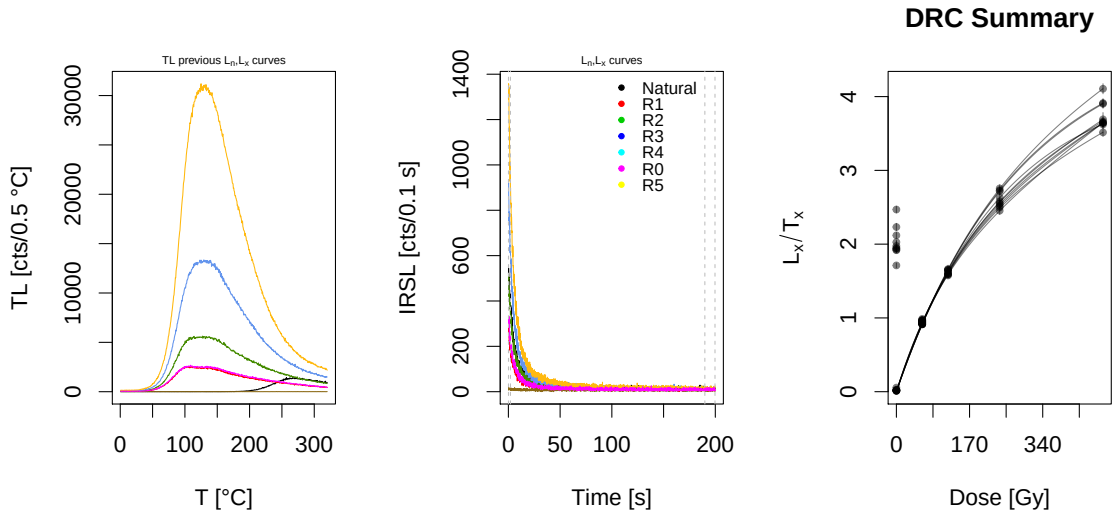


Figure 5.6: Typical TL preheat curves (left), infrared light stimulated shine-down curves (middle), and typical dose-response curves (right) of sample BY3.

### 5.2.6 Dose rate determination

To calculate $\alpha$-, $\beta$- and $\gamma$-dose rates U, Th and K concentrations were measured using high-resolution low background $\gamma$-ray spectrometry (Guibert and Schvoerer, 1991). In order to properly address the $\beta$-dose rate and to improve the accuracy of the $\gamma$-dose rate (derived from $\gamma$-ray spectrometry) in our heterogeneous sediments, we sieved and separated grains less than 2 mm (series 1) and between 1 cm and 2 mm (series 2) following Tribolo et al. (2017). Then the sediment were ground to powder using a planetary mill before being sealed in plastic boxes of 12 $cm^3$ and stored before the measurements for at least three weeks.

Radionuclides concentrations (Tables 5.1, 5.2) from both series were converted into dose rates (Table 5.3) using the conversion factors by Guérin et al. (2011). The water content was measured after storing the sediments samples into an external furnace for around one week. The water content values ranged between $15 \pm 6$ % and $17 \pm 7$ %. Except for sample BY4 for which, the value was $14 \pm 5$ %, however, we increased it up to $16 \pm 6$ % for consistency with the upper unit with the water content of $15 \pm 6$ % and the bottom unit with a water content of $16 \pm 6$ % all (the three units consist of silty clay). The obtained dose rates were corrected for the water content after Guérin and Mercier (2012); Aitken (1998). The effect of grain size attenuation was considered after Guérin et al. (2012). For the $\alpha$-efficiency, we used $0.03 \pm 0.01$ (OSL quartz, Mauz et al. 2006) and $0.085 \pm 0.010$ ($pIRIR_{290}$, polymineral, Schmidt et al. 2018).

The $\alpha$-dose rates were determined considering only the radionuclides concentration of series 1, which ranged from $0.12 \pm 0.02$ Gy $ka^{-1}$ to $0.17 \pm 0.02$ Gy $ka^{-1}$ for the quartz grains and be-

Table 5.1: Radionuclide concentrations x< 2 mm.

| **Sample** | **K** | $\sigma$ | $\mathbf{U_{pre\text{-}Ra}}$ | $\sigma$ | $\mathbf{U_{post\text{-}Ra}}$ | $\sigma$ | **Th** | $\sigma$ |
|---|---|---|---|---|---|---|---|---|
| | [%] | | [ppm] | | [ppm] | | [ppm] | |
| BY1 | 1.57 | 0.02 | 2.23 | 0.10 | 2.28 | 0.03 | 6.63 | 0.07 |
| BY2 | 1.46 | 0.03 | 2.52 | 0.13 | 2.01 | 0.03 | 6.70 | 0.09 |
| BY3 | 1.42 | 0.03 | 2.41 | 0.13 | 1.91 | 0.03 | 6.50 | 0.09 |
| BY4 | 1.73 | 0.03 | 3.91 | 0.15 | 2.34 | 0.04 | 7.70 | 0.10 |
| BY5 | 1.99 | 0.03 | 3.73 | 0.15 | 2.63 | 0.04 | 9.20 | 0.10 |
| BY6 | 1.85 | 0.03 | 4.79 | 0.15 | 2.90 | 0.03 | 8.78 | 0.09 |

Table 5.2: Radionuclide concentrations 2 mm<x<1 cm.

| **Sample** | **K** | $\sigma$ | $\mathbf{U_{pre\text{-}Ra}}$ | $\sigma$ | $\mathbf{U_{post\text{-}Ra}}$ | $\sigma$ | **Th** | $\sigma$ |
|---|---|---|---|---|---|---|---|---|
| | [%] | | [ppm] | | [ppm] | | [ppm] | |
| BY1 | 0.52 | 0.01 | 2.09 | 0.09 | 2.30 | 0.03 | 2.34 | 0.05 |
| BY2 | 0.83 | 0.02 | 2.83 | 0.12 | 2.72 | 0.04 | 3.93 | 0.07 |
| BY3 | 0.84 | 0.02 | 3.07 | 0.12 | 2.86 | 0.04 | 3.68 | 0.06 |
| BY4 | 0.51 | 0.02 | 3.38 | 0.11 | 2.97 | 0.04 | 2.30 | 0.05 |
| BY5 | 0.47 | 0.02 | 3.61 | 0.13 | 3.11 | 0.04 | 2.20 | 0.05 |
| BY6 | 0.64 | 0.01 | 4.22 | 0.11 | 3.25 | 0.03 | 3.02 | 0.05 |

tween $0.34 \pm 0.02\,\mathrm{Gy\,ka^{-1}}$ to $0.49 \pm 0.04\,\mathrm{Gy\,ka^{-1}}$ for the polyminerals. The $\gamma$-dose rates were estimated using the concentrations of radionuclides from series 1 and 2. The final dose rates were presented as a weighted mean of the two obtained dose rates (the relative weight of each fraction was considered as a weight). The final $\gamma$-dose rates range from $0.70 \pm 0.02\,\mathrm{Gy\,ka^{-1}}$ to $0.86 \pm 0.04\,\mathrm{Gy\,ka^{-1}}$. Finally, the $\beta$-dose rate was calculated using the average of the $\beta$-dose rates from series 1 and the weighted mean between series 1 and series 2 (for details see Tribolo et al. 2017). The final $\beta$-dose rates ranged from $1.26 \pm 0.10\,\mathrm{Gy\,ka^{-1}}$ to $1.65 \pm 0.14\,\mathrm{Gy\,ka^{-1}}$

The cosmic-dose rate was estimated from the geographic position and burial depth of the sampled material after Prescott and Hutton (1994) using the function `calc_CosmicDoseRate()` available in the R (R Core Team, 2019) package 'Luminescence' (Kreutzer et al., 2012, 2017). The internal dose rate for quartz was assumed to be zero and the internal dose rate of feldspar was set to $0.10 \pm 0.02\,\mathrm{Gy\,ka^{-1}}$. The $\alpha$, $\beta$ and $\gamma$-dose rate contribute to 5–6 %, 55–58 % and 29–31 % to the entire external dose rates.

It should be mention here that we also employed *in situ* $\gamma$-dose measurements using $Al_2O_3$:C chips (concept and procedure described in Kreutzer et al. 2018). The aluminium tubes containing three chips were inserted to the site November 2018, for samples, BY1 to BY5. The results can be considerably different from the $\gamma$-dose rate determined using $\gamma$-ray spectrometry due to heterogeneities at centimetres' scale in the site. **However, the tubes are still in the site waiting for their retrieval.**

Table 5.3: Dose rates.

| Sample | $\dot{D}_{F_\alpha}$ [Gy ka$^{-1}$] | $\sigma$ | $\dot{D}_{Q_\alpha}$ [Gy ka$^{-1}$] | $\sigma$ | $\dot{D}_\beta$ [Gy ka$^{-1}$] | $\sigma$ | $\dot{D}_\gamma$ [Gy ka$^{-1}$] | $\sigma$ | $\dot{D}_{cosm.}$ [Gy ka$^{-1}$] | $\sigma$ | $\dot{D}_{F_{int.}}$ [Gy ka$^{-1}$] | $\sigma$ |
|---|---|---|---|---|---|---|---|---|---|---|---|---|
| BY1 | 0.38 | 0.03 | 0.13 | 0.02 | 1.35 | 0.10 | 0.70 | 0.02 | 0.24 | 0.02 | 0.10 | 0.02 |
| BY2 | 0.36 | 0.03 | 0.13 | 0.02 | 1.31 | 0.10 | 0.73 | 0.02 | 0.20 | 0.02 | 0.10 | 0.02 |
| BY3 | 0.34 | 0.02 | 0.12 | 0.02 | 1.26 | 0.10 | 0.70 | 0.02 | 0.18 | 0.02 | 0.10 | 0.02 |
| BY4 | 0.41 | 0.03 | 0.15 | 0.02 | 1.45 | 0.12 | 0.76 | 0.03 | 0.17 | 0.02 | 0.10 | 0.02 |
| BY5 | 0.48 | 0.03 | 0.17 | 0.02 | 1.65 | 0.14 | 0.86 | 0.04 | 0.16 | 0.02 | 0.10 | 0.02 |
| BY6 | 0.49 | 0.04 | 0.17 | 0.02 | 1.61 | 0.14 | 0.86 | 0.04 | 0.15 | 0.02 | 0.10 | 0.02 |

F: Feldspar | Q: Quartz | int.: internal dose rate

#### 5.2.6.1 Radioactive disequilibrium

Figure 5.7 shows the ratio of $^{238}$U concentrations from the top and the bottom of the U-series divided by $^{232}$Th, which is chemically immobile (Guibert et al., 2009) for both series 1 and 2. The concentrations of $^{238}$U determined from the top of the chain laid between $2.23 \pm 0.10$ ppm to $4.79 \pm 0.15$ ppm for series 1 and between $2.09 \pm 0.09$ ppm to $4.22 \pm 0.11$ ppm for series 2. The concentrations derived from the bottom of the chain of series 1 vary between $1.91 \pm 0.03$ ppm to $2.90 \pm 0.03$ ppm and from series 2 between $2.30 \pm 0.03$ ppm to $3.25 \pm 0.03$ ppm. The disequilibrium in the U-decay chain is discussed below. We considered the $^{238}$U chain for samples in series 2 in Fig. 5.7 (right) in radioactive equilibrium. However, disequilibria were observed for series 1 for samples BY2 to BY6. Figure 5.7 (left) shows a typical plot of a series of samples that they have been experienced a recent arrival of U. Considering the half-life of $^{230}$Th, i.e. 75 ka, "recent" here refers to the Holocene. As a result, we define two scenarios: first, we determined the dose rate with the effective U concentrations estimated from the top and the bottom separately (scenario 1). In scenario 2, the effective U concentrations from the bottom of the chain is used instead not only for the bottom but also for the top of the chain justifying the recent U arrival. The discrepancies for the ages calculated from two scenarios for both series 1 and 2 are not statistically significant. Therefore, for final age's interpretation we present the results of scenario 2.

### 5.2.7 Results and discussion

The quartz and feldspar ages are listed in Table 5.4. For simplicity, the quartz and feldspar ages (within $2\sigma$ of uncertainty) are shown together in one plot (Fig. 5.8). The ages of samples BY2, BY5, BY6 from quartz and polymineral perfectly agree one another. The polymineral ages of sample BY3 and BY4 seem to be younger than the corresponding quartz ages. However, as it is presented in Fig. 5.8, they overlap one another thus, they are considered statistically indistinguishable. The quartz age of BY1 is younger than its polymineral age. This could be because of a residual dose at the time of deposit (it was 6 Gy after 72 h exposure in the solar simula-

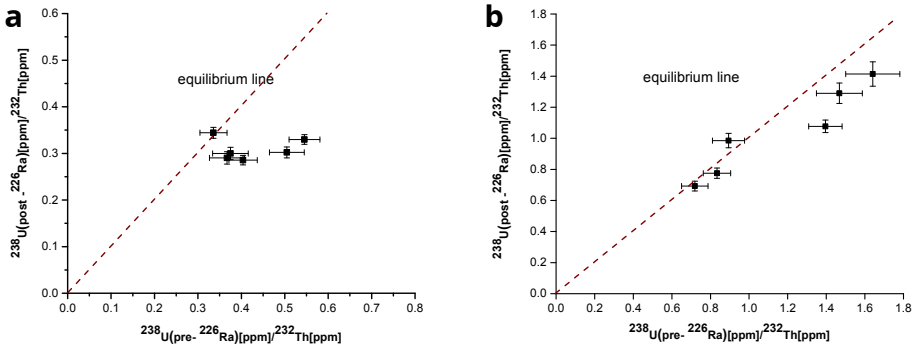


Figure 5.7: Evaluation of the disequilibrium in the decay chain of $^{238}$U for determined dose rates series 1 (left) and series 2 (right). The ratio of $^{238}$U(post-$^{226}$Ra)/$^{232}$Th and $^{238}$U(pre-$^{226}$Ra)/ $^{232}$Th is shown for all the samples. The ratios samples of BY2 to BY6 in series 1 show considerable disequilibria. Series 2 is considered to be in radioactive equilibrium.

tor) which might be significant compared to the relatively low palaeodose of this sample (about 50 Gy). Therefore, for final age presentation quartz OSL is preferred. Since the feldspar ages generally agree with the quartz ages, they can be seen as an indicator of sufficiently bleaching of the sediments. Gaussian distribution after Heydari and Guérin (2018) gives confidence in the accuracy of $D_e$ estimation which does not suffer from underestimation, in particular because the post-IR IRSL ages agree with the quartz OSL ages. Therefore for final age interpretation, we use the quartz OSL results. *It should be noted that the effects of in situ γ-dose rate measurements might change the result of the final age. However, keeping in mind the limestone nature of the rock in the site, it does not seem that in situ measurement shift ages towards the younger ones*.

Table 5.4: Summary of quartz OSL and feldspar post-IR IRSL data (the uncertainties are presented within 1$\sigma$).

| | | *Quartz OSL* | | | | *Feldspar post-IR IRSL* | | |
|---|---|---|---|---|---|---|---|---|
| **Sample** | **n** | $D_e$ [Gy] | $\dot{D}$ [Gy ka$^{-1}$] | Age [ka] | **n** | $D_e$ [Gy] | $\dot{D}$ [Gy ka$^{-1}$] | Age [ka] |
| BY1 | 40 | 34 ± 1 | 2.43 ± 0.11 | 14 ± 1 | 25 | 50 ± 1 | 2.77 ± 0.11 | 18 ± 1 |
| BY2 | 40 | 149 ± 3 | 2.37 ± 0.10 | 63 ± 3 | 20 | 166 ± 3 | 2.70 ± 0.11 | 62 ± 3 |
| BY3 | 39 | 164 ± 6 | 2.26 ± 0.10 | 73 ± 4 | 20 | 165 ± 4 | 2.58 ± 0.10 | 64 ± 3 |
| BY4 | 40 | 175 ± 5 | 2.52 ± 0.13 | 70 ± 4 | 20 | 179 ± 3 | 2.89 ± 0.13 | 62 ± 3 |
| BY5 | 40 | 210 ± 7 | 2.84 ± 0.15 | 74 ± 5 | 20 | 243 ± 8 | 3.25 ± 0.15 | 75 ± 5 |
| BY6 | 40 | 221 ± 8 | 2.79 ± 0.14 | 79 ± 5 | 19 | 258 ± 7 | 3.21 ± 0.15 | 80 ± 5 |

*Notes: $D_e$ is the average equivalent dose and 'n' is the number of measured aliquots.*

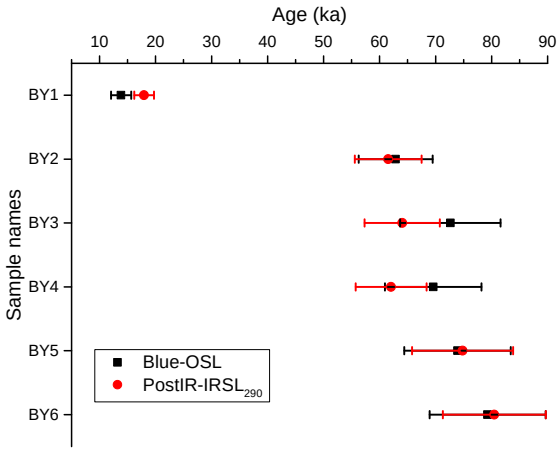


Figure 5.8: OSL quartz (black) and post-IR IRSL polymineral (red) ages (within $2\sigma$ of uncertainty).

## Study IV: References


Aitken, M. J.: An Introduction to Optical Dating, Oxford University Press, 1998.

Bos, A. J. J. and Wallinga, J.: How to visualize quartz OSL signal components, Radiation Measurements, 47, 752–758, 2012.

Buylaert, J. P., Jain, M., Murray, A. S., Thomsen, K. J., Thiel, C., and Sohbati, R.: A robust feldspar luminescence dating method for Middle and Late Pleistocene sediments, Boreas, 41, 435–451, 2012.

Colarossi, D., Duller, G. A. T., and Roberts, H. M.: Exploring the behaviour of luminescence signals from feldspars: Implications for the single aliquot regenerative dose protocol, Radiation Measurements, pp. 1–10, 2017.

Duller, G. A. T.: Distinguishing quartz and feldspar in single grain luminescence measurements, Radiation Measurements, 37, 161–165, 2003.

Guérin, G. and Mercier, N.: Preliminary insight into dose deposition processes in sedimentary media on a scale of single grains: Monte Carlo modelling of the effect of water on the gamma dose rate, Radiation Measurements, 47, 541–547, 2012.

Guérin, G., Mercier, N., and Adamiec, G.: Dose-rate conversion factors: update, Ancient TL, 29, 5–9, 2011.

Guérin, G., Mercier, N., Nathan, R., Adamiec, G., and Lefrais, Y.: On the use of the infinite matrix assumption and associated concepts: A critical review, Radiation Measurements, 47, 778–785, 2012.

Guérin, G., Frouin, M., Talamo, S., Aldeias, V., Bruxelles, L., Chiotti, L., Dibble, H. L., Goldberg, P., Hublin, J.-J., Jain, M., Lahaye, C., Madelaine, S., Maureille, B., McPherron, S. J. P., Mercier, N., Murray, A. S., Sandgathe, D., Steele, T. E., Thomsen, K. J., and Turq, A.: A multi-method luminescence dating of the Palaeolithic sequence of La Ferrassie based on new excavations adjacent to the La Ferrassie 1 and 2 skeletons, Journal of Archaeological Science, 58, 147–166, 2015.

Guibert, P. and Schvoerer, M.: TL dating: Low background gamma spectrometry as a tool for the determination of the annual dose, International Journal of Radiation Applications and Instrumentation. Part D. Nuclear Tracks and Radiation Measurements, 18, 231–238, 1991.

Guibert, P., Lahaye, C., and Bechtel, F.: The importance of U-series disequilibrium of sediments in luminescence dating: A case study at the Roc de Marsal Cave (Dordogne, France), Radiation Measurements, 44, 223–231, 2009.

Hansen, V., Murray, A., Buylaert, J.-P., Yeo, E.-Y., and Thomsen, K.: A new irradiated quartz for beta source calibration, Radiation Measurements, 81, 123–127, 2015.

Heydari, M. and Guérin, G.: OSL signal saturation and dose rate variability: Investigating the behaviour of different statistical models, Radiation Measurements, 120, 96–103, 2018.

Heydari-Guran, S. and Ghasidian, E.: The MUP Zagros Project: tracking the Middle–Upper Palaeolithic transition in the Kermanshah region, west-central Zagros, Iran, Antiquity Project Gallery, 91, 40–7, 2017.

Heydari-Guran, S. and Ghasidian, E.: A report on the second season excavation in Bawa Yawan rocksheleter, 16$^{th}$ Annual Symposium of the Iranian Archaeology (a collection of short articles-2016-2017), pp. 124–127, 2019.

Kreutzer, S., Schmidt, C., Fuchs, M. C., Dietze, M., Fischer, M., and Fuchs, M.: Introducing an R package for luminescence dating analysis, Ancient TL, 30, 1–8, 2012.

Kreutzer, S., Burow, C., Dietze, M., Fuchs, M. C., Schmidt, C., Fischer, M., and Friedrich, J.: Luminescence: Comprehensive Luminescence Dating Data Analysis, URL `https://CRAN.R-project.org/package=Luminescence`, r package version 0.7.5, 2017.

Kreutzer, S., Martin, L., Guérin, G., Tribolo, C., Selva, P., and Mercier, N.: Environmental Dose Rate Determination Using a Passive Dosimeter: Techniques and Workflow for alpha-$Al_2O_3$:C Chips, Geochronometria, 45, 56–67, 2018.

Mauz, B., Packman, S. C., and Lang, A.: The alpha effectiveness in silt-sized quartz: New data obtained by single and multiple aliquot protocols, Ancient TL, 24, 47–52, 2006.

Murray, A. S. and Wintle, A. G.: Luminescence dating of quartz using an improved single-aliquot regenerative-dose protocol, Radiation Measurements, 32, 57–73, 2000.

Prescott, J. R. and Hutton, J. T.: Cosmic ray contributions to dose rates for luminescence and ESR dating: Large depths and long-term time variations, Radiation Measurements, 23, 497–500, 1994.

R Core Team: R: A Language and Environment for Statistical Computing, Vienna, Austria, URL `https://r-project.org`, 2019.

Richter, D., Richter, A., and Dornich, K.: Lexsyg smart — a luminescence detection system for dosimetry, material research and dating application, Geochronometria, 42, 202–209, 2015.

Schmidt, C., Bösken, J., and Kolb, T.: Is there a common alpha-efficiency in polymineral samples measured by various infrared stimulated luminescence protocols?, Geochronometria, 45, 160–172, 2018.

Thomsen, K. J., Murray, A. S., Jain, M., and Bøtter-Jensen, L.: Laboratory fading rates of various luminescence signals from feldspar-rich sediment extracts, Radiation Measurements, 43, 1474–1486, 2008.

Thomsen, K. J., Murray, A. S., Buylaert, J. P., Jain, M., Hansen, J. H., and Aubry, T.: Testing single-grain quartz OSL methods using sediment samples with independent age control from the Bordes-Fitte rockshelter (Roches d'Abilly site, Central France), Quaternary Geochronology, 31, 77–96, 2016.

Tribolo, C., Asrat, A., Bahain, J.-J., Chapon, C., Douville, E., Fragnol, C., Hernandez, M., Hovers, E., Leplongeon, A., Martin, L., Pleurdeau, D., Pearson, O., Puaud, S., and Assefa, Z.: Across the Gap: Geochronological and Sedimentological Analyses from the Late Pleistocene-Holocene Sequence of Goda Buticha, Southeastern Ethiopia, PLOS ONE, 12, e0169 418, 2017.

Wintle, A. G. and Murray, A. S.: A review of quartz optically stimulated luminescence characteristics and their relevance in single-aliquot regeneration dating protocols, Radiation Measurements, 41, 369–391, 2006.

# 6 Discussion and conclusions

## 6.1 The presented studies

This thesis can be broadly divided into two sections. Firstly, I discussed the potential advantages of Bayesian models for application in luminescence dating over commonly used frequentist models. Here, I extensively tested the recently developed R package 'BayLum' (Philippe et al., 2019). Secondly, this thesis presented the first luminescence-based chronologies for Middle-Upper Palaeolithic sites in Iran. Where possible, the chronologies were obtained by applying Bayesian modelling.

### 6.1.1 Bayesian modelling

Chapter 2 (Heydari and Guérin, 2018) tested and detailed the potential of Bayesian modelling to treat two cases: (1) saturation issues in equivalent dose determination, and (2) asymmetric dose distributions due to $\beta$-dose rate heteroginity. This showed that accurate central doses were obtained when Gaussian and lognormal distributions embedded in 'BayLum' were applied. Whilst this study was based on laboratory-irradiated samples (dose-recovery tests), the performance of the Bayesian approach was then further tested on samples from three Palaeolithic sites from Iran.

Chapter 3 presented age results incorporating stratigraphic constraints when the systematic shared errors between samples were modelled after Combès and Philippe (2017) to compare the precision of frequentist and Bayesian chronology (Heydari et al., 2020). The results showed that when including stratigraphic constraints in modelling, the sampling resolution was a crucial component for the precision. If the age intervals do not overlap one another, the advantage of this application in reducing age uncertainties is negligible. By contrast, if sufficient samples are collected from one profile and stratigraphic constraints are applied, the precision of ages can be considerably improved (Ch. 3).

In the next step, Ch. 4 detailed the effect of incorporating, stratigraphic constraints, $^{14}$C ages, and the modelling of systematic shared errors, to determine the Bayesian chronology. The so obtained chronology is more precise than the chronology obtained with the frequentist approach.

### 6.1.2 Age precision through Bayesian modelling

The essential advantage of data processing following the Bayesian school is its ability to incorporate all available chronological data to improve the precision age sequences. Instead of determining an age for one sample as an individual event in one site, a sequence of ages are simultaneously determined comprising all samples' data along with the entire relevant chronological information established for a particular site. Furthermore, a preliminary but powerful chronological knowledge that can be included in the Bayesian modelling is the stratigraphic constraints. Although the ordering of the stratigraphical layers from one site may not be a piece

of sophisticated knowledge to be exploited in chronological modelling, in practice, it can substantially improve the ages' precision.

In this thesis, in Ch. 2 and 3, I showed that the critical component resulting in more precise chronologies for the sites of Mirak and Ghār-e Boof was incorporating the stratigraphic constraints into the Bayesian model. However, due to the strong effect of prior beliefs in the Bayesian school, any doubt in the sequence's order can shift the ages towards wrong results. Hence, the inclusion of the stratigraphic constraints is a delicate task, demanding careful consideration.

Another essential aspect of employing Bayesian inference, particularly for data analysis in luminescence dating (e.g., compared to $^{14}$C dating), is the ability to model systematic error. Systematic errors often contribute around 2–3 % of relative error to the final age estimation (Millard, 2006; Murray and Olley, 2002). Although it is generally desirable to reduce all kinds of systematic effects, this value might appear small compared to the relative uncertainty range of ca 5–10 %, observed in luminescence-based dates (Ch. 1; also Murray and Olley 2002; Duller 2007). However, when the luminescence signal is very bright with a small error of less than 1 % error on the $D_e$ estimation (Duller, 2007), and the environmental radioactivity is very high, the systematic error contribution might form a significant share.

Rhodes et al. (2003) divided the systematic error into shared and unshared parts, and sought through employing Bayesian modelling to reduce the unshared systematic error. Nevertheless, in this thesis, the shared systematic error between samples was modelled in the school of Bayesian using a covariance matrix. This modelling, as reported in Ch. 4, can result in the reduced overall age uncertainties if $^{14}$C dates are included. Additionally, the systematic unshared error was decreased when the stratigraphic error was included in our model similar to the observation reported by Rhodes et al. (2003).

For the site of Mirak, the relative errors on the final ages ranged from 9 % to 16 %. In this case, the systematic error (around 2 % see Ch. 3) is small compared to the random error. However, including the stratigraphic constraints in our Bayesian model, the error was reduced to 6 % to 13 %. For the site of Ghār-e Boof, the relative error on each age (ranging from 4 % to 5 %) is smaller in comparison with the outcome of the site of Mirak. Incorporation of the stratigraphic constraints and $^{14}$C dates resulted in relative errors ranging from 1 % to 4 %, which is a significant improvement in precision compared to the minimum possible error expected to be obtained in luminescence dating (around 5 %).

### 6.1.3 Luminescence-based chronologies in prehistoric context

The establishment of new chronologies of Middle-Upper Palaeolithic sites in Iran in this thesis resulted in new insight into the timing of human presence in the region. Three central studies were carried out to determine chronologies using Bayesian modelling for Palaeolithic sites in three different regional settings.

The Palaeolithic study for the site of Mirak (Ch. 3) presents the first chronological framework for the northern edge of the central desert. This is of particular interest as it is a supposedly attractive corridor for human dispersal. I have obtained the age range of 21–28 ka associated with the Upper Palaeolithic culture for the site of Mirak. However, due to the possibility of sediment reworking and sparse occurrence of *in situ* assemblages, attribution of this period to the Upper Palaeolithic culture of that region should be done cautiously.

This age range, however, is consistent with two preliminary ages produced from the Upper Palaeolithic site of Delazian (21–25 ka and 25–30 ka) (Sec. C.2). Both age ranges seem to be younger than the chronology determined for the site of Garm roud (28–35 cal. ka BP, Berillon et al. 2007; Antoine et al. 2016) located on the northern foothills of the Alborz Mountains. Our established chronology for the edge of the central Iranian desert was also much younger compared to chronological data associated with the Upper Palaeolithic in Zagros. I can cite, for example, our chronology for the Upper Palaeolithic assemblages of Ghār-e Boof (37–42 ka), Kaldar cave (37-39 ka cal. BP, 42–44 ka cal. BP, Bazgir et al. 2017), and Yafteh cave (ca 35–42 ka cal. BP, Otte et al. 2011) located in the central Zagros Mountains. Based on the chronological findings, it appears that early Upper Palaeolithic cultures are observed more often in the Zagros region. Further archaeological research is required to address the chronological differences between Upper Palaeolithic culture in the proximity of the central Iranian desert and Zagros. This was beyond the scope of this thesis.

Our study for the site of Bawa Yawan (Ch. 4) rendered the first luminescence-based Epipalaeolithic age (12–16 ka) in Iran, which was in agreement with $^{14}$C ages for this site. Prior to this, no Epipalaeolithic chronology had been published for Iranian sites. Despite this, the age range I present here is consistent with the established period of the Epipalaeolithic culture in the Levant (23/22–11.5 ka cal. BP in Bar-Yosef and Belfer-Cohen 2010).

In general, chronological data attributed to the Middle Palaeolithic culture in Iran is limited to the age of ca 124 ± 3 ka (U/Th dating), corresponding to the Mousterian industry for the site of Mar Tarik, central Zagros (Jaubert et al., 2009). This age is older than the ages I have obtained for the Middle Palaeolithic assemblages at Mirak (43–55 ka). The chronological outcome associated with Middle Palaeolithic culture for the site of Ghār-e Boof in southern Zagros framed 44–84 ka (CI: 95 %), and for the central Zagros site of Bawa Yawan, the range extends from 56–90 ka. In light of the chronology presented, it would be an exciting future topic to compare the lithic techno-complexes of the sites Mar-Tarik and Bawa Yawan, given the are both located in the Kermanshah Province, separated by only ca 50 km. However, as mentioned above, the preliminary luminescence ages obtained for the Middle Palaeolithic assemblages from Bawa Yawan, are still under debate due to discrepancies between luminescence and $^{14}$C ages from the same units. It is possible that both luminescence dating and $^{14}$C provided correct ages, but that they refer to different events. Here, it is important to understand the reason behind the age discrepancies

before the results can be published.

Additionally, single-grain measurements on 20–41 $\mu$m[1] grains were undertaken to decrease the numbers of grains measured at once, allowing a better understanding of the possible overdispersion due to the $\alpha$- or the $\beta$-dose rate heterogeneity. This work is still in progress, and results will be presented in future papers. Further analysis will likely be required to investigate the reasons of $\alpha$-, and $\beta$-dose rate heterogeneity and to consider their effect on ages through dose rate modelling (e.g., with *DosiVox*, Martin et al. 2015).

The transition from the Middle to the Upper Palaeolithic period is a controversial as it coincided with the demise of Neanderthal and dominance of AMH. From a techno-typological perspective, this particular culture is found where underlying Mousterian assemblages shift consistently towards early Upper Palaeolithic assemblages (e.g., blade production) (Bar-Yosef and Belfer-Cohen, 2010). Thus, the lithic artefacts associated with the transition period reflects some features of Mousterian and blade production.

The Intermediate layer in Mirak, which contains both Middle and Upper Palaeolithic industries, did not seem to provide enough evidence to indicate such a transition. The Upper Palaeolithic assemblages on the top were very sparse (Berillon et al., 2017; Nasab et al., 2019). Here, the possibility of post-depositional mixing also cannot be ruled out. Moreover, the age 26–33 ka for this layer seems to be young compared to current beliefs about the transition period out of Iran ca 50–40 ka (Shea, 2003; Bar-Yosef and Belfer-Cohen, 2010). Ghār-e Boof, the presence of both Middle and Upper Palaeolithic assemblages in sublayers AH IVc and AH IVd with the age interval of 44–50 ka (CI: 95 %) might reflect a transition from Middle to Upper Palaeolithic. However, underlying Middle Palaeolithic assemblages here are also sparse (Bretzke and Conard, 2017; Conard and Zeidi, 2019; Zeidi and Conard, 2019). Further techno-typological-analysis is required to address this possibility adequately.

### 6.1.4 Human migration routes

Figure 1.4 illustrates the chronologies obtained for the investigated Palaeolithic sites in this thesis. Luminescence dating has been successfully tested on quartz and feldspar sediments samples from various sites. However, due to the limitation of such chronological datasets (on top of a few available chronologies already existing for the Iranian plateau) in the current stage, this thesis can only weakly verify the validity of the envisaged human dispersal routes from a dating perspective. The only chronology available for the dispersal route crossing the margin of the central Iranian desert is restricted to the site of Mirak with two additional, but preliminary, ages established for the site of Delazian.

Interpretations have been even more difficult since the originality of the assemblages attributed

[1] In light of the grain size it might be better to apply the term 'micro-aliquot' since there are several grains in the 150 $\mu$m diameter hole of the single grain discs.

to the Upper Palaeolithic site of Mirak is not trustworthy (it might have been affected by reworking). For the Middle-Upper assemblages in the middle of the profile, the upper sublayer could still represent the reworked material, and the second underlying assemblage likely refers to the original in situ findings. The Middle Palaeolithic assemblages at the bottom of the sequence at Mirak are preserved better, which might be attributed to the presence of Neanderthals very late in the Middle Palaeolithic period.

In the southern Zagros, where the site of Ghār-e Boof is located, the exact difference between the techno complex of the top and the bottom of the sequence confirms the presence of different groups of species in that site. The unique location of Ghār-e Boof in the southern Zagros, and close to the Persian Gulf makes the site a suitable candidate, sheltering humans who might have migrated from the Levant and Arabian Peninsula, towards central Asia through the south of Iran. However, the concentration of the assemblages associated with the Middle Palaeolithic is not as dense as the Upper Palaeolithic; thus, it is not straightforward to connect these findings at the current stage to either Neanderthals or modern humans, and more investigation is required. However, the results presented here exhibit the first stratified chronology comprising numbers of samples associated with the Middle Palaeolithic culture at in the south of Iran.

In the central Zagros, the site of Bawa Yawan is located in a unique place where one of the most complete Neanderthal skeletons was found, approximately 500 km to the north in Iraqi Kurdistan at Shanidar cave. Both sites of Bawa Yawan and Shanidar, on top of the Middle Palaeolithic assemblages, render techno-typical tools associated with the Upper Palaeolithic period. Hence, further investigation, particularly dating, might shed light on the Neanderthal disappearance in north-central Zagros over time. Additional ages are advantageous to reveal the local migration routes crossing the valleys in Zagros, contributing to the broader picture of Neanderthal migration towards the east of the Levant.

## 6.2 Limits and future perspectives

In this final section, I present, a few thoughts on the relevance of the obtained chronologies and their significance to a controversial topic like ‘transition’ from Middle to Upper Palaeolithic. It is clear that to sufficiently address such a question, many other factors and information, including detailed typo-technological and taxonomic studies, are required. Moreover, although this thesis provided a brief overview on the limited chronological data available, a comparison of these results simply in terms of the Palaeolithic period the samples were attributed, rather than incorporating detailed knowledge on the assemblages, cannot lead to accurate conclusions.

Analysis of chronological data for sites located in completely different environments of the central, west and southwest of Iran has the advantage of being able to detail a diverse picture across space. However, if one focused on a single region and established a chronology for several

sites there (for example along with one of the supposed corridors of human dispersal), a better comparison of technological assemblages and probable cultural exchanges might be possible, and it may also lead to a better simulation of human dispersal routes in a broader context. Such a study, if combined with palaeoclimate studies, may provide more pieces to the puzzles of human dispersal over time and space.

This thesis tested Bayesian models in detail and applied the various models implemented in the software 'BayLum'. I showed that use of Gaussian or lognormal distributions resulted in more accurate central doses (or palaeodoses) where insufficient bleaching or post-depositional issues can be excluded. However, development of models to address these two latter issues would improve 'BayLum' as a tool for Bayesian data analysis in different depositional environments. This would make it more appropriate for the reality of situations faces in luminescence-dating. The first steps in this direction were made by Christophe et al. (2018) and Peng (2020) who attempted to tackle cases of insufficient bleaching using Bayesian inference. However, the first approach was not incorporated into 'BayLum' before the end of this thesis, and the work by Peng (2020) was published only a few weeks before the thesis deadline. As a result, neither could be tested.

Nevertheless, in the case of the samples analysed in this thesis, insufficient bleaching of quartz grains did not seem to be an issue. For all three chronological studies, post-IR $IRSL_{290}$ signals from K-feldspar were measured to provide insight into the bleaching history of the sediment (due to faster beach rate of quartz OSL signal compared to IRSL signal from K-feldspar). General agreement between determined ages from both protocols implied sufficient bleaching of quartz grains for the sites of Ghār-e Boof and Bawa Yawan. In Mirak, however, feldspar ages were older than corresponding quartz ages. However, this did not necessarily imply insufficient bleaching of the quartz grains, as there was consistency between quartz ages and the alluvial nature of the sediments could explain the insufficient bleaching seen in K-feldspar grains.

In this thesis, modelling systematic shared errors derived from the dose-rate estimation, was mainly limited to $\beta$- and $\gamma$-dose-rates. The $\alpha$-dose-rate for quartz grains with the size of 41–60 $\mu$m in Ghār-e Boof' samples was calculated, but its contribution to the total dose rate (ca 5 %) was not significant, and so was not modelled in the Theta matrix. However, when considering smaller grains, $\alpha$-dose rates should be considered. This would require future versions of the Theta matrix in 'BayLum' to include $\alpha$-efficiency.

One personal recollection at the end of this thesis is that Bayesian modelling requires an in-depth understanding of each step of the calculation. If this understanding is not fully developed, this modelling can be error-prone and lead to incorrect results and conclusions. For example, in Ch. 2, by applying Bayesian models to data obtained from a dose-recovery experiment, with equivalent doses close to the signal saturation limited of quartz, I can obtain an accurate result (compared to underestimated ratio using a frequentist approach). However, as I detailed, this

improvement was accomplished only because the fitting parameters of the dose-response curve were modelled to sample from a truncated Gaussian distribution in which the upper part was not limited. Therefore, although from a physical perspective, the luminescence signal might be in saturation, the model still generates dose-response curves with large $D_0$ values. In other words, running such a model will always lead to a result (here a $D_e$). While in our study, the controlled doses allowed us to assess the accuracy of the result, a question that might arise here is: How much confidence do I have in the outcome for 'real' cases where the true central dose is unknown? Moreover, what is the real dose limitation of this method? Here, it is important to consider that statistical data treatment cannot overcome physical limitations. That being said, although the outcome might seem acceptable, the value might be inaccurate. Thus, the results should always be verified, e.g. by comparison with the outcome of other protocols or the other dating methods.

Another similar example relates to age calculations using models with stratigraphic constraints but without including a Theta matrix, as discussed in Ch. 3. These calculations obtained precise but inaccurate numerical results, as the model did not consider the nature of the systematic shared errors.

Due to the strong effect of stratigraphic order as a prior in Bayesian inference, it should be applied cautiously. This would be important in a case in which one wants to incorporate stratigraphic ordering in the presented Bayesian model to estimate the ages of two samples belonging to one unit or two consecutive units located at the edge of each unit. In such a situation, to satisfy the sample ordering, the age of the sample from the upper unit will always be younger, and the age of the lower sample will be older. However, if those units were accumulated over a short time (below the temporal resolution of luminescence dating), then applying the stratigraphic ordering might result in an underestimated age for the upper sample and an overestimated age for the lower sample.

The Theta matrix function was implemented in 'BayLum' for dating study of Mirak, in which it assumed that the $\gamma$- and $\beta$-dose rate were determined in the lab. In the dating study for Ghār-e Boof, however, *in situ* $\gamma$-dose rate measurements were also considered in the function. Although the general idea of the covariance age matrix and formulation as described in Combès and Philippe (2017) can be applied to any age sequence, the source of uncertainty should be precisely defined according to the instrument or any general assumption which can lead to a systematic error (e.g. internal does rate or $\alpha$-efficiency). Thus, any Theta matrix should precisely reflect the source of systematic shared error accordingly to its measurements and assumptions (not necessarily similar to the one used in this thesis); otherwise one can end up with an erroneous result.

It should be noted here that other tools for Bayesian modelling exist. Tools to provide data analysis for chronological data in archaeology include *OxCal* (Ramsey, 1995) and *Chronomodel*

(Lanos and Dufresne, 2019). While applying these tools was not possible in the framework of this thesis, it would be interesting to employ all three models (*OxCal*, *Chronomodel*, and 'BayLum') on one set of data and assess similarities and differences. In particular, comparison of luminescence chronologies obtained through each tool could be used to investigate the importance of modelling systematic shared error on the accuracy and precision of final chronology.

One last important point that should be considered is that running Bayesian modelling, at least as implemented in 'BayLum', requires a powerful computational environment to obtain precise results. In most instances, these calculations required a multi-core workstation, and was not possible to undertake on an ordinary laptop. Despite this more appropriate hardware, computations for each series of samples might take more than a week to return the first results.

Bayesian and frequentist approaches both have their own advantages and justifications, and this thesis should not leave the reader with the impression that Bayesian statistics outweighs or negates other methods of data treatment. The evident improvement in the precision of Bayesian models is achieved when the sampling resolution adequately allows age intervals that overlap one another and when other independent data such as $^{14}$C ages are incorporated. This improvement in particular is of interest to estimate precisely the transition period, which is vital for Palaeolithic studies. Besides, due to a larger temporal limit of luminescence dating compared to $^{14}$C dates, it can provide a complete chronology from Middle to the Upper Palaeolithic to obtain a comprehensive picture of both periods over time.

In the absence of such information, however, the difference between Bayesian and frequentist chronologies would be negligible. Considering a lengthy process and time-consuming computation required for the Bayesian approach, there will be cases in which frequentist models are preferred. For estimation of the central dose in the case of signal saturation or positively skewed dose distribution (due to $\beta$-heterogeneity), however, Bayesian models are most commonly favourable compared to the frequentist models.

To conclude, it should be noted that although this thesis has compared chronologies obtained from Bayesian and frequentist models to discuss precision, it is necessary to test these statistical tools against reference data to address the matter adequately. This was not part of my thesis, but it could be an interesting topic pursue in the future.

## References

Antoine, P., Bahain, J. J., Ghaleb, B., and Mercier, N.: The chronostratigraphic framework at Garm roud, in: Garm Roud. A Hunting Place in Iran, Upper Palaeolithic, edited by Berillon, G. and Asgari Khanegah, A., pp. 49–55, 2016.

Bar-Yosef, O. and Belfer-Cohen, A.: The Levantine Upper Palaeolithic and Epipalaeolithic, in: South-Eastern Mediterranean Peoples Between 130,000 and 10,000 Years Ago, edited by Garcea, E. A. A., pp. 144–167, Oxbow Books, 2010.

Bazgir, B., Ollé, A., Tumung, L., Becerra-Valdivia, L., Douka, K., Higham, T., van der Made, J., Picin, A., Saladié, P., López-García, J. M., Blain, H.-A., Allue, E., Fernández-García, M., Rey-Rodríguez, I., Arceredillo, D., Bahrololoumi, F., Azimi, M., Otte, M., and Carbonell, E.: Understanding the emergence of modern humans and the disappearance of Neanderthals: Insights from Kaldar Cave (Khorramabad Valley, Western Iran), Scientific Reports, 7, 525–16, 2017.

Berillon, G., Asgari Khaneghah, A., Antoine, P., Bahain, J.-J., Chevrier, B., Zeitoun, V., Aminzadeh, N., Beheshti, M., Chanzanagh, H. E., and Nochadi, S.: Discovery of new open-air Paleolithic localities in Central Alborz, Northern Iran, Journal of Human Evolution, 52, 380–387, 2007.

Berillon, G., Nasab, H. V., Asgari Khaneghah, A., Jamet, G., Akhavan, M., Guérin, G., Heydari, M., Anvari, Z., Auguste, P., Bonilauri, S., Chevrier, B., Zeitoun, V., Mohammadkhani, K., Hashemi, M., Jayez, M., and Darvishi, J.: *Fouille du site Mirak 8:* Rapport Annuel. Programme Paléoanthropologique Franco-Iranien (FIPP), Tech. rep., 2017.

Bretzke, K. and Conard, N. J.: Not Just a Crossroad: Population Dynamics and Changing Material Culture in Southwestern Asia during the Late Pleistocene, Current Anthropology, 58, S449–S462, 2017.

Christophe, C., Philippe, A., Guérin, G., Mercier, N., and Guibert, P.: Bayesian approach to OSL dating of poorly bleached sediment samples: Mixture Distribution Models for Dose (MD 2 ), Radiation Measurements, 108, 59–73, 2018.

Combès, B. and Philippe, A.: Bayesian analysis of individual and systematic multiplicative errors for estimating ages with stratigraphic constraints in optically stimulated luminescence dating, Quaternary Geochronology, 39, 24–34, 2017.

Conard, N. J. and Zeidi, M.: New research on the Paleolithic occupation of Ghar-e Boof, Fars Province, Archaeology, Journal of the Iranian Center for Archaeological Research, 2, 7–16, 2019.

Duller, G. A. T.: Assessing the error on equivalent dose estimates derived from single aliquot regenerative dose measurements, Ancient TL, 25, 15–24, 2007.

Heydari, M. and Guérin, G.: OSL signal saturation and dose rate variability: Investigating the behaviour of different statistical models, Radiation Measurements, 120, 96–103, 2018.

Heydari, M., Guérin, G., Kreutzer, S., Jamet, G., Kharazian, M. A., Hashemi, M., Nasab, H. V., and Berillon, G.: Do Bayesian methods lead to more precise chronologies? 'BayLum' and a first OSL-based chronology for the Palaeolithic open-air site of Mirak (Iran), Quaternary Geochronology, 59, 101 082, 2020.

Jaubert, J., Biglari, F., Mourre, V., Bruxelles, L., Bordes, J. G., Shidrang, S., Naderi, R., Mashkour, M., Maureille, B., Mallye, J. B., Quinif, Y., Rendu, W., and Laroulandie, V.: The Middle Paleolithic occupation of Mar-Tarik, a new Zagros Mousterian site in Bisotun massif (Kerman-shah, Iran), in: Iran Paleolithic, Le Paléolithique d'Iran, edited by Otte, M., Biglari, F., and Jaubert, J., pp. 7–27, Bar International Series, 2009.

Lanos, P. and Dufresne, P.: Chronomodel version 2.0: Software for Chronological Modelling of Archaeological Data using Bayesian Statistics., 2019.

Martin, L., Incerti, S., and Mercier, N.: DosiVox: Implementing Geant 4-based software for dosimetry simulations relevant to luminescence and ESR dating techniques , Ancient TL, 33, 1–10, 2015.

Millard, A. R.: Bayesian analysis of ESR dates, with application to Border Cave, Quaternary Geochronology, 1, 159–166, 2006.

Murray, A. S. and Olley, J. M.: Precision and Accuracy in the optically stimulated luminescence dating of sedimentary quartz: a status review, Geochronometria, 21, 1–16, 2002.

Nasab, H. V., Berillon, G., Jamet, G., Hashemi, M., Jayez, M., Khaksar, S., Anvari, Z., Guérin, G., Heydari, M., Kharazian, M. A., Puaud, S., Bonilauri, S., Zeitoun, V., Sévêque, N., Khatooni, J. D., and Asgari Khaneghah, A.: The open-air Paleolithic site of Mirak, northern edge of the Iranian Central Desert (Semnan, Iran): Evidence of repeated human occupations during the late Pleistocene, Comptes Rendus Palevol, 18, 465–478, 2019.

Otte, M., Shidrang, S., Zwyns, N., and Flas, D.: New radiocarbon dates for the Zagros Aurignacian from Yafteh cave, Iran, Journal of Human Evolution, 61, 340–346, 2011.

Peng, J.: Analyzing statistical age models to determine the equivalent dose and burial age using a Markov chain Monte Carlo method, Geochronometria, 0, 1–14, 2020.

Philippe, A., Guérin, G., and Kreutzer, S.: BayLum - An R package for Bayesian analysis of OSL ages: An introduction, Quaternary Geochronology, 49, 16–24, 2019.

Ramsey, C. B.: Radiocarbon Calibration and Analysis of Stratigraphy: The OxCal Program, Radiocarbon, 37, 425–430, 1995.

Rhodes, E. J., Bronk Ramsey, C., Outram, Z., Batt, C., Willis, L., Dockrill, S., and Bond, J.: Bayesian methods applied to the interpretation of multiple OSL dates: high precision sediment ages from Old Scatness Broch excavations, Shetland Isles, Quaternary Science Reviews, 22, 1231–1244, 2003.

Shea, J. J.: The Middle Paleolithic of the East Mediterranean Levant, Journal of World Prehistory, 17, 313–394, 2003.

Zeidi, M. and Conard, N. J.: The forth season report of survey at Ghār-e Boof in city of Rostam at Fars Province, th Annual Symposium of the Iranian Archaeology, in Persian, 234–238, 2019.

# Acknowledgements

The work in this thesis was gratefully funded by the LaScArBx LabEx supported by the ANR - n° ANR-10-LABX-52. Dr Pierre Guibert and Dr Guillaume Guérin are thanked for the initial project.

I am grateful to Dr Chantal Tribolo for being available, supportive and for providing early versions of manuscripts and this thesis with constructive comments and corrections.

I am grateful for the support I have received from Prof Nicholas Conard and Dr Mohsen Zeidi, Dr Gilles Berillon, Dr Hamed Vahdati Nasab and Dr Saman Heydari-Guran and their team in the field in Iran. Thanks also go to Saman Hamzavi for sending the sediment samples of Ghār-e Boof from Iran.

Merci beaucoup to Julie Faure, Virginie Moineau and Yannick Lefrais for their support in the lab.

Pierre Selva was never tired of fixing various computer problems, and he stood up for me when things got complicated.

Ourida Gaucher was always kind to me and very carrying when my motivation started to fade. Merci pour le soutien moral !

Dr Sebastian Kreutzer inspired my thoughts regarding the maps shown in this thesis turned them into such beautiful pictures. Sebastian also used LaTeX and black magic to create a lovely PDF out of my Word document mess.

Special thanks to Barbara Seray for so professionally working on my French and for the last moment translation of my English summary into French. Ella Walsh minimised the readers' pain by carefully proof-reading this thesis.

Anaël and Vigo patiently talked to me French and generously ignored all my mistakes. Thanks also goes to Chantal & Xavier, Nadia, Nino, Louise for baking cookies and crêpes.

I am happy to have met you, Loïc, Damiza, Sara, Faizah, Sheida, Roshanak, Maïlys, Anna and Léna. Thank you for all the pleasant and funny moments we shared together in Bordeaux.

I am very grateful to my parents, who financially supported my research stay 2016 in France, which finally allowed me to apply for the PhD position at the IRAMAT-CRP2A. Finally, my sincere gratitude goes to my family. Despite the long distance between us, their love and support never faded.

# Appendix - Contents

# A List of other scientific output

***Other scientific output during the time of the PhD thesis***

***Co-author contributions to peer-reviewed publications***

Nasab, H.V., Berillon, G., Jamet, G., Hashemi, M., Jayez, M., Khaksar, S., Anvari, Z., Guérin, G., Heydari, M., Kharazian, M.A., Puaud, S., Bonilauri, S., Zeitoun, V., Sévêque, N., Khatooni, J.D., Khaneghah, A.A. The open-air Paleolithic site of Mirak, northern edge of the Iranian Central Desert (Semnan, Iran): Evidence of repeated human occupations during the late Pleistocene. Comptes Rendus Palevol 18(4), 465–478, 2019. DOI: `https://doi.org/10.1016/j.crpv.2019.02.005`.

Akhavan Kharazian, M., Jamet, G., Puaud, S., Heydari, M., Guérin, G., Hashemi, M., Vahdati Nasab, H., Berillon, G. Geological-archeological study of the Mirk area (Semnan, Iran) using sedimentological and physico-chemical analyzes. Quaternery Journal of Iran 4(3). (in Farsi), 273–290, 2018.

Hashemi, M., Vahdati Nasab, H., Berillon, G., Jamet, G., Azizi, Q., Jayez, Q., Guérin, G., Heydari, M., Akhavan Kharazian, M., Nateghi, A., Abdollahi, A. The Late Pleistocene in the Northern fringes of Iranian Central Desert and the Formation of Archaeological Sites; Case Study: Mirak, Semnan. Quaternary Journal of Iran 3(12). (in Farsi), 405–430, 2018.

Tillier, A.M., Sirakov, N., Guadelli, A., Fernandez, P., Sirakova, S., Dimitrova, I., Ferrier, C., Guérin, G., Heidari, M., Krumov, I., Leblanc, J. C., Miteva, V., Popov, V., Taneva, S., Guadelli, J.L. Evidence of Neanderthals in the Balkans: The infant ra- dius from Kozarnika Cave (Bulgaria). Journal of Human Evolution 111. 54–62, 2017. DOI: `https://doi.org/10.1016/j.jhevol.2017.06.002`

***Conference contributions***

Heydari, M., Guérin, G., Berillon, G., Jamet, G., Hashemi, M., Vahdati-Nasab. Dating the Middle to Upper Palaeolithic in Northern Iran: an OSL-based chronology for the open air site

of Mirak, using dedicated Bayesian modelling. Poster presentation at the 8th Annual European Society for the study of Human Evolution (ESHE) meeting, 13.-15.09.2018. Faro, Portugal, 2018.

Heydari, M., Guérin, G., Christophe, C. OSL signal saturation and dose rate variability: Investigating the behaviour of different statistical models. Oral presentation at the International conference on Luminescence Dating and Electron Spin Resonance (LED). 11.-15.09.2017. Cape Town, South Africa, 2017.

Heydari, M., Guérin, G., Sirakov, N., Sirakova, S., Guadelli, A., Guadelli, J.L., Taneva, S., Dimitrova, I.Luminescence dating applied to the chronology of the Kozarnika cave: comparing various luminescence signals (OSL, IR50, pIRIR290, VSL). Poster presentation at the UK LED 11.-13.07.2016. Liverpool, United Kingdom. 2016

# B Additional figures

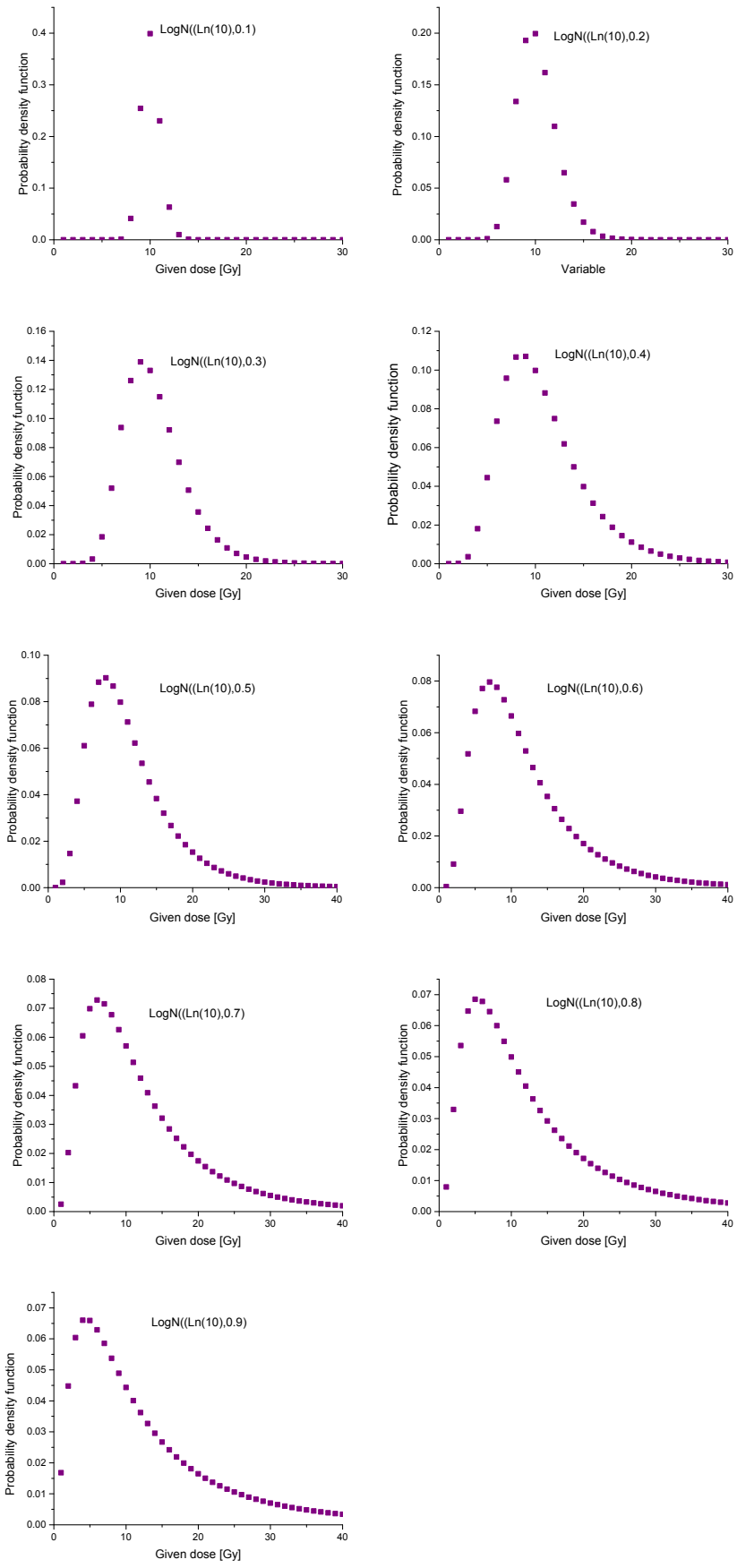


Figure B.1: Construction lognormal distributions with different dispersion values.

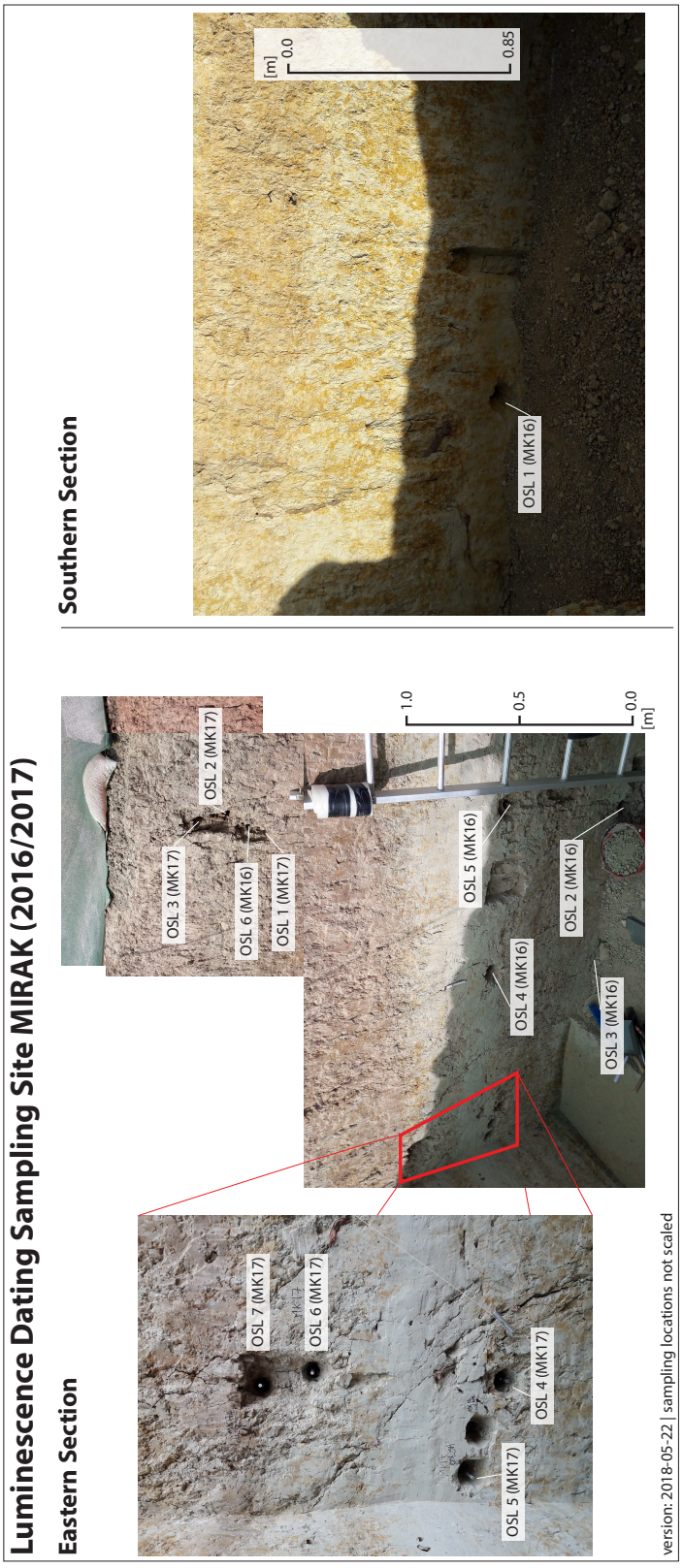


Figure B.2: Profile photos site Mirak with indicated OSL sampling positions for the east and the south trench. Photos: M. Heydari.

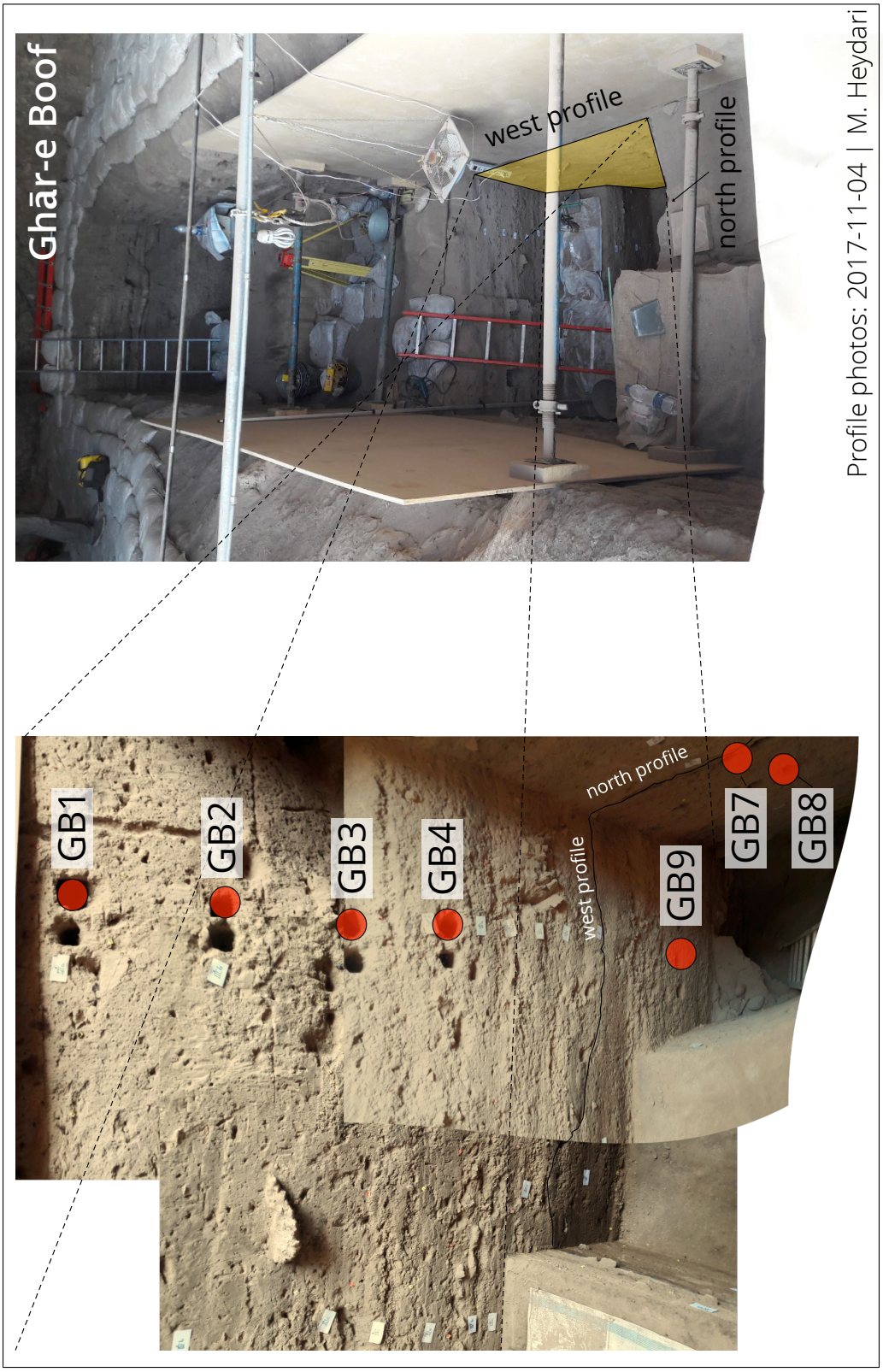


Figure B.3: Profile photos site Ghāre-Boof with some of the luminescence sampling positions indicated at the west and north profile. Photos: M. Heydari.

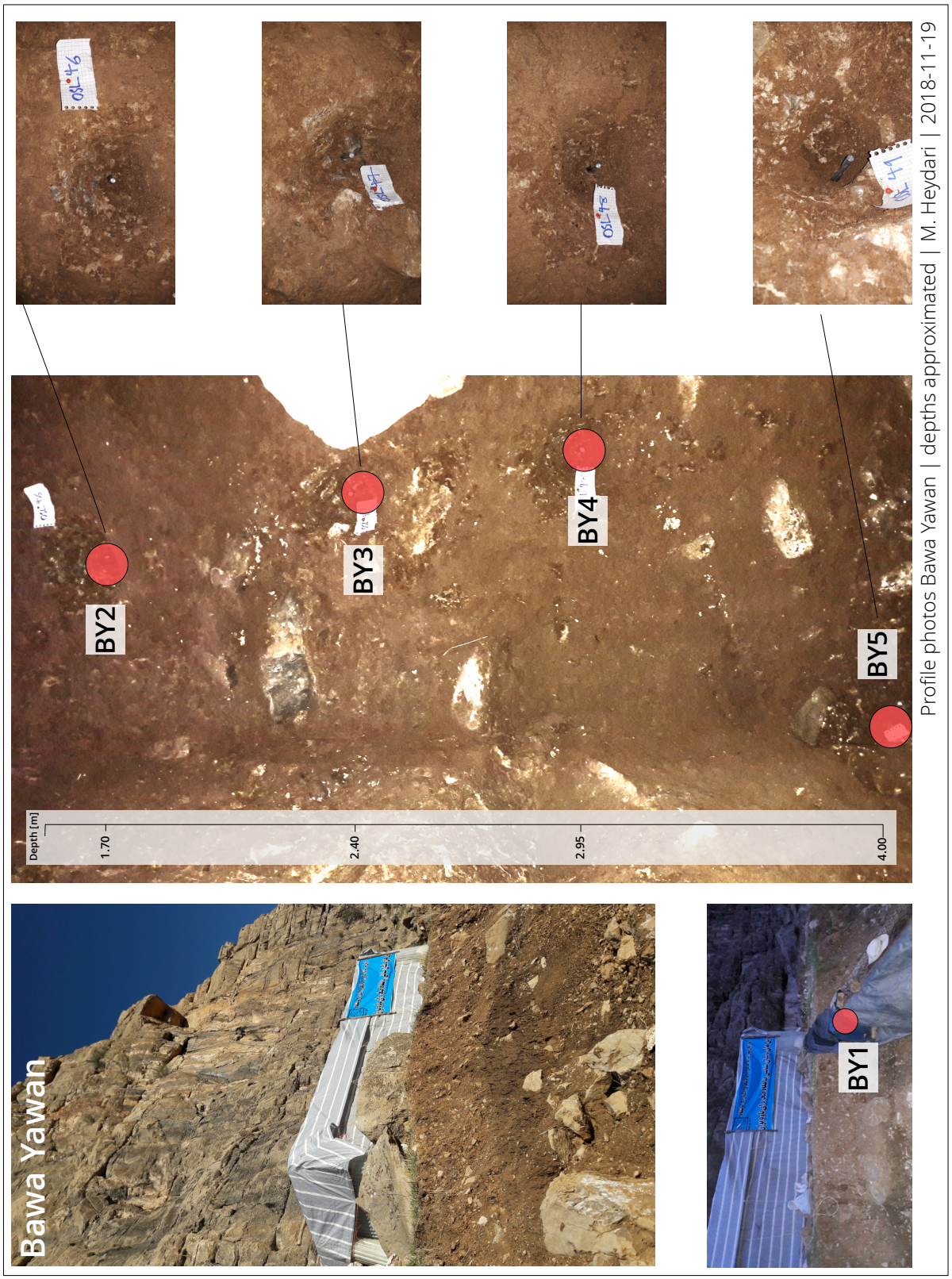


Figure B.4: Profile photos site Bawa Yawan with luminescence sampling positions. Photos: M. Heydari.

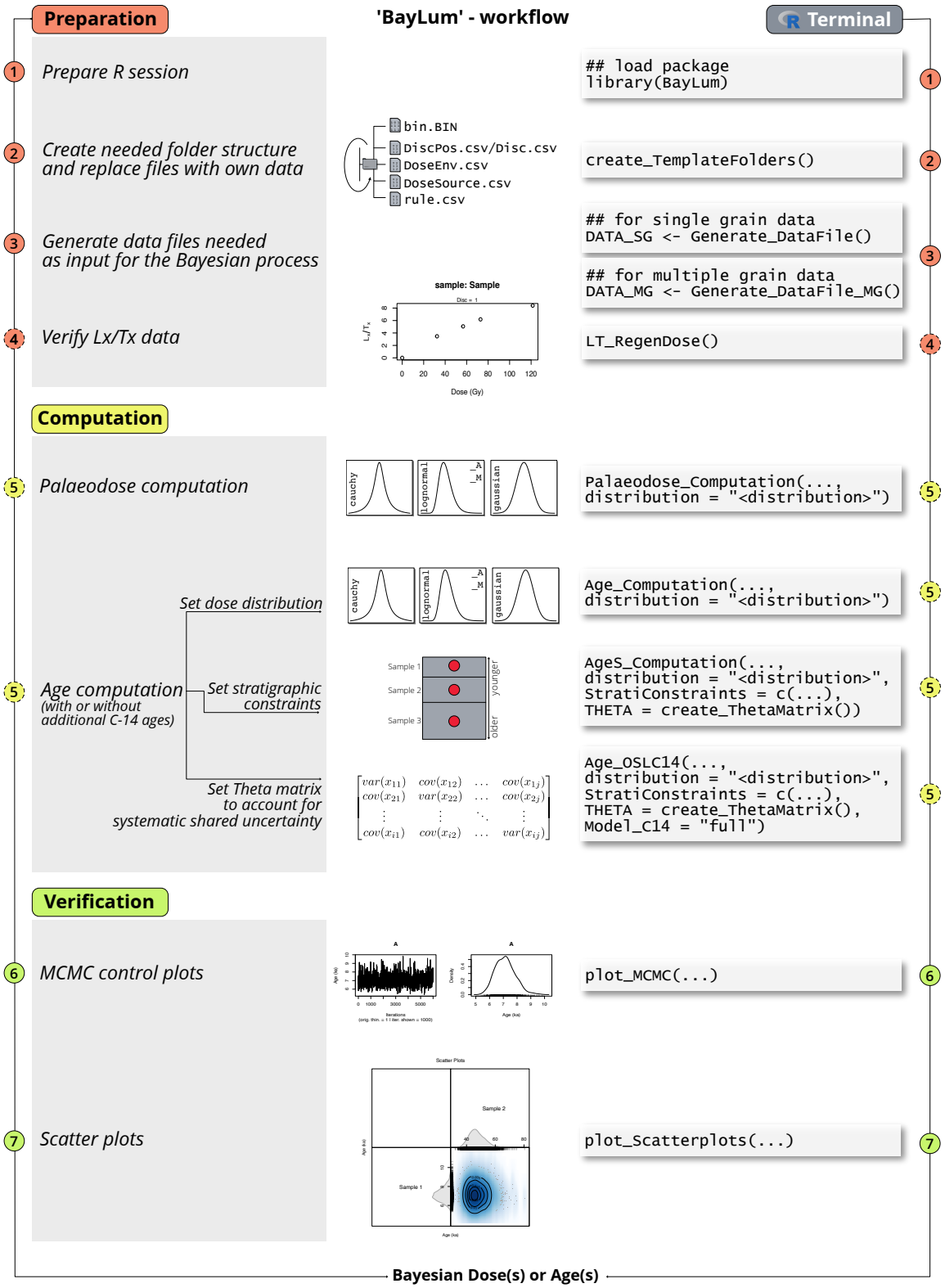


Figure B.5: Workflow chart 'BayLum'.

# C Additional dating results

## C.1 Mirak - pit S2

Here the age information of two samples (Mk17-8 and Mk17-9) from pit S2 are listed. The age of sample Mk15-8 belonging to the pit was presented as part of the study in Ch. 3.

Table C.1: Estimated radioisotope concentrations using $\gamma$-ray spectrometry Mirak pit S2.

| **Sample** | **K** (%) | $\mathbf{U_{pre\text{-}Ra}}$ (ppm) | $\mathbf{U_{post\text{-}Ra}}$ (ppm) | **Th** (ppm) |
|---|---|---|---|---|
| Mk17-8 | $1.51 \pm 0.03$ | $2.13 \pm 0.17$ | $1.90 \pm 0.03$ | $5.80 \pm 0.10$ |
| Mk17-9 | $2.10 \pm 0.04$ | $2.67 \pm 0.20$ | $3.12 \pm 0.04$ | $13.20 \pm 0.15$ |

Table C.2: Estimated dose-rates and equivalent doses for two samples. The water contacts for samples Mir 8 and Mir 9 are $4 \pm 2$ % and $22 \pm 9$ %.

| **Sample** | $\dot{D}_{int}$ (Gy ka$^{-1}$) | $\sigma$ | $\dot{D}_{\gamma}$ (Gy ka$^{-1}$) | $\sigma$ | $\dot{D}_{\beta}$ (Gy ka$^{-1}$) | $\sigma$ | $\dot{D}_{cosm.}$ (Gy ka$^{-1}$) | $\sigma$ | $\dot{D}_{total}$ (Gy ka$^{-1}$) | $\sigma$ | $D_e$ (Gy) | $\sigma$ | **Age** (ka) | $\sigma$ |
|---|---|---|---|---|---|---|---|---|---|---|---|---|---|---|
| Mk17-8 | 0.06 | 0.03 | 0.83 | 0.01 | 1.45 | 0.03 | 0.15 | 0.02 | 2.49 | 0.05 | 96 | 3 | 38 | 2 |
| Mk17-9 | 0.06 | 0.03 | 1.19 | 0.06 | 1.78 | 0.11 | 0.14 | 0.02 | 3.18 | 0.13 | 232 | 10 | 73 | 5 |

## C.2 Delazian

The open-air site of Delazian is located at the edge of central Iranian desert (Dasht-e Kavir) close to the open-air site of Mirak in Semnan province (Fig. 1.1). Several mounds are observed in the area, and lithic artefacts are exposed on the surface by to deflation (the same pattern as in Mirak area, Ch. 3). The surface investigation on lithic artefact revealed that the human occupation attributed to the Upper Palaeolithic period (Vahdati Nasab and Clark, 2014). Two blocks of sediments were taken to get an idea about the occupation time. The OSL ages of these two samples resulted in 21–25 ka and the older one 25–30 ka. The tables below list the result of equivalent doses, dose-rate and obtained ages. The dating procedure (sample preparation and data analysis using the frequentist approach) was similar to the procedure applied to the Mirak samples.

Table C.3: Estimated radioisotope concentrations using $\gamma$-ray spectrometry Delazian.

| **Sample** | **K** (%) | **$U_{pre\text{-}Ra}$** (ppm) | **$U_{post\text{-}Ra}$** (ppm) | **Th** (ppm) |
|---|---|---|---|---|
| Delazian 1 | $1.82 \pm 0.03$ | $2.31 \pm 0.16$ | $2.22 \pm 0.03$ | $7.30 \pm 0.10$ |
| Delazian 2 | $1.61 \pm 0.03$ | $2.30 \pm 0.17$ | $2.06 \pm 0.04$ | $6.80 \pm 0.11$ |

Table C.4: Estimated dose-rates, equivalent doses and ages Delazian.

| **Sample** | $\dot{D}_{int}$ | $\sigma$ | $\dot{D}_{\gamma}$ | $\sigma$ | $\dot{D}_{\beta}$ | $\sigma$ | $\dot{D}_{cosm.}$ | $\sigma$ | $\dot{D}_{total}$ | $\sigma$ | $D_e$ | $\sigma$ | **Age** | $\sigma$ |
|---|---|---|---|---|---|---|---|---|---|---|---|---|---|---|
| | (Gy ka$^{-1}$) | | (Gy ka$^{-1}$) | | (Gy ka$^{-1}$) | | (Gy ka$^{-1}$) | | (Gy ka$^{-1}$) | | (Gy) | | (ka) | |
| Delazian1 | 0.06 | 0.03 | 0.99 | 0.03 | 1.73 | 0.08 | 0.15 | 0.02 | 2.93 | 0.09 | 81 | 3 | 28 | 1 |
| Delazian2 | 0.06 | 0.03 | 0.91 | 0.03 | 1.56 | 0.07 | 0.15 | 0.02 | 2.67 | 0.09 | 61 | 2 | 23 | 1 |

# References

Vahdati Nasab, H., Clark, G.A. The Upper Paleolithic of the Ira-nian Central Desert: the Delazian Sites, Semnan Province–a CaseStudy. Archäologische Mitteilungen aus Iran und Turan (AMIT) 46, 1–21, 2014.

# D Additional R code

***R code used to create the data presented in Ch. 2.***

The fancy part of the code that enabled the server to send me the results via email was written by Sebastian Kreutzer.

```
##clear workspace
rm(list = ls())

##load needed packages
library(BayLum)
library(foreach)
library(doParallel)
library(mailR)

# Config ------------------------------------------------------------------

##set general path to all documents
Path <- c("/home/mheidari/CALQ/200Gy/")

##set distribution names, for each distribution one folder exist
#Distribution <- c("gaussian", "lognormal_A", "lognormal_M", "cauchy")
Distribution <- c("cauchy")

##set number of iterations, should have the same length as 'Distribution'
Iter <- c(50000,50000,50000,5000000)
Iter <- c(1e+06)
#Iter <- c(100,100,100,100)

##further settings, valid for all runs
t <- 5
Nb_chaines <- 3

##mail setting
to <- "maryam.heydari@u-bordeaux-montaigne.fr"

#=============================================================================#
# DO NOT TOUCH BEYOND THIS POINT ------------------------------------------

cat("\n-------------------------------------------------------------␣\n")
cat("Bayesian␣Processor")
cat("\n-------------------------------------------------------------␣\n")

##1st loop
for(d in 1:length(Distribution)){
```

```
40
41    ##terminal feedback
42    writeLines(paste0("Running␣calculations␣for␣", Distribution[d], "␣..."))
43
44    ##write log-file
45    write(
46      x = paste0(Sys.time(),":\tstart␣calculation␣for␣", Distribution[d]),
47      file=paste0(Path,"/process.log"),
48      append = TRUE)
49
50
51    ##set path
52    path <- paste(c(Path,Distribution[d]),collapse = "/")
53
54    ##extract folder names
55    sampleNames <- list.files(path)
56
57    ##2nd loop
58    ###use parallel processcing
59    registerDoParallel(cores=8)
60
61    foreach (i = 1:length(sampleNames)) %dopar% {
62
63      ##write log-file
64      write(
65        x = paste0(Sys.time(),":\tstart␣calculation␣for␣sample␣", sampleNames[i]),
66        file=paste0(Path,"/process.log"),
67        append = TRUE)
68
69      ##terminal feedback
70      cat(paste0("\t>>␣Sample␣", sampleNames[i], "␣...\n"))
71
72      ##get names
73      Names <-
74        list.dirs(
75          paste0(Path, "/", Distribution[d], "/", sampleNames[i]),
76          recursive = FALSE,
77          full.names = FALSE
78        )
79
80      ##Generate Data File
81      if(length(Names)!=0){
82        FolderNames <- paste0("/",sampleNames[i],"/",Names)
83        BinPerSample <- length(Names)
84
85      }else{
86        FolderNames <- paste0("/",sampleNames[i])
87        BinPerSample <- 1
88
89      }
90
91      DATA1 <- BayLum::Generate_DataFile(
92          Path = path,
```

```
93          FolderNames = FolderNames,
94          BinPerSample = BinPerSample,
95          Nb_sample = 1
96        )
97
98
99        ##set path for these results
100       results_path <-  paste(c(
101         Path, "Results", Distribution[d], sampleNames[i]
102       ), collapse = "/")
103
104       ##create needed directory
105       dir.create(
106         path =  results_path,
107         showWarnings = FALSE,
108         recursive = TRUE
109       )
110
111       ##show dose response curve
112       pdf(file = paste0(results_path,"/DRC_",Distribution[d],"_",sampleNames[i],".pdf"), paper = "a4")
113         BayLum::LT_RegenDose(
114           DATA = DATA1,
115           Path = path,
116           FolderNames = FolderNames,
117           Nb_sample = 1,
118           BinPerSample = BinPerSample
119         )
120       dev.off()
121
122       ##calculate a paleodose
123       P <- BayLum::Palaeodose_Computation(
124         DATA1,
125         SampleNames = sampleNames[i],
126         Nb_sample = 1,
127         BinPerSample = BinPerSample,
128         SavePdf = TRUE,
129         OutputFileName = paste0("MCMCplot_",Distribution[d],"_",sampleNames[i]),
130         OutputFilePath = paste0(results_path,"/"),
131         SaveEstimates = TRUE,
132         OutputTableName = paste0("_",Distribution[d],"_",sampleNames[i]),
133         OutputTablePath = paste0(results_path,"/"),
134         LIN_fit = FALSE,
135         Origin_fit = TRUE,
136         distribution = Distribution[d],
137         Iter = Iter[d],
138         t = t,
139         Nb_chaines = Nb_chaines
140       )
141
142     ##compress results in a ZIP
143     zipfile <- paste0(Path,"/",Sys.Date(), "_",Distribution[d],"_",sampleNames[i],".zip")
144     zip(zipfile = zipfile,
145       files = paste0(Path,"/Results/",Distribution[d],"/",sampleNames[i]), )
```

```
146
147     ##mail results
148     send.mail(
149       from = "maryam.heydari@u-bordeaux-montaigne.fr",
150       to = to,
151       encoding = "utf-8",
152       subject = paste0("[BayLum Processing Results] ", Distribution[d], " - ", sampleNames[i]),
153       body = paste0(
154         "Dear ",
155         system("whoami", intern = TRUE),
156         "\n\n please find attached your results for sample ", sampleNames[i], ",",
157         "\n calculated using the ", Distribution[d], " distribution! \n\n",
158         "Additionally, your results have been archived on the server.",
159         "\n\n\n - Your friendly IRAMAT-CRP2A RStudio Server - \n\n"
160       ),
161       smtp = list(
162         host.name = "smtp.u-bordeaux3.fr",
163         port = 25,
164         ssl = FALSE
165       ),
166       authenticate = FALSE,
167       send = TRUE,
168       attach.files = zipfile,
169       file.names = basename(zipfile),
170       debug = FALSE
171     )
172
173     ##write log-file
174     write(
175       x = paste0(Sys.time(),":\t", "file '",basename(zipfile), "' sent via email to ",to),
176       file=paste0(Path,"/process.log"),
177       append = TRUE)
178
179     ##remove file
180     file.remove(zipfile)
181
182   } ##end 2nd loop
183 } ##end 1st loop
184 #============================================================================#
```